

Thesis Changes Log

Name of Candidate: Mohammad Ebadi

PhD Program: Petroleum Engineering

Title of Thesis: Fluid transport in tight rocks: multi-scale AI-driven characterization paradigm

Supervisor: Assoc. Prof. Dmitry Koroteev

The thesis document includes the following changes in answer to the external review process.

According to the comments by dear reviewers, the following changes have been applied to the main body of the thesis. **ALL THE APPLIED CORRECTIONS IN THE REVISED MANUSCRIPT HAVE BEEN HIGHLIGHTED IN YELLOW.**

Line 18: The supervisor's title has been corrected.

Lines 64 – 66: The sentence has grammatically been revised.

Lines 77 – 79: The text has been added to clarify what the thesis is about.

Lines 100, 103, 105: The authors' names have been added to the title of papers published in various conferences.

Lines 267 – 270: Figure 2 has been added to the text to give the main idea behind the prepared thesis.

Lines 276 – 283: A short introduction to digital rock physics has been added to the text.

Lines 284 – 298: The objectives of the thesis have explicitly been added to the text.

Line 328: The last row of Table 1 has been corrected.

Lines 365 – 368: The storage mechanisms in shale gas resources have clearly been stated.

Lines 368 – 370: It has been mentioned how the adsorption on the surface of the clay is.

Lines 386 – 387: The coefficients have been clarified.

Line 388: The velocity direction has been determined.

Line 389: The direction of the grid cell area has been determined.

Line 390: The supposed control volume has been stated.

Lines 410 – 413: More description about kerogens has been added.

Lines 414 – 422: The nonlinear terms have been addressed.

Lines 423 – 431: The required information about different scales (Homogenization) has been provided.

Lines 442 – 479: The brief background of classic solvers has been stated.

Lines 515 – 525: The performance of PSO versus Newton's method has been discussed in more detail.

Lines 698 – 703: The reason why the output of CNNs can be better even than the original training data has been elaborated.

Lines 738 – 739: The reason why different results have been generated is discussed.

Lines 756 – 758: The dependency of pore-scale simulations to the applied method of image processing has been underlined.

Lines 775 – 778: How the downsampling mimics the imaging with lower resolutions has been explained.

Lines 790 – 792: The details of fitting a trendline into the results of downsampling have been discussed.

Lines 804 – 806: Equations mentioned in Figure 16 have been addressed.

Lines 807 – 818: A conclusion paragraph has been added to the text.

Lines 823 – 836: The abstract has been removed, and a more general introduction has been added.

Lines 837 – 838: The influence of Chapter 2 on the roadmap of the thesis has schematically been illustrated.

Lines 866 – 879: The abstract has been removed, and a more general introduction has been added.

Lines 880 – 881: The influence of Chapter 3 on the roadmap of the thesis has schematically been illustrated.

Lines 908 – 918: The abstract has been removed, and a more general introduction has been added.

Lines 919 – 920: The influence of Chapter 4 on the roadmap of the thesis has schematically been illustrated.

Lines 944 – 954: The abstract has been removed, and a more general introduction has been added.

Lines 955 – 956: The influence of Chapter 5 on the roadmap of the thesis has schematically been illustrated.

Lines 990 – 1000: The abstract has been removed, and a more general introduction has been added.

Lines 1001 – 1002: The influence of Chapter 6 on the roadmap of the thesis has schematically been illustrated.

Lines 1026 – 1091: The overall conclusions of the research and future visions and opportunities have been thoroughly discussed.

Figures 3 – 16: They have been linked to their corresponding chapters.

Figure 9: The scale has been added.

1
2
3
4
5
6
7
8
9
10
11
12
13
14
15
16
17
18
19
20
21
22
23
24

Skolkovo Institute of Science and Technology

FLUID TRANSPORT IN TIGHT ROCKS: MULTI-SCALE AI-DRIVEN
CHARACTERIZATION PARADIGM

Doctoral Thesis

by

MOHAMMAD EBADI

DOCTORAL PROGRAM IN PETROLEUM ENGINEERING

Supervisor

Associate Professor Dmitry Koroteev

Moscow - 2021

(© Mohammad Ebadi 2021)

25
26
27
28
29

30

31
32
33

34

35

36

37

38

39

40

41

42

43

I hereby declare that the work presented in this thesis was carried out by myself at Skolkovo Institute of Science and Technology, Moscow, except where due acknowledgement is made, and has not been submitted for any other degree.

Candidate (Mohammad Ebadi)
Supervisor (Prof. Dmitry Koroteev)

Abstract

44

45 Even during the period of energy transition, there is no doubt that unconventional oil
46 and gas resources will play a significant role in the future energy market. The energy transition
47 pushes the exploration and production of oil and gas to be more marginal and minimize the
48 carbon footprint. Marginality of production is having the maximum production plateau and the
49 minimum cost of the production operation. It requires to have accurate development and
50 management scenarios. Latter can be achieved by having an in-depth understanding of fluid
51 flow in tight porous media.

52 The deviation from Darcy's law because of various storage and flow mechanism is the
53 most challenging aspect of modelling fluid flow in unconventional hydrocarbon resources.
54 Therefore, it is highly required to take the effects of Knudsen diffusion, slippage, adsorbed gas
55 and dissolved gas into account. However, it leads to form a second-order highly nonlinear
56 partial differential equation. Using the classic derivation-dependent approaches like Newton's
57 method to solve the derived governing equation numerically is challenging due to the
58 requirement of making proper initial guesses, forming the Jacobian matrix and its inversion.
59 As a result, the current research has put forward great efforts to use soft computing techniques
60 of metaheuristic algorithms and machine learning approaches to solve the supposed equation
61 easier and with less computational cost.

62 Regarding the microscopic scale and applying pore-scale physics, having a large
63 portion of pores with a size less than the spatial resolution of micro X-ray computed
64 tomography images is the main obstacle required to practically come across. Accordingly, a
65 novel workflow of digital image processing based on deep learning algorithms and other
66 important image-based operators has been proposed. Typically, the supposed images are

67 suffering from noises, and they are supposed to be treated with various filters. But, the
68 parameters of filters are usually expected to be adjusted by experienced users. As a result, it
69 has been tried to use deep learning to filter images with minor troubles. Then, the clean images
70 have been implemented with classic approaches of digital rock physics to observe their
71 credibility in case of being applied to the tight porous media. After that, it has been tried to
72 employ a deep learning operator to generate images with various synthetic lower resolutions.
73 Having the corresponding porosities versus their synthetic resolution, it becomes possible to
74 develop an exponential model capable of predicting the porosity for the theoretical spatial
75 resolution of 0-micron meter per voxel. Finally, the computed porosity has been taken to
76 predict the permeability free of biases.

77 The research shows that using various artificial intelligence methods can generate
78 accurate results for fluid flow simulation in unconventional porous media with less
79 computational cost and difficulties.

80

81

Publications

82 Journals:

83 1. Bezyan Y, Ebadi M, Gerami S, Rafati R, Sharifi M., Koroteev D. A novel approach for
84 solving nonlinear flow equations: The next step towards an accurate assessment of shale
85 gas resources. *Fuel*. 2019 January; 236: 622-635.

86 2. Ebadi M, Zabihifar SH, Bezyan Y, Koroteev D. A nonlinear solver based on an adaptive
87 neural network, introduction and application to porous media flow. *Journal of Natural
88 Gas Science and Engineering*. 2021 March; 87: 103749.

89 3. Sidorenko M, Orlov D, Ebadi M, Koroteev D. Deep learning in denoising of micro-
90 computed tomography images of rock samples. *Computer & Geosciences*. 2021 June;
91 151; 104716.

92 4. Orlov D, Ebadi M, Muravleva E, Volkhonskiy D, Erofeev A, Savenkov E, Balashov V,
93 Belozarov B, Krutko V, Yakimchuk Ivan, Evseev N, Koroteev D, Different methods of
94 permeability calculation in digital twins of tight sandstones. *Journal of Natural Gas
95 Science and Engineering*. 2021 March; 87: 103750.

96 5. Ebadi M, Orlov D, Makhotin I, Krutko V, Belozarov B, Koroteev D. Strengthening the
97 digital rock physics, using downsampling for sub-resolved pores in tight sandstones.
98 *Journal of Natural Gas Science and Engineering*. 2021 May; 89: 103869.

99 Conferences:

100 1. Ebadi M, Makhotin I, Orlov D, Koroteev D. Digital Rock Physics in Low-Permeable
101 Sandstone, Downsampling for Unresolved Sub-Micron Porosity Estimation. SPE Europec,
102 Virtual, December 2020.

- 103 2. Ebadi M, Bezyan Y, Zabihifar S H, Koroteev D. An Artificial Intelligence-Based Nonlinear
104 Solver for Hydrocarbon Reservoir Simulations. SPE Europec, Virtual, December 2020.
- 105 3. Ebadi M, Koroteev D. Towards a Reliable Determination of Saturation Pressure: A Hybrid of
106 Mouth Brooding Fish MBF Algorithm and Flash Calculations. SPE/IATMI Asia Pacific Oil &
107 Gas Conference and Exhibition, Bali, Indonesia, October 2019.

108

109

Acknowledgment

110 I would like to express my sincere gratitude to my supervisor, Professor Dmitry
111 Koroteev, for his continuous support of my PhD study and related research. His patience,
112 motivation, and immense knowledge are outstanding. Furthermore, the level of
113 professionalism that he performs is incredible. His guidance helped me in all the time of
114 research and writing of the thesis and the papers. I could not have imagined having a better
115 supervisor and mentor for my PhD study.

116 My sincere thanks also go to Dr Orlov, who provided me with an opportunity to join
117 his pore-scale industrial projects. I highly need to appreciate his patience when I asked him my
118 endless questions about digital rock physics! In terms of brainstorming and suggesting brilliant
119 ideas, his creativity is remarkable. I have to confess that it was impossible to have some of the
120 publications if I had not applied his comments, Большое спасибо!

121

122

Dedication

123 Grandmothers always have time to talk and make you feel special. In fact, a garden of
124 love grows in their hearts. When nothing goes well, you just need to call them! God bless them.

125 I would like to dedicate my thesis to my grandmother, who passed away while I was
126 doing my PhD. She meant and continues to mean a lot to my beloved family and me. She will
127 remain the symbol of self-scarification, patience and kindness forever. I never forget her
128 unconditional, parental and deep love for us.

129 My dear “Madarjoon”, I do know that you are always there, in our hearts, watching
130 over and guiding us. Your memories will never fade. I will miss you more than words can say.
131 Rest in peace.

132

Table of Contents

134	Abstract	3
135	Publications	5
136	Acknowledgment	7
137	Dedication	8
138	Table of Contents	9
139	List of Figures	11
140	List of Tables	13
141	1. Introduction	14
142	1.1 The Importance of Developing Unconventional Resources	14
143	1.2 Macroscopic Scale	19
144	1.2.1 Fluid Flow and Storage Mechanisms in Shale Gas Plays	19
145	1.2.2 Modelling and Simulation	22
146	1.2.3 Solvers	26
147	1.2.3.1 Classic Approach	26
148	1.2.3.2 Particle Swarm Optimization (PSO)	29
149	1.2.3.3 Adaptive Neural Network (AdNN)	32
150	1.3 Microscopic Scale	36
151	1.3.1 Digital Image Processing	41
152	1.3.1.1 Deep Learning for Noise Reduction	42
153	1.3.2 Pore-Scale Simulation	43
154	1.3.2.1 Implementation of the Classic Approaches	44
155	1.3.2.2 Effects of Sub-Resolved Pores	48
156	2. A novel approach for solving nonlinear flow equations: The next step towards an	
157	accurate assessment of shale gas resources	54

158	3. A nonlinear solver based on an adaptive neural network, introduction and	
159	application to porous media flow	70
160	4. Deep learning in denoising of micro-computed tomography images of rock	
161	samples	88
162	5. Different methods of permeability calculation in digital twins of tight sandstones	
163		102
164	6. Strengthening the digital rock physics, using downsampling for sub-resolved	
165	pores in tight sandstones	116
166	7. Conclusions and Future Research	131
167	References	134
168		

List of Figures

170	Figure 1: Hydrocarbon Resource Extraction Risk Triangle	16
171	Figure 2: The multiscale analyses of unconventional resource, and the challenges	17
172	Figure 3: (a) The validation of Newton’s method and PSO approach versus the analytical	
173	solution for 300 grids (b) Performance of the PSO versus Newton’s method to solve	
174	corresponding simultaneous equations (Chapter 2, <i>Figure 5</i>)	31
175	Figure 4: The proposed nonlinear solver based on using AdNN (Chapter 3, <i>Figure 1</i>)	33
176	Figure 5: The results of using AdNN versus results of applying Newton’s method (Chapter 3,	
177	<i>Figure 3</i>)	34
178	Figure 6: The computational efficiency of the AdNN-solver (Chapter 3, <i>Figure 11, 12</i>)	35
179	Figure 7: The primary trend of DIP (Chapter 36, <i>Figure 3</i>)	37
180	Figure 8: Comparing the results of PSD and the spatial resolution of μ xCT images (Chapter 36,	
181	<i>Figure 2</i>)	40
182	Figure 9: The effects of the implemented DIP (a) The original image (b) The clean image	
183	(Chapter 4, <i>Figure 2</i>)	42
184	Figure 10: The schematic of the implemented RED-Net (Chapter 4, <i>Figure 4</i>)	43
185	Figure 11: The implemented DIP in a glance (Chapter 5, <i>Figure 2</i>)	45
186	Figure 12: The results of permeability computations based on the variety of methods (Chapter	
187	5, <i>Figure 4</i>)	46
188	Figure 13: Effects of image processing on the permeability anisotropy analysis (Chapter 5,	
189	<i>Figure 5</i>)	47
190	Figure 14: The effect of downsampling on the measured porosities (Chapter 6, <i>Figure 6</i>)	50
191	Figure 15: Estimation of ϕ_A by using the introduced procedure (Chapter 5, <i>Figure 8</i>)	51
192	Figure 16: Estimation of k_A with the help of computed β (Chapter 6, <i>Figure 10</i>)	52

193	Figure 17: Chapter 2 in a glance	55
194	Figure 18: Chapter 3 in a glance	71
195	Figure 19: Chapter 4 in a glance	89
196	Figure 20: Chapter 5 in a glance	103
197	Figure 21: Chapter 6 in a glance	117
198		

199

List of Tables

200 Table 1: Different flow regimes as a function of K_n 20

201 Table 2: Effects of using various loss functions 43

202

203

1. Introduction

204

1.1 The Importance of Developing Unconventional Resources

205

206

207

208

209

210

211

212

213

214

215

216

217

Hydrocarbon resources are dwindling, while many research has recently indicated that unconventional hydrocarbon reservoirs can supply great energy values with minimum adverse effects on the environment [1]. Accordingly, providing more natural gas has become a priority for authorities and a challenging hot topic for researchers [2]. Besides new technological advances in both fields of hydraulic fracturing and horizontal well drilling, being faced up with a fast decline in conventional reserves have caused attention to be drawn towards the unconventional resources such as tight and ultra-tight plays [3], which have been playing a progressively leading role in the energy market during very recent years [4]. For instance, it is statistically reported that “The Shale Gas Revolution” caused shale gas to be taken as a reliable energy source in the USA [5]. In fact, shale gas comprised just less than 2% of domestic outputs within the early years of the current century [6]. Surprisingly, today it accounts for almost a third. It has even been estimated that 46% of produced gas in the USA during 2035 will be from shale gas plays [7].

218

219

220

221

222

223

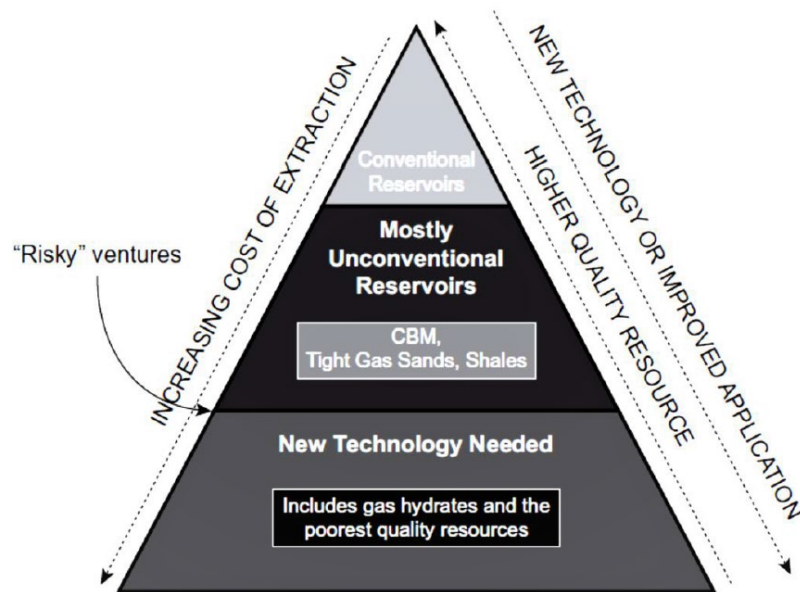
224

Before starting relevant discussions, it is critical to understand what an unconventional reservoir is. The definition is highly reliable to conventional reservoirs, which are generally defined as high permeability, high-quality reservoirs where all it has to be done is drilling a vertical well and running a perforation operation at the productive interval that causes the well to flow at profitable rates [8]. Conversely, unconventional resources are routinely characterized as low-quality reservoirs that have to be stimulated to produce commercial flow rates and recover commercial volumes of hydrocarbon [9]. In more details, high viscosity oil and low

225 permeability are the main reasons to label a reservoir as a low-quality resource [10]. However,
226 the application of long horizontal well coupling with hydraulic fracturing in case of tight and
227 ultra-tight reservoirs and taking advantages of thermal methods to reduce the viscosity of heavy
228 oil can effectively stimulate the formations in most cases [8,11].

229 The unconventional oil and gas endowment is orders of magnitude greater than the
230 conventional resources that have been the principal objectives of production and exploration
231 for the past 120 years [12]. To picture the described concept, it is necessary to become familiar
232 with the “Hydrocarbon Resource Extraction Risk Triangle” idea shown in **Figure 1**. The shown
233 notion illustrates that the high-quality reservoirs are at the top of the triangle, while going
234 deeper into this triangle causes facing up with lower quality reservoirs [13,14]. The “risky”
235 undertaking may also be explained by the fact that we are currently on a steep learning curve
236 regarding the technologies necessary to create a gas hydrate production [15] financially.
237 Technically, unconventional deposits can be grouped into three general categories:

- 238 I. Unconventional resources, which include ultra-tight sandstones and carbonates
239 and source rocks.
- 240 II. Unconventional oil and gas fluids, comprising sour/acid gases, bitumen, and
241 heavy oil.
- 242 III. Hydrocarbons “locked in rocks” such as oil shale and methane hydrates (an
243 immature source rock)



244

245

Figure 1: Hydrocarbon Resource Extraction Risk Triangle

246

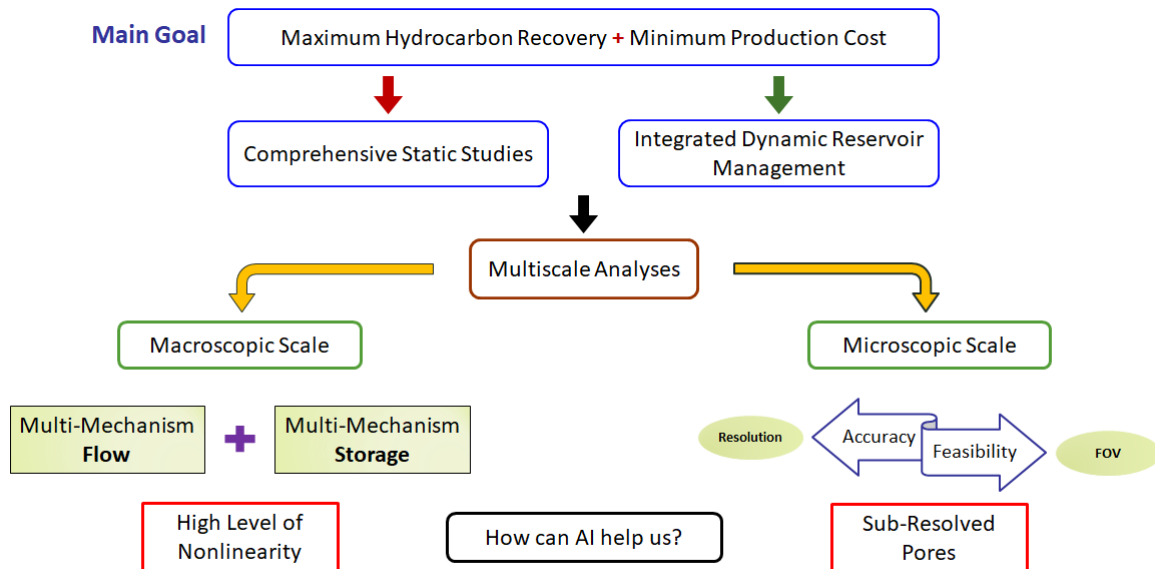
The Hydrocarbon Resource Extraction Risk Triangle shows that high-grade deposits are small and difficult to find but easy to extract, and more enormous resources can be found in deeper levels, but they do need higher product prices and improved technology to be extracted [15]. Nevertheless, the world needs more energy under all developing scenarios, leading to this issue that unconventional resources play an ever-increasing role in our energy supply [16,17]. Due to this fact, the world’s emerging economies will require sustained oil and gas use for the foreseeable future, which cannot be prepared with declining conventional oil and gas reservoirs. As a result, it can be deduced that developing unconventional resources is an inevitable topic, and it is a requirement to do research projects about unconventional reservoir studies.

256

To put it another way, it can be concluded that tight hydrocarbon reservoirs are statistically and practically known as potential options to guarantee a sustainable energy supply into future markets [18,19]. The supposed potential can be turned into action only if the technical risks of developing such unconventional oil and gas reservoirs be minimized

259

260 considerably. It can be achieved by employing various reservoir management and simulation
 261 scenarios. However, the inherent complexity and nonlinearity of tight and ultra-tight
 262 hydrocarbon resources are the main obstacles that make it challenging to use classic approaches
 263 [20]. Therefore, it is where using modern methods like machine learning techniques can be
 264 implemented. The current research has made significant attempts to macroscopically and
 265 microscopically examine how it is possible to take advantage of various machine-learning
 266 approaches to obtain more accurate and practical characterizations of tight and ultra-tight
 267 porous media. Accordingly, the general trend of the research and the main challenges has been
 268 visualized in Figure 2.



269

270 **Figure 2:** The multiscale analyses of unconventional resource, and the challenges

271 Based on the previous literature, a second-order nonlinear partial differential equation
 272 describing fluid flow in a shale gas reservoir has first been developed regarding the
 273 macroscopic scale. Then, it has been tried to solve the equation with soft computing approaches
 274 than classic ones. Regarding the microscopic scale, a tight sandstone sample taken from the

275 Achimovskiy formation has been studied based on the classic approaches of digital rock
276 physics. Generally, digital rock physics blends microtomographic imagery with sophisticated
277 models of material properties. It is utilized in complementary laboratory studies to better
278 understand critical transport-related physical processes and efficient mechanical
279 characteristics. Digital rock physics blends microtomographic imagery with sophisticated
280 models of material properties. It is utilized in complementary laboratory studies to better
281 understand critical transport-related physical processes and efficient mechanical
282 characteristics. However, the main challenge of using digital rock physics is those pores that
283 cannot be seen in the images or are technically known as sub-resolved pores. The current
284 research has endeavoured to figure out how to use modern image processing techniques to
285 overcome the addressed issue.

286 All in all, the main objectives of the prepared thesis in case of the macroscopic analyses
287 can be outlined as below:

- 288 • Making an investigation about the storage and flow phenomena in tight and
289 ultra-tight porous media (**Chapter 2**)
- 290 • Using AI-based solvers to handle the nonlinearity of governing equations of
291 fluid flow in tight and ultra-tight porous media (**Chapters 2 and 3**)

292 and for the microscopic investigation, there are:

- 293 • Using AI techniques to suppress the noise of computed tomography images
294 (**Chapter 4**)
- 295 • Checking the applicability of classic methods to analyze the petrophysical
296 properties of tight samples (**Chapter 5**)

- 297 • Extraction of bulk petrophysical properties from computed tomography
298 images by means of digital image processing (**Chapter 6**)

299 **1.2 Macroscopic Scale**

300 Fluid flow in porous media can be described by the following transport mechanisms:
301 molecular diffusion, Knudsen diffusion, surface diffusion, and viscous flow [21]. The fluid
302 transport mechanism in the typical oil and gas reservoir with large pore sizes is the viscous
303 flow described by Darcy's law [22]. Darcy's law is a phenomenological resulting constitutive
304 equation that addresses the fluid flow in porous media [23]. Darcy's law has been developed
305 under certain conditions. The most limiting assumption of Darcy's law is its development based
306 on the laminar flow governed by viscous forces [24]. However, the fluid flow with high
307 velocities in porous media where the inertial forces are more significant than the viscous forces,
308 the flow is turbulent [25]. It can be corrected by adding an inertial term to Darcy's equation,
309 known as the Forchheimer term [2]. A series of previous experimental and field research has
310 indicated that fluid flow in ultra-tight and tight porous media noticeably deviates from the
311 results generated by the implementation of Darcy's law [26]. It is due to a couple of reasons,
312 such as nanoscale pores or even mature or immature organic contents in the main body of the
313 studying porous media [27]. The following two sections discuss the phenomena mentioned
314 above and how their effects can be taken into account in the form of a governing equation.

315 **1.2.1 Fluid Flow and Storage Mechanisms in Shale Gas Plays**

316 The significant differences between shale gas reserves and conventional hydrocarbon
317 resources related to natural nanoscale pores and organic content have been briefly examined
318 [28]. Darcy's law and standard continuous flow equations generally underestimate the flow

319 rate when applied to the tight and ultra-tight porous medium of shale gas deposits [29]. It is
 320 mainly related to the zero-velocity boundary condition, which is the deriving assumption. The
 321 Knudsen number (K_n) is commonly used as an explanatory indicator when attempting to
 322 understand the notion of multi-mechanism flow in ultra-tight porous media [30,31]. The
 323 different flow regimes could be categorized by Knudsen Number:

$$K_n = \frac{\lambda}{d} \quad (1)$$

324 where λ is technically specified in shale gas reservoirs as the mean distance travelled
 325 by a gas molecule before the interaction with the other molecule that modifies its track, energy
 326 or other features. Also, d stands for the pore diameter. The categorization of flow types based
 327 on K_n has been introduced in **Table 1**.

328 **Table 1:** Different flow regimes as a function of K_n

K_n	Flow Type
$K_n < 10^{-3}$	Continuum Flow
$10^{-3} < K_n < 10^{-1}$	Slip Flow
$10^{-1} < K_n < 10$	Transition Flow
$10 < K_n$	Free Molecular Flow

329
 330 According to detailed investigations on the morphology and pore size distribution of
 331 shale gas reservoirs, pore diameters in shale gas resources vary from 1 to 200 nm, leading with
 332 K_n corresponding values ranging from 0.0002 to 6, respectively [32]. Overall, flow in shale gas

333 reservoirs is a multi-mechanism phenomenon that includes transition flow, slip flow and
334 continuum flow [33]. Generally, an apparent permeability (k_{app}) model taking the effects of all
335 the flow regimes into account is usually employed to facilitate the simulation procedure more
336 effectively.

337 The economics of shale gas plays is technically the critical factor in evaluating the
338 quality of shale gas resources. The storage mechanisms in shale gas plays are the free
339 compressed gas and the adsorbed layer on the surface of kerogens already full of **dissolved** gas
340 [34]. The mode of gas storage is influenced by surface area and the size of pores. Typically,
341 because the macropores do not play a leading role in surface area, they are assumed to be the
342 main path for the transportation of free compressed gas [35]. Following the same logic,
343 mesopores and micropores are the essential sites for gas adsorption. Moreover, geological
344 conditions like reservoir temperature, moisture content and reservoir pressure could impact the
345 amount of free, adsorbed, and dissolved gas [36].

346 In other words, not taking the adsorbed gas that has a semi-liquid physical state with a
347 greater density than the free compressed gas into account leads to some significant
348 underestimation [37]. The impacts of adsorbed gas could become more prominent when
349 combined with a substantial quantity of surface area in shale gas reservoirs that is tenfold more
350 than in conventional reservoirs. The standard Langmuir isotherm is the most often used
351 adsorption isotherm because it considers a dynamic instantaneous equilibrium at constant
352 temperature and pressure between adsorbed and non-adsorbed gas [38]. Furthermore, the
353 adsorbed layer, which consists of gas molecules that adhere to **kerogen** surfaces, limits the
354 possible conductance for the passage of free and previously desorbed gas [39]. As a result,
355 because the methane molecule radius is similar to the pore diameters, the adsorbed gas has a
356 detrimental influence on permeability. However, below a threshold pressure, the adsorbed

379 results in the **release of immobile** gas molecules (adsorbed gas) from the surface of kerogens.
 380 The desorption causes thermodynamical disturbances on the surfaces of kerogens generating
 381 concentration gradients between bodies of kerogens and their surfaces. That is the primary
 382 reason why solute gas is transferred from the bulk of kerogen to its surfaces.

383 **Regarding the field units**, A one-dimensional (1D) model for a conventional porous
 384 media can be developed based on mass **conservation law** as below [44]:

$$-\left((\rho_f v A)_{x+dx} \Delta t - (\rho_f v A)_x \Delta t\right) = V_b \phi \left((\rho_f)_{t+dt} - (\rho_f)_t\right) \quad (2)$$

385 where

$$v = -(5.615)(0.001127) \frac{k \partial p}{\mu \partial x} \quad (3)$$

386 where **0.001127** is the constant to convert Darcy's unit to field units, and **5.615** is the conversion
 387 **factor to change from bbl to ft³**. The insertion of **Equation 3** into **Equation 2** results in:

$$\frac{\partial}{\partial x} \left(0.00633kA \frac{\rho_f \partial p}{\mu \partial x}\right) \Delta x = \frac{\partial}{\partial t} V_b (\rho_f \phi) \quad (4)$$

388 where **v is the velocity in x-direction**, *k* is permeability (*md*), *A* is the surface area (*ft²*) **of the**
 389 **grid cell in the yz-plane**, *μ* is viscosity (*cp*), *ρ_f* is the density of free or compressed gas
 390 (*lb_m/ft³*), *φ* is porosity, *V_b* is the bulk volume (*ft³*) **of the control volume (grid cell)**, and *Δx*
 391 is the length of each grid (*ft*) after the discretization.

392 As mentioned earlier, the fluid flow in a shale gas play is a multi-mechanism
 393 phenomenon. To have the effects of all the mechanisms as a single parameter, substituting the
 394 *k* with *k_{app}* in **Equation 4** can make the model representing the complexity of a multi-

395 mechanism flow more accurately and adequately. The next step to make **Equation 4**
 396 representing the shale gas plays more practically is the effects of adsorbed gas into account. It
 397 becomes possible by adjusting the accumulation term as:

$$\frac{\partial}{\partial x} \left(0.00633 k_{app} A \frac{\rho_f \partial p}{\mu \partial x} \right) \Delta x = \frac{\partial}{\partial t} V_b (\rho_f \phi + (1 - \phi) \rho_a) \quad (5)$$

398 where ρ_a represents the mass of adsorbed gas per volume of solid. Having the definition for
 399 the concepts of gas compressibility (C_g), Langmuir isotherm and chain rule, it is possible to
 400 reformulate **Equation 5** as:

$$\frac{\partial}{\partial x} \left(0.00633 k_{app} A \frac{\rho_f \partial p}{\mu \partial x} \right) \Delta x = \frac{\partial p}{\partial t} C_g \rho_f V_b (\phi + (1 - \phi) K_a) \quad (6)$$

401 where $K_a = \partial \rho_a / \partial \rho_f$. The solute gas and its quantity in kerogen can be calculated with the
 402 help of Henry's law, where the solute gas in kerogen is proportional to the pressure. The effects
 403 of solute gas can be added to **Equation 6** as a source term. The idea has been taken from the
 404 concepts implemented in fractured reservoirs [45]. It leads to the development of a **discretized**
 405 second-order nonlinear partial differential equation governing the multi-mechanism flow and
 406 storage in shale gas plays as:

$$\frac{\partial}{\partial x} \left(0.00633 k_{app} A \frac{\rho_f \partial p}{\mu \partial x} \right) \Delta x + q_k^* = \frac{\partial p}{\partial t} C_g \rho_f V_b (\phi + (1 - \phi) K_a) \quad (7)$$

407 where q_k^* is the mass flux from kerogen to matrix (lb_m/day), and it is represented as:

$$q_k^* = D_k A_k \frac{\partial c}{\partial z} \quad (8)$$

408 The kerogen diffusion coefficient is represented as D_k (ft^2/day) and A_k is the kerogen
409 surface area (ft^2). Also, the concentration gradient in the z -direction is represented as $\partial c/\partial z$.
410 About kerogens, it is necessary to consider that they are in contact with each grid block like a
411 coating surface. With the beginning of natural depletion that continued by desorption from the
412 surface of kerogens, the concentration profile within the kerogen body is changed. It causes
413 kerogen to feed in the z -direction (perpendicular to the xy -plane) to the grid body.

414 Regarding **Equation 7**, it must be mentioned that the nonlinear terms dependent to
415 pressure are:

- 416 • k_{app} computed by Darabi et al – Described in **Chapter 2 Table 2** and *Equation 17*
- 417 • ρ_f computed by $\rho = \frac{pM}{zRT}$ in which z is the *gas compressibility factor* that can
418 numerically be computed by the model presented by Hall-Yarborough
- 419 • μ computed by Lee-Gonzalez-Eakin
- 420 • q_k^* as described in **Chapter 2 Equations 2, 18, 19**
- 421 • C_g as described in **Chapter 2 Equations 9, 10**
- 422 • K_a as described in **Chapter 2 Equations 11, 13, 15, 16**

423 One of the main concerns that should be considered is the different scales existing in
424 the introduced governing equation (**Equation 7**). It must first be underlined that the flow in the
425 porous media has been modelled in one dimension. Then, it has been assumed that the layer of
426 kerogen around the porous media has the 1/50 thickness of the porous media. From the
427 homogenization point of view, the referred assumption helps to solve the problem with
428 concurrent methods. In concurrent methods, both scales are simultaneously addressed in the
429 problem formulation. In addition, it should be added that both scales are coupled together by

430 pressure passing that technically remarks as a serial method. On the contrary, the assumption
431 has caused the final model not perfectly representing reality.

432 1.2.3 Solvers

433 The discretization based on the finite difference method is supposed to be employed to
434 solve **Equation 7** numerically. The result is a set of simultaneous algebraic equations stated
435 as:

$$C_1 Y + C_2 = 0 \quad (9)$$

436 Y represents the vectors of unknowns (pressures), and C1 and C2 represent the matrixes of
437 coefficients and dependencies, respectively [46]. Going through the compressibility of gases
438 and their dependency on the pressure, the subsequence of discretization (**Equation 9**) results
439 in a set of nonlinear simultaneous algebraic equations [1]. Thus, finding a suit of pressures that
440 satisfies **Equation 9** at each time step is the main target of applying nonlinear solvers.

441 1.2.3.1 Classic Approach

442 Some analytical and numerical approaches have been introduced so far to solve various
443 types of PDEs. Although the application of analytical methods yields exact and continuous
444 results in time and space, the stated methods are not applicable in cases of PDEs with a high
445 level of nonlinearity or irregular boundaries. Hence, numerical methods under different
446 scenarios have been put forward. The discretization procedure is a globally accepted method
447 to expand the nonlinear PDEs into a system of nonlinear simultaneous algebraic equations.
448 Solving a system of nonlinear equations by approximating them with a system of linear
449 equations to have the benefits of linear solvers is usually avoided. In addition, increasing the
450 errors and inaccuracy in predicting the reservoir performance is known as the major drawback

451 of the linearization procedures. Instead, it is highly recommended to tackle problems directly
452 by using nonlinear solvers, which can converge more accurately towards the correct solutions.

453 Routinely, Newton's method is the most extensively used solver of nonlinear equations.
454 The simplicity and high convergence rate are persuasive enough to frequently apply the
455 introduced technique to solve nonlinear simultaneous algebraic equations. However, the
456 performance of Newton's method is strongly dependent on making a proper initial guess.
457 Evaluation of n^2 partial derivatives, computing the inversion of the Jacobian matrix including
458 $f(n)$ by $f(n)$ linear systems for a certain number of iterations in each time step causing a high
459 computational cost of $O(n^3)$ are the main disadvantages of Newton's method. As a result,
460 various attempts have been made to remove the aforementioned disadvantages. The
461 modification of the Secant method known as Broyden's, which have been developed for
462 multivariable functions, is the adjustment of Newton's method by approximating the Jacobian
463 matrix. Although Broyden's method eliminates the computation of partial derivatives and the
464 inversion of the Jacobian matrix after the first step of the root-finding process, its superlinear
465 convergence rate has made it slower than Newton's method. Both the mentioned methods only
466 converge when the proper initial guesses are chosen. Accordingly, the Steepest Descent
467 approach with a linear convergence rate towards solutions was introduced to overcome the
468 difficulties of a reasonable initial guess. Nevertheless, the Steepest Descent approach also
469 requires the relevant calculations of the Jacobian matrix within each iteration, which is too
470 much costly. Another well-known technique to solve nonlinear simultaneous algebraic
471 equations is the Homotopy or continuation method, which widens the domain of the converges.
472 This method changes an easy problem to a complex target problem. However, the same as other
473 referred methods, Homotopy is a strong function of derivatives as well. Requiring more
474 functions and Jacobian inverse evaluation, and mathematical algebraic operations in

475 comparison with other Newton-type methods are also other significant aspects of Homotopy.
 476 Generally, the heavily derivation-dependent, the high computational cost of the Jacobian
 477 matrix and its inversions, and the lack of ability to deal with ill-conditioned matrixes can
 478 theoretically be known as the most problematic aspects of classic nonlinear solvers. It should
 479 also be reminded that forming the Jacobian matrix for some particular cases is unmanageable.

480 Technically, Newton's method is stated as:

$$[p_{new}] = [p_{old}] - J^{-1}[f(p_{old})] \quad (10)$$

481 within each time step, p_{old} shows the pressures of the last iteration, J^{-1} represents the inversion
 482 of the Jacobian matrix, and $f(p_{old})$ indicates the outputs of nonlinear simultaneous algebraic
 483 equations. **Equation 10** generates p_{new} which is expected to be inserted into **Equation 9** and
 484 causes the generation of outputs with a magnitude of error less than what has been produced
 485 by p_{old} . The Jacobian matrix is developed based on all first-order partial derivation of a vector-
 486 valued function. Technically, the Jacobian matrix is defined as:

$$J = \frac{df}{dx} = \left[\frac{\partial f}{\partial x_1} \quad \dots \quad \frac{\partial f}{\partial x_n} \right] = \begin{bmatrix} \frac{\partial f_1}{\partial x_1} & \dots & \frac{\partial f_1}{\partial x_n} \\ \vdots & \ddots & \vdots \\ \frac{\partial f_m}{\partial x_1} & \dots & \frac{\partial f_m}{\partial x_n} \end{bmatrix} \quad (11)$$

487 Using Newton's method can have real challenges and difficulties. For instance, the
 488 quality of convergence in Newton's method is strongly dependent on the quality of initial
 489 guesses [47]. Also, for some problems, the arrangement of the Jacobian matrix is somehow
 490 unmanageable. Moreover, forming all the arrays based on derivations can be time-consuming
 491 and difficult. Finally, it is necessary to add this point that the computational cost of Newton's

492 method is notably high because of making an inversion of the Jacobian matrix for a certain
493 number of iterations [48].

494 **1.2.3.2 Particle Swarm Optimization (PSO)**

495 In order to overcome the addressed challenges of making proper initial guesses and
496 forming the Jacobian matrix, the application of Particle Swarm Optimization (PSO) is
497 recommended. PSO is a free-derivation optimization method [49]. It does not need proper
498 initial guesses to find the most optimized suite of pressures that their production by C_l in
499 **Equation 9** results in a close-to-zero matrix. Inspired by social systems among organisms such
500 as fish schooling and birds flocking, PSO has been represented as a stochastic optimization
501 technique [50]. PSO is a metaheuristic optimization algorithm that can practically be employed
502 to solve multidimensional optimization problems.

503 Beginning with an arbitrary collection of particles or prospective solutions containing
504 pressure numbers, the workflow tries to enhance solutions depending on their properties,
505 hopefully generating a certain quantity of zeros. The main target of PSO is to reach the
506 supposed goal iteratively [51]. Accordingly, the velocity of particles is changed by means of
507 velocity vectors that are functions of random factors.

$$x_{i,j}^{k+1} = x_{i,j}^k + v_{i,j}^{k+1} \quad (12)$$

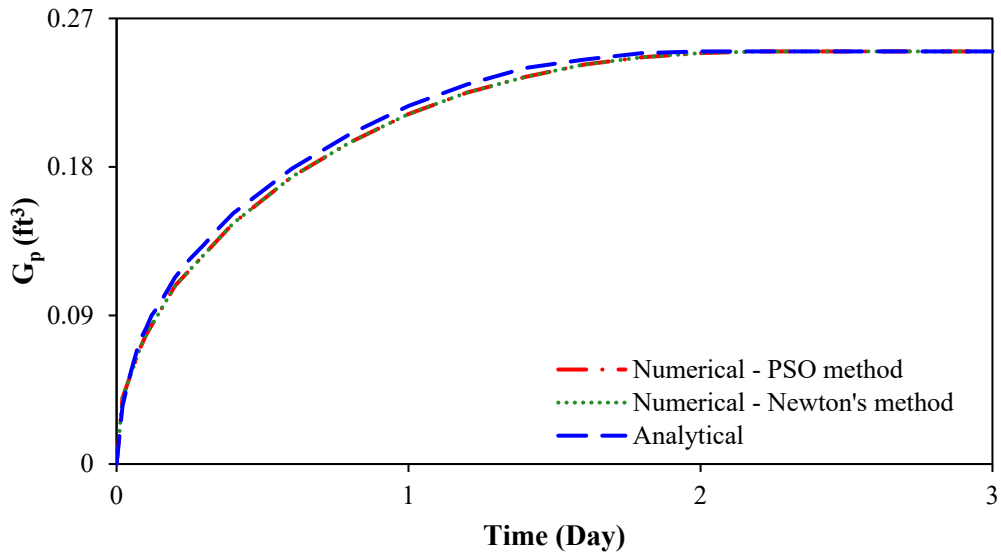
508 where

$$v_{i,j}^{k+1} = v_{i,j}^k + c_1 r_1 (x_{lbest\ i,j}^k - x_{i,j}^k) + c_2 r_2 (x_{gbest\ i,j}^k - x_{i,j}^k) \quad (13)$$

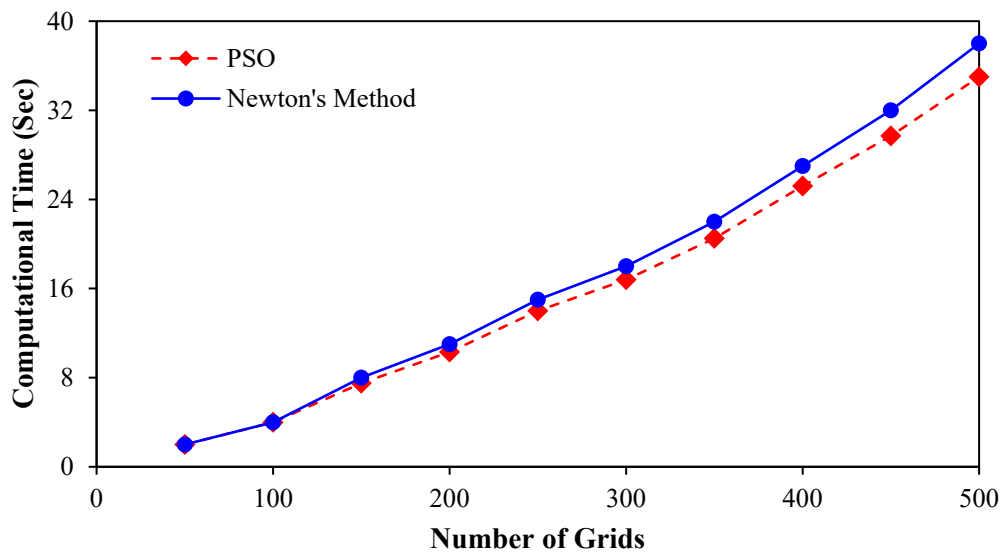
509 During the k th iteration, $x_{i,j}^k$ and $v_{i,j}^k$ are the position and velocity of the j th element of
510 the i th particle. Also, r_1 and r_2 are two numbers uniformly and randomly distributed with the

511 range of 0 and 1. The x_{gbest} and x_{lbest} indicate the best positions experienced so far by the
512 whole population and the i th particle. Furthermore, the confidence of each particle in itself and
513 the population are represented by c_1 and c_2 , respectively. Regarding a 1D geological model,
514 the comparison between using Newton's method and the PSO approach has been shown in
515 **Figure 3.** The results indicate that the PSO can generate results as accurately as Newton's
516 method but with fewer challenges like making proper initial guesses or derivative dependency.
517 The results underline that using PSO instead of Newton's method could generate results
518 slightly faster. It is shown in **Figure 3,b** where the model with the 200 grids more converges
519 0.7 seconds faster. The difference between time convergences goes up to 1.2 seconds if the
520 number of grids increases to 300. The maximum difference has been observed for 500 grids,
521 where the difference is 3 seconds. However, it is a questionable issue if the dimensions changes
522 to 2 or 3. In addition, the next chapter has perfectly shown that using nonlinear AI-based solvers
523 in the case of multiphase flow does not generate the same results. In other words, it can be
524 deduced that PSO can overcome the nonlinearity of the developed models, but its application
525 with respect to time is questionable.

526



(a)



(b)

527 **Figure 3:** (a) The validation of Newton's method and PSO approach versus the analytical
 528 solution for 300 grids (b) Performance of the PSO versus Newton's method to solve
 529 corresponding simultaneous equations (**Chapter 2, Figure 5**)

530

1.2.3.3 Adaptive Neural Network (AdNN)

531

532

533

534

535

536

537

Using various machine learning approaches like Artificial Neural Networks (ANNs) to solve partial differential equations has been a topic of various outstanding research. However, going through the literature shows that using ANNs to solve partial differential equations is either with the help of already gathered data or by the use of various simulation outputs. Therefore, it can be deduced that although using ANNs can solve problems like **Equation 9** easier without the traditional difficulties of using Newton's method, there is still a data collection problem.

538

539

540

541

542

543

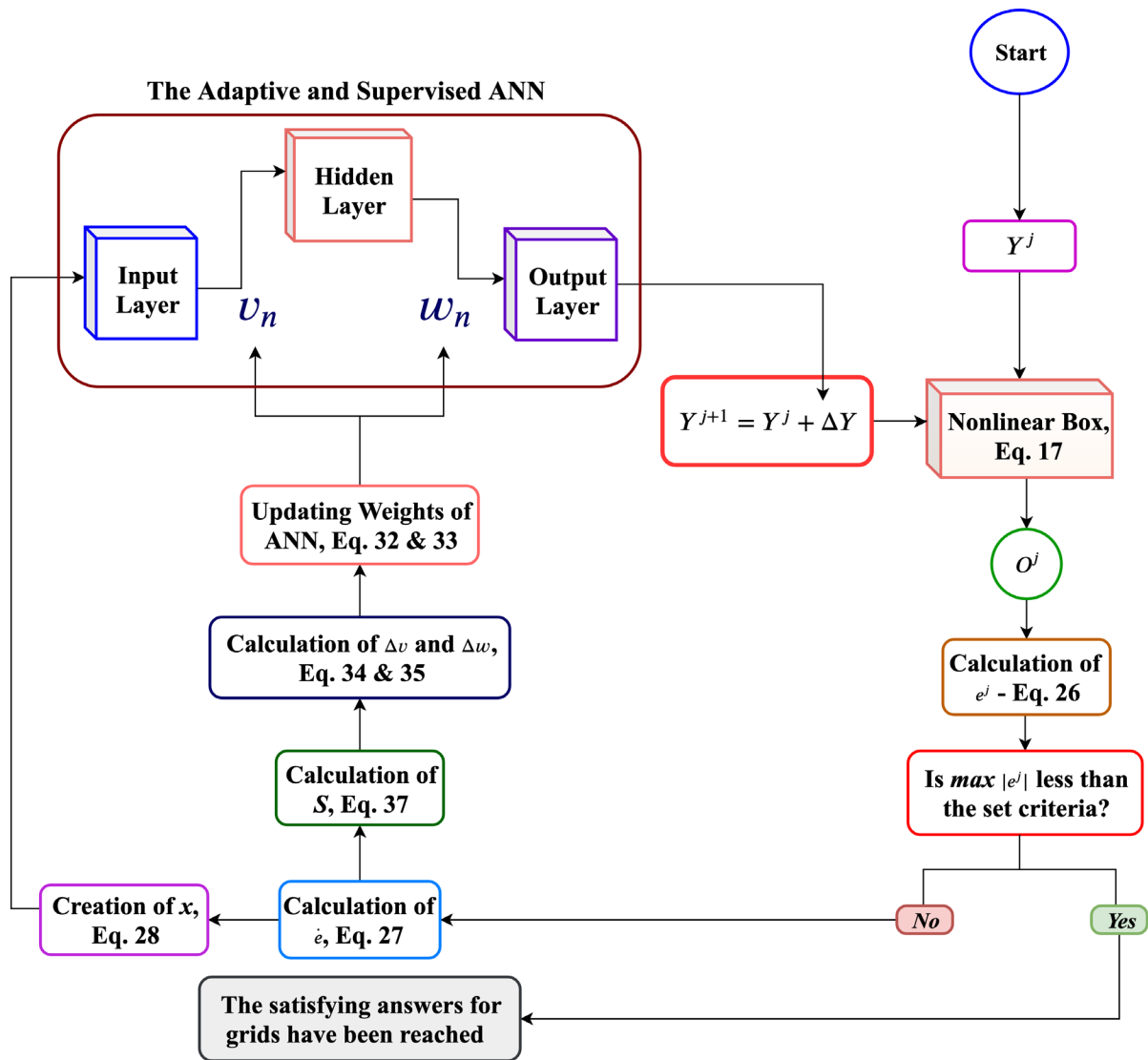
544

545

546

547

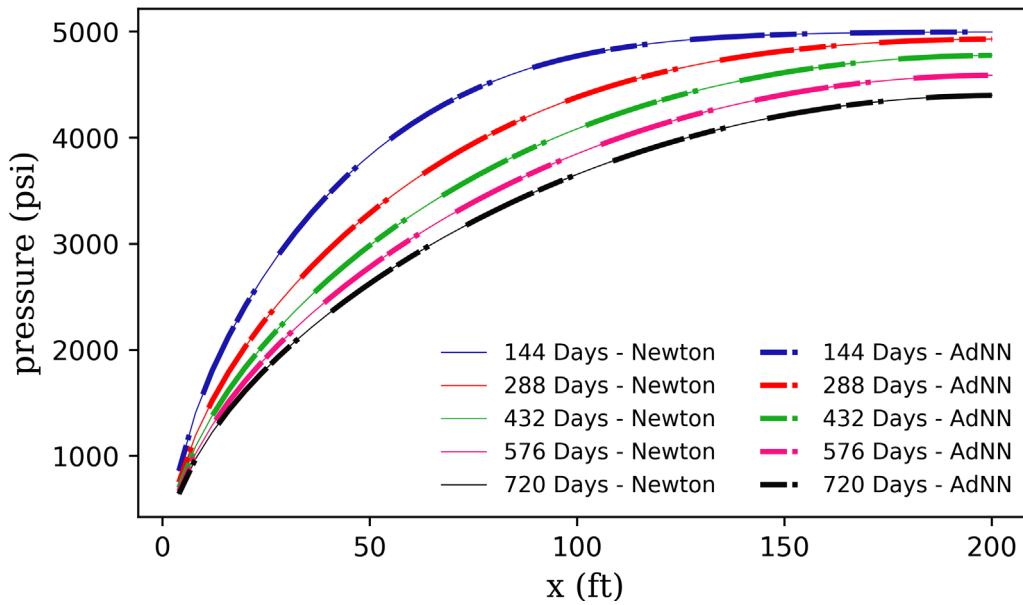
Adaptive Neural Network (AdNN) is technically recognized as a subset of machine learning methods that can adjust its randomly distributed weights and minimize its loss function with no help of previously collected data [51]. Regarding **Equation 9**, an AdNN tries to find a suite of pressures that their employment generates a matrix of relative zeros. **Figure 4** shows the proposed algorithm based on the papers presented in **3**. The proposed workflow takes advantages of adaptive laws to modify the weights of AdNN, which is supposed to generate the corrections to the initial set of pressures [52]. Then, the corrected pressures are inserted into the nonlinear simultaneous algebraic equations [53]. Eventually, comparing the output matrix of answers with the preset criteria determines if the procedure should keep iterating until finding the most proper set of pressures or stop the computations.



548

549 **Figure 4:** The proposed nonlinear solver based on using AdNN (**Chapter 3, Figure 1**)

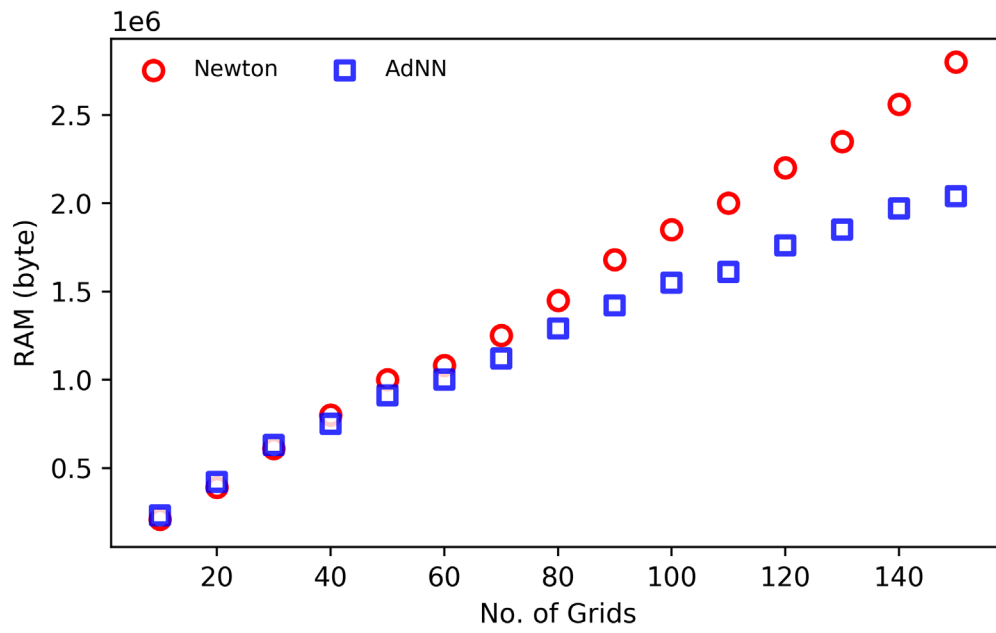
550 The success of the implemented algorithm has been illustrated in **Figure 5**. It is
 551 shown that the produced outputs are as close as possible to those generated by Newton's
 552 method.



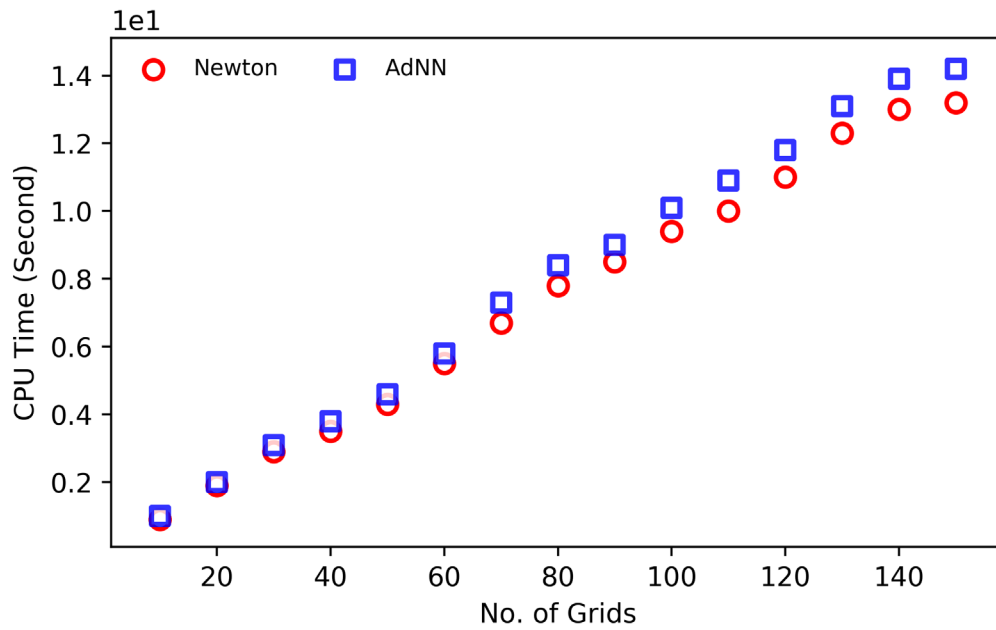
553

554 **Figure 5:** The results of using AdNN versus results of applying Newton's method (Chapter 3,
555 **Figure 3)**

556 One of the most important aspects of using such a methodology is its computational
557 efficiency. The examination of computational efficiency can be done based on the observations
558 of RAM usage and CPU Time. The results of the analysis have been indicated in **Figure 6**.
559 Because the proposed workflow is free of calculating the derivatives, the RAM usage is less
560 than Newton's method. It becomes even more important for the larger number of grids. The
561 CPU Time measurement shows that using the represented workflow has almost the same
562 performance as Newton's method although it is observed that Newton's method is faster for
563 the larger number of grids.



(a)



(b)

564 **Figure 6:** The computational efficiency of the AdNN-solver (**Chapter 3, Figure 11, 12**)

565

1.3 Microscopic Scale

566

567

568

569

570

571

572

573

The production from unconventional resources like tight and ultratight hydrocarbon reservoirs can be guaranteed if the prior reservoir studies are undertaken precisely [54]. As a result, carrying out experimental investigations such as Routine Core AnaLysis (RCAL) and Special Core AnaLysis (SCAL) to reveal the petrophysical parameters as accurate as possible has always been recommended as the most promising plan. However, using classic laboratory methods to determine the parameters like the permeability of tight porous media is time-consuming, expensive and inaccurate [55]. Therefore, having a detailed experimental plan for a large number of samples taken from an unconventional resource is impractical.

574

575

576

577

578

579

580

581

582

Accordingly, Digital Rock Physics (DRP) has been introduced as a state-of-the-art technology that takes advantage of microtomographic imaging and advanced numerical simulations to complement laboratory investigations to understand relevant physical processes [56]. It is evident that in recent years, pore-scale modelling has been recognized as a standard and precious approach to estimate and predict the properties of porous media. Pore-scale modelling can effectively be employed to study flow simulation in porous media by modelling the void spaces and pore throats. Also, it results in the observation and understanding of various phenomena at the microscopic scale to accurately determine favourite properties, such as permeability, capillary pressure, and relative permeability curves [57].

583

584

585

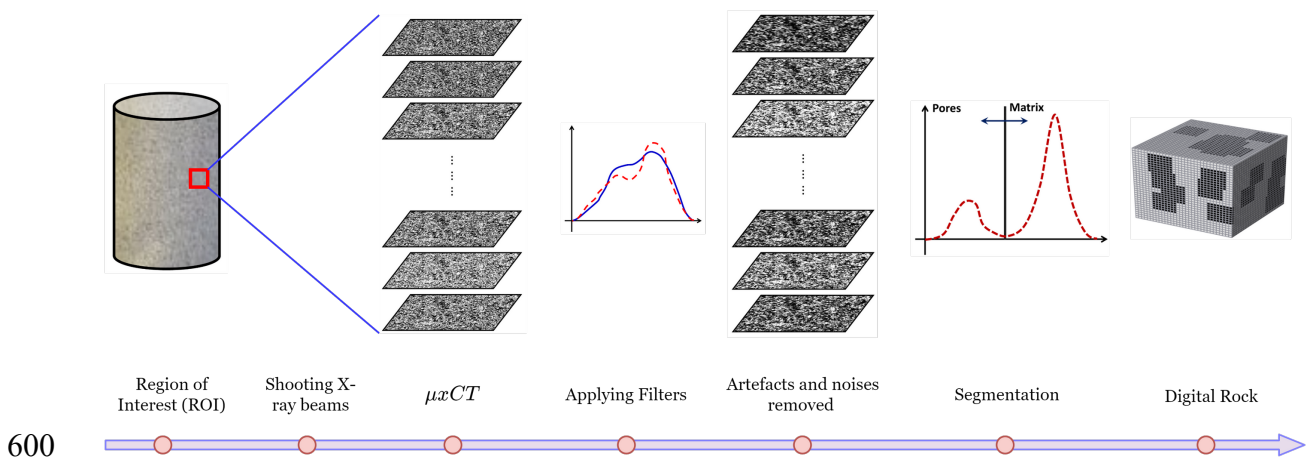
586

587

Micro x-ray Computed Tomography (μ xCT) is the most widely accessible and non-destructive method among various imaging techniques [58]. Technically, the object is placed between the stationary source and the detector of the μ xCT setup, and by its rotation, images are collected from different angles [59]. After generating sinograms applied by back-projection, 2D cross-sections are created using superimposition [60]. Routinely, μ xCT images

588 suffer from noises and artifacts such as roundoff errors, electronic, statistical, and random
 589 noises [61]. After filtering, the images need to be binarized. Following the thresholding
 590 method, the black voxels are labelled to void space, and white ones to grains lead to
 591 reconstructing the 3D sample used in further flow simulations [62]. More details about the
 592 mechanisms of image acquisition and processing and how the system and codes have been
 593 adjusted are described in **Chapter 5**.

594 Accordingly, the general procedure of Digital Image Processing (DIP) can be illustrated
 595 in **Figure 7**. It starts with imaging the rock sample. Then, the generated sinograms are
 596 undertaken with the computed tomography to create the supposed μ xCT images. As mentioned
 597 before, image filters are employed to reduce noise levels and increase the quality of images.
 598 The procedure continues with the application of the segmentation algorithm. The resultant
 599 binary cube is subjected to the various Pore-Scale Simulation (PSS) methods.



601 **Figure 7: The primary trend of DIP (Chapter 36, Figure 3)**

602 Direct Numerical Simulation (DNS) and Pore Network Modeling (PNM) are two
 603 general PSS methods that simultaneously find the pressure and velocity profile [63]. Although
 604 the PNM is a suitable method for modelling multiphase flow, its application causes losing

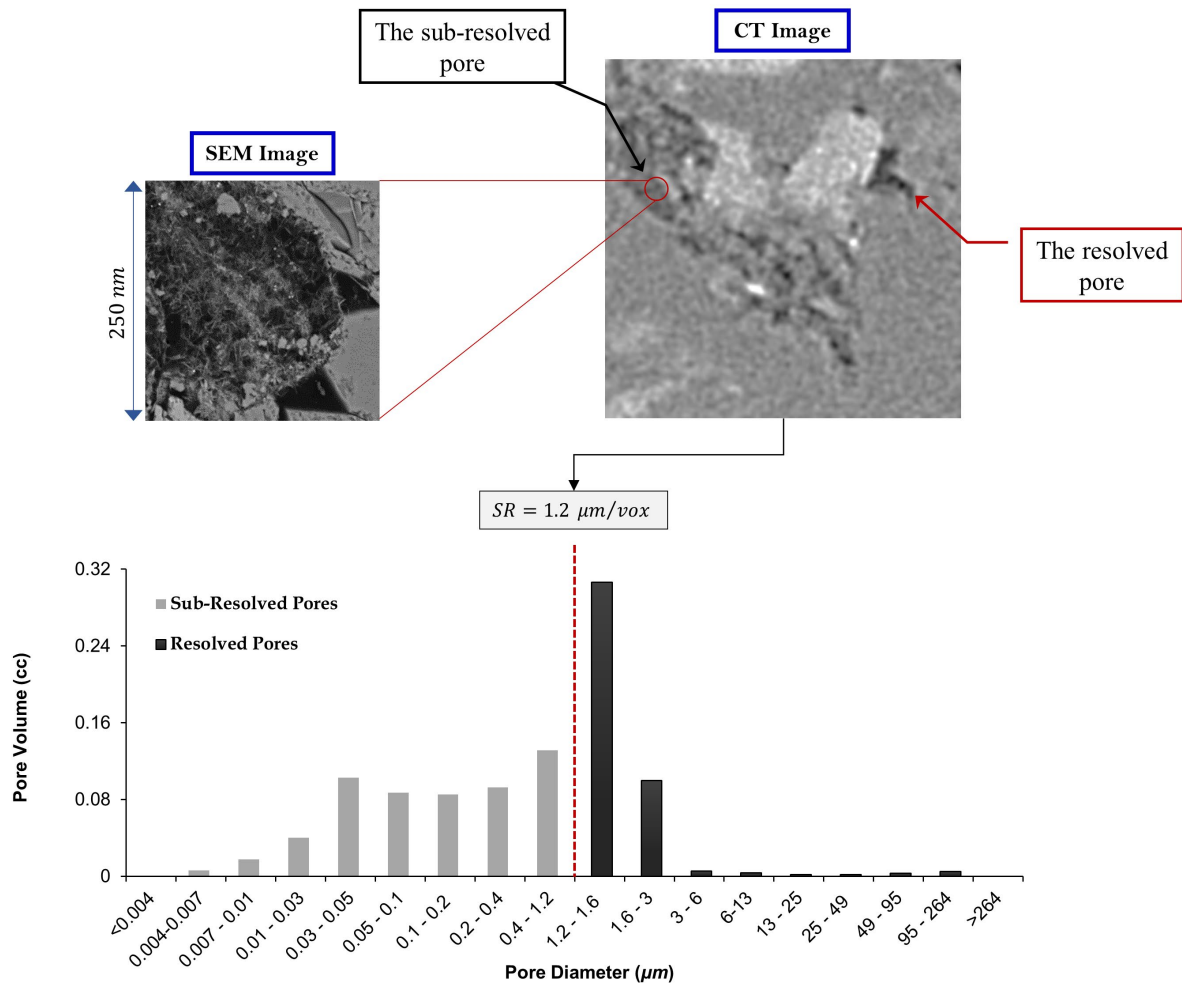
605 details of pore structures [64]. It leads to the increasing of numerical errors due to the imposed
606 idealization of porous spaces. In contrast, the DNS method is typically recommended as an
607 appropriate method for modelling single-phase flow because of its better computational
608 efficiency [65]. The DNS method is implemented directly on the captured images so that the
609 void spaces are detected, discretized, and then the relevant fluid flow equations are solved. The
610 basis of DNS is solving Navier-Stokes Equations (NSE) on grids directly coming from μ xCT
611 images. It causes studying the effects of pores structure and their effects on flow simulation.
612 Following the Computational Fluid Dynamics (CFD), finite-volume, finite-difference, and
613 finite-element are well-known methods that can be employed to solve the NSE with high
614 computational power [66]. In more detail, the CFD method is a top-to-bottom solution method
615 in which the first step is considering NSE. The second one is constructing a computational
616 domain then meshing it. After that, in various calculations such as pressure gradients, accuracy
617 is determined, and finally, the boundary conditions are applied, and the equations are solved.
618 The main dynamic parameter of single-phase flow is permeability, which highly depends on
619 the structures and connectivity among pores.

620 Although μ xCT images can be generated at different resolutions and Fields of View
621 (FOV), there are restrictions in choosing the resolution [67]. When the resolution is low, parts
622 of pores with minimal dimensions are not recognizable and lead to porosity calculation errors.
623 It is also impossible to properly segment throats by Digital Image Processing (DIP). As a result,
624 the permeability calculations are severely suffering from a high level of uncertainty. On the
625 other hand, more details about pore structures can be obtained at higher resolutions even though
626 it equals a narrow FOV and a failure to achieve a representative physical volume where the
627 porosity changes are negligible [68]. In other words, the major challenge restricting the
628 accuracy of rock properties calculations is the appropriate choice of resolution and the FOV. It

629 is due to the fact that there is an inverse relationship between them so that with increasing
630 resolution, FOV decreases and vice versa.

631 The discussed trade-off can become even more challenging when DRP technology is
632 supposed to be implemented in a tight and ultra-tight rock sample. To picture the situation more
633 understandable, it is highly required to consider the two concepts of spatial image resolution
634 and Pore Size Distribution (PSD) [69]. The value of spatial resolution indicates the physical
635 dimension that represents a voxel of the image. For instance, the spatial resolution of 1.2
636 micrometers per voxel ($1.2 \mu\text{m}/\text{vox}$) reveals the fact that the elements of the object with a size
637 less than $1.2 \mu\text{m}/\text{vox}$ cannot be seen in the reconstructed cross-sections. On the other hand, one
638 of the most important petrophysical characteristics for each core sample is its PSD.
639 Technically, the PSD is a histogram that represents information about the relative abundance
640 of each pore sizes in a represented core sample [70].

641 In the case of overlapping the PSD with the spatial resolution of μxCT images taken
642 from a tight sandstone sample from Achimovskiy formation, a large portion of pores cannot be
643 seen in the reconstructed images (**Figure 8**). Consequently, the computation results of PSS can
644 be questionable. It must be reminded that increasing the spatial resolution of μxCT images is
645 not a practical solution because of losing the representativeness of the images [71]. Therefore,
646 the question that needs to be answered is how to take the effects of “sub-resolved” pores into
647 account [72].



648

649 **Figure 8:** Comparing the results of PSD and the spatial resolution of μ xCT images (**Chapter**
 650 **36, Figure 2**)

651 To answer the raised question, a series of samples have firstly been taken from the
 652 Achimovskiy formation. Then, they have first been undertaken with the DIP tuned with the
 653 deep learning method. After having all the quality-increased images of DRP, it has been tried
 654 to check how much the classic approaches can be employed. Next, with the help of DIP and an
 655 operator named downsampling mainly used in deep learning, the effects of sub-resolved pores
 656 have implicitly been taken into account for the porosity and permeability calculations.

657

1.3.1 Digital Image Processing

658

As depicted in **Figure 7**, noise suppression is among the most vital elements of DIP.

659

Typically, image denoising is defined as finding a clean image from a noisy image. In other

660

words, a noisy image is the summation of a noise component and an original image. The most

661

important step of noise reduction is the minimization of feature loss in the cleaned image. The

662

various image filters can be classified into two main types of spatial and transform domain

663

filters. Within the spatial domain filters, the relevant mathematical operations are directly

664

applied to original noisy images [73].

665

On the contrary, transform domain filters are those in which the target image is first

666

supposed to be decomposed into different frequency components. Then, the treatment is done

667

on the resultant components, and the outcomes finally form a clean image. Regarding all the

668

types of filters and their corresponding domains, the trial-and-error attempts have shown that

669

the sequential implementation of the bandpass and bilateral can noticeably improve the quality

670

of images without much amount of feature loss. The bandpass filter removes the background

671

variations and the noise. It attenuates very high and very low frequencies but keeps the

672

midrange ones. In other words, the bandpass filter can simultaneously enhance edges and

673

reduce the noises [61].

674

Also, the bilateral filter has been used because of its edge-preservation, nonlinearity

675

and smoothness. However, the usage of classic DIP needs to know about the optimum values

676

of filter parameters which can only be obtained by testing various sets of numbers. Also, the

677

implementation of both filters on more than 1400 sequential images is time-consuming and

678

computationally expensive [74]. They have been taken as the main incentive to use deep

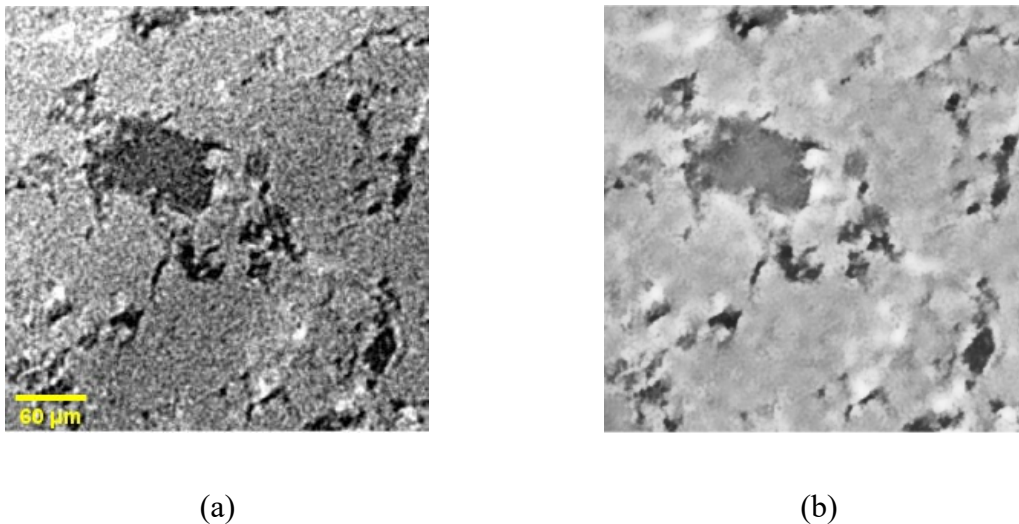
679

learning for image denoising. Deep learning layers perform nothing but an approximation of a

680 transfer function between the input and the output. More details about deep learning and their
681 impacts to the image processing have been discussed in **Chapter 4**.

682 1.3.1.1 Deep Learning for Noise Reduction

683 After finishing the images acquisition, the tomographically computed images have been
684 stacked on each other. Then, a cube with the size of 1400^3 voxels has been cropped from the
685 central part of the stacked images. As described earlier, the cropped cube has been undertaken
686 with the bandpass and bilateral filters to generate clean images, **Figure 9**.

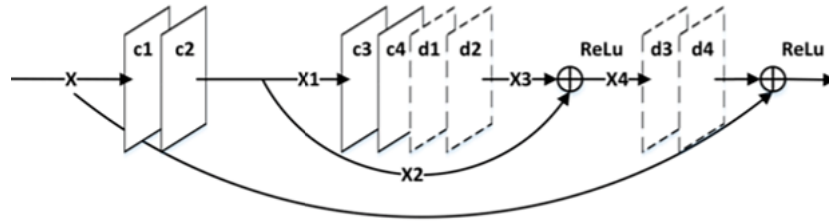


687 **Figure 9:** The effects of the implemented DIP (a) The original image (b) The clean image

688 **(Chapter 4, Figure 2)**

689 The noisy images and the clean ones have been used as the training data for a supervised
690 image denoising method based on deep learning. In more details, a Residual Encoder-Decoder
691 Net (RED-Net) has been employed. The applied RED-Net is formed based on a stack of
692 convolutional layers (encoder) and deconvolutional layers (decoder) [75]. The employed RED-
693 Net has schematically been shown in **Figure 10**. All the used convolutional and

694 deconvolutional layers have 64 kernels with the size of 3 by 3. Also, the padding is one, and
 695 the implemented activation function is ReLU.



696

697 **Figure 10:** The schematic of the implemented RED-Net (**Chapter 4, Figure 4**)

698 The performance of the implemented RED-Net using various loss functions has been
 699 evaluated with the help of full-reference and no-reference matrices. **Table 2** shows the
 700 measured Signal-to-Noise Ratio (SNR) for using different loss functions. The SNR of using
 701 some loss functions is better than the SNR of the ground truths.

702 **Table 2:** Effects of using various loss functions

	Source	GT	L_1	L_2	SSIM	VGG1_1	VGG3_1	VGG3_4
SNR	0.108	0.558	0.493	0.528	0.582	0.590	0.546	0.576

703

704 1.3.2 Pore-Scale Simulation

705 The most important parameters that are expected to be computed correctly based on
 706 DRP are porosity (ϕ) and permeability (k). According to the generated black and white model,
 707 due to the implementation of a segmentation algorithm, the total porosity can be known as the
 708 ratio of black voxels over all voxels [76]. However, there are several methods for k
 709 computation. Basically, k is defined as:

$$k = -\frac{\mu \bar{U}}{\frac{\Delta p}{L}} \quad (14)$$

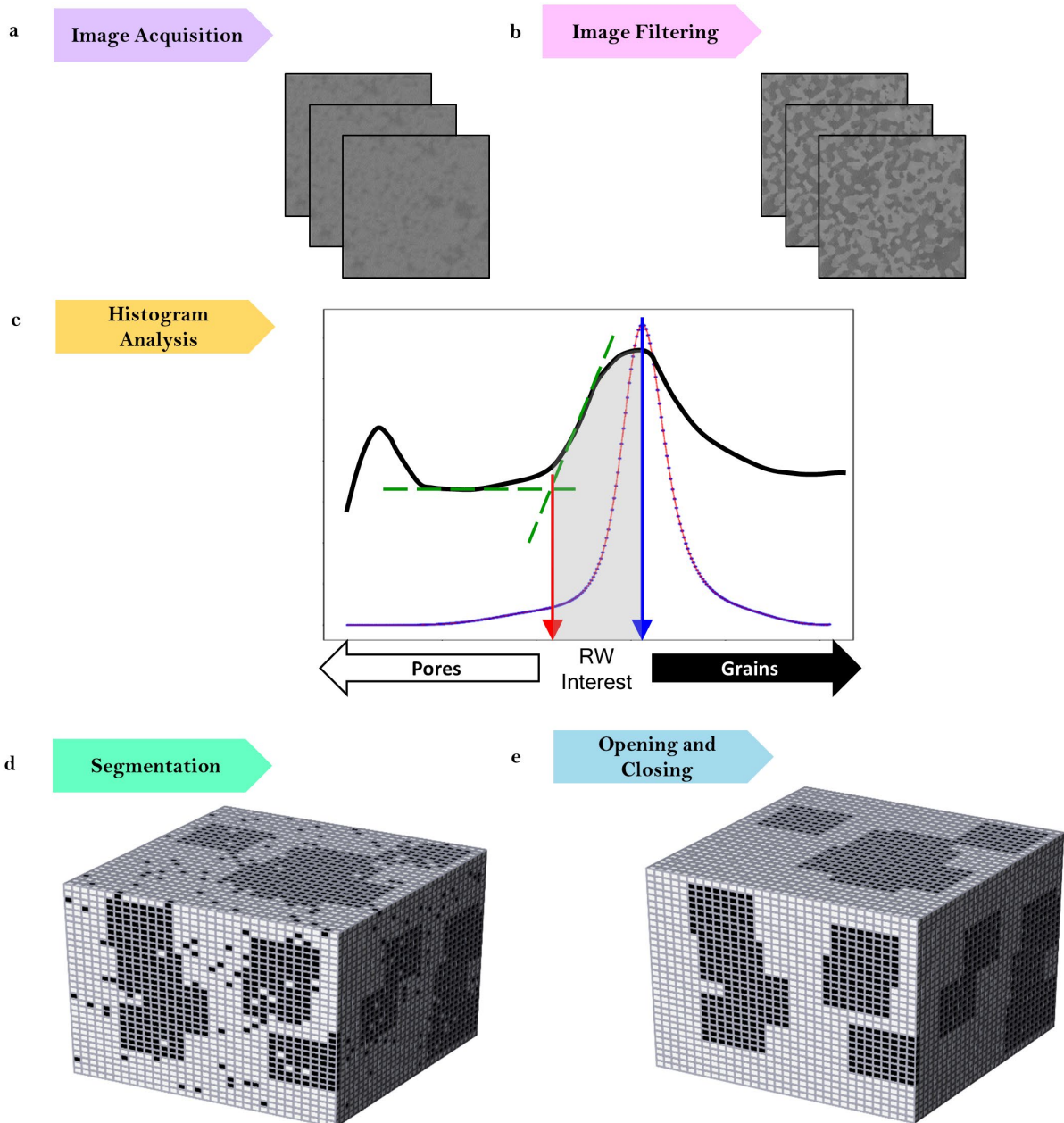
710 where $\frac{\Delta p}{L}$ is the pressure gradient, μ is viscosity and \bar{U} shows the average flow velocity in the
711 entire flow domain. Computation of \bar{U} is the leading interest for various researches. It can be
712 computed based on one of the following methods:

- 713 • Direct Simulation
- 714 • Lattice Boltzmann Method
- 715 • Pore Network Modelling

716 Regarding the tight formations, the basic idea is that how much using these methods is
717 reliable when a large portion of pores cannot literally be seen in the images. The idea has wholly
718 been discussed in the next part. Also, it has been figured out that how it is possible to use the
719 classic approaches to consider the effects of sub-resolved pores.

720 **1.3.2.1 Implementation of the Classic Approaches**

721 As discussed earlier, the most important concern of applying DRP methods to tight
722 formation is that a large portion of pores cannot be seen in the μ xCT images. As a result, using
723 classic DRP methods is questionable. In terms of DIP, the filtered images are supposed to be
724 binarized in order to form a digital rock sample. In spite of using many conventional global
725 segmentation algorithms, it has been observed that implementing a double-threshold method
726 like Random Walker (RW) algorithm can generate segmented images that their post-processing
727 with some morphological operators results in a binary model with the minimum loss of
728 information, **Figure 11**.



729

730

Figure 11: The implemented DIP in a glance (**Chapter 5, Figure 2**)

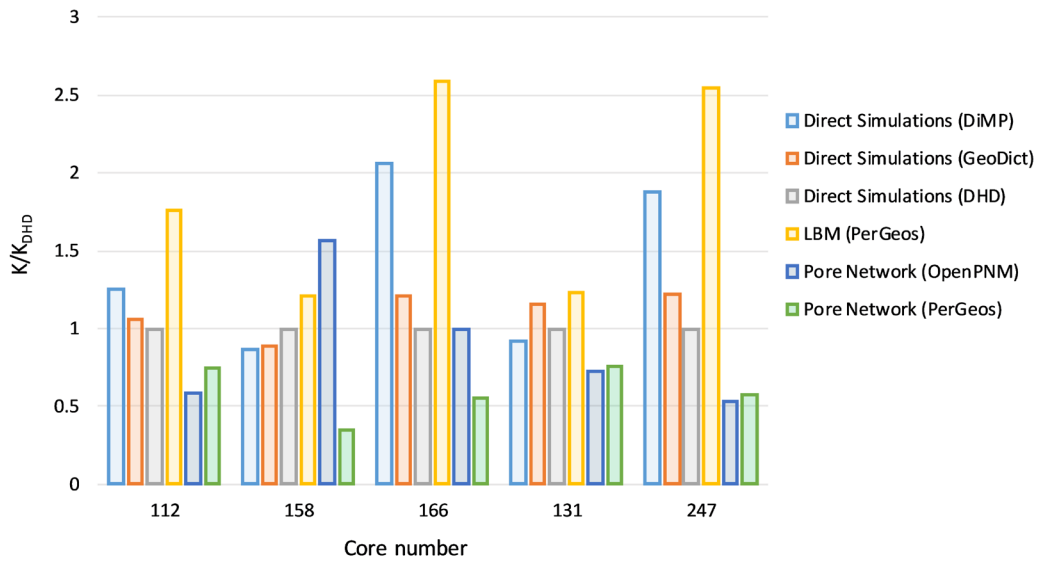
731

732

733

734

The next step is the employment of the already mentioned PSS methods. Accordingly, the permeability of 5 samples has been computed based on what has been described in **Pore-Scale Simulation**. Based on the generated results illustrated in **Figure 12**, it can be interpreted that there are no steady trends among the generated results.



735

736 **Figure 12:** The results of permeability computations based on the variety of methods

737

(Chapter 5, Figure 4)

738

It is necessary to consider that the differences among the generated results are due to

739

the various numerical methods that the corresponding commercial simulators have used. Next,

740

the dependency of the overall procedure to the implemented DIP has been observed. It needs

741

to be highlighted that the supposed sensitivity analysis has been done based on the method of

742

the Direct Simulation method. The Manual DIP is the first workflow implemented for all the

743

gathered images. The method is based on using a typical Personal Computer (PC). Therefore,

744

the resultant binarized cubes have the size of 400^3 voxels after running Otsu's algorithm. After

745

that, the same procedure of PSS has been repeated for the 600^3 voxels generated by

746

Schlumberger through carrying the Cross-Laboratory Control DIP out. Eventually, the third

747

type of DIP has been employed by taking advantage of a High-Performance Computer (HPC)

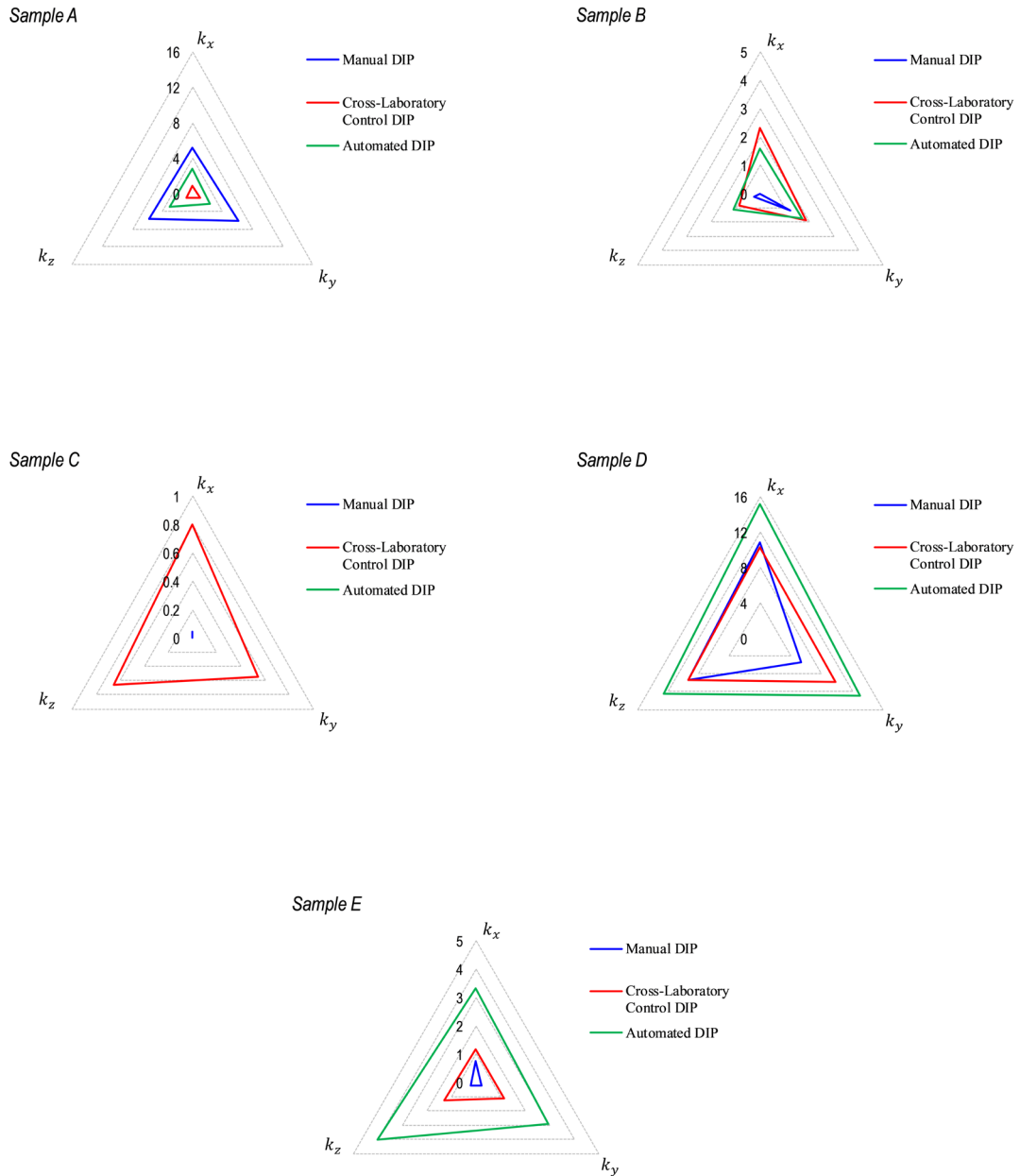
748

unit. The implemented Automated DIP can produce not only a binary cube with the size of

749

1400^3 voxels but also uses the RW algorithm, which is remarked as an advanced double-

750 threshold algorithm. The anisotropic permeability analysis of using various DIP has been
751 indicated in **Figure 13**.



752 **Figure 13:** Effects of image processing on the permeability anisotropy analysis (**Chapter 5,**
753 **Figure 5**)

754 In conclusion, it is believed that the complexity of pore geometry existing in tight
755 sandstones is the main reason that why there is a kind of deviation in calculated permeability
756 values. In other words, due to the high level of the inherent complexity within the supposed
757 samples, the results of pore-scale simulations are strongly dependent on the applied size of the
758 sample and the applied segmentation algorithm.

759 1.3.2.2 Effects of Sub-Resolved Pores

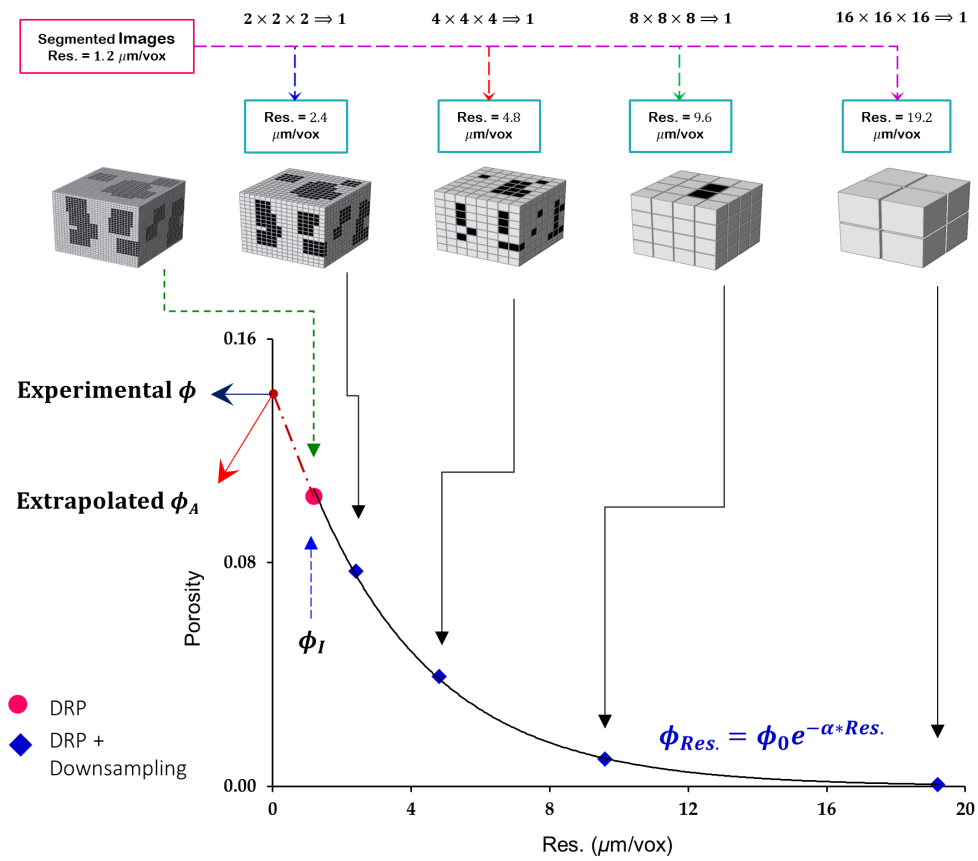
760 The image-based computations of petrophysical properties are typically suffering from
761 biases. In other words, there are several important considerations when comparing DRP results
762 with lab measurements. One of the most significant factors that affect the quality of DRP results
763 is the degree of resolved rock components. Moreover, the DRP results are impacted by each
764 step shown in **Figure 11**. Besides, it should be considered that the computed results are based
765 on a micron-scale while the measurements have been made at the core scale.

766 Consequently, the biases are created in the computed results, even for those perfectly
767 homogeneous samples. To put it in another way, a systematic offset has been observed when
768 comparing the computed porosity and permeability with those coming from the laboratory
769 measurements. In some details, it has been noticed that the image-based porosities are 50% less
770 than the expected values [77], and also, the computed permeabilities are 10-times greater than
771 the experimental values [60]. Further analyses show that applying a deep-learning operator
772 known as downsampling can synthetically reduce the spatial while not changing the physical
773 size. Running the downsampling allows the researchers to have a set of computed porosities
774 versus the synthetic spatial resolution.

775 To put it more simply, downsampling mimics the trend of multi-scale imaging. Like
776 losing more details (observing fewer pores) for lower spatial resolution, the downsampling can

777 be considered a method to generate synthetic images with the lower resolution if the maximum
778 operator is applied. For instance, the images of the sample can have a spatial resolution of 1.2
779 $\mu\text{m}/\text{vox}$. The sequential applying of the downsampling operator can generate the synthetic
780 resolution of 2.4, 4.8, 9.6 and 19.2 $\mu\text{m}/\text{vox}$.

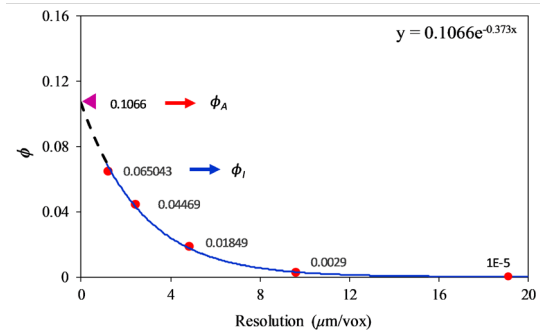
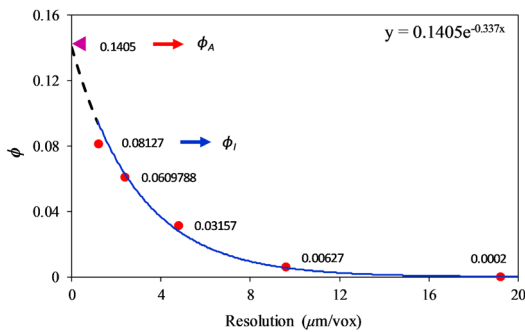
781 Then, there is a possibility of computing the porosity for each one of the mentioned
782 resolutions. The analyses made to the Achimovskiy formation show that the scatter can
783 accurately be modelled with an exponential trendline. The generated model provides the
784 opportunity to estimate the porosity for the spatial resolution of 0 $\mu\text{m}/\text{vox}$, which is
785 theoretically possible but physically not. The procedure has graphically been illustrated in
786 **Figure 14**. The implementation of the method to 5 samples taken from Achimovskiy formation
787 has been performed in **Figure 15**.

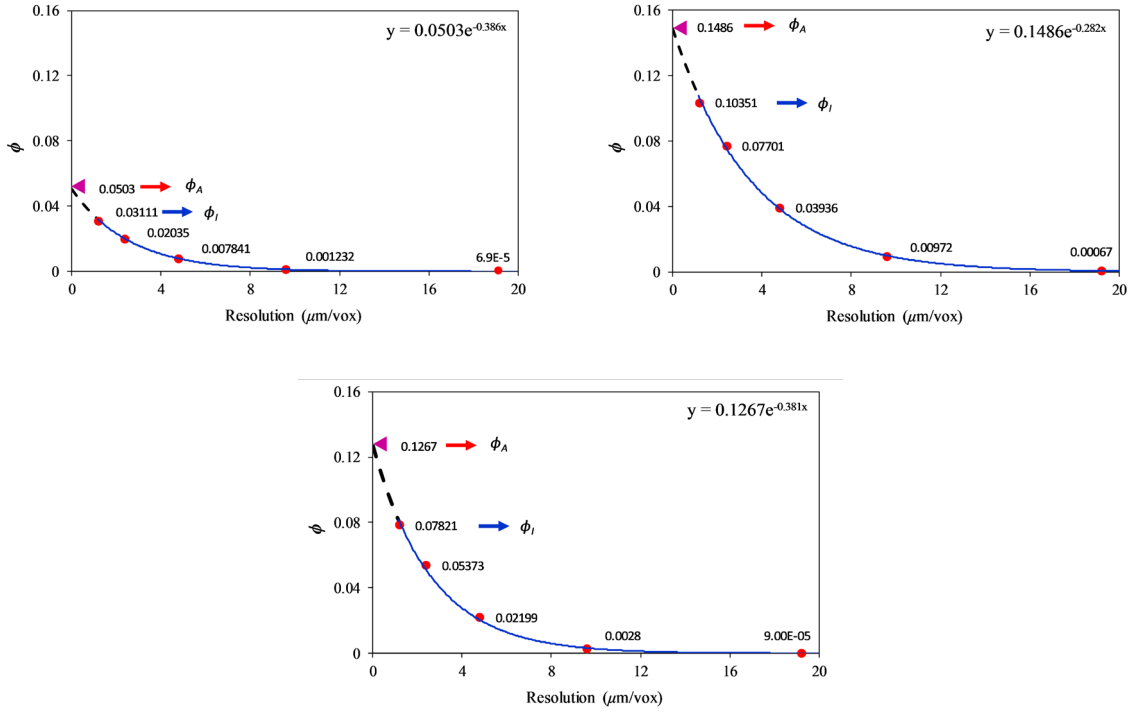


788

789 **Figure 14:** The effect of downsampling on the measured porosities (**Chapter 6, Figure 6**)

790 **It is required to mention that both parameters of ϕ_0 and α are determined based on the**
 791 **fitting procedure. Regarding the micro-scale resolution, it is possible to consider $Res.$ as zero**
 792 **in the obtained equation and then estimate the porosity at the intersection with the y-axis.**





793 **Figure 15:** Estimation of ϕ_A by using the introduced procedure (**Chapter 5, Figure 8**)

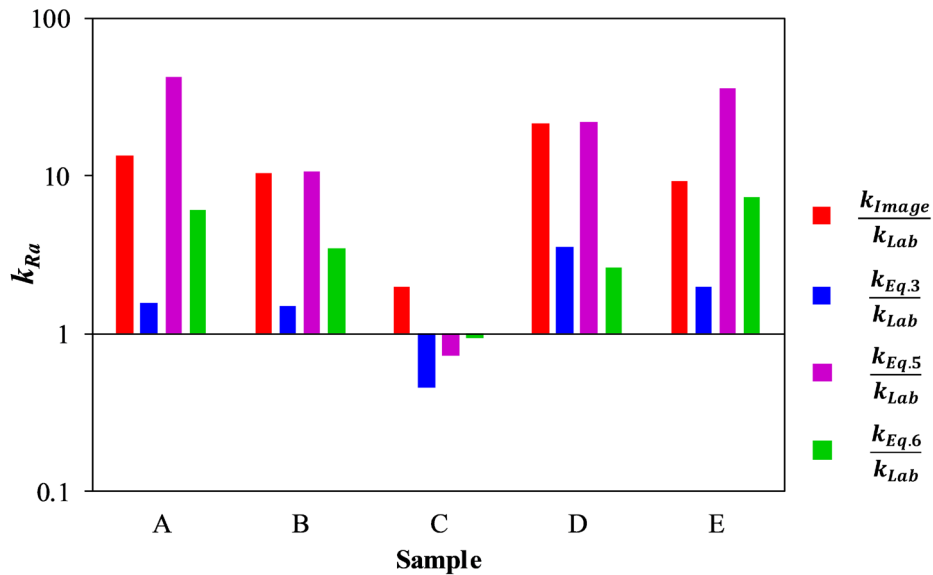
794 The whole procedure results in the estimation of **actual** porosity (ϕ_A). Regarding the
 795 porosity coming from Images (ϕ_I), it is possible to estimate the bias between both types of
 796 porosities as:

$$\beta = \left(\frac{\phi_A}{\phi_I}\right)^3 \left(\frac{1 - \phi_I}{1 - \phi_A}\right)^2 \quad (15)$$

797 where β shows the bias. Then, β can be employed to compute the Actual permeability (k_A)
 798 based on Image permeability (k_I) as:

$$\frac{k_I}{k_A} = \beta \quad (16)$$

799 It has been observed that using the discussed procedure to find the k_A has been
 800 successful enough so that the ratios of k_A over the experimental permeability values are closer
 801 to unity than other approaches, **Figure 16**.



802

803 **Figure 16:** Estimation of k_A with the help of computed β (**Chapter 6, Figure 10**)

804 $k_{Eq.3}$, $k_{Eq.5}$ and $k_{Eq.6}$ shown in the legend have fully be described in **Chapter 6** where the
 805 relevant paper has been presented there. It must be underlined that all the supposed equations
 806 have the same notation in the supposed paper.

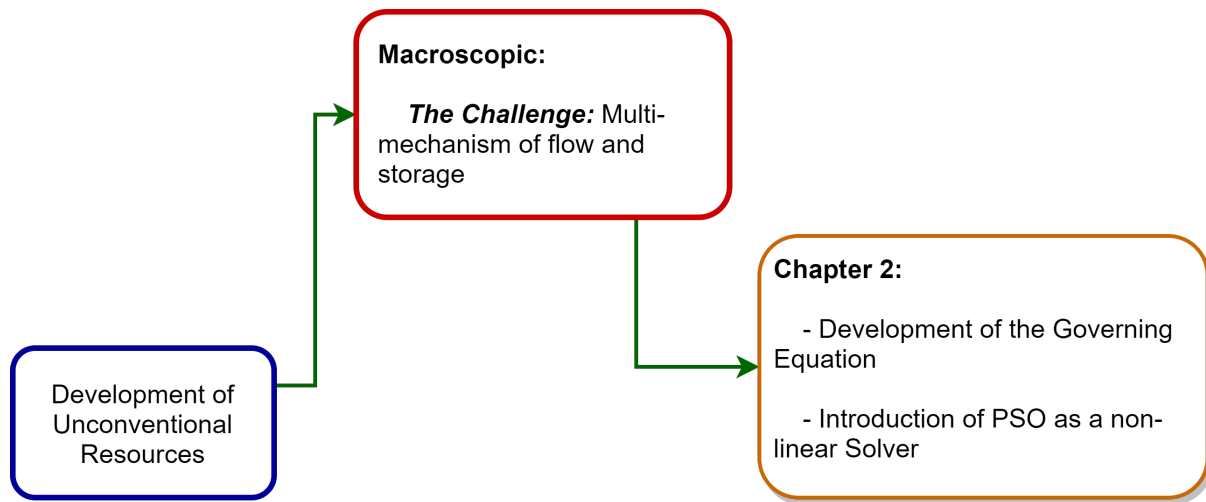
807 To sum up, **Chapters 2** and **3** will show two successful samples of applying artificial
 808 intelligence methods to overcome and manage the inherent nonlinearity of macroscopic fluid
 809 flow and storage in tight and ultra-tight porous media. The main microscopic challenge that
 810 the current research has tried to figure out is whether the current technology of digital rock
 811 physics can take the effects of sub-resolved pores into account. The outcomes of image
 812 processing indicate that applying new technologies like using advanced neural networks for
 813 noise suppression (**Chapter 4**) is inevitable. In terms of pore-scale simulation, **Chapter 5** has

814 shown that the implementation of classic approaches cannot generate satisfying results.
815 Therefore, a hybrid workflow based on digital image processing, downsampling and empirical
816 correlation has been developed in **Chapter 6**. Finally, the thesis has been summarized in
817 **Chapter 7**, where my challenges within doing the thesis have been addressed, and the probable
818 solutions for the following studies have been discussed.

819

820 **2. A novel approach for solving nonlinear flow equations: The**
821 **next step towards an accurate assessment of shale gas**
822 **resources**

823 Fluid flow in tight and ultra-tight porous media is a function of various flow and storage
824 mechanisms. Taking the effects of slippage, diffusion, desorption and dissolved gas as the
825 essential phenomena of ultra-tight porous media like shale gas resources into account
826 noticeably increases the inherent nonlinearity of fluid flow governing equations. The
827 implementation of classic solvers like Newton's method can generate satisfying results only if
828 a proper initial guess has already been made. Moreover, the usage of Newton's method is based
829 on making derivatives and forming the Jacobian matrix, which can be challenging. Going
830 through Newton's method clarifies that it tries to find a series of pressures that lead the
831 nonlinear simultaneous algebraic equations to generate zeros based. The same idea can be
832 employed by means of metaheuristic optimization methods that are going to find the best
833 colony of particles (pressures), making the algebraic equations equal to zeros. The presented
834 paper has first tried to show the most important phenomena of shale gas resources and then
835 propose a new application of Particle Swarm Optimization (PSO) as a nonlinear solver. Also,
836 the impact of the prepared paper to the roadmap of the research has been shown in **Figure 17**.



837

838

Figure 17: Chapter 2 in a glance

839

CRedit author statement:

840

1. **Yashar Bezyan:** Conceptualization, Methodology, Investigation, Writing –

841

Original Draft, Software

842

2. **Mohammad Ebadi:** Conceptualization, Methodology, Investigation,

843

Writing - Original Draft, Validation, Visualization

844

3. **Shahab Gerami:** Methodology, Supervision

845

4. **Roozbeh Rafati:** Formal Analysis, Supervision

846

5. **Mohammad Sharifi:** Formal Analysis, Writing – Original Draft

847

6. **Dmitry Koroteev:** Writing – Review & Editing, Supervision, Project

848

Administration

849



Full Length Article

A novel approach for solving nonlinear flow equations: The next step towards an accurate assessment of shale gas resources

Yashar Bezyan^a, Mohammad Ebadi^{b,*}, Shahab Gerami^c, Roozbeh Rafati^d, Mohammad Sharifi^e, Dmitry Koroteev^b

^a Department of Petroleum Engineering, Science and Research Branch, Islamic Azad University, Tehran, Iran

^b Skolkovo Institute of Science and Technology, Skolkovo Innovation Centre, Moscow Building 3, Moscow 143026, Russia

^c IOR Research Institute, Tehran, Iran

^d School of Engineering, University of Aberdeen, Aberdeen AB24 3UE, United Kingdom

^e Department of Petroleum Engineering, Amirkabir University of Technology, Tehran, Iran



ARTICLE INFO

Keywords:

Shale gas reservoirs
Apparent permeability
Adsorbed gas
Kerogen distribution
Newton's method
Particle swarm optimization

ABSTRACT

As ultra-tight porous media that include organic contents, shale gas resources are technically known as complex systems having various mechanisms that impact storage and flow. The slippage, Knudsen diffusion, the process of desorption, an adsorbed layer that affects apparent permeability, and solute gas in kerogen are recognized to be the most important ones. However, simultaneous effects of multi-mechanism flow and storage, and influences of scattered organic contents on shale gas flow behaviour are not well-understood yet.

According to the mass conservation law, a basic mathematical model has been developed to investigate, step-by-step, the effects of different changes that are introduced, and examine whether patterns of how kerogen is distributed affect the production plateaus. The discretization of the second-order nonlinear Partial Differential Equation (PDE) that is evolved results in a certain number of nonlinear simultaneous algebraic equations, which are conventionally solved with the application of Newton's method. To overcome the inherent difficulties of the initial guess, the derivations, and the inversion of the Jacobian matrix, a new application of Particle Swarm Optimization (PSO) as a nonlinear solver was applied to extract the anticipated pressure profile for each step in time outside the bounds of the reference equations.

The results show that not only can the PSO effectively meet the required criteria, but also it performed faster than conventional techniques, especially in cases with a larger number of grids that encompass more phenomena. It was further revealed that the insertion of a multi-mechanism apparent permeability model in which the pore radius is also a pressure-dependent parameter causes the lower rate of production. A higher level of production has been recorded after including storage terms of adsorption and solute gas in kerogens. Although different patterns of kerogen distribution have finally overlapped, the different taken trend of each production profile underlines the impact of kerogen distribution as an important parameter within the procedure of history matching.

1. Introduction

Shale gas resources, which are discussed on a daily basis, have drawn many researchers' attentions towards the new wonder of "The Shale Gas Revolution". This slowly growing movement started the century by compromising just less than 2 percent of domestic outputs. Surprisingly, today it accounts for nearly one-third, and the projection is that by 2030s is a half of the gas produced in the USA and China will be from shale gas resources [1]. Recent industrial and scientific advances have caused experts to conclude that organic-rich shales have

the potential to be regarded not only as sources containing typical oil and gas, but also as reservoirs to be produced [2].

Applying modern methods like high pressure mercury injection (up to 60,000 psi) and novel photo techniques have proved the existences of nano scale pores and throats in organic-rich shale gas resources [3,4]. Nano scale pores have strong effects on the storage and flow in shale gas resources. First, they provide large exposed surface areas known to hold the potential for a considerable amount of adsorbed gas. Also, Darcy's law is not applicable to shale gas resources because it has originally been developed for micro scale pores [3–10]. Moreover, the trapped

* Corresponding author.

E-mail address: Mohammad.Ebadi@Skoltech.ru (M. Ebadi).

<https://doi.org/10.1016/j.fuel.2018.08.157>

Received 14 May 2018; Received in revised form 4 July 2018; Accepted 30 August 2018
0016-2361/ © 2018 Elsevier Ltd. All rights reserved.

Nomenclature	
Δx	length of each grid; <i>ft</i>
A	surface area; ft^2
A_K	kerogen surface area; ft^2
C	net heat of adsorption; <i>Dimensionless</i>
c	concentration; lb_m/ft^3
C_g	gas compressibility; psi^{-1}
d	pore diameter; <i>ft</i>
D	kerogen diffusivity coefficient; ft^2/Day
D_f	surface roughness; <i>Dimensionless</i>
d_m	normalized molecular size; <i>ft</i>
E_1	heat of adsorption for the first layer; <i>Dimensionless</i>
E_k	heat of higher layers; <i>Dimensionless</i>
k	absolute permeability; <i>md</i>
K_a	differential equilibrium partitioning coefficient; <i>Dimensionless</i>
k_{app}	apparent permeability; <i>md</i>
k_H	Henry's constant; $lb/(psi \cdot ft^3)$
K_n	Knudsen number; <i>Dimensionless</i>
M	molecular weight; lb_m
n	number of gas moles; $lb \text{ mol}$
P	pressure; <i>psi</i>
P_{cte}	constant pressure; <i>psi</i>
P_m	initial pressure; <i>psi</i>
P_l	Langmuir pressure; <i>psi</i>
P_o	saturation pressure of the gas; <i>psi</i>
P_{ST}	standard pressure; <i>psi</i>
q_k	mass flux from kerogen to matrix (kerogen mass flux); lb_m / day
R	gas constant; $(psi \cdot ft^3)/(lb \text{ mol} \cdot ^\circ R)$
r	pore radius; <i>ft</i>
r_{eff}	effective pore radius; <i>ft</i>
r_{mol}	radius of gas molecules; <i>ft</i>
T	temperature; $^\circ F$
t	time; <i>day</i>
t_{ads}	thickness of the adsorbed layer; <i>ft</i>
T_{ST}	standard temperature; $^\circ F$
V	gas volume of adsorption; ft^3/lb_m
V_b	bulk volume; ft^3
V_L	Langmuir volume; ft^3 / lb_m
V_m	maximum volume of adsorbed gas for a single molecular layer; ft^3/lb_m
Z	compressibility factor; <i>Dimensionless</i>
z	height; <i>ft</i>
<i>Greek letters</i>	
α	adsorbed layer fitting slope; ft/psi
δ'	size ratio; <i>Dimensionless</i>
ζ	tangential momentum accommodation coefficient; <i>Dimensionless</i>
λ	mean free path; <i>ft</i>
μ	viscosity; <i>cp</i>
ρ_a	density of adsorbed gas; lb_m/ft^3
ρ_{avg}	averaged density; lb_m/ft^3
ρ_b	bulk density; lb_m/ft^3
ρ_f	density of free or compressed gas; lb_m/ft^3
ρ_s	density of solute gas; lb_m/ft^3
τ	tortuosity; <i>Dimensionless</i>
ν	Darcy's velocity; (ft/day)
ϕ	porosity; <i>Dimensionless</i>

organic content, kerogen, is also one of the other most special and unique characteristics of shale gas resources that has an impact on the storage and flow of gas [4,11,12].

Last relevant research has discovered that the organic constituents cover part of the bulk rock, and are irregularly distributed in the shale gas media. Dispersed organic materials within the shales can affect flow and storage mechanisms [5,12–15]. Specifically, gas is typically stored in pores, and adsorbed on the oil-wet surface of nano scale pores on organic contents that can also have noticeable effects on the non-Darcy's flow [16–19]. On the contrary, the water-wet nature of clays caused the provided empty sites to be filled with water. Therefore, it has been concluded that a notable fraction of the adsorbed gas is stored in the kerogen pores [12,20,21]. Besides that, more research has indicated that a portion of gas molecules remain in the solid part of the organic matter in the form of solute gas [4,22,23]. Indeed, the scattering of the kerogen is the substantial parameter that has a great impact on the modelling and simulation of storage and flow in the shale gas resources [5,12–15].

To describe the fluid flow of gas as a compressible fluid in conventional porous media, the benefits of Darcy's equation have been combined with the continuity equation. The strong functionality of gas parameters such as density, viscosity, and Z-factor on the pressure is the main reason why the supposed governing equation is presumed to be a nonlinear partial differential equation (PDE). In addition, the inclusion of other pressure-dependent phenomena with shale gas resources like apparent permeability, adsorption, and the release of gas from kerogen bodies lead the supposed second-order PDE towards a higher level of nonlinearity [24]. Undoubtedly, handling the nonlinear equations is one of the most challenging problems in numerical computations. Although there are possibilities of applying linearization techniques, the generation of results which are not satisfyingly accurate enough is the main reason to use methods which can directly solve the supposed

nonlinearity. Among the different conventional techniques that have ever been proposed to solve the equations referred to, Newton's method is undoubtedly the one that is the most extensively used [25].

However, performance and convergence for Newton's algorithm are strongly dependent on the proper initial guess. Also, the heavily derivation-dependent, high computational cost of Jacobian matrix, and lack of ability to deal with ill-conditioned matrixes are known to be other disadvantages [25,26]. Therefore, researchers' attentions have been drawn towards proposing more advanced methods that meet the required level of accuracy, and with the less computational cost for solving the nonlinear problems [27–29]. Particle swarm optimization (PSO) as an evolutionary and modern optimizer, which can find the optimal solution in the space that is being searched, has recently been proposed to deal with the nonlinearity of different engineering problems [30,31]. Although there is some couple of research in which the PSO has been applied to solve nonlinear equations, the current research has taken advantages of PSO to solve a certain number of nonlinear simultaneous algebraic equations generated after the discretization of the supposed PDE.

In more details, a basic conventional Darcy's law has been modified to account for the effect of slippage, Knudsen diffusion, and impacts of the adsorbed layer on the apparent permeability. Moreover, gas desorption from the pore walls and effects of solute gas in bulks of kerogens are considered to correct the accumulation term. While the generated nonlinear simultaneous algebraic equations generated have been conventionally solved, the applicability of PSO as a free-derivation solver has also been investigated. At the final step, the positions of organic matters and their distribution effects on the fluid flow behaviour were investigated numerically.

2. Relevant phenomena to shale gas

The considerable dissimilarities among shale gas reservoirs with conventional oil and gas resources due to the existence of organic contents and natural nano scale pores, have been analysed in brief.

2.1. Multi-mechanism flow and apparent permeability

Generally, using conventional continuum flow equations and Darcy's law underestimate the flow rate when used for the ultra-tight porous media of shale gas resources. That is due to the assumption of zero-velocity boundary condition [8,32–36]. To figure out the concept of multi-mechanism flow in ultra-tight porous media, the Knudsen number (K_n) is normally considered to be a clarifying index [3]. The various flow regimes can be identified as:

$$K_n = \frac{\lambda}{d} \tag{1}$$

where λ in shale gas reservoirs is physically defined as the average distance travelled by a gas molecule before colliding with another molecule that changes its energy, track, or other properties [37]. Classifications of flow regimes based on K_n , and the relevant information and highlights have been reported in Table 1.

Detailed studies about the morphology and pore size distribution of shale gas reservoirs show that the pore sizes in the shales under study ranges from 1 to 200 nm, resulting in the generation of K_n relating between 0.0002 and 6, respectively [41–43]. Altogether, it can be deduced that flow in shale gas reservoirs is a multi-mechanism phenomena including continuum flow, slip flow, and transition flow [34,40]. The topic under discussion about flow in shale gas reservoirs, and relevant complexities has been graphically depicted in Fig. 1.

There is an enlarged thin section of shale gas matrixes including different ranges of pore sizes leading to the generation of various K_n , and their corresponding flow regimes as well.

According to previous studies on characterizing of flow in ultra-tight porous materials, the first classic apparent permeability model specific for shale gas resources was proposed by Javadpour [4]. This model describes the multi-mechanism flow in the bundle of nano tubes based on pressure forces and Knudsen diffusion. More details are described in Table 2. The opportunity for advancements in order to make the former model more suitable for porous media was taken by Darabi et al. [8]. Porosity, permeability and tortuosity as the main characteristic of a typical porous media were incorporated into the previous model. The new model accounts for some complexities in gas flow through ultra-tight natural porous media. For example, local heterogeneity is one of the main factors which is routinely ignored in previous models, but it was inserted into the new model, with satisfying results.

2.2. Adsorbed gas

Calculations of gas-in-place in shale gas reservoirs have repeatedly

Table 1
Different flow regimes as a function of Knudsen number (K_n) [8,37–40].

Knudsen Number (K_n)	Flow Regimes	Remarks
$K_n < 10^{-3}$	Continuum Flow (C)	<ul style="list-style-type: none"> • Surface velocity of gas molecule at pore wall is zero • Darcy's law is applicable • The λ of gas molecules has a negligible value in comparison with the pore radius
$10^{-3} < K_n < 10^{-1}$	Slip Flow (S)	<ul style="list-style-type: none"> • The theory of continuum flow breaks down • The frequency of molecules' collisions with pore wall is not insignificant anymore
$10^{-1} < K_n < 10$	Transition Flow (T)	<ul style="list-style-type: none"> • Molecules strike against the pore walls and lean towards slipping on pore walls instead of having zero velocity • λ is in the comparable magnitude of order with pore sizes
$10 < K_n < \infty$	Free-Molecular Flow (F)	<ul style="list-style-type: none"> • Molecules travel more autonomously from each other • Collisions of gas molecules with flow boundaries occur more repeatedly in comparison with the inter-molecule collisions

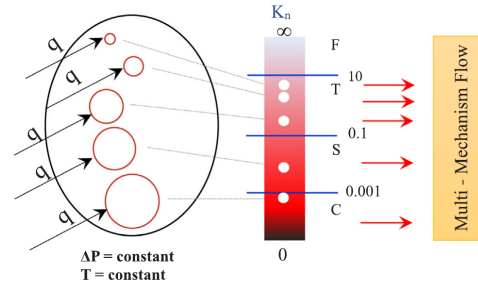


Fig. 1. Multi-mechanism flow in a thin section of a shale gas reservoir as a function of K_n .

been reported as a challenging issue. That is due to the fact that the final volume is not only a function of compacted free gas but is also intensively influenced by what is adsorbed on the surface of kerogens [5,16], Fig. 2.

In other words, disregarding the adsorbed gas having a semi-liquid physical state with greater density than the free compressed gas leads to some remarkable underestimation. The effects of the adsorbed gas can become more pronounced when they accompany with the noticeable amount of surface area in shale gas reservoirs that is exponentially larger than what it is in conventional reservoirs [5,7,44,45]. Specifically, the pore structure and TOC are the most important parameters affecting adsorption, although other factors like depth, temperature, moisture, and pressure can have their own importance [45–47]. Through consideration of a dynamic instantaneous equilibrium at a constant pressure and temperature between non-adsorbed and adsorbed gas, the classic Langmuir isotherm is the most common adsorption isotherm that is routinely used [44–46]. More details can be found in Table 3. Some challenges such as the simplicity of the monolayer adsorption assumption of gas molecules at high pressures have also been taken as excuses to apply other models like BET [48].

Also, the gas molecules which stick to pore surfaces, known as the adsorbed layer, limit the available conductance for the flow of free and already desorbed gas. Subsequently, the adsorbed gas has a negative effect on permeability, since the methane molecule radius is comparable to the pore sizes.

On the other hand, below a certain critical pressure, the adsorbed molecules begin to be desorbed. In fact, gas molecule desorption occurring due to the pressure reduction decreases the thickness of the adsorbed layer, which results in an improvement in permeability. The significance of the adsorbed layer on the flow path properties has led recent research to predict the thickness of adsorbed gas molecule according to alteration in pressure [9,49–51]. Some couple of relevant research is shown brief in Table 4.

Table 2
Analytical reviews of multi-mechanism apparent permeability models.

Model	Correlation	Remarks
Javadpour [4]	$k_{app} = 1.95 \frac{\mu M}{\rho_{avg} T} \left(\frac{T}{M} \right)^{0.5} + 7.9 F \frac{\mu^2}{\rho_{avg}}$ $F = 1 + 1.56 \left(\frac{T}{M} \right)^{0.5} \frac{\mu}{\rho_{avg} T} \left(\frac{2}{\zeta} - 1 \right)$	<ul style="list-style-type: none"> - F is known as the slip coefficient - ζ is a function of pressure, temperature, gas type and wall surface smoothness - ζ is an experimental parameter - ζ is in the range of 0 to 1
Darabi et al. [8]	$k_{app} = 31.326 \frac{\mu M}{\rho_{avg} T} \frac{\phi}{\tau} (\delta')^{D_f - 2} \tau_f \left(\frac{T}{M} \right)^{0.5} + Fk$	<ul style="list-style-type: none"> - Suitable for a network of interconnected tortuous micro pores and nano pores - F is the same as before - ϕ/τ has been introduced to model Knudsen flow through porous media - D_f considers effects of pore surface roughness as one of the local heterogeneity on the Knudsen diffusion - D_f varies between 2 and 3 - δ' is the ratio size and defined as d_m/d - $k = \frac{r^2}{8}$

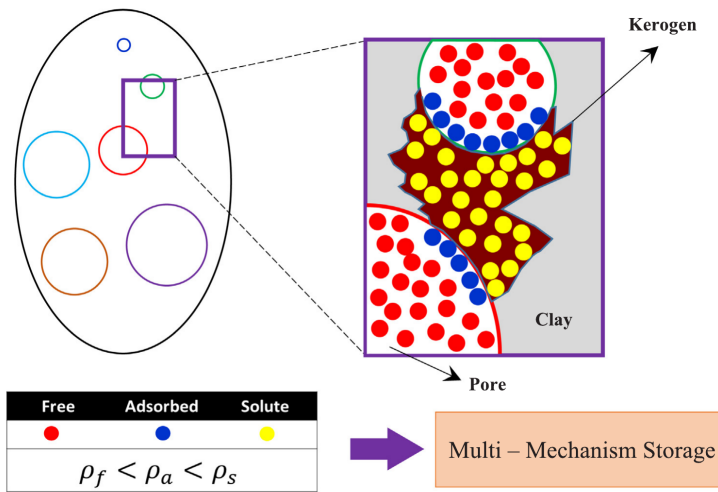


Fig. 2. Schematic of storage in a thin section of a shale gas reservoir, different pore sizes have colourfully and schematically been distinguished.

2.3. Kerogen

Kerogen is the organic material analogous to the bitumen that has the capability of storing hydrocarbons in a dissolved state. Recent researches have theoretically and experimentally been reported that a noticeable part of the gas-in-place in shale reservoirs is in the form of a solute stored in the kerogen [4,18,20,52]. It also states that the solute gas could contribute to the total gas production when an imbalance in

concentration is created between the gas on the surface and within the kerogen bulk owing to the gas desorption [4]. Even so, few studies have been conducted on the gas transport mechanism in kerogen medium. Most of the scientists believe that gas production from kerogen is a slow process and Fickian flow is the predominant transport mechanism. The second law of Fick in the Cartesian coordinate and z-direction is represented as [22,53–56]:

Table 3
Adsorption isotherms routinely used in petroleum industries.

Model	Correlation	Remarks
Langmuir [44–47]	$V = V_L \frac{P}{P_L + P}$	<ul style="list-style-type: none"> - It follows a stabilized trend at high pressures - The model is applicable for all types of surfaces - The model describes a mono-layer of adsorbed gas - It works based on 2 fitting parameters - Generally known as isotherm of Type I
BET [48]	$V_L = \frac{V_m C P}{(P_0 - P) \left[1 + \frac{(C-1)P}{P_0} \right]}$	<ul style="list-style-type: none"> - It is the general form of Langmuir isotherm - It follows an ascending trend at higher pressures - It is specified for homogeneous surfaces - The model describes multilayer of adsorbed gas - $C = \exp((E_1 - E_L)/RT)$ - It works based on a couple of fitting parameters - Generally known as isotherm of Type II

Table 4
Effects of adsorbed layer thickness on shale permeability.

Model	Correlation	Remarks
Sakhaee-pour and Bryant [49]	$t_{ads} = \alpha P$	<ul style="list-style-type: none"> Useful for pores less than 50 nm and organic contents Thickness of the adsorbed layer is 0.7 nm in pressures above 4061 psi. α is a fitting slope Easy to be applied in permeability models Low computational efforts are required It is supported with experimental results The thickness reduces linearly with pressure reduction Not reflecting the actual thickness of the adsorbed layer
Singh et al. [50]	$t_{ads} = 2r_{mol}$	<ul style="list-style-type: none"> Considering molecules are in the sphere shape $r_{mol} = (3V/4\pi)^{1/3}$ $V = \frac{ZnRT}{P}$ It is based on thermodynamical concepts Huge computational efforts are required

$$\frac{\partial^2 c}{\partial z^2} = \frac{1}{D} \frac{\partial c}{\partial t} \tag{2}$$

where c is concentration, D is the diffusion coefficient, and z and t represent the space and time, respectively.

3. Methodology

The current study considers a comprehensive model in which a variety of flow and storage mechanisms occur in a mathematical model of the organic-rich shale. Pressure reduction due to the production of free gas molecules causes desorption of molecules stuck on the surface of kerogen. The latter causes a disturbance in the system, leading to the creation of a concentration gradient between the pore walls and bodies of kerogens. This will be the main reason for the transmission of solute gas from the bulk of a kerogen to its surfaces. The arrangement is schematically presented in Fig. 3.

In particular, the block under study includes a non-organic part known as clay which has no effects on the main flow of gas molecules. The green sign indicates the direction of the main non-Darcy flow of free molecules (red) and those which have already been desorbed (blue)

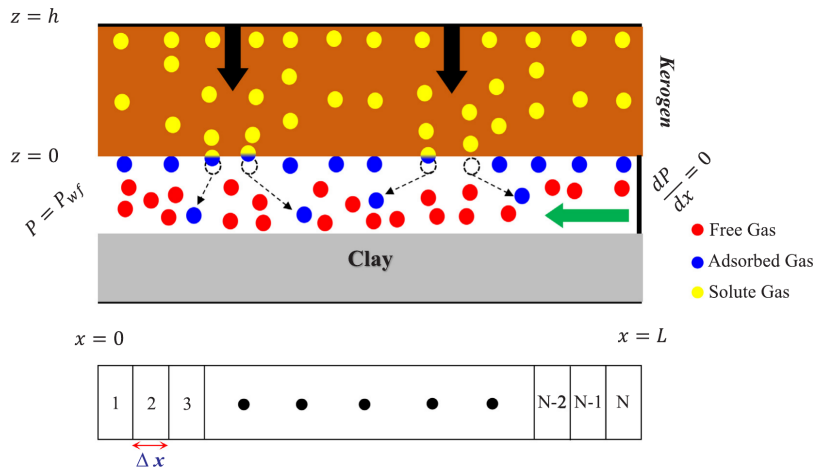


Fig. 3. Schematic of the supposed physical model.

Table 5
PSO parameters [68].

Parameter	Value
c_1	2
c_2	2
Number of particles	30
Number of parameters (pressures) in each particle	Number of grids

due to the pressure reduction. The gas molecules flow from a no-flow boundary towards a constant pressure mode. Of course, there is an organic part known as kerogen containing solute gas (yellow). Black signs show the diffusion of solute gas molecules towards the interface between kerogen and pore space. The procedure has been symbolized with bicoloured circles. The multi-mechanism process that is pictured was developed in gradual steps from a basic model towards an advanced one representing a shale gas system.

3.1. Model description

Through taking advantages of the conservation mass equation for a single grid, a one-dimensional (1D) model of a conventional porous media can be developed as [24]:

$$-(\rho_f v A)_{x+\Delta x} \Delta t - (\rho_f v A)_x \Delta t = V_b \phi ((\rho_f)_{t+\Delta t} - (\rho_f)_t) \tag{3}$$

It can be rearranged as:

$$-\frac{\partial(\rho_f v A)}{\partial x} \Delta x = V_b \frac{\partial}{\partial t} (\phi \rho_f) \tag{4}$$

where v is Darcy's velocity and defined as:

$$v = -(5.615)(0.001127) \frac{k \partial P}{\mu \partial x} \tag{5}$$

Combining Eqs. (5) and (4) yields [24,57]:

$$\frac{\partial}{\partial x} \left(0.00633 k A \frac{\rho_f \partial P}{\mu \partial x} \right) \Delta x = \frac{\partial}{\partial t} V_b (\rho_f \phi) \tag{6}$$

where k is absolute permeability, A is the cross-section area, ρ_f is free gas density, μ is gas viscosity, P is pressure, Δx is the length of each grid, t is time, V_b is the bulk volume and ϕ is the porosity. Specifying an initial and two boundary conditions is necessary to find a solution for

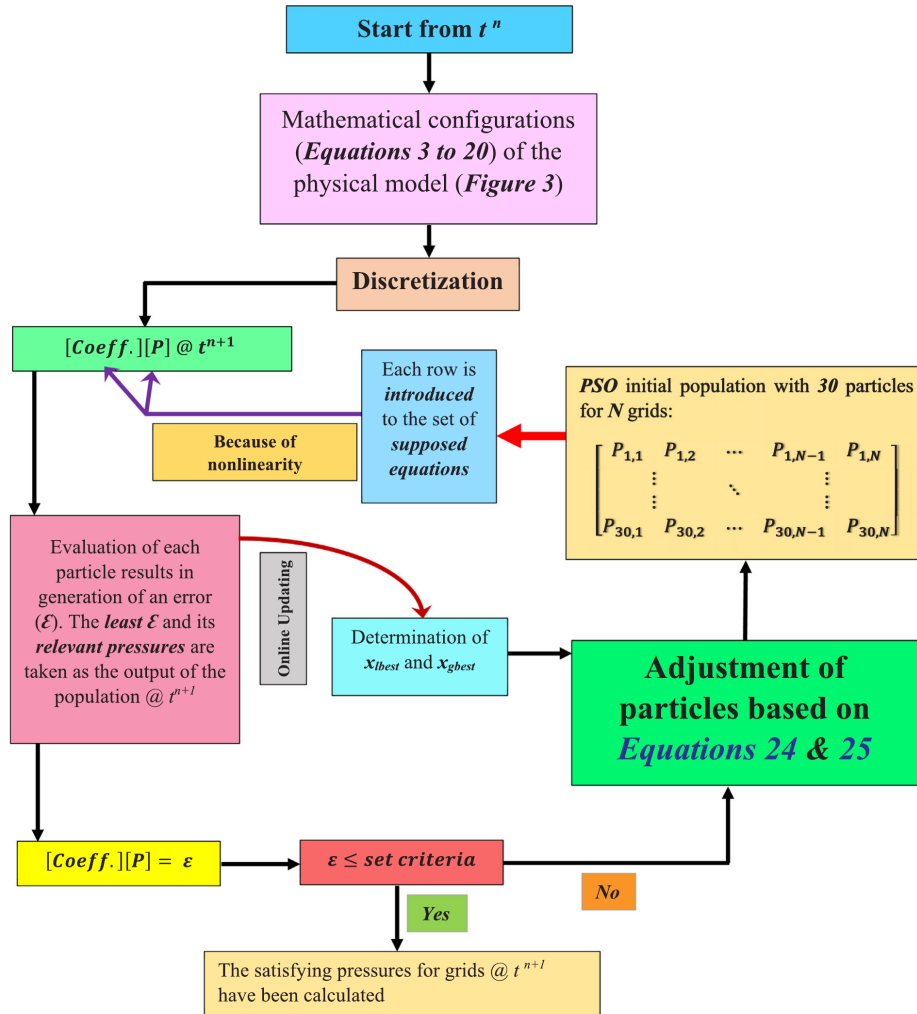


Fig. 4. The schematic of the proposed hybrid of PSO and conventional techniques.

Eq. (6). For the initial condition, it is assumed that the pressure is uniform and stable all over the model before production begins. One side of the 1D sample is faced with a constant pressure boundary, which is mathematically recalls the Dirichlet situation, in which the flow rate is dynamic and the constant pressure plays the role of a chock. On the other hand, the sample is controlled by a Neumann state with a no-flow boundary or isolation condition. These conditions can be mathematically translated as [22,50]:

$$\text{Initial Condition: } P = P_{in} \text{ @ } t = 0; \quad 0 < x < L$$

$$\text{Left Boundary Condition: } P = P_{le} \text{ @ } t > 0; \quad x = 0$$

$$\text{Right Boundary Condition: } \frac{\partial P}{\partial x} = 0 \text{ @ } t > 0; \quad x = L$$

3.2. Fluid flow equation

In order to obtain the proper model for unconventional shale gas reservoirs, the basic model has been combined with flow and storage characteristics of shale gas resources that have already been discussed. To simulate and consider the effect of slippage and diffusion in nano pores, the absolute permeability has been replaced with apparent permeability, Eq. (7) [4,8].

$$\frac{\partial}{\partial x} \left(0.00633 k_{app} A \frac{\rho_f \partial P}{\mu \partial x} \right) \Delta x = \frac{\partial}{\partial t} V_b (\rho_f \phi) \tag{7}$$

where k_{app} is the apparent permeability. It is calculated based on the model proposed by Darabi et al. [8]. Besides compressed gas in the pore voids, adsorbed gas on pore walls is considered to be another type of storage (accumulation). Therefore, Eq. (7) is turned into [8,48,58]:

Table 6
Initial values of parameters [8,22,48].

Parameter	Value
Temperature (°F)	200
Initial Pressure (psi)	5000
C1%	100
k (mD)	0.0008
ϕ	0.14
X (ft)	4
P_{wf} (psi)	400
α	0.8
τ	4
D_r	2.5
P_L (psi)	1240
V_L (ft ³ /lb)	0.08015
ρ_b (lb/ft ³)	164.185
ρ_g (lb/ft ³)	0.04236
D (ft ² /day)	2.15×10^{-10}
k_{H_2} (lb/psi-ft ³)	3.2×10^{-4}
Duration (day)	4

$$\frac{\partial}{\partial x} \left(0.00633 k_{app} A \frac{\rho_f \partial P}{\mu \partial x} \right) \Delta x = \frac{\partial}{\partial t} V_b (\rho_f \phi + (1-\phi)\rho_a) \tag{8}$$

where ρ_a is the density of the adsorbed gas (the mass of adsorbed gas per volume of solid). Chain rule and compressibility definition are employed to find a simple expression for the right side. Mathematically, it can be stated as [24,58]:

$$C_g = \frac{1}{\rho_f} \frac{\partial \rho_f}{\partial P} \tag{9}$$

$$\frac{\partial \rho_f}{\partial t} = \frac{\partial \rho_f}{\partial P} \frac{\partial P}{\partial t} = C_g \rho_f \frac{\partial P}{\partial t} \tag{10}$$

where C_g is the gas compressibility. For the second term, it can be presented mathematically as [48,58]:

$$\frac{\partial \rho_a}{\partial t} = \frac{\partial \rho_a}{\partial \rho_f} \frac{\partial \rho_f}{\partial P} \frac{\partial P}{\partial t} = \frac{\partial \rho_a}{\partial \rho_f} C_g \rho_f \frac{\partial P}{\partial t} \tag{11}$$

Based on Eqs. (10) and (11), Eq. (8) can be reformed as [8,41,60]:

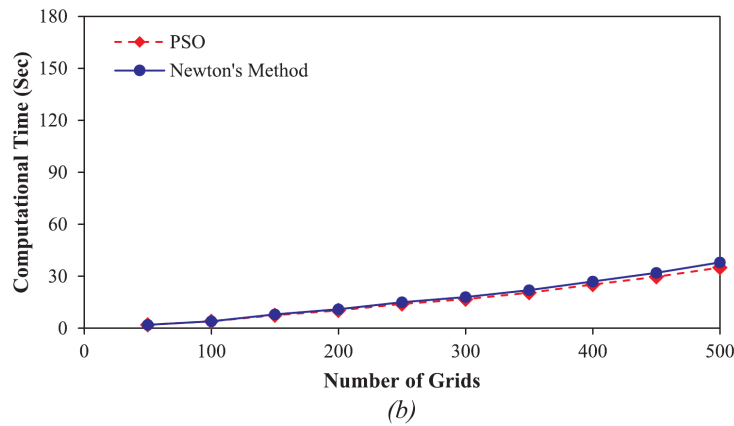
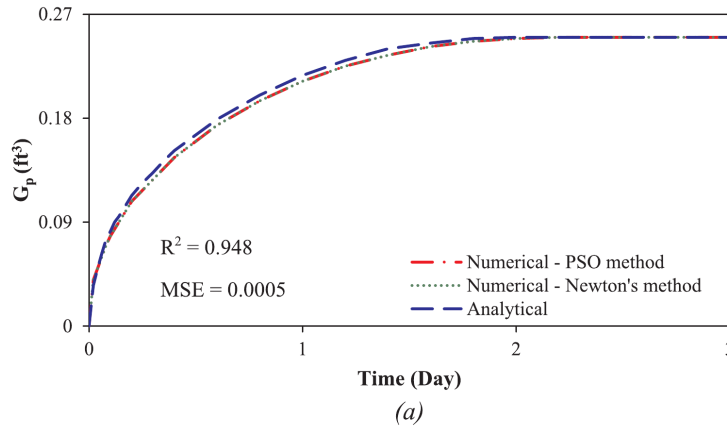


Fig. 5. (a) Validation of the applied numerical methods for 300 grids (b) Performance of the PSO versus Newton's method to solve corresponding simultaneous equations.

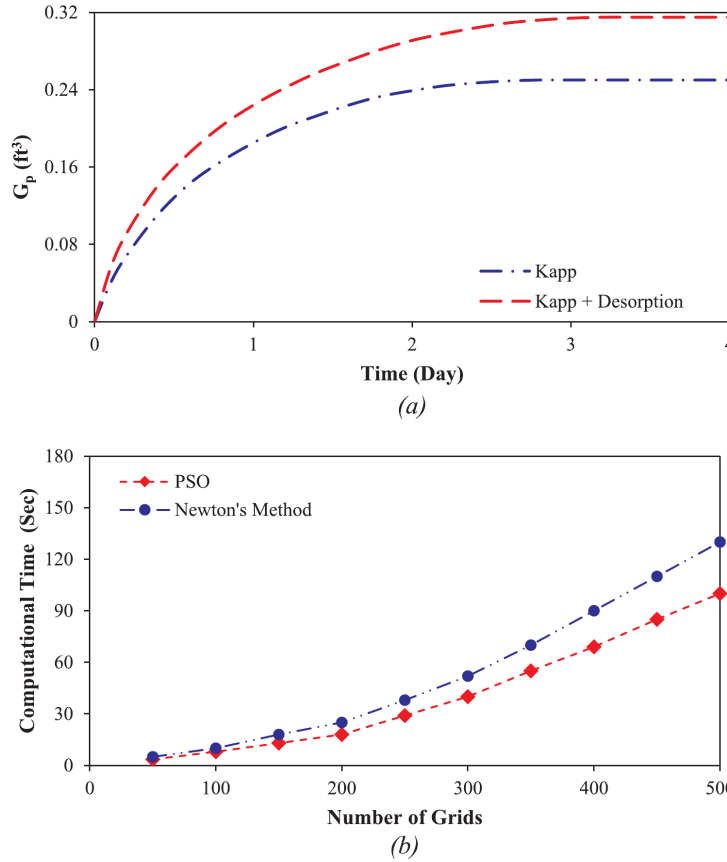


Fig. 6. (a) The production profile as a function of the apparent permeability and desorption phenomenon for 300 grids (b) Effectiveness of PSO technique to solve a large number of non-linear simultaneous equations with higher levels of complexities.

$$\frac{\partial}{\partial x} \left(0.00633k_{app}A \frac{\rho_f \partial P}{\mu \partial x} \right) \Delta x = \frac{\partial P}{\partial t} V_b C_g \rho_f \left(\phi + (1-\phi) \frac{\partial \rho_a}{\partial \rho_f} \right) \quad (12)$$

Moreover, Patzek et al. [59] defined the differential equilibrium partitioning coefficient of gas at a given temperature as:

$$K_a = \frac{\partial \rho_a}{\partial \rho_f} \quad (13)$$

Taking the advantages of Eq. (13) causes Eq. (12) to be formed as [48,58]:

$$\frac{\partial}{\partial x} \left(0.00633k_{app}A \frac{\rho_f \partial P}{\mu \partial x} \right) \Delta x = \frac{\partial P}{\partial t} C_g \rho_f V_b (\phi + (1-\phi)K_a) \quad (14)$$

In order to obtain a mathematical expression for \$\rho_a\$ and its derivative, the mass balance of adsorbed gas is formed as [48]:

$$\rho_a V_b (1-\phi) = \rho_f (P_{ST}, T_{ST}) \rho_b V_b V \quad (15)$$

where \$\rho_f (P_{ST}, T_{ST})\$ represents gas density in standard conditions, and \$V\$ is volume of adsorbed gas per bulk volume of the rock. Rearrangement of the latter equation results in:

$$\rho_a = \frac{\rho_f (P_{ST}, T_{ST}) \rho_b V}{(1-\phi)} \quad (16)$$

Since the adsorbed molecules occupy a portion of the flow path, it is necessary to modify the pore diameter during the procedure of desorption. The alteration within the thickness of the adsorbed layer, and the subsequent effects on the apparent permeability, has been modelled based on the following:

$$r_{eff} = r - t_{ads} \quad (17)$$

where \$r_{eff}\$ is the effective pore radius, \$r\$ is the pore radius, and \$t_{ads}\$ is the thickness of the adsorbed layer. The thickness of the adsorbed layer responds according to what has been represented by Sakhaeepour and Braynt [49] in Table 4.

Besides that, it is assumed that the solute gas obeys Eq. (2), and diffuses linearly in the \$z\$ direction within the kerogen body. The quantity of the gas that is solute in the kerogen can be calculated according to Henry's law, in which the solute gas is proportional to the pressure of the gas in the pore, which is represented as [22,54,60]:

$$c = k_{H} P \quad (18)$$

where \$k_{H}\$ is Henry's constant, and \$P\$ is pressure. To solve Eq. (2), the

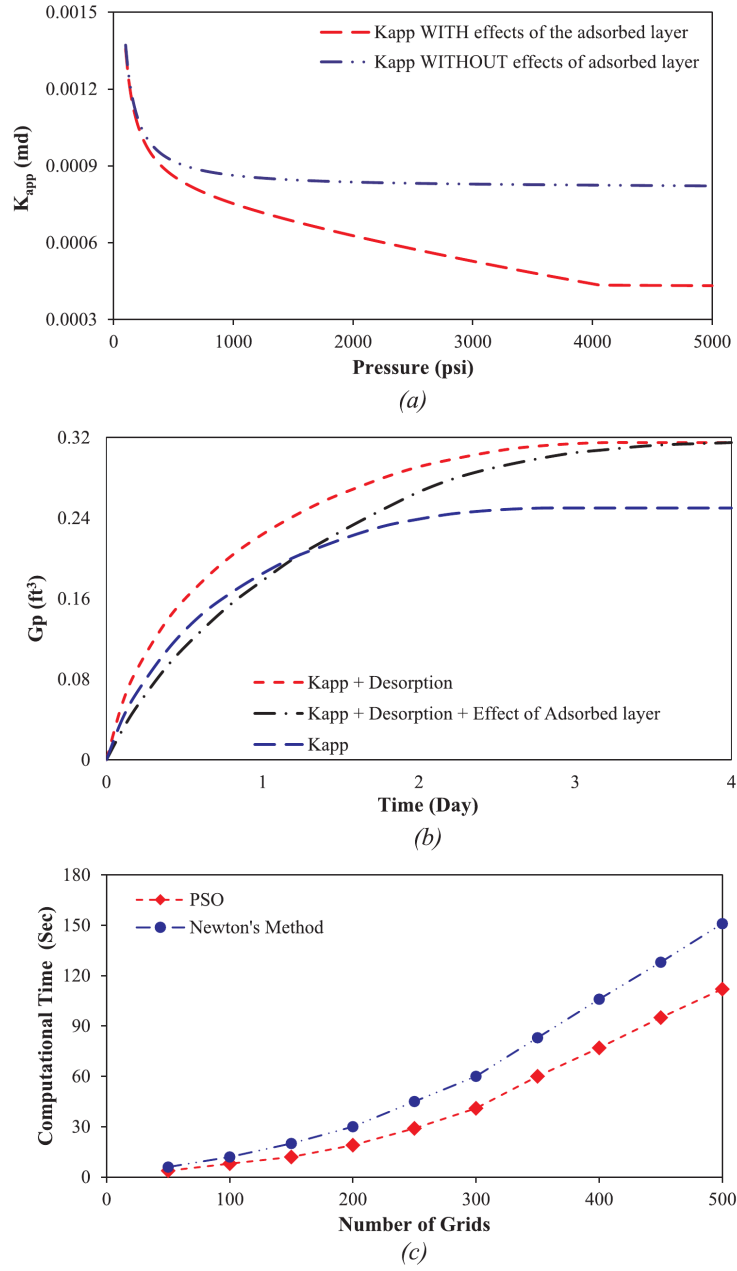


Fig. 7. (a) Effects of the adsorbed layer on the values of apparent permeability in different pressures (b) Profiles of cumulative production as a function of the adsorbed layer for 300 grids (c) PSO method vs. Newton's method in case of including the adsorbed layer effects.

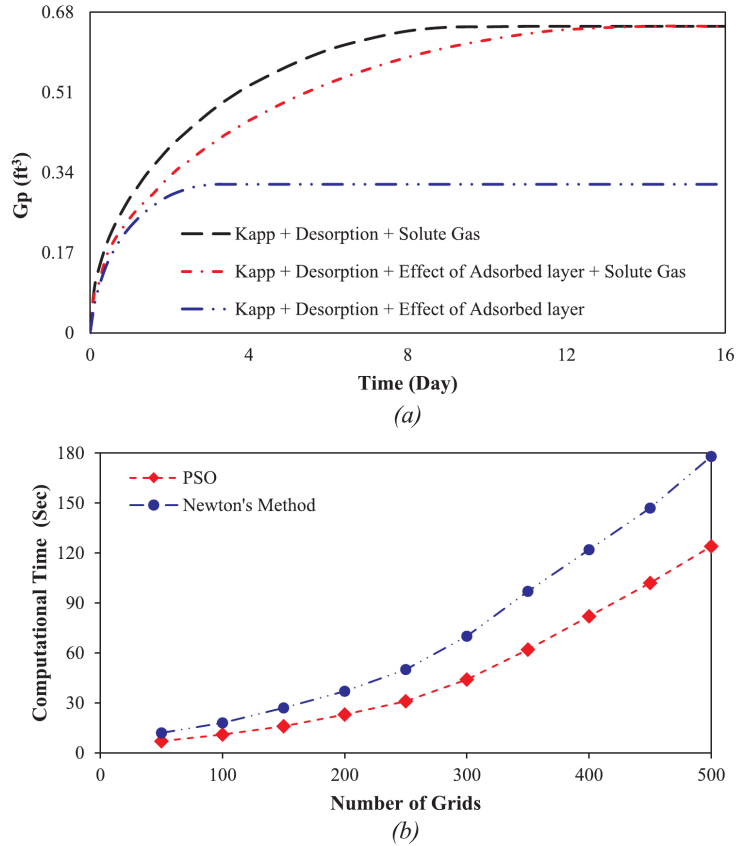


Fig. 8. (a) Effects of kerogen inclusion on the trend and value of the cumulative production for 300 grids (b) How the PSO can reduce the Computational Time in the most complicated case based on the number of grids.

initial and boundary conditions have been set. The supposed initial condition is given as below:

$$\text{Initial Condition: } c_{in} = k_H P_n \text{ @ } t = 0; 0 \leq z \leq h$$

The interface between the kerogen and pore wall is considered to be the inner boundary at $z = 0$ where the gas concentration in the element under study would be:

$$\text{Boundary Condition 1: } c = k_H P; z = 0; t > 0$$

The outer body of kerogen is surrounded by clay minerals which cannot feed gas molecules. Accordingly, the no-flow boundary is set for the outer boundary of the kerogen at $z = h$ which can mathematically be presented as [22,53,54,56]:

$$\text{Boundary Condition 2: } \frac{\partial c}{\partial z} = 0; z = h; t > 0$$

Eventually, the rate of mass transfer between kerogen and pore space can be calculated by [22,54]:

$$q_k^* = D_k \cdot A_k \cdot \frac{\partial c}{\partial z} \tag{19}$$

where q_k^* is kerogen mass flux, D_k is kerogen diffusion coefficient, and A_k is kerogen surface area. To consider the effect of kerogen q_k^* , it is

inserted as a source term to the left side of the equation. Furthermore, it has notably been discussed that the dimensions of kerogens are 10 times greater than pore sizes [22,54,55]. It must be remembered that the introduced term has originally been inspired from fractured reservoirs, technically known as double-porosity media. Accordingly, after the insertion of Eq. (19) into the main Eq. (14), the final form of the governing partial differential equation is [22,54,60]:

$$\frac{\partial}{\partial x} \left(0.00633 k_{app} A \frac{\rho}{\mu} \frac{\partial P}{\partial x} \right) \Delta x + q_k^* = \frac{\partial P}{\partial t} V_b C_g \rho_f (\phi + (1-\phi)K_a) \tag{20}$$

Eq. (20) is the mathematical expression of what is happening in Fig. 3.

3.3. Solver

To numerically solve the resulted governing equation, the application of discretization based on the finite difference method generates standard simultaneous equations. It can mathematically be stated as:

$$[Coeff.][P] = 0 \tag{21}$$

where $[Coeff.]$ represents the matrix of coefficients and $[P]$ is the matrix of unknown pressures. By regarding the thermodynamical nature of

Table 7
Effects of complexity versus volume of calculations for both applied solvers (■ is about the computational time of Newton's Method and ■ is about the PSO).

Characteristics	Number of Grids				
	100	200	300	400	500
Basic Model	4	11	18	27	38
	4	10	17	25	35
Basic Model + Kapp	8	20	32	50	88
	6	14	24	38	65
Basic Model + Kapp + Desorption	10	25	52	90	130
	8	18	40	69	100
Basic Model + Kapp + Desorption + Effects of the Adsorbed Layer	12	30	60	106	151
	8	19	41	77	112
Basic Model + Kapp + Desorption + Effects of the Adsorbed Layer + Kerogen	18	37	70	122	178
	11	23	44	82	124

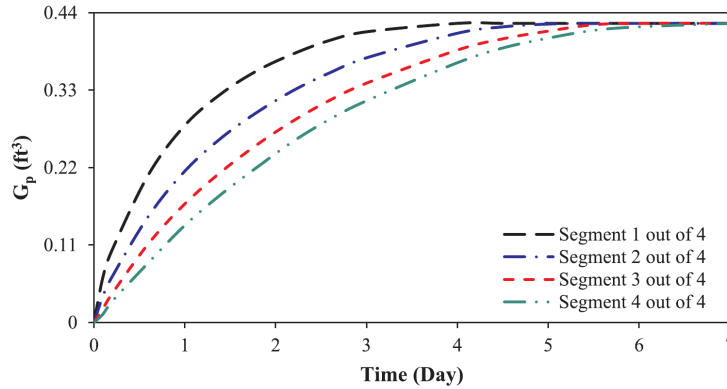


Fig. 9. Cumulative production as a function of kerogen distributions for 300 grids.

gases, the produced simultaneous equations that are produced are nonlinear. Usually, Newton's method which takes advantages of the Jacobian matrix is employed to solve simultaneous nonlinear equations [24]. It is technically performed as [25]:

$$[P_{new}] = [P_{old}] - J^{-1}[f(P_{old})] \tag{22}$$

in which J^{-1} is the inversion of the Jacobian matrix, $f(P_{old})$ represents the responses of nonlinear simultaneous algebraic equations, P_{old} is the pressure within the last iteration and the P_{new} symbolizes adjusted pressures. In the Jacobian matrix, each row represents one block and the columns stand for corresponding derivations based on existing variables. Technically, the Jacobian matrix is the matrix of all first-order partial derivatives of a vector-valued function. It is mathematically defined as [25]:

$$J = \frac{df}{dx} = \begin{bmatrix} \frac{\partial f}{\partial x_1} & \dots & \frac{\partial f}{\partial x_n} \\ \vdots & \ddots & \vdots \\ \frac{\partial f_m}{\partial x_1} & \dots & \frac{\partial f_m}{\partial x_n} \end{bmatrix} \tag{23}$$

It must be considered that the quality of the initial guess has a significant impact on the convergence of Newton's method. However, there are some situations in which that arrangement of the Jacobian matrix is somehow unmanageable [25]. For instance, it is understood that forming the Jacobian matrix needs to have the derivations for pressure-dependent parameters. Some of parameters like apparent permeability can be subjected into both classical and numerical derivations. Choosing between one of these two is challenging because developing these classical methods are time-consuming, and the numerical ones have inherent errors. On the other hand, for parameters like the Z-factor, which is supposed to undergo numerical derivation while choosing one of the methods of backward, central, or forward causes that generate of different results again [24,25]. Moreover, the

computational cost of Newton’s method is also considerable because the inversion of the Jacobian matrix must be calculated for a certain number of iterations in each time step.

To overcome the addressed challenges of the initial guess and the relevant difficulties with the Jacobian Matrix, the PSO as a free derivation technique which does not need to have an initial guess can conclude the group of pressures, which their product with the matrix of coefficients in each time step generates a relative zeros matrix [30,31,61].

In short, PSO is a stochastic optimization technique inspired by social systems among organisms such as birds flocking and fish schooling. This robust technique which has recently drawn many petroleum researchers’ attentions, can effectively be employed to solve multidimensional optimization problems [62–67]. Starting with a set of random particles or potential solutions including the numbers of pressures, the algorithm makes attempts to improve solutions based on their corresponding qualities, which ideally generates a certain number of zeros. To iteratively reach the supposed goal, each particle changes its values by using velocity vectors that are altered with the effects of random factors. The procedure can mathematically be stated as [68]:

$$x_{ij}^{k+1} = x_{ij}^k + v_{ij}^{k+1} \tag{24}$$

where

$$v_{ij}^{k+1} = v_{ij}^k + c_1 r_1 (x_{lbest,ij}^k - x_{ij}^k) + c_2 r_2 (x_{gbest,ij}^k - x_{ij}^k) \tag{25}$$

r_1 and r_2 are uniformly distributed random numbers within the range of 0 to 1. In the k th iteration, v_{ij}^k and x_{ij}^k are the j th component of the i th particle’s velocity and position vector, respectively. Also, x_{lbest} and x_{gbest} reflect the best positions experienced so far by the i th particle and the whole population as well. Moreover, c_1 and c_2 , show each particle’s confidence in itself and in the population, correspondingly [68]. The applied values for the relevant parameters of PSO have been laid out in Table 5.

Graphically, the proposed procedure has been indicated in Fig. 4, where the functionality of the PSO has been performed step by step.

4. Results and discussions

Based on the initial values of the parameters stated in Table 6, the basic homogenous model which has mathematically been introduced with Eq. (6) was solved by applying Newton’s and PSO methods.

The generated production results have been presented in Fig. 5, where they have been compared against outputs from the analytical solution of the pictured model addressed in well-known references [69]. According to the statistical parameters of R-square (R2) and Minimum Square Error (MSE), the developed model applied with the both numerical methods satisfyingly performed in keeping with the analytical outputs. In terms of computational time, it can also be inferred that there is not a very broad difference between both applied solvers, and they perform nearly the same.

By regarding the model for apparent permeability proposed by Darabi et al. [8], and what has been described about the phenomena of adsorption under the title of the Langmuir isotherm, it is possible to analyse Eq. (14) based on applying the solvers being referred to. The effects of inserting the apparent permeability, which symbolizes the slippage and Knudsen diffusion, and the desorption process on the production profile, are shown in Fig. 6.

To examine the effects of the adsorbed layer on the trend of apparent permeability, the model proposed by Darabi et al. [8] has been coupled with what was suggested by Sakhaee-pour and Bryant [49]. Specifically, the radius referred to in the presumed apparent permeability model turns into a function of pressure based on a linear relationship. The results are vividly apparent in the first part of Fig. 7. The thickness of the adsorbed layer has been assumed as what was mentioned in Table 4. Below the 4061 psi, the effective flow path gradually

becomes enhanced until the gas molecules on the pore walls are entirely desorbed. Ultimately, if lower than the 500 psi pressure, the adsorbed layer has a negligible effect, and causes the effective flow path and intrinsic pore diameter to become identical.

The second part represents the importance of adsorbed layer effects on the production profile in comparison with the exclusion of the considering effect and apparent permeability model solely without any second storage mechanism. At the early time of production, the trend of inclusion has lower production rather than both cases. It can be labelled so that the lower amounts of desorption process at the beginning of the production leads to a thicker adsorbed layer. It means that the flow path at the beginning has a smaller size than what it really is. As production continues, the desorption process accelerates, and the adsorbed layer starts to diminish. Eventually, at a later time, since the total gas in place is identical, both trends are going to meet each other and reach a peak of cumulative production, although they followed different paths.

Adding the adsorbed layer to the previously discussed phenomena, apparent permeability and desorption, amplifies the level of complexities which can noticeably, effectively, and robustly be overcome by applying the PSO method shown in the third part. While implementing Newton’s method as a conventional technique takes as long as 151 s in the highest number of grids, this proposed solver only needs 112 s.

The process of evolution for the basic model approaches towards the final step by including the effects of solute gas stored in kerogens. Impacts of the solute gas stored in organic contents on production profiles are illustrated in Fig. 8(a). It can clearly be observed that inserting solute gas effects causes a significant jump in the level of stabilization, or the amount of gas produced, which follows previous expectations about gas-in-place assumptions. With this in mind, it can be concluded that solute gas effects play a leading role in the reserve estimations, and discounting it leads to be faced up with significant errors. Moreover, including the effects of solute gas results in a dramatic shift in stabilization. While the developed model without solute gas effects stabilizes after 4 days, the fully developed model levels off after 14 days which shows the slow process of diffusion within kerogen bodies. There is also another trend that includes the solute gas effects but disregards the importance of the adsorbed layer. Without the adsorbed layer, the surface of kerogen is affected more readily due to the higher permeability that has already been shown in Fig. 7. The faster process for depletion within the kerogen starts and less time is required to reach the peak of the cumulative production. In the second part of Fig. 8, the fully developed model has been subjected to two different solvers. As can be understood, less time is required to solve the presumed nonlinear equations, even in a small number of grids, when the PSO technique is applied.

The overall results of applying the PSO algorithm as a solver in comparison with the conventional method, in terms of computational time, are illustrated in Table 7. The time spent with the PSO and Newton’s to solve the required simultaneous equations are represented in red and blue, respectively. Based on the fact that both techniques nearly require equal time for a basic model including different numbers of grids, it can be inferred that applying the PSO for normal cases can be a noticeable plus. It is clear that adding different items into the basic model for the lowest number of grids causes the recording of various computational time with the difference of 60%. However, the robustness of PSO can be vividly highlighted when a complex model includes grids as large as 500, in which the PSO has recorded 124 s, which is 31% less than what has already been spent by implementing Newton’s method. Interestingly, it is also possible to conclude that the complexity and heterogeneity of the model under study do not have the highest level of impact on the amount of computational time. In fact, the tabulated performances of both implemented solvers show that having 400 grids in the most complex case, last row requires shorter time than having 500 grids, excluding solute gas effects. In other words, increasing in the number of nonlinear simultaneous algebraic equations takes shorter computational time than making the supposed system

more complex by the inclusion of more phenomena.

Furthermore, it was decided to investigate whether the trend showing cumulative production is a function of kerogen distribution. During four different scenarios, with an equal amount of total gas in place, one segment included the kerogen with the relevant phenomena of desorption, gas diffusion, and effects of an adsorbed layer, while the other three segments are only an ultra-tight porous media with the related special effects of apparent permeability. In other words, the length of the physical model (Fig. 3) was divided equally into 4 main segments, and under each scenario only one segment contains kerogen. The results are illustrated in Fig. 9.

Within each pattern, the considered segment is assigned with the kerogen, and the remaining ones have a clay matrix. Technically, the higher production in the first segment during the earlier time period can be excused due to the fact that the first segment has the kerogen source. It means that the signal of pressure reduction reaches the adsorbed layer more quickly, which causes the beginning of desorption and an improvement in apparent permeability. This is due to the reason that the desorption process causes the adsorbed layer to become thinner, which directly causes the effective pore radius to become larger in size and has a positive influence in terms of approaching towards a larger value for apparent permeability. After that, the signal is referred to starts triggering the kerogen body to initiate the depletion process. After a certain amount of time passes so that the pressure of the last grid in the physical model has become equal to the presumed Dirichlet boundary condition, and there is no more solute gas in the kerogen body, the corresponding production profile starts to stabilize. The position of kerogen with more distance from the outlet causes receiving the signal to be received at a later time, even though the same described chain reactions are going to happen. Although the final value of cumulative production is the same for all scenarios, it can be concluded that kerogen distribution has an important effect on the production profile, and it could generally be determined as an effective parameter in a history matching procedure.

5. Conclusion

In this study, a multi-mechanism conceptual model was developed to investigate the effects of non-Darcy's flow, desorption, adsorbed layer impact, gas diffusion from kerogen bodies and kerogen distribution on the production of shale gas reservoirs. A smart optimization approach has also been introduced to solve the supposed nonlinear simultaneous algebraic equations.

The adsorption phenomena, which mainly occur on the pore walls of organic media, increases the cumulative gas production, although it has also a negative side effect on permeability for the ultra-tight porous media. In other words, the reduction in permeability, due to the existence of the adsorbed layer, hinders bringing up total production to the maximum value. Furthermore, it is assumed that the monolayer of adsorbed gas covers the pore surfaces.

Solute gas in kerogen bodies contributes to the total gas production. Kerogen has substantial effects on transportation and storage phenomena of shale gas reservoirs. Desorption and gas diffusion from a kerogen body to its surfaces are the mainly relevant phenomena with organic materials. Various distribution of kerogen creates different production profiles, which makes it an important parameter in history matching for shale gas reservoirs.

PSO as a modern optimizer is a smart and robust technique to solve nonlinear simultaneous algebraic equations. In comparison to Newton's method, PSO is a free derivation solver with a lower computational cost which is also independent to initial guess. Furthermore, it converges faster to the solution, and it is more striking when smaller steps of discretization are chosen and complex phenomena are inserted into the governing equation that increases the nonlinearity of the system.

The developed model can be taken to study multi-dimensional systems with effects of multi-phase flow. Also, its advantages can be

taken to do detailed and deep research about the behaviour of compositional systems in ultra-tight porous media. The effect of gravity is another aspect that can easily be introduced into the extended model. Several of the addressed issues that have been addressed can be considered for future studies.

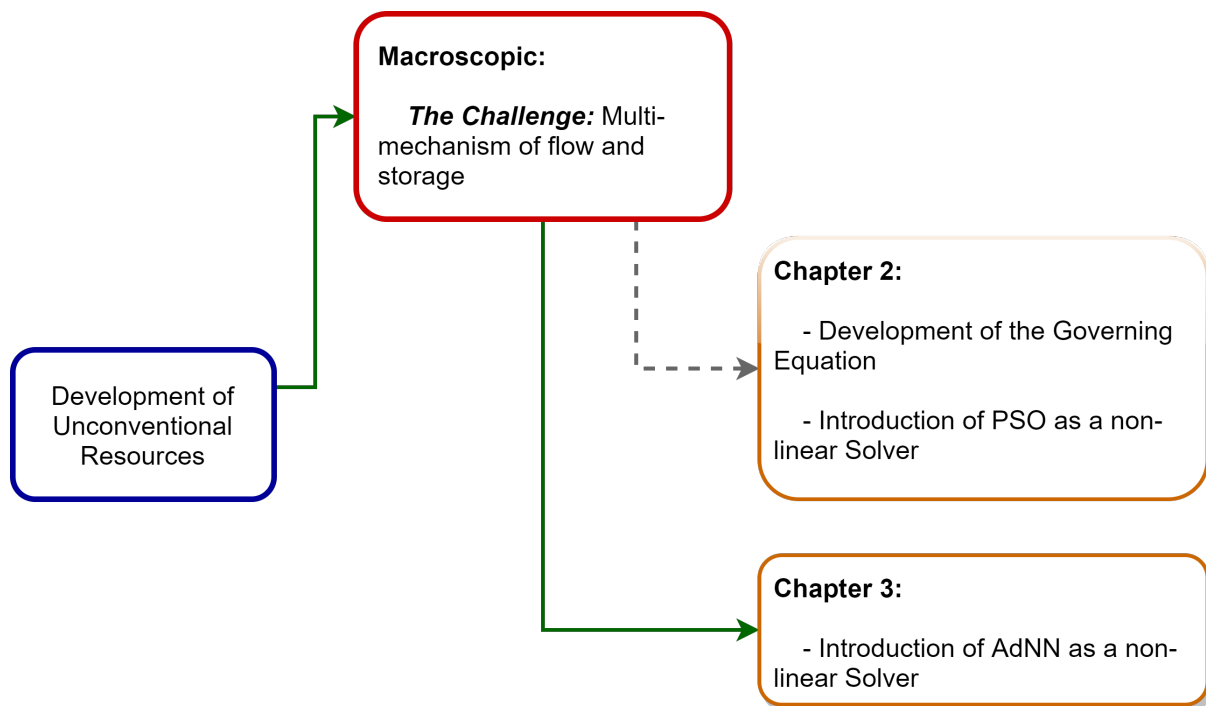
References

- [1] Holditch SA. Unconventional oil and gas resources development- Let's do it right. *J Unconventional Oil Gas Resour* 2013;1–2:2–8.
- [2] Speight JG. *Shale Gas Production Processes*. first ed. Gulf Professional Publishing. Elsevier; 2013.
- [3] Javadpour F, Fisher D, Unsworth M. Nanoscale gas flow in shale gas sediments. *J Can Pet Technol* 2007;46(10):55–61.
- [4] Javadpour F. Nanopores and apparent permeability of gas flow in mudrocks (shales and siltstone). *J Can Pet Technol* 2009;48(8):16–21.
- [5] Ambrose RJ, Hartman RC, Diaz-Campos M, Akkutu IY, Sondergeld CH. Shale gas-in-place calculations part i: new pore-scale considerations. *SPE J* 2012;17(1):219–29.
- [6] Fathi E, Akkutu IY. Matrix heterogeneity effects on gas transport and adsorption in coalbed and shale gas reservoirs. *Transp Porous Media* 2009;80(2):281–304.
- [7] Cui X, Bustin AM, Bustin RM. Measurements of gas permeability and diffusivity of tight reservoir rocks: Different approaches and their applications. *Geofluids* 2009;9(3):208–23.
- [8] Darabi H, Ettehad A, Javadpour F, Sepehrnoori K. Gas flow in ultra-tight shale strata. *J Fluid Mech* 2012;710:641–58.
- [9] Singh H, Javadpour F, Ettehadavakol A, Darabi H. Nonempirical apparent permeability of shale. *SPE Reserv Eval Eng* 2013;17(3):414–24.
- [10] Kang SM, Fathi E, Ambrose RJ, Akkutu IY, Sigal RF. Carbon dioxide storage capacity of organic-rich shales. *SPE J* 2011;16(04):842–55.
- [11] Hashmy KH, Abueita S, Barnett C, Jonkers JH. Log-based identification of sweet spots for effective fracs in shale reservoirs. In: *SPE Canadian Unconventional Resources Conference*, Calgary, Canada; 2011.
- [12] Yan B, Wang Y, Killough JE. Beyond dual-porosity modeling for the simulation of complex flow mechanisms in shale reservoirs. *Comput Geosci* 2016;20(1):69–91.
- [13] Akkutu IY, Fathi E. Multiscale gas transport in shales with local kerogen heterogeneities. *SPE J* 2012;17(4):1002–11.
- [14] Wasaki A, Akkutu IY. Permeability of organic-rich shale. *SPE J* 2015;20(6):1384–96.
- [15] Silin D, Kneafsey T, Berkeley L. Shale gas: nanometer-scale observations and well modelling. *J Can Pet Technol* 2012;51(6):464–75.
- [16] Haghshenas B, Clarkson CR, Chen S. New Models for Reserve Estimation and Non-Darcy Gas Flow in Shale Gas Reservoirs. In: *SPE/EAGE European Unconventional Resources Conference and Exhibition*, Vienna, Austria; 2014.
- [17] Swami V, Settari A, Javadpour F. A Numerical Model for Multi-Mechanism Flow in Shale Gas Reservoirs with Application to Laboratory Scale Testing. In: *SPE Annual Conference & Exhibition incorporating SPE Europe*, London, UK; 2013.
- [18] Ross DK, Bustin RM. The importance of shale composition and pore structure upon gas storage potential of shale gas reservoirs. *Mar Pet Geol* 2009;26(6):916–27.
- [19] Passey QR, Bohacs KM, Esch WL, Klimentidis, Sinha S. From Oil-Prone Source Rock to Gas-Producing Shale Reservoir - Geologic and Petrophysical Characterization of Unconventional Shale Gas Reservoirs. In: *SPE International Oil and Gas Conference and Exhibition*, Beijing, China; 2010.
- [20] Jin Z, Firoozabadi A. Thermodynamic modeling of phase behavior in shale media. *SPE J* 2016;21(1):190–207.
- [21] Jin Z, Firoozabadi A. Phase behavior and flow in shale nanopores from molecular simulations. *Fluid Phase Equilib* 2016;430:156–68.
- [22] Swami V, Settari A. A Pore Scale Gas Flow Model for Shale Gas Reservoir. In: *SPE Unconventional Resources Conference*, Pittsburgh, USA; 2012.
- [23] Guo C, Wu K, Wei M. Study on gas flow through nano pores of shale gas reservoirs. *Fuel* 2015;143:107–17.
- [24] Ertekin T, Abou-Kassem JH, King GR. *Basic Applied Reservoir Simulation*. Texas: Society of Petroleum Engineers; 2001.
- [25] Faires JD, Burden RL. *Numerical Methods*. Cengage Learning; 2003.
- [26] Deb KP, Akter F, Imtiaz SY, Hossain ME. Nonlinearity and solution techniques in reservoir simulation: a review. *J Nat Gas Sci Eng* 2017;46:845–64.
- [27] Noor MA, Waseem M. Some iterative methods for solving a system of nonlinear equations 2009; 11: 369–75.
- [28] Karr CL, Weck B, Freeman LM. Solutions to systems of nonlinear equations via Genetic Algorithm. *Eng Appl Artif Intell* 1998;11:369–75.
- [29] Luo YZ, Tang GJ, Zhou LN. Hybrid approach for solving systems of nonlinear equations using luo chaos optimization and quasi-Newton method. *Appl Soft Comput* 2008;8:1068–73.
- [30] Mo Y, Liu H, Wang Q. Conjugate direction particle swarm optimization solving systems of nonlinear equations. *Comput Math Appl* 2009;57:1877–82.
- [31] Jaberipour M, Khorram E, Karimi B. Particle swarm algorithm for solving systems of nonlinear equations. *Comput Math Appl* 2011;62:566–76.
- [32] Wu Y, Pruess K, Persoff P. Gas flow in porous media with klinkenberg effects. *Transp Porous Media* 1998;32(1):117–37.
- [33] Firouzi M, Alnoaimi K, Kovscek A, Wilcox J. Klinkenberg effect on predicting and measuring helium permeability in gas shales. *Int J Coal Geol* 2014;123:62–8.
- [34] Wang H, Marongiu-Porcu M. Impact of shale-gas apparent permeability on production: combined effects of non-darcy flow/gas-slippage, desorption, and

- geomechanics. *SPE Reserv Eval Eng* 2015;18(4):495–507.
- [35] Javadpour F, McClure F, Naraghi ME. Slip-corrected liquid permeability and its effect on hydraulic fracturing and fluid loss in shale. *Fuel* 2015;160:549–59.
- [36] Fathi E, Tinni A, Akkuthu IV. Correction to Klinkenberg slip theory for gas flow in nano-capillaries. *Int J Coal Geol* 2012;103:51–9.
- [37] Beskok A, Karniadakis GE. Report: A model for flows in channels, pipes, and ducts at micro and nano scales. *Microscale Thermophys Eng* 1999;3(1):43–77.
- [38] Roy S, Raju R, Chuang HF, Cruden BA, Meyyappan M. Modeling gas flow through microchannels and nanopores. *J Appl Phys* 2003;93(8):4870–9.
- [39] Ziarani AS, Aguilera R. Knudsen's permeability correction for tight porous media. *Transp Porous Media* 2012;91(1):239–60.
- [40] Nazari Moghaddam R, Jamiolahmady M. Slip flow in porous media. *Fuel* 2016;173:298–310.
- [41] Song W, Yao J, Li Y, Sun H, Zhang L, Yang Y, et al. Apparent gas permeability in an organic-rich shale reservoir. *Fuel* 2016;181:973–84.
- [42] Geng L, Li G, Zitha P, Tian S, Sheng M, Fan, X. A diffusion-viscous flow model for simulating shale gas transport. *Fuel* 2016;181:887–94.
- [43] Freeman CM, Moridis GJ, Blasingame TA. A numerical study of microscale flow behavior in tight gas and shale gas reservoir systems. *Transp Porous Media* 2011;90(1):253–68.
- [44] Wu K, Li X, Wang C, Yu W, Chen Z. Model for surface diffusion of adsorbed gas in nanopores of shale gas reservoirs. *Ind Eng Chem Res* 2015;54(12):3225–36.
- [45] Heller R, Zoback M. Adsorption of methane and carbon dioxide on gas shale and pure mineral samples. *J Unconventional Oil Gas Resour* 2014;8:14–24.
- [46] Yu W, Sepehrmoori K. Simulation of gas desorption and geomechanics effects for unconventional gas reservoirs. *Fuel* 2014;116:455–64.
- [47] Yuan W, Pan Z, Li X, Yang Y, Zhao C, Connell LD, et al. Experimental study and modelling of methane adsorption and diffusion in shale. *Fuel* 2014;117:509–19.
- [48] Yu W, Sepehrmoori K, Patzek TW. Modeling gas adsorption in marcellus shale with langmuir and BET isotherms. *SPE J* 2016;21(2):589–600.
- [49] Sakhaee-pour A, Bryant SL. Gas permeability of shale. *SPE Reserv Eval Eng* 2012;15(04):401–9.
- [50] Singh H, Javadpour F. Langmuir slip-Langmuir sorption permeability model of shale. *Fuel* 2016;164:28–37.
- [51] Kazemi M, Takbiri-Borujeni A. An analytical model for shale gas permeability. *Int J Coal Geol* 2015;146:188–97.
- [52] Svrček WY, Mehrotra AK. Gas solubility, viscosity and density measurements for athabasca bitumen. *J Can Pet Technol* 1982;21(4):31–8.
- [53] Etminan SR, Javadpour F, Maini BB, Chen Z. Measurement of gas storage processes in shale and of the molecular diffusion coefficient in kerogen. *Int J Coal Geol* 2014;123:10–9.
- [54] Huang T, Guo X, Chen F. Modeling transient pressure behavior of a fractured well for shale gas reservoirs based on the properties of nanopores. *J Nat Gas Sci Eng* 2015;23:387–98.
- [55] Mi L, Jiang H, Li J. The impact of diffusion type on multiscale discrete fracture model numerical simulation for shale gas. *J Nat Gas Sci Eng* 2014;20:74–81.
- [56] Chen F, Duan Y, Wang K, Li X, Liao Y. A novel pressure transient response model considering multiple migration mechanisms in shale gas reservoir. *J Nat Gas Sci Eng* 2015;22:321–34.
- [57] Lee J, Wattenbarger RA. *Gas Reservoir Engineering*. first ed. Texas: Society of Petroleum Engineers; 1996.
- [58] Yu W, Huang S, Sepehrmoori K. Development of a Semi-Analytical Model for Simulation of Gas Production in Shale Gas Reservoirs. In: *Unconventional Resources Technology Conference, Denver, USA; 2014*.
- [59] Patzek TW, Male F, Marder M. Gas production in the barnett shale obeys a simple scaling theory. *PNAS* 2013;110(49):19731–6.
- [60] Cui G, Liu J, Wei M, Shi R, Elsworth D. Why shale permeability changes under variable effective stresses: new insights. *Fuel* 2018;213:55–71.
- [61] Cherry J. *Optimization strategies for shale gas asset development 2016*.
- [62] Eberhart R, Kennedy J. A new optimizer using particle swarm optimization. In: *Proceeding of the sixth International Symposium on Micro Machine and Human Science 1995*; 1: 39–43.
- [63] Ahmadi MA. Neural network based unified particle swarm optimization for prediction of asphaltene precipitation. *Fluid Phase Equilib* 2012;314:46–51.
- [64] Ahmadi MA, Ebadi M, Yazdanpanah A. Robust intelligent tool for estimating dew point pressure in retrograded condensate gas reservoirs: application of particle swarm optimization. *J Petrol Sci Eng* 2014;123:7–19.
- [65] Ahmadi MA, Zendehtboudi S, Dusseault MB, Chatzis I. Evolving simple-to-use method to determine water–oil relative permeability in petroleum reservoirs. *Petroleum* 2016;2(1):67–78.
- [66] Al-Mudhafar WJ, Dalton CA, Al musabeh MI. Metamodeling via Hybridized Particle Swarm with Polynomial and Splines Regression for Optimization of CO₂-EOR in Unconventional Oil Reservoirs. In: *SPE Reservoir Characterisation and Simulation Conference and Exhibition, Abu Dhabi, UAE; 2017*.
- [67] Ahmadi MA, Ebadi M, Shokrollahi A, Majidi SJ. Evolving artificial neural network and imperialist competitive algorithm for prediction oil flow rate of the reservoir. *Appl Soft Comput* 2013;13(2):1085–98.
- [68] Gazi V, Passino KM. *Particle Swarm Optimization*. Springer, Berlin: *Swarm Stability and Optimization*; 2011.
- [69] Hagoort J. *Fundamentals of Gas Reservoir Engineering*. first ed. New York: Elsevier; 1988.

864 **3. A nonlinear solver based on an adaptive neural network,**
865 **introduction and application to porous media flow**

866 Regarding the universal approximation theory that states a Single Hidden Layer (SHL)
867 neural network has the capability of estimating any nonlinear, continuous, and unknown
868 functions, the capability of using neural networks to solve the partial differential equations has
869 always taken many the researchers' attention. Despite the previous attempts in which multi-
870 layer perceptron networks were tried to fit the gathered data, the presented paper has
871 investigated the possibility of using Adaptive neural networks as the nonlinear solver. In
872 comparison with the previous research, the most important advantage of the proposed
873 workflow is that it does not need to be trained based on the gathered data. The training
874 procedure goes based on generated errors by the output of the simultaneous nonlinear algebraic
875 equations and adaptive laws. Moreover, the proposed solver has the independence to the
876 physics of the problem. In other words, although it is an artificial intelligence-based solver, it
877 works like classic mathematical methods. However, the required runtime for the convergence
878 is longer than generally recorded for Newton's method. Also, the impact of the prepared paper
879 to the roadmap of the research has been shown in **Figure 18**.



880

881

Figure 18: Chapter 3 in a glance

882

CRedit author statement:

883

1. **Mohammad Ebadi:** Conceptualization, Methodology, Software, Formal

884

Analysis, Investigation, Writing – Original Draft, Visualization

885

2. **Seyed Hassan Zabihifar:** Conceptualization, Methodology

886

3. **Yashar Bezyan:** Conceptualization, Methodology, Software, Writing –

887

Original Draft

888

4. **Dmitry Koroteev:** Writing – Review & Editing, Supervision, Project

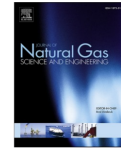
889

administration



Contents lists available at ScienceDirect

Journal of Natural Gas Science and Engineering

journal homepage: <http://www.elsevier.com/locate/jngse>

A nonlinear solver based on an adaptive neural network, introduction and application to porous media flow

Mohammad Ebadi^a, Seyed Hassan Zabihifar^b, Yashar Bezyan^{c,*}, Dmitry Koroteev^a

^a Skolkovo Institute of Science and Technology, Moscow, Russia

^b Bauman Moscow State Technical University, Moscow, Russia

^c Department of Mechanical, Industrial, and Aerospace Engineering, Concordia University, Montreal, Quebec, Canada

ARTICLE INFO

Keywords:

Adaptive neural network
Fluid flow in porous media
Newton's method
Nonlinear solvers
Hydrocarbon reservoir simulation

ABSTRACT

Sensitivity to derivatives and a need for proper initial guesses are the main disadvantages of classic nonlinear solvers like Newton's method. To overcome the obstacles, a numerical solver for second-order nonlinear Partial Differential Equations (PDEs) based on an Adaptive Neural Network (AdNN) is introduced. While using Newton's method needs to form the Jacobian matrix and its inversion, which both of them are time-consuming and dependent on the nature of the problem, the proposed solver tries to find the roots of the algebraic equations by changing the weights of AdNN by the help adaptive laws. The proposed approach has been applied to solve the governing PDEs of the gas flow in shale resources and the immiscible two-phase flow of water and oil in hydrocarbon reservoirs as two highly nonlinear phenomena. The generated profiles of pressures and saturations show a satisfying match with the outputs of Newton's method. However, using the presented algorithm not only removes the former necessities but also helps the community to solve the relevant PDEs governing the critical elements of the energy market in the future with a higher level of confidence.

1. Introduction

The proper and accurate simulation of fluid flow in the porous media of hydrocarbon reservoirs can have a significant impact on the sustainable supply of energy for the coming years (Bilgen and Sarikaya, 2016). Reservoir simulation is a robust numerical tool to describe the chemical and physical transport phenomena and dominating forces (i.e. capillary, gravity and viscous) in oil and gas resources to forecast the behavior of the system under various development scenarios for maximizing the ultimate recovery (Fernandes et al., 2018; Ahmadi and Ebadi, 2014). The mathematical description based on the mass conservation law and transport equation (Darcy's equation) has been developed to model the fluid flow in the porous media. The stated processes are described by the second-order nonlinear Partial Differential Equations (PDEs) with variables being functions of time and space simultaneously (Huang et al., 2020). In more details, transmissibility, the coefficient of accumulation and fluid compressibility are the most effective nonlinear terms of governing PDEs (Vaferi et al., 2016).

Some analytical and numerical approaches have been introduced so far to solve various types of PDEs (Wang et al., 2019). Although the application of analytical methods yields exact and continues results in

time and space, the stated methods are not applicable in cases of PDEs with a high level of nonlinearity or irregular boundaries (Abou-Kassem et al., 2006). Hence, numerical methods under different scenarios have been put forward (Awadalla and Voskov, 2018). The discretization procedure is a globally accepted method to expand the nonlinear PDEs into a system of nonlinear simultaneous algebraic equations (Jayasinghe et al., 2019). Solving a system of nonlinear equations by approximating them with a system of linear equations in order to have benefits of linear solvers is usually avoided (Mishev et al., 2009). In addition, increasing the errors and inaccuracy in the prediction of the reservoir performance are known as the major drawbacks of the linearization procedures (Voskov and Tchelepi, 2012). Instead, it is highly recommended to tackle problems directly by taking the advantages of nonlinear solvers, which are capable of converging more accurate towards the correct solutions (Younis et al., 2010).

Routinely, Newton's method is the most extensively used solver of nonlinear equations (Nichita, 2018). The simplicity and the high rate of convergence are persuasive enough to frequently apply the introduced technique to solve nonlinear simultaneous algebraic equations (Spence et al., 2020). However, the performance of Newton's method is strongly dependent on making a proper initial guess. Evaluation of n^2 partial

* Corresponding author.

E-mail addresses: yashar.bezyan@concordia.ca, Yashar.Bezyan@Concordia.ca (Y. Bezyan).

<https://doi.org/10.1016/j.jngse.2020.103749>

Received 7 June 2020; Received in revised form 25 August 2020; Accepted 6 December 2020

Available online 17 December 2020

1875-5100/© 2020 Elsevier B.V. All rights reserved.

derivatives, computing the inversion of the Jacobian matrix including $f(n)$ by $f(n)$ linear systems for a certain number of iterations in each time step causing a high computational cost of $O(n^3)$ are the main disadvantages of Newton's method (Bezyan et al., 2019). Moreover, the serious probability of not converging for large time steps due to the high level of nonlinearity is another considerable weakness of Newton's method (Zotos, 2018; Flashner and Guttalu, 1988).

As a result, various attempts have been made to remove the aforementioned disadvantages. The modification of the Secant method known as Broyden's which have been developed for multivariable functions is the adjustment of Newton's method by approximating the Jacobian matrix (Fernandes et al., 2018). Although Broyden's method eliminates the computation of partial derivatives and the inversion of the Jacobian matrix after the first step of the root-finding process, its superlinear convergence rate has made it slower than Newton's method (Broyden, 1965; Incerti et al., 1979). Both the mentioned methods only converge when the proper initial guesses are chosen. Accordingly, the Steepest Descent approach with a linear rate of convergence towards solutions was introduced to overcome the difficulties of an appropriate initial guess. Nevertheless, the Steepest Descent approach also requires the relevant calculations of the Jacobian matrix within each iteration, which is too much costly (Quarteroni et al., 2006). Another well-known technique to solve nonlinear simultaneous algebraic equations is the Homotopy or continuation method which widens the domain of the converges (Ortega and Rheinboldt, 1970). This method changes an easy problem to the complex target problem (He, 2004). However, the same as other referred methods, the Homotopy is a strong function of derivatives as well. Requiring more functions and Jacobian inverse evaluation, and mathematical algebraic operations in comparison with other Newton-type methods are also other significant aspects of Homotopy (Luo et al., 2008; Mehta, 2011). Generally, the heavily derivation-dependent, the high computational cost of the Jacobian matrix and its inversions, and the lack of ability to deal with ill-conditioned matrixes can theoretically be known as the most problematic aspects of classic nonlinear solvers. It should also be reminded that forming the Jacobian matrix for some particular cases is unmanageable (Crevacore et al., 2019).

Therefore, advantages of other modern methods like soft computing have also been taken to overcome the difficulties. For instance, the behavior of a nonlinear Differential Equation (DE) has been imitated by an Artificial Neural Network (ANN) which has classically been trained with the gathered sample points of 2D heat and wave equations (Rudd and Ferrari, 2015). In some studies, data required to train an ANN simulating the mechanism of a nonlinear PDE have been collected from the results generated with the application of numerical methods like finite difference (Ranković and Savić, 2011). Incremental training of the network with the sensor data has been discussed in the literature (Wang and Shi, 2014). The online sensor data have been gathered and used to train the ANN to predict the performance of a reactor for the coming times. After receiving more sensor data, a fixed number of data points, including the newest ones and excluding the oldest records, have been taken to retrain the network for further predictions. The idea of increasing the nodes in the hidden layer of an ANN to reach the minimal error through the conduction of a two-stage gradient descent training algorithm has been discussed as well (Jianyu et al., 2003). The results of an analytical solution have been used as a reference to find the best structure of an ANN to generate the least amount of error. It has become possible by using a global search method known as the Genetic Algorithm (GA) (Tsoulos et al., 2009). Some research in which supposed PDEs have been approximated with applications of ANN without training points have shortly been mentioned in the following. Technically, the generation of zeros as a result of multiplication between a fixed part reflecting boundary conditions and a variable part responding with an ANN for different grids is the main idea behind (Raja and ul Islam Ahmad, 2012). Minimizing the summation of all products is the concept

that can be reached with the most optimized values of the ANN relevant parameters, weights, and biases. In another research (Parisi et al., 2003), the changeable part, which is sensitive to coordinations of grids in the target plate, works based on an ANN in which the relevant parameters have been optimized with the GA. The time-independent form of the Schrodinger equation as an ODE and PDE have been approximated with a hybrid of ANN and the eigenvalue in (Shirvany et al., 2008, 2009). Although assigning a unique ANN to each discretized point causes heavy computation, it leads to approximate very complex PDEs accurately (Beidokhti and Malek, 2009). It has also been proved that the changeable part can be approximated with the Fourier's transform. It becomes possible by employing an ANN to determine the required coefficient (Rudd and Ferrari, 2015). Moreover, it has been shown that feeding the network indirectly with inputs which had already been turned into Chebyshev polynomials increases the flexibility and robustness of the approximation method (Mall and Chakraverty, 2015, 2016). In other words, the limited numbers of inputs can be extended to a certain level, which makes the ANN generating more satisfying results. To sum up, it is possible to interpret that applying the machine learning techniques to solve the nonlinear PDEs has mainly been done either with the help of ANNs trained with data physically describe the supposed phenomena or by taking advantage of the various aspects of the classic math.

The current research represents a user-friendly algorithm that numerically solves the nonlinear PDEs through making a hybrid between the concept of discretization and the Adaptive Neural Network (AdNN) which is a branch of soft computing that can adapt its weights and minimize the loss function without the help of already gathered data (Widrow and Lehr, 1993; Palnitkar and Cannady, 2004). Put the matter another way, each porous media flow problems has its governing equation which means Newton's method must be modified for different problems because each of them has own unique Jacobian matrix. Therefore, Jacobian matrix has to be completely recalculated and written again as a programming code regarding any alteration in the physics of the problem. All of these steps are very time-consuming and accompany with unwanted mistakes whereas AdNN solver is designed based on a constant pattern which makes it possible to apply for any porous media flow and phenomena. Besides, the AdNN-based algorithm not only is independent to Jacobian matrix and the difficulties of classic solvers but also the implemented particular type of AdNN is trained with no need for measured, recorded, or experimental data. Instead, the generated errors by the nonlinear simultaneous algebraic equations are taken as the input to the network and adaption laws. Then, the adaption laws firstly correct the network parameters, and then the network generates the output correspondingly. It should necessarily be considered that there is no cross-validation nor testing for the applied AdNN. It performs as a solver, which learns how much correction it should make to the initial values within each iteration. The procedure continues iteratively and stops when all the generated errors are less than an already set criterion.

The one dimensional (1D) models of the gas flow in ultra-tight porous media of shale gas resources and the immiscible two-phase (oil and water) flow in hydrocarbon resources are the two nonlinear problems that have numerically been solved with the application of the AdNN-based solver compared with Newton's method results. It will be discussed that the output results of AdNN show perfect agreement with Newton's method answers, while AdNN does the same with less computational efforts since it is derivative independent. Moreover, it will be proved that AdNN can be used for any fluid flow problem by implementing the same pattern of designing the network structure. It is done by solving two bench mark problems, gas flow in shale gas and oil/water in conventional porous medium.

2. Methodology

2.1. Shale gas resources

Experimental studies have proved the existence of nanoscale pores in organic-rich shale gas resources (Javadpour, 2009; Zhang et al., 2019). They have enormous impacts on the flow and storage of shale gas resources. Not only the nanoscale pores provide a large exposed surface area for adsorbed gas, but also they cast doubt on the validity of applying Darcy's law, which has been initially developed for microscale pores (Sheng et al., 2019). It is believed that slippage and transition are the main flow mechanisms, and gas molecules are adsorbed on the surface of pores and organic matter as the second type of storage. (Naraghi et al., 2018). The complexity of the pictured situation in shale gas resources can be modeled based on highly nonlinear PDEs. Accordingly, different research have attempted to develop a fluid flow in shale gas resources based on multi-mechanisms of flow and storage (Javadpour, 2009; Darabi et al., 2012). Regarding the mass conservation equation, the following second-order nonlinear PDE which takes the effects of multi-mechanisms of flow and storage into account has been proposed (Bezyan et al., 2019).

$$\frac{\partial}{\partial x} \left(\beta_c k_{app} A \frac{\rho_f}{\mu} \frac{\partial p}{\partial x} \right) \Delta x \pm q_{mc} = \frac{V_b}{\alpha_c} \frac{\partial p}{\partial t} c_g \rho_f \left(\varphi + (1 - \varphi) \frac{\partial \rho_a}{\partial p_f} \right) \quad (1)$$

The derivation of Eq. (1), its relevant parameters and the considered boundary conditions are thoroughly discussed in A.

2.2. Immiscible two-phase flow

The simulation studies of multiphase flow have a high level of importance in different engineering aspects of porous media. Therefore, many studies have ever been done to provide accurate results under different scenarios and properties (Rostami et al., 2019; Aljehani et al., 2018). The case of immiscible two-phase (water and oil) flow in a water-wet porous medium can be modeled based on the following equations:

$$\frac{\partial}{\partial x} \left(\beta_c k_A \frac{k_{ro}}{\mu_o B_o} \frac{\partial p_o}{\partial x} \right) \Delta x \pm q_{osc} = \frac{V_b}{\alpha_c} \frac{\partial}{\partial t} \left(\varphi \frac{(1 - S_w)}{B_o} \right) \quad (2)$$

$$\frac{\partial}{\partial x} \left(\beta_c k_A \frac{k_{rw}}{\mu_w B_w} \left(\frac{\partial p_o}{\partial x} - \frac{\partial p_c}{\partial x} \right) \right) \Delta x \pm q_{wsc} = \frac{V_b}{\alpha_c} \frac{\partial}{\partial t} \left(\varphi \frac{S_w}{B_w} \right) \quad (3)$$

The background of both equations and the description of the connected parameters are discussed in B. Describing the immiscible multiphase flow of oil and water in a porous medium, using Eq. (2) and Eq. (3), is strongly nonlinear due to the existence of k_r terms. It should be considered that B and μ have nonlinearity impacts, but not as effective as the relative permeability or boundary conditions.

2.3. The classic solver

Following the discretization based on the finite difference method, Eq. (1) representing the compressible fluid flow in shale gas reservoirs and Eqs. (2) and (3) as the mathematical expression for the immiscible multiphase flow of oil and water in a porous medium can numerically be stated as:

$$C_1 Y + C_2 = 0 \quad (4)$$

where Y is the vector of unknowns, and both C_1 and C_2 are dependent matrices of coefficients to Y . By regarding the thermodynamical nature of gases or the strong dependency of k_r to saturations, Eq. (4) is a set of nonlinear simultaneous algebraic equations either for shale gas reservoirs or the immiscible multiphase flow of oil and water in a porous medium. Typically, Newton's method, which takes advantage of the Jacobian matrix, is employed to solve nonlinear simultaneous algebraic

equations. Newton's method is mathematically performed as:

$$J \delta Y = -R \quad (5)$$

where δY is:

$$\delta Y = Y^{j+1} - Y^j \quad (6)$$

where Y is the vector of unknown parameters. The superscript of j and $j+1$ shows the current and next iterations, respectively. For shale gas reservoirs, Y is defined as:

$$Y = (p_i)^T \quad (7)$$

in which $i = 1, 2, 3, \dots, N$, and N is the number of grids. Similarly, Y for the immiscible multiphase flow of oil and water in a porous medium is:

$$Y = (S_{w_i}, p_{o_i})^T \quad (8)$$

Also, J is the Jacobian matrix composed by the partial derivatives of the residuals shown as R which is:

$$R = (R_i)^T \quad (9)$$

where the size of R_i equals to the number of existing phases. In other words, while it has one value for each grid in the single-phase compressible fluid flow in shale gas resources, it has the following form for the immiscible multiphase flow of oil and water as:

$$R_i = (R_{w_i}, R_{o_i})^T \quad (10)$$

As a result, J for the immiscible multiphase flow of oil and water has the following form of:

$$\begin{bmatrix} \frac{\partial R_{w_1}}{\partial S_{w_1}} & \frac{\partial R_{w_1}}{\partial p_{o_1}} & \dots & \frac{\partial R_{w_1}}{\partial S_{w_N}} & \frac{\partial R_{w_1}}{\partial p_{o_N}} \\ \frac{\partial R_{o_1}}{\partial S_{w_1}} & \frac{\partial R_{o_1}}{\partial p_{o_1}} & \dots & \frac{\partial R_{o_1}}{\partial S_{w_N}} & \frac{\partial R_{o_1}}{\partial p_{o_N}} \\ \vdots & \vdots & \ddots & \vdots & \vdots \\ \frac{\partial R_{w_N}}{\partial S_{w_1}} & \frac{\partial R_{w_N}}{\partial p_{o_1}} & \dots & \frac{\partial R_{w_N}}{\partial S_{w_N}} & \frac{\partial R_{w_N}}{\partial p_{o_N}} \\ \frac{\partial R_{o_N}}{\partial S_{w_1}} & \frac{\partial R_{o_N}}{\partial p_{o_1}} & \dots & \frac{\partial R_{o_N}}{\partial S_{w_N}} & \frac{\partial R_{o_N}}{\partial p_{o_N}} \end{bmatrix}_{2N \times 2N} \quad (11)$$

Furthermore, J for the single-phase compressible fluid flow in shale gas reservoirs is:

$$\begin{bmatrix} \frac{\partial R_1}{\partial p_1} & \dots & \frac{\partial R_1}{\partial p_N} \\ \vdots & \ddots & \vdots \\ \frac{\partial R_N}{\partial p_1} & \dots & \frac{\partial R_N}{\partial p_N} \end{bmatrix}_{N \times N} \quad (12)$$

2.4. The alternative approach

The universal approximation theory states that a Single Hidden Layer (SHL) neural network has the capability of estimating any nonlinear, continuous, and unknown functions. (Boudjedir, 2012; Zabihifar et al., 2007). Accordingly, Li and Zheng initially took advantage of a supervised ANN tuned with adaptive laws (AdNN) to solve three benchmark systems of nonlinear simultaneous algebraic equations formerly reported in the literature (Li and Zeng, 2008).

Through carrying some modifications out, the main launched idea can innovatively be applied to estimate Y so that Eq. (4) generates the matrix of zeros. The conduction of such an approach to numerically solve highly-nonlinear Eq. (1) and the pair of Eqs. (2) and (3) provides the opportunity of removing the Jacobian matrix and its inversion.

Putting the matter another way, the designed solver is not dependent on the nature of problems anymore because it does not use the Jacobian

matrix. Specifically, any physical changes in foundations of regarding problems should manually be reflected in the Jacobian matrix through recalculations and modifications of its derivatives. It is shown by Eqs. (11) and (12), where each one represents its relevant problem. Surprisingly and thanks to the implemented adaptive laws, the AdNN-based solver takes the effects of the same changes automatically. The proposed technique has schematically been illustrated in Fig. 1.

To iteratively conclude the satisfying Y within each time step, a set of initial values which are not necessarily proper or even following a specific pattern are firstly fed to Eq. (4). Then, O^j as the generated matrix of output is compared with the desired one to produce the corresponding matrix of tracking errors noted as e^j , Eq. (13).

$$e^j = D - O^j \tag{13}$$

ere D represents the desired answers which based on Eq. (4) is a matrix of zeros during all iterations of calculating satisfying Y within each time step. Unless the $\max |e^j|$ is less than the primary set criterion, the algorithm proceeds through the calculation of \dot{e} as the derivative of error in respect to time.

$$\dot{e} = \frac{e^j - e^{j-1}}{\Delta t_{CCS}} \tag{14}$$

where e^{j-1} is the matrix of tracking error in the previous iteration, and Δt_{CCS} is the time difference between Consecutive Computational Steps. Then, X as the matrix of inputs to the adaptive and supervised neural network should be prepared as:

$$X = [e_1^j, \dot{e}_1, D_1, \dots, e_N^j, \dot{e}_N, D_N]^T \tag{15}$$

Consequently, ΔY as the corresponding output of the one-step more trained network is employed to calculate the corrected pressures for the

next iteration as:

$$Y^{j+1} = Y^j + \Delta Y \tag{16}$$

Functionally, $\Delta \bar{Y}$ is calculated through the supposed network as below:

$$\Delta Y = (w^j)^T \sigma_{new} \left((v^j)^T X \right) \tag{17}$$

where σ_{new} is a type of RBF sigmoid activation function that considers an equal action for positive and negative input values, and it is firstly stated as:

$$\sigma_{new}(e) = \frac{1}{1 + e^{|e|}} \tag{18}$$

To have a proper ΔY in terms of concluding the most satisfying pressures, iteratively updating of v and w as weights of the network should be considered through applications of adaptation laws. Regarding the weights of the previous iteration, the procedure of adaption can mathematically be stated as:

$$v^j = v^{j-1} + \Delta v \tag{19}$$

$$w^j = w^{j-1} + \Delta w \tag{20}$$

where

$$\Delta v = F_v X S^T (w^{j-1})^T \sigma'_{new} (v^{j-1} X) \tag{21}$$

$$\Delta w = F_w \sigma_{new} (v^{j-1} X) S^T \tag{22}$$

with any constant positive definite design matrix of F_w and F_v . In fact, the adaption laws are optimising the weights so that the network is going to receive the less magnitude of errors in the next iteration. Also,

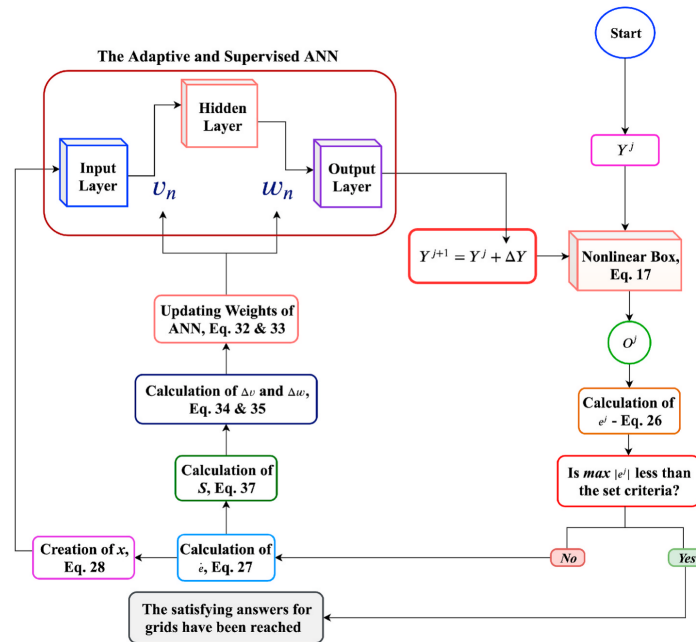


Fig. 1. The schematic of the proposed algorithm to numerically solve second-order nonlinear PDEs with the application of a supervised AdNN.

the derivative of the activation function is:

$$\sigma'_{\text{new}}(v^{j-1}X) = \sigma_{\text{new}}(v^{j-1}X)(1 - \sigma_{\text{new}}(v^{j-1}X)) \tag{23}$$

and, the filtered tracking error known as S is:

$$S = \dot{e} + \lambda e^j \tag{24}$$

where $S = [S_1, \dots, S_N]^T$ and $\lambda \in \mathbb{R}^{n \times n}$ is a diagonal matrix known as the coefficient of error. It can mathematically be interpreted that the iterative convergence of S towards zero implies the simultaneous convergence of e^j and \dot{e} to zero as well. In other words, approaching S towards zero does mean that subsequent v and w causes the network to produce a ΔY that insertion of its corresponding Y^{j+1} into Eq. (4) generates an almost zero matrix and satisfies the required level of error. Additionally, Fig. 2 shows precisely how the implemented fully-connected AdNN in the represented algorithm works based on taking the input vector and generating the favorite response, respectively.

3. Results and discussions

The represented algorithm has been applied to solve both discussed simulation problems. In the first part, a single-component 1D shale gas model has been chosen as a basis for comparison between the concerned algorithm and Newton's method. Then, the same kind of comparison between both types of solvers has also been made for an immiscible two-phase flow system. Finally, the computational efficiency of the proposed algorithm has been compared to Newton's method.

3.1. Simulation of shale gas resources

The performance of the assumed shale model with parameters stated in Table 1 has been considered to be simulated by both the AdNN-based algorithm and Newton's solver.

Also, the number of neurons (nn) in the hidden layer, coefficient of error (λ), and constant positive values of F_w and F_v are the four parameters of the represented algorithm, which have been determined based on the sensitivity analysis, see C, to make the proposed solver performing as robust and accurate as possible, Table 2.

The results of the simulation based on the implementation of both solvers have comparatively been represented for five periods in Fig. 3. For various periods of the production, the results represent the substantial agreement between the performance of the AdNN-based solver and Newton's method.

Furthermore, Fig. 4 shows the reliability of the AdNN-based solver. According to the concept of Minimum Square Error (MSE) (Rostami et al., 2019), the first part shows that as much as time goes by, the

Table 1
Various parameters of the shale model (Bezyan et al., 2019; Darabi et al., 2012).

Parameter	Value
Temperature (°F)	237
Initial Pressure (psi)	5000
C_1	100
k (md)	0.0008
ϕ	0.15
Length (ft)	200
P_{wf} (psi)	400
Duration (days)	720
α	0.8
τ	4
D_f	2.5
P_i (psi)	1240
$V_L (\frac{ft^3}{lb})$	0.07277
$\rho_b (\frac{lb}{ft^3})$	164.038
Δx (ft)	4
Δt (days)	2

Table 2
The parameters of the AdNN-based solver and their optimum values.

Parameter	Value
nn	9
λ	1200
F_w	3000
F_v	1600

proposed AdNN-based solver generates results more dissimilar to those converged by Newton's method. Also, it can be seen that the hump showing the maximum of the difference between both generated pressure profiles by both solvers approaches to the other boundary in time while getting enlarged. In other words, the AdNN-based solver generates close results to outputs of Newton's method for the early stages of production, while its convergences for the final stages can relatively be different.

Regarding the fact that k_{app} is the most representative flow parameter of shale resources, it has analogously been examined how much the pressure difference, which has already shown in Fig. 4(b), causes dissimilarity in the results of relevant calculations. For that reason, grids numbers 1, 25, and 50 have been chosen to observe the trends of k_{app} temporally, Fig. 5. Not only the outputs show a remarkable consistency in the produced results of both solvers, but also it could be concluded

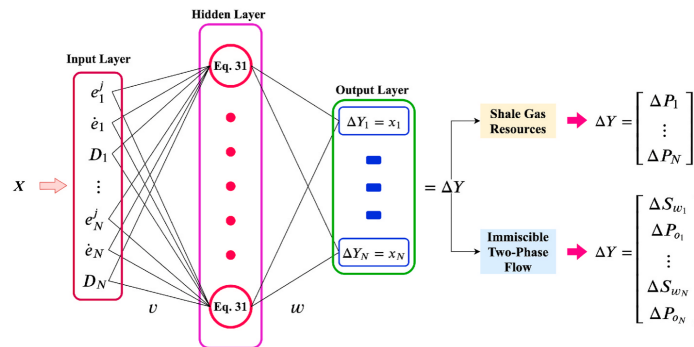


Fig. 2. The implemented supervised AdNN to iteratively converge to correct answers.

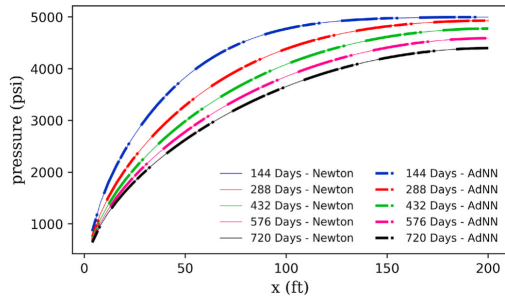


Fig. 3. The comparison of pressure profiles generated by Newton's method and AdNN-based algorithm at different time intervals.

that the converged pressures by the AdNN-based solver are close enough to the results of Newton's method.

3.2. Simulation of immiscible two-phase flow

A basic model of immiscible two-phase flow has been designed to check the reliability of the AdNN-based solver. The relevant parameters have been reported in Table 3. The supposed model has a water injection well in the first block and an oil production well in the last block.

Like the previous part, Table 4 shows the parameters of the AdNN-based solver that has been set by trial-and-error to solve the problem of immiscible two-phase flow. Apart from nn, which has been increased for one neuron, the rest is the same, which shows the robustness and overwhelming adaptability of the AdNN-based solver.

The results of applying the AdNN-based solver for the case described in Table 4 has been shown in Figs. 6 and 7 based on p_o and S_w , respectively. Generally, it could be observed that the results of the AdNN-based solver is in satisfying agreement with Newton's method in terms of p_o and S_w .

Moreover, it could be deduced that the solver makes overestimations to predict the pressure before the front of the injected water, but after that, it starts following an uprising trend of underestimation, Fig. 8 (a). Similarly, the most significant differences between the calculated saturation profiles at each time happens near the front between the water and oil. It can also be seen that the magnitude of the hump showing the difference grows as a function of time, Fig. 8 (b). The overall comparison between the generated results show that the absolute differences

between produced profiles of pressures and saturations are 12.5 psi and 5×10^{-5} , respectively. Based on the scale of pressures and saturations in hydrocarbon reservoirs, it can be concluded that the calculated deviations are negligible.

In addition, the MSE comparison between generated profiles of pressures and saturations have been shown in Fig. 9. It could be observed that the error of converged profiles of both variables follows an uprising trend over time. However, the small magnitude of the calculated MSE approves the feasibility and validation of the AdNN-based solver.

In terms of the relative permeability, the overlapping of curves at various times proves that the results of applying the AdNN-based solver have the least amount of divergence from the results of Newton's method, Fig. 10.

3.3. Computational efficiency

The efficiency of an algorithm depends on its design and implementation. Since every algorithm uses computer resources to run, internal memory usage is an important consideration to analyze the algorithm. Based on the usage of Random Access Memory (RAM) show in Fig. 11, the performance of the algorithm has been evaluated. The domain has been split into various numbers of grids. Then, each model with the different numbers of grids has been simulated 10 times, and the median of the results has been selected as the corresponding memory usage. The results show that the AdNN-based algorithm has the same RAM usage for the small number of grids. However, for the larger number of grids, it can be seen that the algorithm takes less memory than Newton's method. It is basically due to the removal of the Jacobian matrix. Regarding the removal of the Jacobian matrix and its different sizes for the two problems, the contrast between the two trends in the case of immiscible two-phase flow is more noticeable than the difference of trends in shale gas resources.

The next index to evaluate the computational efficiency of the represented algorithm is CPU Time. The same pattern of 10 times running the algorithm has been implemented for the supposed number of grids. The median of recorded CPU Times is plotted versus the relevant number of grids in Fig. 12.

It can be observed that the AdNN-based solver cannot perform as fast as Newton's method for the larger number of grids. However, it does not necessarily mean that Newton's method should always be considered as the first option. The fast convergence of Newton's method is guaranteed only if it is possible to form the related Jacobian matrix and make the proper initial guesses.

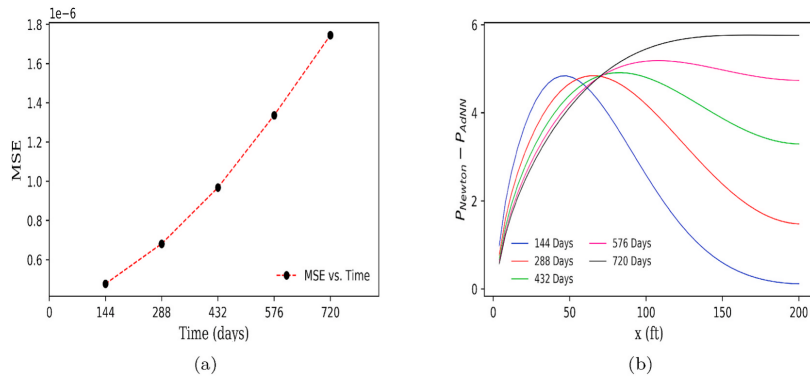


Fig. 4. Newton's method vs. AdNN-based solver (a) MSE (according to the normalized pressures) (b) Pressure Difference.

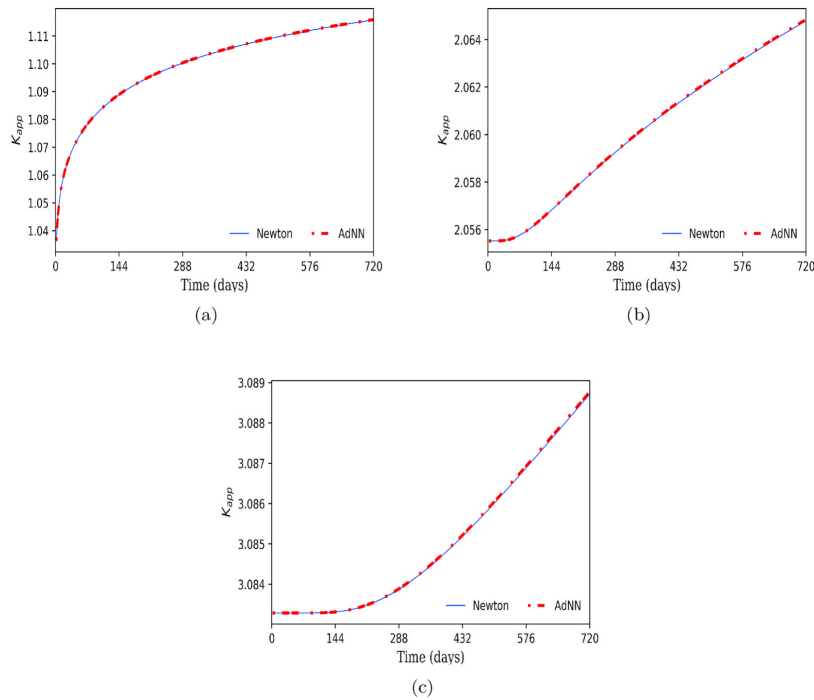


Fig. 5. The comparison of generated k_{app} based on the applied solvers. (a) Grid No. 1, (b) Grid No. 25, and (c) Grid No. 50.

Table 3
Various parameters of the immiscible two-phase model (Ertekin et al., 2001).

Parameter	Value
Temperature (°F)	237
Initial Pressure (psi)	5000
P_b (psi)	2884
k (md)	30
φ	0.15
Length (ft)	600
Duration (days)	200
μ_{ob}	0.2884
S_{wc}	0.16
q_{winj} (bbl/Day)	100
q_{oprod} (bbl/Day)	80
Δx (ft)	15
Δt (days)	20

Table 4
Structure of the AdNN-based solver for the case of immiscible two-phase flow.

Parameter	Value
nn	10
λ	1200
F_w	3000
F_v	1600

4. Conclusion

Fluid flow in porous media is one of the most critical aspects of engineering. The modeling and simulation of compressible flow in ultra-tight porous media of shale resources or immiscible multiphase flow in hydrocarbon reservoirs are complex phenomena that are described with highly nonlinear second-order PDEs. The proper understanding of the supposed PDEs can be acquired by employing numerical solutions with the implementation of nonlinear solvers. The classical scheme for fully implicit cases is Newton’s method. However, inherent difficulties such as proper initial guesses, strongly dependent on the Jacobian matrix and its inversion causing high computational costs, and the probability of not converging in case of large time steps have routinely been faced in many experiences. In this study, Adaptive Neural Network has been proposed as a general solver and an alternative approach to classic methods. The introduced technique is a trade-off between the Numerical and soft computing approaches, which can use finite difference, finite element or finite volume to discretize the PDEs, and then implement AdNN to solve the discretized system of nonlinear equations. Instead of using the derivations of PDEs to find the roots, AdNN minimizes the errors generated by inserting an initial set to the algebraic equations by an iterative procedure and just through adjusting the weights of AdNN by means of adaption laws. In other words, the introduced algorithm neither has the difficulties of applying the conventional numerical methods like forming the Jacobian matrix, nor it has the inherent problems of data gathering in case of using standard soft computing methods. To put it more simply, AdNN is not dependent on the physics of the problems and corresponding governing equations and can be applied to any problems of fluid flow in porous media. It was successfully approved by implementing the presented algorithm to simulate the

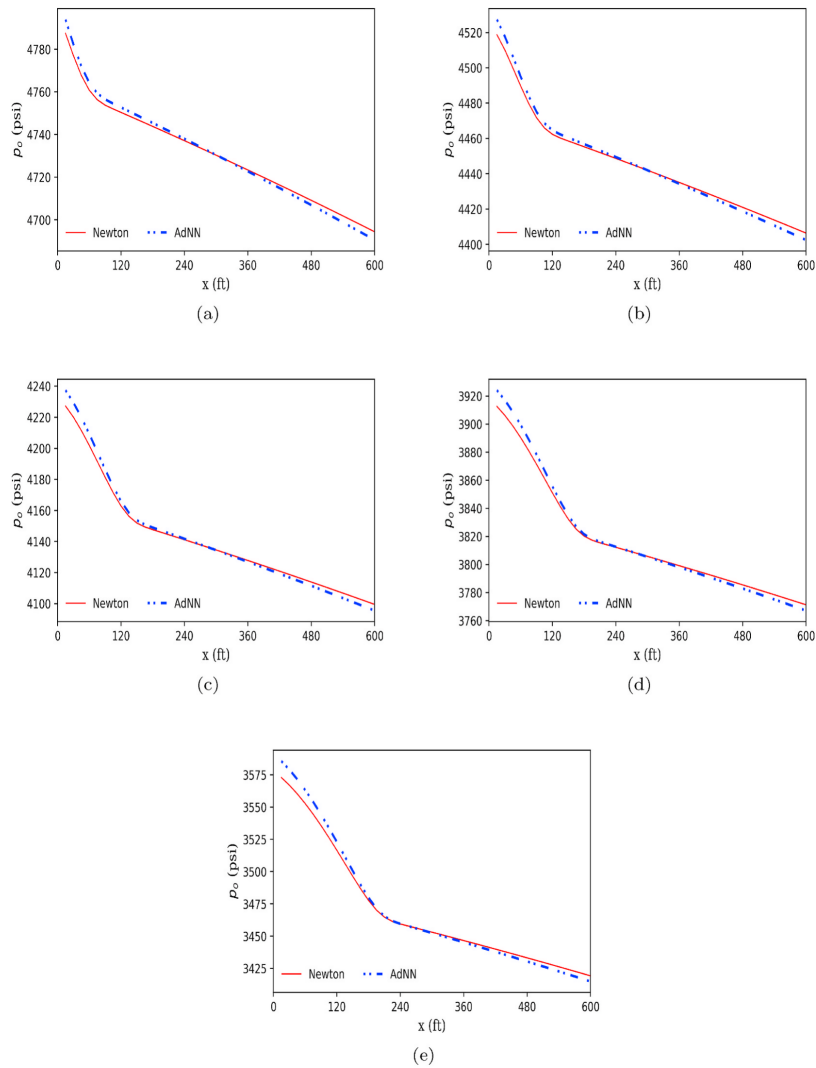


Fig. 6. The comparison of oi pressure distributions generated by both solvers (a) 40 Days (b) 80 Days (c) 120 Days (d) 160 Days (e) 200 Days.

compressible flow in the ultra-tight shale resources and immiscible two-phase flow in a porous media. In both cases, the evolved algorithm has been capable of simulating pressure profile and saturation as accurate as Newton’s method. Moreover, in terms of computational efficiency, AdNN occupies a lower amount of RAM than Newton’s method, while CPU time for AdNN is higher than Newton’s method, specifically for two-phase flow. The demonstrated algorithm can be recommended for other nonlinear fields as a robust solver. It can also be taken as one of the

main principles of the coming hybrid of physics-based and soft-computing enabled simulators.

Declaration of competing interest

The authors declare that they have no known competing financial interests or personal relationships that could have appeared to influence the work reported in this paper.

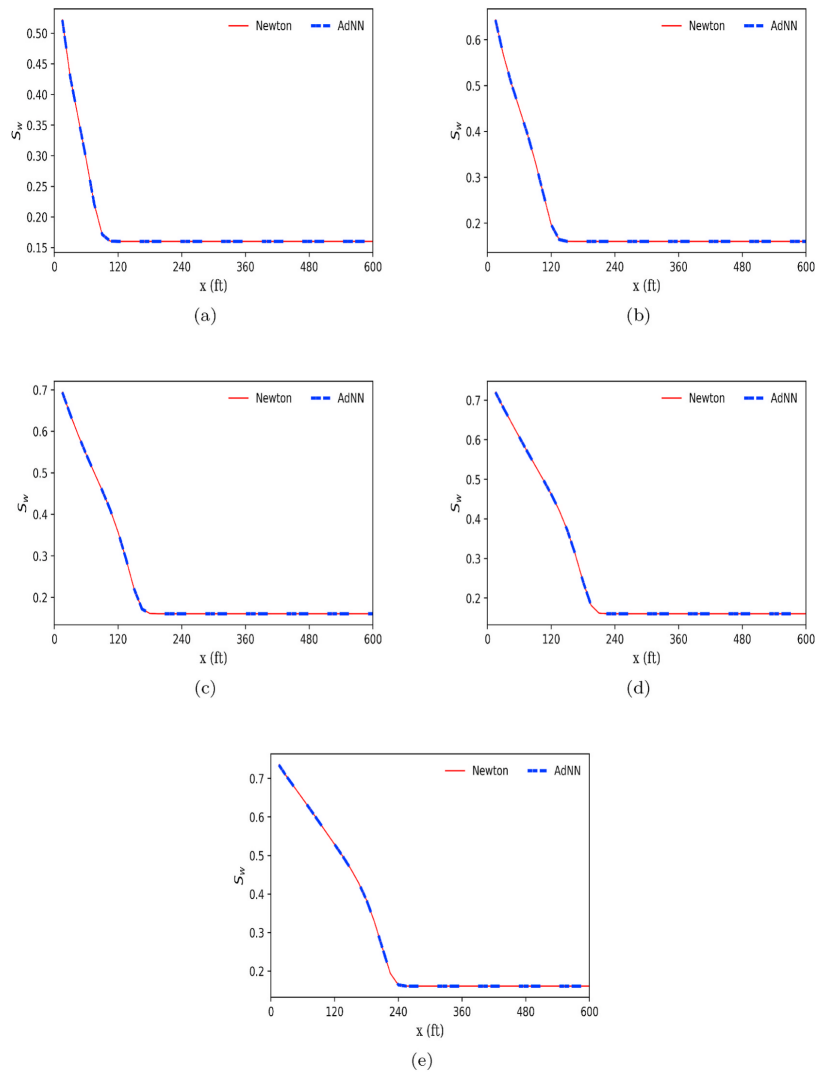


Fig. 7. The comparison of water saturation distributions generated by both solvers (a) 40 Days (b) 80 Days (c) 120 Days (d) 160 Days (e) 200 Days.

Appendix A. Fluid flow in shale gas resources

Typically, the mass conservation equation for a single grid is introduced based on a one-dimensional (1D) model of a conventional porous media as below (Ertekin et al., 2001; Ahmed, 2019):

$$-\frac{\partial(\alpha_c \rho u A)}{\partial x} \Delta x \pm q_{mc} = V_b \frac{\partial}{\partial t} (\phi \rho) \tag{A.1}$$

where u ($\frac{ft}{day}$) based on Darcy's law is defined as:

$$u = -\beta_c \frac{k}{\mu} \frac{\partial p}{\partial x} \tag{A.2}$$

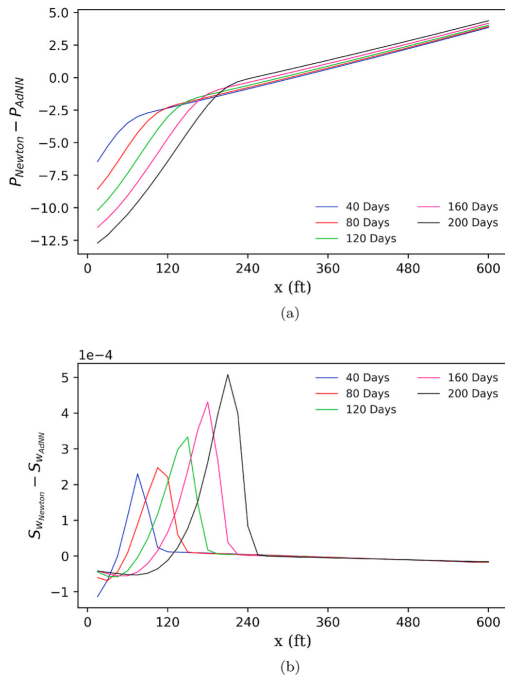


Fig. 8. Differences between generated profiles (a) Pressure profiles (b) Saturation profiles.

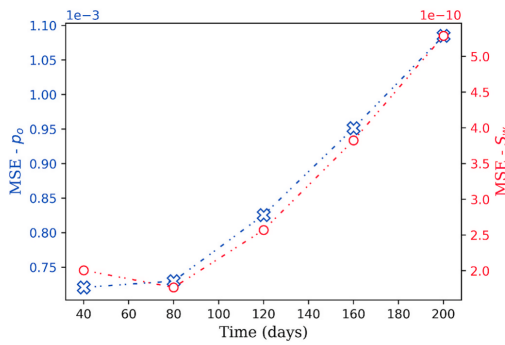


Fig. 9. MSE evaluation of Newton's method vs. AdNN-based solver.

combining Eq. (A.1) and Eq. (A.2) results in:

$$\frac{\partial}{\partial x} \left(\beta_c k A \frac{\rho}{\mu} \frac{\partial p}{\partial x} \right) \Delta x \pm \frac{q_{mc}}{\alpha_c} = \frac{V_b}{\alpha_c} \frac{\partial}{\partial t} (\rho \varphi) \tag{A.3}$$

where \$A\$ is the cross section area (\$ft^2\$), \$\Delta x\$ is the length of each grid (\$ft\$), \$\mu\$ is viscosity (\$cp\$), \$\rho\$ is density of the fluid (\$\frac{lb}{ft^3}\$), \$k\$ is absolute permeability (\$md\$), \$t\$ is time (\$day\$), \$p\$ is pressure (\$psi\$), \$\varphi\$ is the porosity and \$V_b\$ is the bulk volume (\$ft^3\$), \$\alpha_c\$ is the volume conversion factor whose numerical value for the field unit is 5.615, and \$\beta_c\$ is transmissibility conversion factor which equals to 0.001127 in the field unit system. Finally, \$q_{mc}\$ is the rate of mass depletion through wells which is positive for injection and negative for the production (\$\frac{lb}{ft^3}\$).

Because of two storage mechanisms of free compressed and adsorption, the corresponding notations of densities are presented as \$\rho_f\$ and \$\rho_a\$.

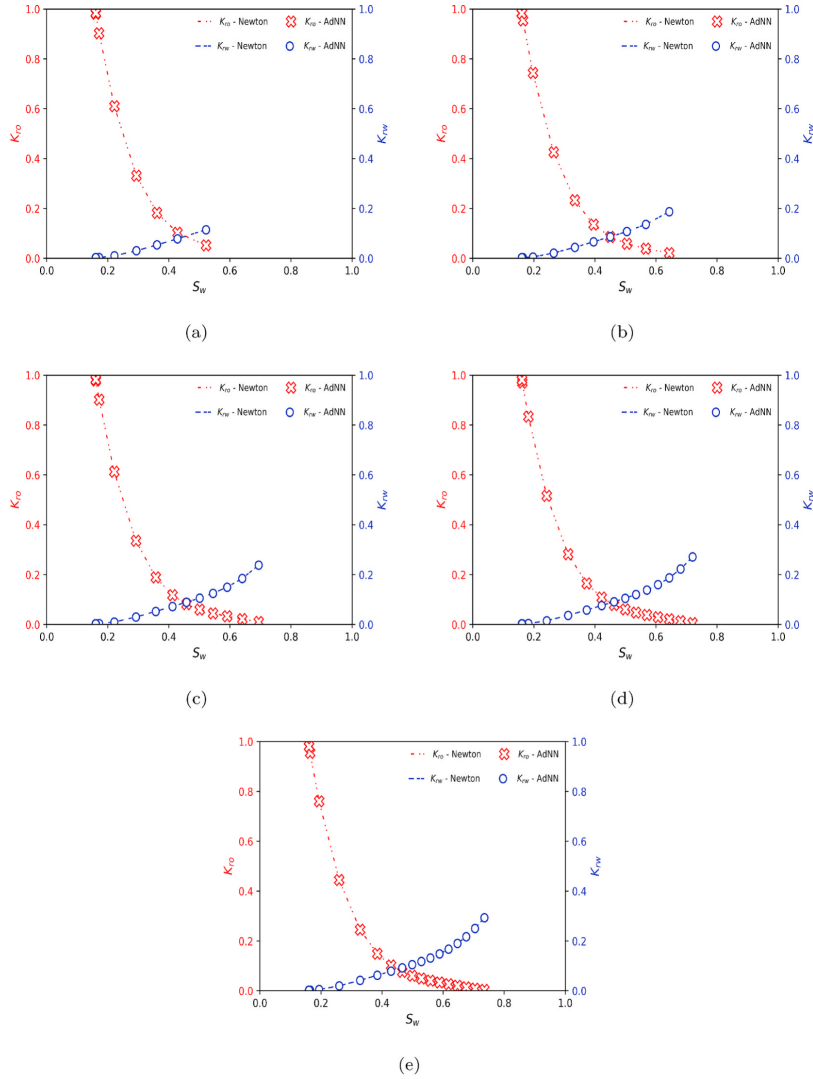


Fig. 10. The comparison of relative permeability curves as the results of the both solvers (a) 40 Days (b) 80 Days (c) 120 Days (d) 160 Days (e) 200 Days.

respectively. Then, the effects of slippage and diffusion in nanopores are considered by replacing the permeability with the multi-mechanism apparent permeability model (k_{app}) which is the function of pressure and pore radius, simultaneously (Darabi et al., 2012; Kulga et al., 2018).

$$\frac{\partial}{\partial x} \left(\beta_r k_{app} A \frac{\rho_f}{\mu} \frac{\partial p}{\partial x} \right) \Delta x \pm \frac{q_{mc}}{\alpha_c} = \frac{V_b}{\alpha_c} \frac{\partial}{\partial t} (\rho_f \varphi) \tag{A.4}$$

Besides the compressed gas in the pore space, the adsorbed gas as another type of storage mechanism is added to the accumulation term of mass conservation law and turn Eq. A.4 into:

$$\frac{\partial}{\partial x} \left(\beta_r k_{app} A \frac{\rho_f}{\mu} \frac{\partial p}{\partial x} \right) \Delta x \pm \frac{q_{mc}}{\alpha_c} = \frac{V_b}{\alpha_c} \frac{\partial}{\partial t} (\rho_f \varphi + (1 - \varphi) \rho_a) \tag{A.5}$$

where ρ_a is density of the adsorbed gas. In other words, ρ_a is the mass of adsorbed gas per volume of the rock. A more straightforward expression is

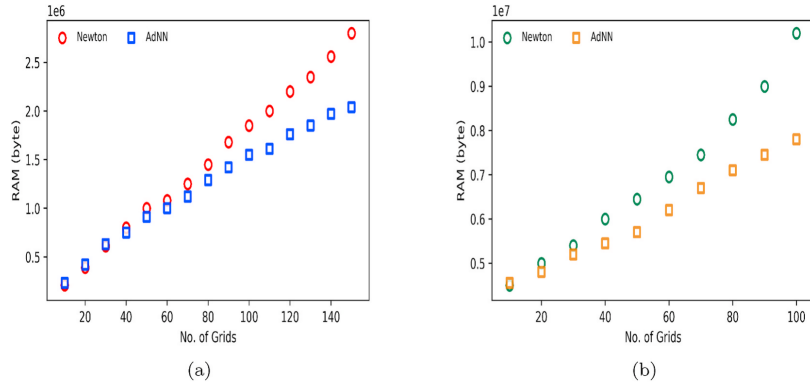


Fig. 11. Computational Efficiency of AdNN vs. Newton's method (a) Shale Gas Resources (b) Immiscible Two-Phase Flow.

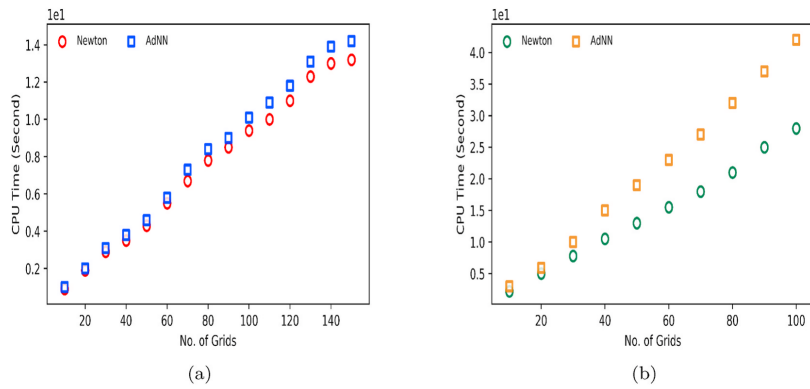


Fig. 12. Computational Efficiency of AdNN vs. Newton's method (a) Shale Gas Resources (b) Immiscible Two-Phase Flow.

proposed for the right side of Eq. A.5 through taking advantages of the chain rule and compressibility concept as below:

$$c_g = \frac{1}{\rho_f} \frac{\partial \rho_f}{\partial p} \tag{A.6}$$

where c_g is the gas compressibility (psi^{-1}). Therefore,

$$\frac{\partial \rho_f}{\partial t} = c_g \rho_f \frac{\partial p}{\partial t} \tag{A.7}$$

and

$$\frac{\partial \rho_a}{\partial t} = \frac{\partial \rho_a}{\partial \rho_f} \frac{\partial \rho_f}{\partial p} \frac{\partial p}{\partial t} = \frac{\partial \rho_a}{\partial \rho_f} c_g \rho_f \frac{\partial p}{\partial t} \tag{A.8}$$

based on Eq. A.7 and A.8, Eq. A.5 is finalized as:

$$\frac{\partial}{\partial x} \left(\beta k_{app} A \frac{\rho_f}{\mu} \frac{\partial p}{\partial x} \right) \Delta x \pm \frac{q_{mc}}{\alpha_c} = \frac{V_b}{\alpha_c} \frac{\partial p}{\partial t} c_g \rho_f \left(\varphi + (1 - \varphi) \frac{\partial \rho_a}{\partial \rho_f} \right) \tag{A.9}$$

In order to obtain a mathematical expression for ρ_a and its derivative, the mass balance of adsorbed gas is formed as (Yu et al., 2016)

$$\rho_a = \frac{\rho_f (P_{ST}, T_{ST}) \rho_b}{(1 - \varphi)} V \tag{A.10}$$

where $\rho_f(P_{ST}, T_{ST})$ is the gas density in standard conditions, ρ_b is bulk density, and V is volume of adsorbed gas per bulk volume of the rock.

Technically, Eq. A.9 describes the gas flow in the ultra-tight porous media of shale gas resources based on a variety of flow and storage mechanisms. Eq. A.9 is numerically solved based on the following initial and boundary conditions.

Initial Condition at $t = 0$ and $0 < x < L$:

$$p = p_{in}$$

Left Boundary Condition at $t > 0$ and $x = 0$:

$$p = p_{cfc}$$

Right Boundary Condition at $t > 0$ and $x = L$:

$$\frac{\partial p}{\partial x} = 0$$

Appendix B Immiscible flow of water and oil in porous media

The incompressible two-phase flow in homogeneous porous media can mathematically be described with the following PDEs:

$$\frac{\partial}{\partial x} \left(\beta_o kA \frac{k_{ro}}{\mu_o B_o} \frac{\partial p_o}{\partial x} \right) \Delta x \pm q_{osc} = \frac{V_b}{\alpha_c} \frac{\partial}{\partial t} \left(\phi \frac{S_o}{B_o} \right) \quad (\text{B.1})$$

$$\frac{\partial}{\partial x} \left(\beta_w kA \frac{k_{rw}}{\mu_w B_w} \frac{\partial p_w}{\partial x} \right) \Delta x \pm q_{wsc} = \frac{V_b}{\alpha_c} \frac{\partial}{\partial t} \left(\phi \frac{S_w}{B_w} \right) \quad (\text{B.2})$$

where k_r shows the relative permeability and B is the formation volume factor ($\frac{bB}{S_{TB}}$). The subscriptions of o and w represent the properties for oil and water, respectively. For oil and water wells, the q_{osc} and q_{wsc} show either production or injection rates at standard conditions.

There are four unknowns of p_o , p_w , S_o , and S_w although there are merely two flow equations. With the assistance of auxiliary equations, the saturation equation and the capillary pressure relationship, two unknowns could be eliminated, and PDEs are coupled to each other.

The constraints equation is defined as the sum of phase saturation which is equal to one and expressed as:

$$S_o + S_w = 1 \quad (\text{B.3})$$

and the oil/water capillary relationship as a function of saturation is:

$$p_c(S_w) = p_o - p_w \quad (\text{B.4})$$

where $p_c(S_w)$ is estimated based on the model developed in the literature (Shams et al., 2015). By insertion of Eq. B.3 and B.4 into equations Eq. B.1 and B.2, the number of unknowns reduces to two terms of p_o and S_w as:

$$\frac{\partial}{\partial x} \left(\beta_o kA \frac{k_{ro}}{\mu_o B_o} \frac{\partial p_o}{\partial x} \right) \Delta x \pm q_{osc} = \frac{V_b}{\alpha_c} \frac{\partial}{\partial t} \left(\phi \frac{(1 - S_w)}{B_o} \right) \quad (\text{B.5})$$

$$\frac{\partial}{\partial x} \left(\beta_w kA \frac{k_{rw}}{\mu_w B_w} \left(\frac{\partial p_o}{\partial x} - \frac{\partial p_c}{\partial x} \right) \right) \Delta x \pm q_{wsc} = \frac{V_b}{\alpha_c} \frac{\partial}{\partial t} \left(\phi \frac{S_w}{B_w} \right) \quad (\text{B.6})$$

the relevant numerical solutions can properly be developed according to the following initial and boundary conditions for a 1D model having an injection well in the first grid and a production well in the last one.

Initial Condition at $t = 0$ and $0 < x < L$:

$$p_o = p_{in}$$

$$S_w = S_{wc}$$

Left Boundary Condition at $t > 0$ and $x = 0$:

$$\frac{\partial p_o}{\partial x} = 0$$

Right Boundary Condition at $t > 0$ and $x = L$:

$$\frac{\partial p_o}{\partial x} = 0$$

Appendix C. Sensitivity analysis of AdNN structure

The most optimized structure of AdNN for solving each one of the supposed problems has been concluded based on measuring the CPU Time of convergence for the first time-step of introduced problems in Tables 1 and 3. In further detail, a basic structure of an AdNN has been initialized, as reported in Table C.1. The effects of changing a parameter is observed by running the modified AdNN for 10 times while the other parameters are kept constant. Then, the median of all recorded times is reported as the CPU Time for the concerning parameter. More information about the applied method are in the previous literature (Ahmadi et al., 2014a, 2014b).

Table C.1
Initial structure of AdNN before running the sensitivity analysis

Parameter	Value
nn	8
λ	1400
F_w	2500
F_v	1600

Regarding the fluid flow in the shale gas resource, the results of the sensitivity analysis are shown in Figure C.1. It should be noted that the tested ranges have been recommended by similar research (Zabihifar et al., 1007).

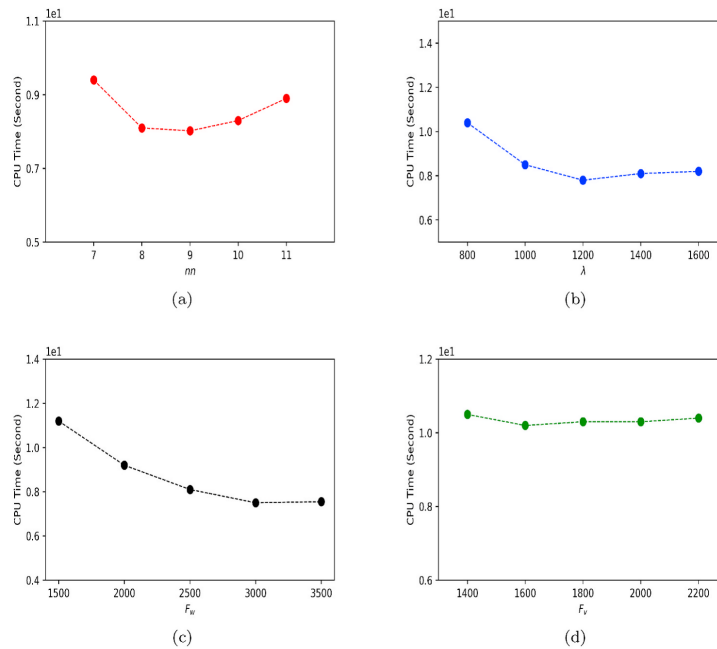


Fig. C.1. Determination of the most optimized AdNN structure to solve Eq. 1 (a) Effects of nn changes (b) Effects of λ changes (c) Effects of F_w changes (d) Effects of F_v changes.

The results show that the AdNN with 9 neurons makes the convergence faster than others. The reason why larger numbers of neurons are not faster is due to their higher cost of computations. The λ of 1200 causes the best performance. The larger values cause overshooting, and smaller ones make slow convergence. The F_w of 3000 causes the best adaption, while the other adaptive coefficient of F_v seems to have ignorable effects. Accordingly, an AdNN having parameters reported in Table 2 is applied to solve Eq. (1).

Similarly, the primary AdNN with parameters of Table C.1 has been undertaken with the same sensitivity analysis, and the results are shown in Figure C.2.

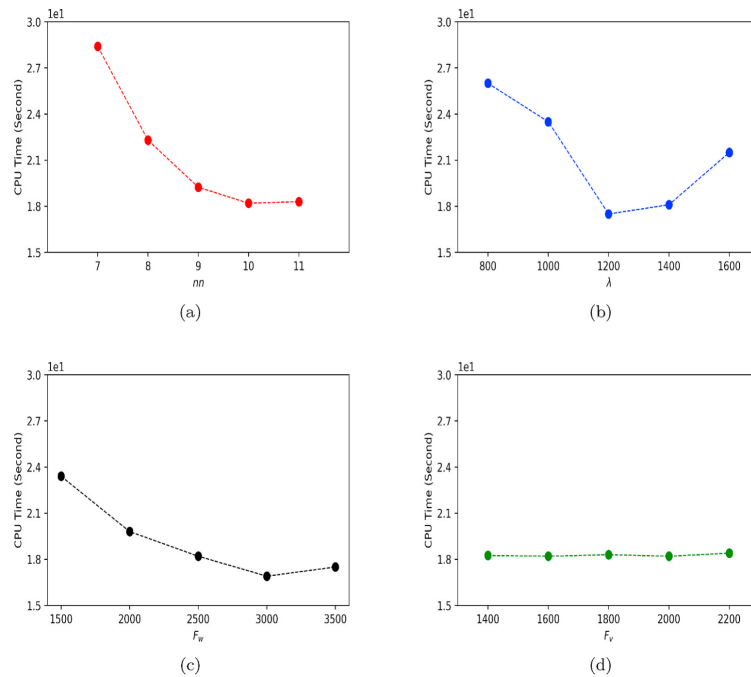


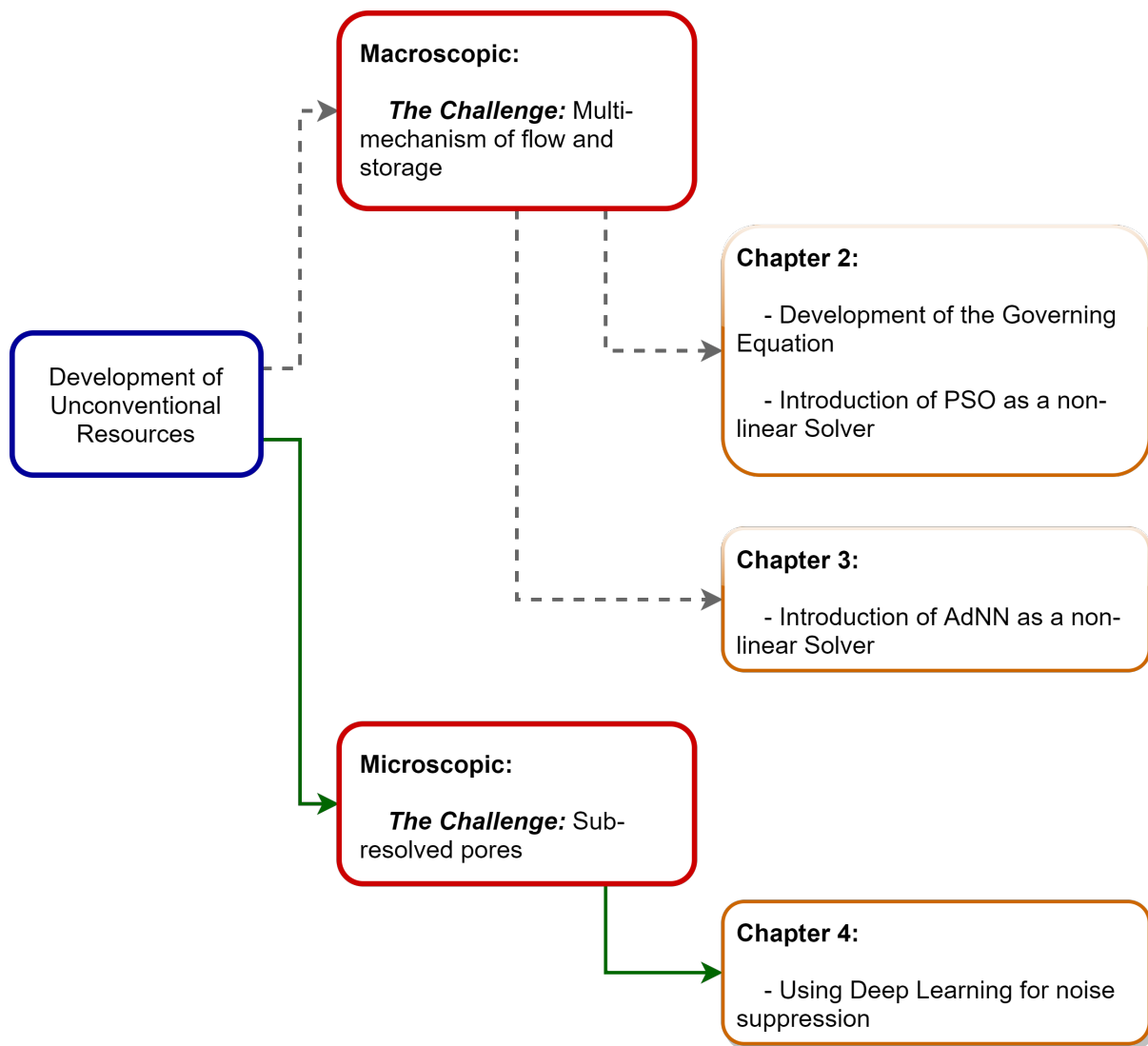
Fig. C.2. Determination of the most optimized AdNN structure to solve Eq. 2 and Eq. 3 (a) Effects of nn changes (b) Effects of λ changes (c) Effects of F_w changes (d) Effects of F_r changes.

Regarding the previous reasons discussed about the corresponding trend of each parameter, an AdNN with parameters reported in Table 4 is applied to solve Eq. (2) and Eq. (3).

References

- Abou-Kassem, J.H., Ali, S.F., Islam, M.R., 2006. Linearization of flow equations. In: Petroleum Reservoir Simulations. Elsevier, pp. 283–323. <https://doi.org/10.1016/b978-0-9765113-6-6.50014-9>.
- Ahmadi, M.A., Ebadi, M., 2014. Evolving smart approach for determination dew point pressure through condensate gas reservoirs. Fuel 117, 1074–1084. <https://doi.org/10.1016/j.fuel.2013.10.010>.
- Ahmadi, M.A., Ebadi, M., Yazdanpanah, A., 2014a. Robust intelligent tool for estimating dew point pressure in retrograded condensate gas reservoirs: application of particle swarm optimization. J. Petrol. Sci. Eng. 123, 7–19. <https://doi.org/10.1016/j.petrol.2014.05.023>.
- Ahmadi, M.A., Ebadi, M., Marghmaleki, P.S., Fouladi, M.M., 2014b. Evolving predictive model to determine condensate-to-gas ratio in retrograded condensate gas reservoirs. Fuel 124, 241–257. <https://doi.org/10.1016/j.fuel.2014.01.073>.
- Ahmed, T., 2019. Principles of waterflooding. In: Reservoir Engineering Handbook. Elsevier, pp. 901–1107. <https://doi.org/10.1016/b978-0-12-813649-2.00014-1>.
- Aljehani, A.S., Wang, Y.D., Rahman, S.S., 2018. An innovative approach to relative permeability estimation of naturally fractured carbonate rocks. J. Petrol. Sci. Eng. 162, 309–324. <https://doi.org/10.1016/j.petrol.2017.12.055>.
- Awadalla, T., Voskov, D., 2018. Modeling of gas flow in confined formations at different scales. Fuel 234, 1354–1366. <https://doi.org/10.1016/j.fuel.2018.08.008>.
- Beidokhti, R.S., Malek, A., 2009. Solving initial-boundary value problems for systems of partial differential equations using neural networks and optimization techniques. J. Franklin Inst. 346 (9), 898–913. <https://doi.org/10.1016/j.jfranklin.2009.05.003>.
- Bezyan, Y., Ebadi, M., Gerami, S., Rafati, R., Sharifi, M., Koroteev, D., 2019. A novel approach for solving nonlinear flow equations: the next step towards an accurate assessment of shale gas resources. Fuel 236, 622–635. <https://doi.org/10.1016/j.fuel.2018.08.157>.
- Bilgen, S., Sarikaya, I., 2016. New horizon in energy: shale gas. J. Nat. Gas Sci. Eng. 35, 637–645. <https://doi.org/10.1016/j.jngse.2016.09.014>.
- Boudjedir, H., 2012. Dual neural network for adaptive sliding mode control of quadrotor helicopter stabilization. International Journal of Information Sciences and Techniques 2 (4), 1–14. <https://doi.org/10.5121/ijist.2012.2401>.
- Broyden, C.G., 1965. A class of methods for solving nonlinear simultaneous equations. Math. Comput. 19 (92) <https://doi.org/10.1090/s0025-5718-1965-0198670-6>, 577–577.
- Crevacore, E., Stefano, S.D., Grillo, A., 2019. Coupling among deformation, fluid flow, structural reorganisation and fibre reorientation in fibre-reinforced, transversely isotropic biological tissues. Int. J. Non Lin. Mech. 111, 1–13. <https://doi.org/10.1016/j.ijnonlinmec.2018.08.022>.
- Darabi, H., Etehad, A., Javadpour, F., Sepehrnouri, K., 2012. Gas flow in ultra-tight shale strata. J. Fluid Mech. 710, 641–658. <https://doi.org/10.1017/jfm.2012.424>.
- Ertekin, T., Abou-Kassem, J.H., King, G.R., 2001. Basic Applied Reservoir Simulation. Society of Petroleum Engineers.
- Fernandes, B.R.B., Marcondes, F., Sepehrnouri, K., 2018. Development of a fully implicit approach with intensive variables for compositional reservoir simulation. J. Petrol. Sci. Eng. 169, 317–336. <https://doi.org/10.1016/j.petrol.2018.05.039>.
- Flashner, H., Guttalu, R., 1988. A computational approach for studying domains of attraction for non-linear systems. Int. J. Non Lin. Mech. 23 (4), 279–295. [https://doi.org/10.1016/0020-7462\(88\)90026-1](https://doi.org/10.1016/0020-7462(88)90026-1).
- He, J.-H., 2004. Comparison of homotopy perturbation method and homotopy analysis method. Appl. Math. Comput. 156 (2), 527–539. <https://doi.org/10.1016/j.amc.2003.08.008>.
- Huang, J., Jin, T., Chai, Z., Barrufet, M., Killough, J., 2020. Compositional simulation of three-phase flow in mixed-wet shale oil reservoir. Fuel 260, 116361. <https://doi.org/10.1016/j.fuel.2019.116361>.
- Incerti, S., Parisi, V., Zirilli, F., 1979. A new method for solving nonlinear simultaneous equations. SIAM J. Numer. Anal. 16 (5), 779–789. <https://doi.org/10.1137/0716057>.
- Javadpour, F., 2009. Nanopores and apparent permeability of gas flow in mudrocks (shales and siltstone). J. Can. Petrol. Technol. 48 (8), 16–21. <https://doi.org/10.2118/09-08-16-da>.
- Jayasinghe, S., Darmofal, D.L., Dow, E., Galbraith, M.C., Allmaras, S.R., 2019. A discretization-independent distributed well model. SPE J. 24 (6), 2946–2967. <https://doi.org/10.2118/198898-pa>.
- Jianguo, L., Siwei, L., Yingjian, Q., Yaping, H., 2003. Numerical solution of elliptic partial differential equation using radial basis function neural networks. Neural Network. 16 (5–6), 729–734. [https://doi.org/10.1016/s0893-6080\(03\)00083-2](https://doi.org/10.1016/s0893-6080(03)00083-2).

- Kulga, B., Artun, E., Ertekin, T., 2018. Characterization of tight-gas sand reservoirs from horizontal-well performance data using an inverse neural network. *J. Nat. Gas Sci. Eng.* 59, 35–46. <https://doi.org/10.1016/j.jngse.2018.08.017>.
- Li, G., Zeng, Z., 2008. A neural-network algorithm for solving nonlinear equation systems. In: 2008 International Conference on Computational Intelligence and Security. IEEE. <https://doi.org/10.1109/cis.2008.65>.
- Luo, Y.-Z., Tang, G.-J., Zhou, L.-N., 2008. Hybrid approach for solving systems of nonlinear equations using chaos optimization and quasi-Newton method. *Appl. Soft Comput.* 8 (2), 1068–1073. <https://doi.org/10.1016/j.asoc.2007.05.013>.
- Mall, S., Chakraverty, S., 2015. Numerical solution of nonlinear singular initial value problems of emden-fowler type using Chebyshev neural network method. *Neurocomputing* 149, 975–982. <https://doi.org/10.1016/j.neucom.2014.07.036>.
- Mall, S., Chakraverty, S., 2016. Single layer Chebyshev neural network model for solving elliptic partial differential equations. *Neural Process. Lett.* 45 (3), 825–840. <https://doi.org/10.1007/s11063-016-9551-9>.
- Mehta, D., 2011. Numerical polynomial homotopy continuation method and string vacua. *Advances in High Energy Physics* 1–15. <https://doi.org/10.1155/2011/263937>, 2011.
- Mishev, I.D., Beckner, B.L., Terekhov, S.A., Fedorova, N., 2009. Linear solver performance optimization in reservoir simulation studies. In: SPE Reservoir Simulation Symposium. Society of Petroleum Engineers. <https://doi.org/10.2118/119266-ms>.
- Naraghi, M.E., Javadpour, F., Ko, L.T., 2018. An object-based shale permeability model: non-Darcy gas flow, sorption, and surface diffusion effects. *Transport Porous Media* 125 (1), 23–39. <https://doi.org/10.1007/s11242-017-0992-z>.
- Nichita, D.V., 2018. New unconstrained minimization methods for robust flash calculations at temperature, volume and moles specifications. *Fluid Phase Equil.* 466, 31–47. <https://doi.org/10.1016/j.fluid.2018.03.012>.
- Ortega, J., Rheinboldt, W., 1970. General iterative methods. In: *Iterative Solution of Nonlinear Equations in Several Variables*. Elsevier, pp. 181–239. <https://doi.org/10.1016/b978-0-12-528550-6.50018-1>.
- Palnitkar, R., Cannady, J., 2004. A review of adaptive neural networks. In: *IEEE SoutheastCon. Proceedings.*, IEEE. <https://doi.org/10.1109/secon.2004.1287896>.
- Parisi, D.R., Mariani, M.C., Laborde, M.A., 2003. Solving differential equations with unsupervised neural networks. *Chem. Eng. Process: Process Intensification* 42 (8–9), 715–721. [https://doi.org/10.1016/s0255-2701\(02\)00207-6](https://doi.org/10.1016/s0255-2701(02)00207-6).
- Quarteroni, A., Sacco, R., Saleri, F., 2006. Rootfinding for nonlinear equations. In: *Texts in Applied Mathematics*. Springer Berlin Heidelberg, pp. 247–284. https://doi.org/10.1007/978-3-540-49809-4_6.
- Raja, M.A.Z., ul Islam Ahmad, S., 2012. Numerical treatment for solving one-dimensional bratu problem using neural networks. *Neural Comput. Appl.* 24 (3–4), 549–561. <https://doi.org/10.1007/s00521-012-1261-2>.
- Ranković, V., Savić, S., 2011. Application of feedforward neural network in the study of dissociated gas flow along the porous wall. *Expert Syst. Appl.* 38 (10), 12531–12536. <https://doi.org/10.1016/j.eswa.2011.04.039>.
- Rostami, S., Rashidi, F., Safari, H., 2019. Prediction of oil-water relative permeability in sandstone and carbonate reservoir rocks using the CSA-LSSVM algorithm. *J. Petrol. Sci. Eng.* 173, 170–186. <https://doi.org/10.1016/j.petrol.2018.09.085>.
- Rudd, K., Ferrari, S., 2015. A constrained integration (CINT) approach to solving partial differential equations using artificial neural networks. *Neurocomputing* 155, 277–285. <https://doi.org/10.1016/j.neucom.2014.11.058>.
- Shams, M., El-Banbi, A.H., Khairy, M., 2015. Capillary pressure considerations in numerical reservoir simulation studies-conclusion maps. In: SPE North Africa Technical Conference and Exhibition. Society of Petroleum Engineers. <https://doi.org/10.2118/175760-ms>.
- Sheng, G., Javadpour, F., Su, Y., 2019. Dynamic porosity and apparent permeability in porous organic matter of shale gas reservoirs. *Fuel* 251, 341–351. <https://doi.org/10.1016/j.fuel.2019.04.044>.
- Shirvany, Y., Hayati, M., Moradian, R., 2008. Numerical solution of the nonlinear schrodinger equation by feedforward neural networks. *Commun. Nonlinear Sci. Numer. Simulat.* 13 (10), 2132–2145. <https://doi.org/10.1016/j.cnsns.2007.04.024>.
- Shirvany, Y., Hayati, M., Moradian, R., 2009. Multilayer perceptron neural networks with novel unsupervised training method for numerical solution of the partial differential equations. *Appl. Soft Comput.* 9 (1), 20–29. <https://doi.org/10.1016/j.asoc.2008.02.003>.
- Spence, T., Hosters, N., Behr, M., 2020. A multi-vector interface quasi-Newton method with linear complexity for partitioned fluid-structure interaction. *Comput. Methods Appl. Mech. Eng.* 361, 112810. <https://doi.org/10.1016/j.cma.2019.112810>.
- Tsoulos, I.G., Gavrilis, D., Glavas, E., 2009. Solving differential equations with constructed neural networks. *Neurocomputing* 72 (10–12), 2385–2391. <https://doi.org/10.1016/j.neucom.2008.12.004>.
- Vaferi, B., Eslamloueyan, R., Ghaffarian, N., 2016. Hydrocarbon reservoir model detection from pressure transient data using coupled artificial neural network—wavelet transform approach. *Appl. Soft Comput.* 47, 63–75. <https://doi.org/10.1016/j.asoc.2016.05.052>.
- Voskov, D.V., Techelepi, H.A., 2012. Comparison of nonlinear formulations for two-phase multi-component EoS based simulation. *J. Petrol. Sci. Eng.* 82–83, 101–111. <https://doi.org/10.1016/j.petrol.2011.10.012>.
- Wang, M., Shi, H., 2014. An adaptive neural network prediction for nonlinear parabolic distributed parameter system based on block-wise moving window technique. *Neurocomputing* 133, 67–73. <https://doi.org/10.1016/j.neucom.2013.11.030>.
- Wang, W., Fan, D., Sheng, G., Chen, Z., Su, Y., 2019. A review of analytical and semi-analytical fluid flow models for ultra-tight hydrocarbon reservoirs. *Fuel* 256, 115737. <https://doi.org/10.1016/j.fuel.2019.115737>.
- Widrow, B., Lehr, M.A., 1993. Adaptive neural networks and their applications. *Int. J. Intell. Syst.* 8 (4), 453–507. <https://doi.org/10.1002/int.4550080403>.
- Younis, R., Techelepi, H.A., Aziz, K., 2010. Adaptively localized continuation-Newton method—nonlinear solvers that converge all the time. *SPE J.* 15 (2), 526–544. <https://doi.org/10.2118/119147-pa>.
- Yu, W., Sepehrmoori, K., Patzek, T.W., 2016. Modeling gas adsorption in marcellus shale with Langmuir and BET isotherms. *SPE J.* 21 (2), 589–600. <https://doi.org/10.2118/170801-pa>.
- S. H. Zabihifar, A. S. Yushchenko, H. Navvabi, Robust Control Based on Adaptive Neural Network for Rotary Inverted Pendulum with Oscillation Compensation, *Neural Computing and Applications*:doi:10.1007/s00521-020-04821-x.
- Zhang, Y., Li, D., Sun, X., Li, P., 2019. New theoretical model to calculate the apparent permeability of shale gas in the real state. *J. Nat. Gas Sci. Eng.* 72, 103012. <https://doi.org/10.1016/j.jngse.2019.103012>.
- Zotos, E.E., 2018. On the Newton–raphson basins of convergence of the out-of-plane equilibrium points in the copenhagen problem with oblate primaries. *Int. J. Non Lin. Mech.* 103, 93–103. <https://doi.org/10.1016/j.ijnonlinmec.2018.05.002>.



919

920

Figure 19: Chapter 4 in a glance

921 **CRedit author statement:**

922 1. **Mikhail Sidorenko:** Conceptualization, Methodology, Software, Formal
 923 Analysis, Writing – Original Draft, Visualization, Writing – Review &
 924 Editing

925 2. **Denis Orlov:** Conceptualization, Methodology, Validation, Formal
 926 Analysis, Resources, Supervision, Writing – Review & Editing

- 927 3. **Mohammad Ebadi:** Conceptualization, Methodology, Resources, Data
928 Curation, Writing – Original Draft, Writing – Review & Editing
929 4. **Dmitry Koroteev:** Conceptualization, Writing – Review & Editing,
930 Supervision, Project Administration



Deep learning in denoising of micro-computed tomography images of rock samples

Mikhail Sidorenko^{a,*}, Denis Orlov^{a,b,2}, Mohammad Ebadi^{a,3}, Dmitry Koroteev^{a,b,4}

^a Skolkovo Institute of Science and Technology, Moscow, Russia

^b Digital Petroleum LLC, Moscow, Russia

ARTICLE INFO

Keywords:

Deep learning
Computed tomography
Image enhancement

ABSTRACT

Nowadays, the advantages of Digital Rock Physics (DRP) are well known and widely applied in comprehensive core analysis. It is also known that the quality of the 3D pore scale model drastically influences the results of rock properties simulation, which makes the preprocessing stage of DRP very important. In this work, we consider the application of Deep Convolutional Neural Networks (CNNs) for the preprocessing of CT images, specifically for denoising, in two setups - conventional fully-supervised learning and the self-supervised learning, when the only available data is the noisy images. To train CNNs in a supervised setup, we use images processed by a combination of bilateral and bandpass filters. We trained CNNs of the same architecture with different loss functions to find out how the choice of a loss function influences the model's performance. Some of the obtained CNNs yielded the highest quality in terms of full-reference and no-reference metrics and significant histogram effect (bimodal intensity distribution). Images denoised with these models were qualitatively and quantitatively better than the reference "ground truth" images used for training. We use the Deep Image Prior algorithm to train denoising models in a self-supervised setup. The obtained models are much better than ones obtained in fully-supervised setup, but are too slow, as they are optimization-based rather than feed-forward. Such an algorithm can be used in the dataset generation for feed-forward meta-models. These results could help to develop an AI-based instrument to build high-quality 3D segmented models of rocks for DRP applications.

1. Introduction

Digital Rock Physics (DRP) is a widespread and advanced method for hydrocarbon reservoirs study. The main idea of DRP is to replace conventional methods of a rock properties estimation with computations on a digital rock core twin obtained with micro-scale X-ray Computed Tomography (μ XCT). DRP can significantly reduce the time required for obtaining properties of interest and avoid the degradation of a core sample after a series of laboratory experiments. Another advantage of the DRP is that it enables the reproduction of some conditions in a rock sample, which are difficult or impossible to create in a conventional laboratory setting.

The workflow of DRP can be divided into three stages: acquiring images of a rock core sample using micro-computed CT, preprocessing

the obtained stack of CT images, and simulation of physical processes in rock. Since CT images usually possess noise and some artifacts, preprocessing of a 3D image must include image enhancement stage (denoising, artifacts removal, brightness correction) followed by segmentation. Segmented images are then fed into some simulator, which numerically solves the system of differential equations. It was shown that the quality of segmented images has a strong influence on the simulation results, which makes the preprocessing stage very important (Andrä et al., 2013).

The comparison of the influence upon segmentation results among the original image, the denoised images by DIP approach and the CNN-based method with different losses, and the results by the classical methods (bilateral filter) presented in Fig. 1. The total porosity (φ) of binary images varies from 11 % to 38 % and point that image quality

* Corresponding author.

E-mail address: Mikhail.Sidorenko@skoltech.ru (M. Sidorenko).

¹ ideas and their implementation, design of experiments, data analysis, drafting.

² ideas, data description, design of experiments, drafting.

³ ideas, data acquisition, data description, drafting.

⁴ academic advisor, ideas, design of experiments, drafting.

<https://doi.org/10.1016/j.cageo.2021.104716>

Received 18 March 2020; Received in revised form 21 September 2020; Accepted 11 February 2021

Available online 2 March 2021

0098-3004/© 2021 Elsevier Ltd. All rights reserved.

enhancement is vital to build an adequate model of a rock.

All activities in 3D model creation could be divided into two pipelines. The first pipeline is dedicated to preprocessing original images for noise and artefact removing. The reason is the better quality of images – the better results of binarization and probably segmentation. Many algorithms have been developed and tested for this purpose (Buades et al., 2005). Opportunities for deep learning (DL) algorithms for denoising and image enhancement are promising. There are some publications about image super-resolution problem (Wang et al., 2019; Da Wang et al., 2019; Chen et al., 2020). Both Image denoising and Image super-resolution are subproblems of the general problem – image enhancement. In this work we concentrated mostly on the image denoising. The second pipeline is more focused on direct segmentation of original images without any preprocessing. It is known (Ronneberger et al., 2015; Long et al., 2015; Karimpouli and Tahmasebi, 2019; Garcia-Garcia et al., 2017), that end-to-end solutions can provide better results and use of deep learning (DL) algorithms for segmentation of noisy images seems to be a good way to go too.

Applying DL in both pipelines requires too much training data, i.e., pairs of images and their corresponding masks (denoised or segmented). The creation of a dataset, including CT images of a rock core sample, may be very time-consuming and, it would take several independent experts from the field to get masks of high quality. So the point is to find out how to prepare these datasets for DL algorithms training in automatic or semiautomatic ways. For image preprocessing, perspectives are

much better because of the existence of non-reference metrics, which characterize stand alone image. For segmentation, it is challenging to prepare dataset without expert help. In this work, we focused on the first pipeline for 3D model creation because of high opportunities for automation. The main goal was to investigate the applicability of DL algorithms to make a high quality easy in use denoising instrument for reservoir engineers.

Image enhancement problems have been attracting considerable interest in the computer vision research community for several decades (Tikhonov and Arsenin, 1977; Yang et al., 1996; Tomasi and Manduchi, 1998; Dabov et al., 2007; Buades et al., 2011). After the CNNs were shown to have an excellent performance in image recognition tasks (Krizhevsky et al., 2012), there were many works related to their application to image enhancement problems (Zhang et al., 2017, 2018; Zhao et al., 2015; Mao et al., 2016; Yang et al., 2017a). Having a dataset including pairs of degraded and clean images is a must for the training of CNNs. In many works, the authors generate the datasets from clean images by adding some degradation in it. But there are some cases when only degraded images are available, and the creation of the dataset for a CNN becomes a problem. For example, due to the physical limitations of computed tomography, obtaining a high-resolution CT image of a rock core sample without noise and artifacts is getting too complicated.

Recently, there were proposed image enhancement methods (Ulyanov et al., 2018; Lehtinen et al., 2018; Laine et al., 2019) that do not require clean images at all. The performance of these methods is at least

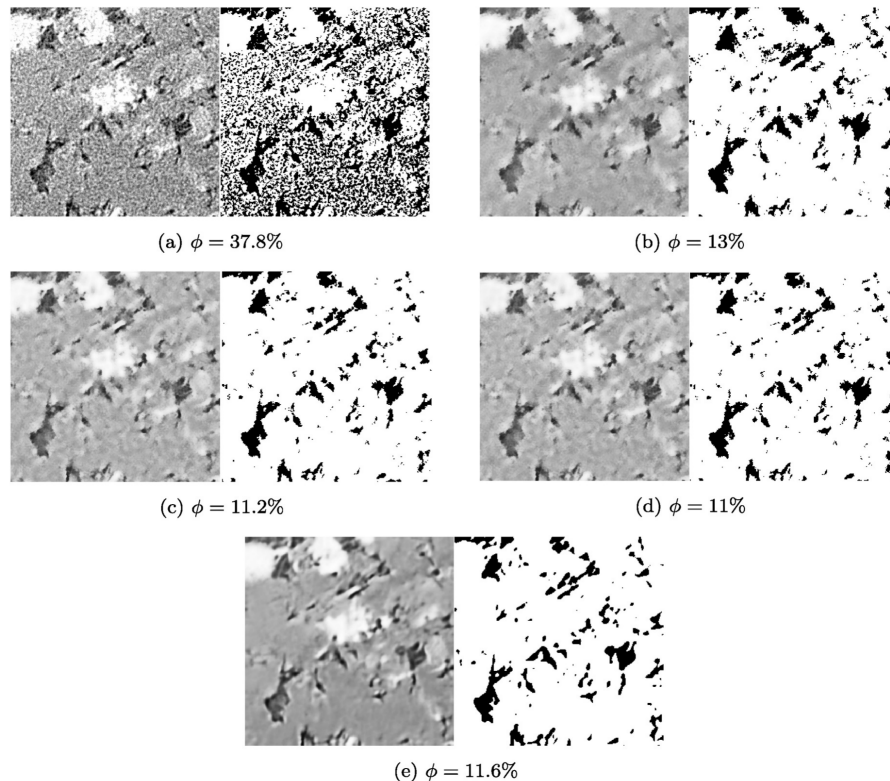


Fig. 1. Results of OTSU binarization (Otsu, 1979) for a slice from the test set. (a) - original image with noise, (b) - reference image. Images enhanced with different models: (c) - RED-Net with SSIM loss, (d) - RED-Net with Perceptual loss (VGG1_1), (e) - Deep Image Prior algorithm.

good as the state of the art CNNs trained on large datasets. But, all of these self-supervised methods assuming that we need to apply optimization procedure for each image independently and, thus, are too slow. But, when clean data is difficult to obtain, as in our case, these can be the methods of choice.

Another option is to create a dataset by creating reference (clean) images, using some self-supervised denoising methods. But the question arises: will the performance of a CNN trained in this setting be better than of the algorithm used for reference images generation? In this work, we show that in this setting, it is possible to train a CNN, which yields the results of higher quality compared to the reference images, by choosing appropriate loss function.

The following paper is organized as follow. In section 2, we describe the process of dataset collection, which was used in our experiments. In section 3, the architecture of denoising CNNs, training setup, validation scheme, and quality metrics are described. The discussion of the obtained results is provided in section 4.

2. Dataset

A modern General Electric v|tomex L240 CT system, which allows performing precise investigations of porous media structures on small samples, has been used to project different samples of Achimovka formation. The system is equipped with 2 X-ray sources (240 kV microfocus tube and 180 kV high-power nano focus tube) and handles large samples up to 500 × 800 mm and 50 kg. As a tight sandstone formation located in the Western Siberia of Russia, core samples from Achimovka with the porosity in the range of 13–15% and absolute permeability of 0.3–0.5 md have been selected for further projection and generation of the μxCT images. The projection of the supposed samples with a diameter of 8 mm has been made with the technical features reported in Table 1. Next, the acquired stack of CT images with the resolution of 1.2 μm/voxel was centrally cropped to the region of interest (ROI), forming the target cubes with the final size of 1400³ voxels (Fig. 2).

For training a NN in a supervised learning framework, each object in the training dataset must have corresponding general truth answer (label). In the case of the image enhancement problem, and mainly, image denoising, the object is an original image with noise, and the answer is its denoised version. Accordingly, all slices of the formed cubes were firstly normalized and then applied with a combination of various filters. For increasing the quality of images and suppressing the adverse effects of artifacts, roundoff errors, and various types of noises, all images were sequentially applied with a bandpass filter as a transform domain (Yang et al., 2017b), and then with a bilateral filter as a spatial operator (Landis and Keane, 2010). According to the Python programming, the packages of Numpy, OpenCV, scikit-image, trackpy, and scipy have been used to read the images, change their datatype, normalize them, suppress the noises, and eventually write the clean images. The reconstructed original and filtered images are available online (Ebadi, 2020). An example of a training pair is presented in Fig. 3.

Table 1
Technical configuration of the scanning system.

Item	Value	Unit
High Voltage	60	kV
Tube Current	90	μA
Beam exit window, material	Beryllium	–
Averaging (Number of projections)	8	–
Timing (Exposure)	2000	ms
Total number of projections	2400	–
Spatial Resolution	1.2	μm
Duration of scanning	14.5	Hours

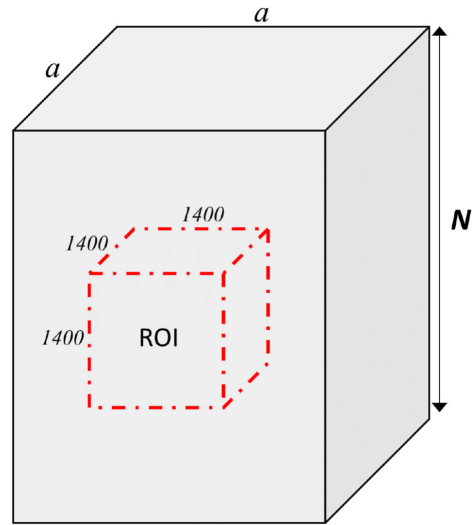


Fig. 2. Stack of N CT images having a × a voxels. After the central cropping, the final cube has 1400³ voxels.

3. Methodology

3.1. Supervised image denoising

For a supervised image denoising problem, we used the Residual Encoder-Decoder network (RED-Net) (Mao et al., 2016). This network can be presented as stacked convolutional layers (encoder) followed by deconvolutional layers (decoder). The network is trained in the residual learning framework. For this purpose, the authors introduced symmetric skip-connections between the corresponding convolutional and deconvolutional layers in the network (Fig. 4). This modification tackles vanishing gradients problem and, therefore, speeds up training, and also makes it possible to use information from the down layers in the up layers, preserving fine details in the image.

Another specific of this architecture is that it preserves spatial sizes of all feature maps (i.e., there are no downsampling/upsampling layers in the network). It was done to preserve fine image details while eliminating low-level corruption. The main drawback of this strategy is the enormous sizes of produced feature maps, which results in low inference speed and high GPU memory consumption during training/inference. As already proposed, the inference of this network can be accelerated by downsampling feature maps after some layer (Mao et al., 2016).

All convolutional and deconvolutional layers have 64 kernels of size 3 × 3 with padding 1 and are followed by ReLU activation layer. We also added a batch normalization layer before each activation to speed up convergence and introduce regularization (Ioffe and Szegedy, 2015).

3.2. Self-supervised image denoising

As the ground truth images corresponding to the noisy CT slices are difficult to obtain, it is natural to use self-supervised denoising algorithms that require only noisy data. As such, in this work, we considered Deep Image Prior (DIP) denoising algorithm proposed in (Ulyanov et al., 2018).

Let \hat{y} is a noisy image and y is the corresponding ground truth, then the image denoising problem is equivalent to the maximization of a posterior probability:

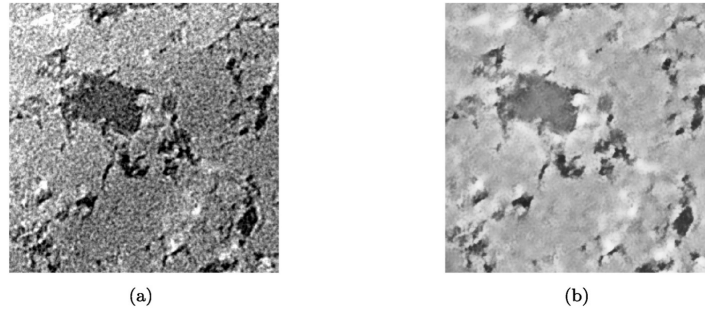


Fig. 3. Example of images from the dataset. (a) – Source (noisy) image, (b) – Target (denoised) image.

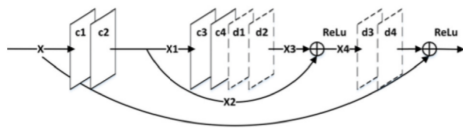


Fig. 4. Example of the RED-net architecture [(Mao et al., 2016)].

$$y^* = \underset{y}{\operatorname{argmax}} p(y|\hat{y}) = \underset{y}{\operatorname{argmax}} p(\hat{y}|y)p(y) \tag{1}$$

where $p(\hat{y}|y)$ is the conditional probability density function (pdf) of a noisy image \hat{y} given a corresponding clean image y and $p(y)$ is the pdf of a clean image. Intuitively, $p(\hat{y}|y)$ contains some information about the noise model and also called a likelihood, and $p(y)$ conveys some prior knowledge of how clean image might look like and called a prior.

The maximization problem above is usually expressed as the corresponding minimization problem:

$$\begin{aligned} y^* &= \underset{y}{\operatorname{argmax}} p(y|\hat{y}) \\ &= \underset{y}{\operatorname{argmax}} p(\hat{y}|y)p(y) \\ &= \underset{y}{\operatorname{argmin}} -\log p(\hat{y}|y) - \log p(y) \\ &= \underset{y}{\operatorname{argmin}} E(y, \hat{y}) + R(y) \end{aligned} \tag{2}$$

The main ideas of (Ulyanov et al., 2018) are the following:

- optimization over the parameter space of some bijective parametric function $f : \theta \rightarrow y$ makes the optimization problem unconstrained; as a parametric function they proposed to use a CNN with some fixed input z , trained for a given noisy image
- there is no need in the explicit prior $R(y)$ as the architecture of the learnable function f already contains necessary prior information

Finally, the optimization problem is:

$$\theta^* = \underset{\theta}{\operatorname{argmin}} E(f_{\theta}(z), \hat{y}), y^* = f_{\theta^*}(z) \tag{3}$$

with the mean squared error as the target function $E(f_{\theta}(z), \hat{y}) = \|f_{\theta}(z) - \hat{y}\|_2^2$.

It was also shown, that during training a CNN in this setting learns some structured patterns rather than noise, but after thousands of training iterations, the CNN learns the noise and the target function $E(f_{\theta}(z), \hat{y})$ is minimized to the optimal solution $f_{\theta^*}(z) = \hat{y}$, which is wrong. “Early stopping” criteria (Bishop, 2007) should be applied to avoid such a solution. During the training, the model is evaluated on a holdout validation dataset after each epoch. If the performance of the

model on the validation dataset starts to degrade (e.g. loss begins to increase or accuracy begins to decrease), then the training process is stopped.

3.3. Training setup

All models have been implemented and trained in the PyTorch framework (Paszke et al., 2017). For a supervised denoising model, we have empirically estimated that the faster training converges to a better local minimum when using Adam optimizer (Kingma and BaAdam, 2014) instead of conventional Stochastic Gradient Descent (SGD). The initial learning rate was set to 10^{-3} . We also used the learning rate scheduling - when the loss on the validation set does not decrease, the learning rate reduced by a factor of 10 until it reaches value 10^{-5} . We did not use weight decay regularization as the model did not overfit much. As a stop criteria we used “Early stopping” criteria (Bishop, 2007).

Due to the specific architecture of the RED-Net (no downsampling/upsampling layers), the feature maps of the hidden layers were extensive, and if we trained the network on images of the full size (1400×1400), it would not fit in GPU memory. That is why we trained NN on random crops of the input images. We have analyzed how different crop sizes affect a model’s performance: $128 \times 128, 256 \times 256, 512 \times 512$. It should be mentioned that with increasing the size of a crop CNN converges faster and find a better local minimum, but for training GPU with a lot of RAM is required. With increasing the size of a crop, it was also necessary to decrease a mini-batch size to fit in memory. Error curves comparison for different crop size could be found in Fig. 5a and b. Anyone can see that the increasing the size of the crop didn’t improve the performance significantly, thus, we could train the CNN on small crops to fit in GPU limitations without significant performance degradation.

The DIP model was trained with standard architecture proposed in (Ulyanov et al., 2018). The learning rate was tuned to obtain the best result in a minimal number of training iterations. We experimented on several slices with the DIP algorithm and chose the number of iterations such that the result looks plausible. Adam optimizer was also used in this case. Image crops of size 256×256 were used during training. In Fig. 5c the corresponding error curve for DIP is presented.

In this work, we’ve trained a RED-Net with different loss functions. Error curves comparison for different losses and the same crop size 128×128 presented in Fig. 5d. We trained CNNs on NVIDIA GPU Tesla V100. For RED-Net it took about 12 h to converge. The DIP algorithm usually converged to the plausible result in 1–2 min. The similar work was done in (Zhao et al., 2015) and (Yang et al., 2017a), and their ideas may be interesting to apply to denoising of CT images of rock cores. We believe that a NN trained with appropriate loss function may yield results with quality even better than the corresponding reference.

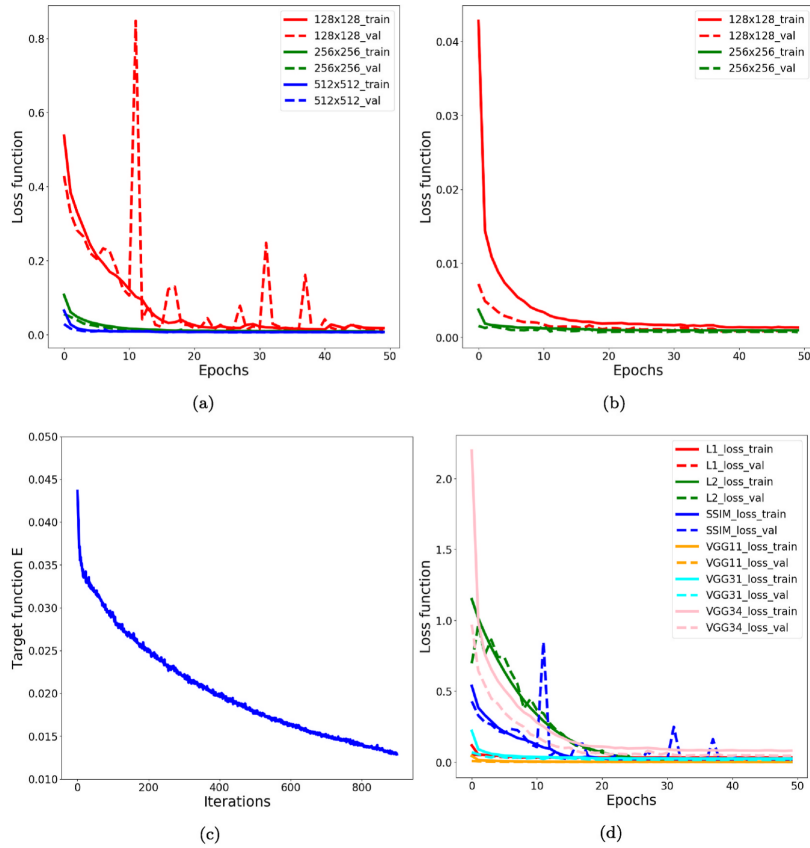


Fig. 5. Error curves. (a) - RED-Net with SSIM loss and different crop sizes, (b) - RED-Net with Perceptual loss (VGG1_1) and different crop sizes, (c) - Deep Image Prior algorithm, (d) - Error curves comparison for different losses and the same crop size 128 × 128.

3.3.1. *L1* Loss

L1 loss function (aka Mean Average Error) maps an object-reference pair to a positive real number:

$$\mathcal{L}(I, \hat{I}) = \frac{1}{nm} \sum_i^n \sum_j^m |I_{ij} - \hat{I}_{ij}| \tag{4}$$

3.3.2. *L2* Loss

L2 loss function has become a loss function of choice for neural networks used in image enhancement problems:

$$\mathcal{L}(I, \hat{I}) = \frac{1}{nm} \sum_i^n \sum_j^m (I_{ij} - \hat{I}_{ij})^2 \tag{5}$$

Its popularity may be explained by the fact that it's a differentiable function, and it's implemented in many deep learning frameworks by default. Another attractive property of *L2* loss is that the minimization of it provides a maximum likelihood estimate in the case of independent and identically distributed Gaussian noise (Zhao et al., 2015). It is beneficial in cases when the noise is i.i.d. Gaussian, but it is not the case for the rock core CT scans because the noise in some patch of CT scan highly depends on the rock properties in this patch and, therefore,

depends on a particular position. Another drawback of *L2* loss, as was stated in (Zhao et al., 2015), is that it introduces splotchy artifacts on a processed image. Moreover, this loss does not correlate well with human perception of image quality.

3.3.3. *SSIM* loss

Structural similarity index (SSIM), which was proposed in (Wang et al., 2004) as a metric of image quality that in contrast to PSNR metric (and *L2* loss) inspired by the human visual system and, therefore, correlate with human's perception of image quality better. For a given pair of images, SSIM is computed patch-wise, using the following formula:

$$SSIM(p, \hat{p}) = \frac{(2\mu_p \mu_{\hat{p}} + c_1)(2\sigma_{p\hat{p}} + c_2)}{(\mu_p^2 + \mu_{\hat{p}}^2 + c_1)(\sigma_p^2 + \sigma_{\hat{p}}^2 + c_2)}, \tag{6}$$

where $\mu_p, \mu_{\hat{p}}$ are the averages, $\sigma_p^2, \sigma_{\hat{p}}^2$ are the variances, $\sigma_{p\hat{p}}$ is the covariance of patches of the reference and predicted images correspondingly, c_1 and c_2 are constants included to avoid instability when dividing by values close to zero. After the SSIM was computed for each possible patch with sliding Gaussian window of size 11 × 11 (as in

(Wang et al., 2004)), the SSIM of a pair of images is computed as the average of the SSIMs of patches:

$$\mathcal{L}(I, \hat{I}) = \frac{1}{n} \sum_i SSIM(p_i, \hat{p}_i) \tag{7}$$

The SSIM loss can be computed using 2D convolutions and element-wise matrix multiplications, and, therefore, is a differentiable function. In (Zhao et al., 2015), they used SSIM loss to train NNs, but they used a simplified version of it to speed up computations. We tried both variants of this loss function but got decent results only when using the full version.

3.3.4. Perceptual loss

In (Yang et al., 2017a), instead of computing L_2 loss between a processed with NN image and its corresponding ground truth, they proposed to compute L_2 loss between their projections in high-dimensional feature space. This is achieved with a deep CNN (VGG-19) pertained on the ImageNet dataset, which acts only as a feature extractor. During the training, the weights of the feature extractor are not changed.

After the feature maps were obtained, the loss is computed as the MSE between feature maps of processed image and the reference one:

$$\mathcal{L}(I, \hat{I}) = \frac{1}{nmc} \sum_i \sum_j \sum_k \left(F_{ijk} - \hat{F}_{ijk} \right)^2 \tag{8}$$

As in (Yang et al., 2017a), we have tried to compute perceptual loss between feature maps generated by the first ReLU layer in the first block (VGG1_1), the first and the fourth ReLU layers in the third block (VGG3_1, VGG3_4) as shown in Fig. 6.

Also, we have tried to train the NN with the perceptual loss function from scratch, and with weights initialized from the same NN trained with L_2 loss, but the decent results were obtained only in the second case.

3.4. Validation scheme

It's a common practice in machine learning to train a model on one part of data, called the training set, and estimate its performance on another one (validation set) (Goodfellow et al., 2016) to get an unbiased estimation of a model's generalization error and detect overfitting. One uses the estimation of a model's performance on a validation set to select the hyperparameters of a learning algorithm. It usually results in overfitting of hyperparameters to a validation set after several iterations of model selection. Thus, it is recommended to use another holdout dataset (test set) to get the final estimation of a model's performance.

In this work, we have used a CT scan of one rock sample for training and validation, and CT scan of another rock sample for testing trained RED-Net models. We have split the training data into train and validation sets in the following way: the first 1260 slices of $1400 \times 1400 \times 1400$ CT scan were used for training, and all the remain slices for validation.

Such validation scheme is more robust than, for instance, randomly chosen subsets because the subsequent slices are very similar, and if a model was trained on ten subsequent slices, except one of them, it would show excellent performance on this slice but give a very poor approximation of generalization error. Even though models were trained on image crops, they were validated on the full-size images because the final model is supposed to process the full-size images. This was possible because of fully-convolutional type of trained CNNs.

For the DIP algorithm, we used these train and validation sets for hyperparameters tuning and the test set for the final evaluation of the obtained model.

3.5. Quality metrics

The algorithms for the image enhancement problem are evaluated with image quality assessment (IQA) metrics, that can be full-reference (FR) (Wang et al., 2003, 2004), or no-reference (NR) (Zhu and Milanfar, 2010; Kong et al., 2013). The former compares the images, obtained from an enhancement model, with the corresponding reference images without any degradation in it, which are assumed to be the ground truth. There are several settings where only degraded images are available, and the acquisition/creation of the corresponding reference images of high quality may be too expensive or even impossible. As a solution, no-reference metrics can be used in such cases. To evaluate the quality of trained models in this work, we have used both FR and NR IQA techniques. The reference images for FR metrics were obtained, as described in Section 2.

The most straightforward FR metric is the Peak Signal-to-Noise ratio (PSNR), which was used in many works related to image enhancement problems (Ulyanov et al., 2018; Zhang et al., 2017, 2018). This metric is related to the pixel-wise Mean Squared Error (MSE) through the following formula:

$$PSNR(I, \hat{I}) = 20 \log_{10} \frac{1}{MSE(I, \hat{I})}, \tag{9}$$

where I and \hat{I} are the reference and predicted images, respectively, with pixels' values in the range $[0, 1]$.

In (Wang et al., 2003; Zhao et al., 2015), it was shown that PSNR does not correlate well with human's perception of image quality. For example, if we compute PSNR of an image and its copy shifted by one pixel, we get low PSNR, even though the two images are approximately the same. It means that PSNR is a low-level metric, and it does not take into account high-level information of an image. To tackle the problem, we also used another FR metric - structural similarity index (SSIM) (Wang et al., 2004) to evaluate the performance of trained models.

As a simple NR IQA metric, signal-to-noise ratio (SNR) was used. Mathematically, SNR is the ratio between the mean and standard deviation of intensity values in a patch of an image:

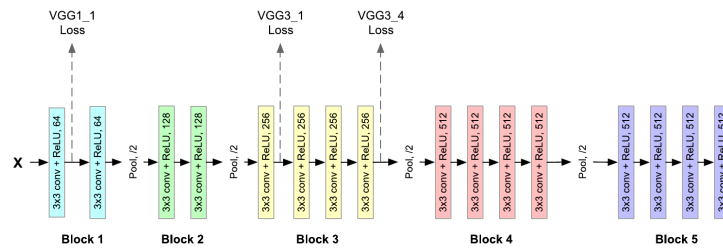


Fig. 6. Perceptual loss computation with pretrained VGG-19 network.

$$SNR(I_i) = \frac{\mu_i}{\sigma_i} \tag{10}$$

where I_i is the i -th sliding window and μ_i and σ_i are the mean and standard deviation of pixels from this window correspondingly. The overall SNR is the average across all SNRs for sliding windows.

A more comprehensive NR metric was proposed in (Kong et al., 2013). Given a noisy image I and the same image enhanced with denoising NN \hat{I} , the removed noise can be estimated as the difference between them $M = I - \hat{I}$. Then two structural similarity maps $N = SSIM(I, M)$, $P = SSIM(I, \hat{I})$ are computed with the same procedure as for estimating the SSIM between two images. As opposed to the stated in 3.2, SSIM, in this case, is based only on the structure comparison term, assuming that the luminance and contrast are preserved by the denoising algorithm. Each element of N reflects how much noise was removed from the corresponding homogeneous region, and each element of P shows the structure preservation in the corresponding high structured region. In our case, the size of the region where we calculate N and P was 7×7 pixels.

For illustration consider some homogenous region in the noisy image. Suppose that we managed to remove the noise as much as possible from this region. Then structurally the removed noise (M) will be nearly the same as the noisy image in this region, and, therefore, similarity (N) between them will be high. On the other hand, if the denoising algorithm fails, the structure should be dissimilar. Another situation will be for P value, which is computed from the input noisy image I and the denoised image \hat{I} , when we remove almost all the noise in the homogenous region. In this case, I and \hat{I} images will be totally different, and P value will be deficient. Now let us consider highly textured regions. If the denoising algorithm good enough to preserve the image structure (meaningful information) the similarity between I and \hat{I} will be high and the value of P will also be high. However, the value of N will be low because the I and M are enormously different in this case. I will include information about the highly textured structure and M - about homogenous noise mask.

A good denoising algorithm should maintain the right balance and satisfy both conditions (for homogenous and highly textured regions). In regions with large N values (i.e., homogeneous regions that are not dominated by image structures), the other term P should be as small as possible, and vice versa. Considering those terms as two random

variables, a natural choice for modelling such observation is the correlation coefficient, which computes the dependency relation between them. In our work we used a module of Pearson's correlation coefficient between N and P , which can be used as the quality Kong metric.

The final goal of the CT-image denoising is to obtain an image, which can be segmented with good quality using some fast and simple segmentation algorithms like (Otsu, 1979). The success of such algorithms for an image depends on the separability of the image histogram modes. Thus, as another criteria of the image quality, the number of modalities in the image histogram was used. The enhanced images were also evaluated visually by experts in image processing and micro geology.

4. Results and discussions

In this section, we provide the results obtained from our experiments. In Fig. 7 the results of image denoising with RED-Net architecture CNNs trained with different loss functions, are presented. From the figure, it can be seen that images denoised with CNNs (c - h) are better in comparison with our reference images according to applied non-reference quality metrics.

To verify this quantitatively, the metrics from 3.4 are calculated for all models, see Table 2 and Table 3. All models were evaluated on images from the test set, and the mean and standard deviation of a particular metric are provided in the tables. From Table 2 it can be seen that in terms of PSNR, the best models are the ones trained with per-pixel loss functions L_1 and L_2 . The rest of the models have low PSNRs, but high

Table 2
Full-reference metrics for trained models (mean and standard deviation are calculated for samples from the test set).

	Source	GT	L_1	L_2
PSNR	17.031 ± 0.712	∞	28.119 ± 0.891	27.819 ± 0.899
SSIM	0.553 ± 0.005	1.000	0.952 ± 0.002	0.951 ± 0.001
	SSIM	VGG1_1	VGG3_1	VGG3_4
PSNR	26.287 ± 0.832	24.718 ± 0.607	22.205 ± 1.253	21.777 ± 1.278
SSIM	0.966 ± 0.001	0.965 ± 0.001	0.961 ± 0.002	0.961 ± 0.003

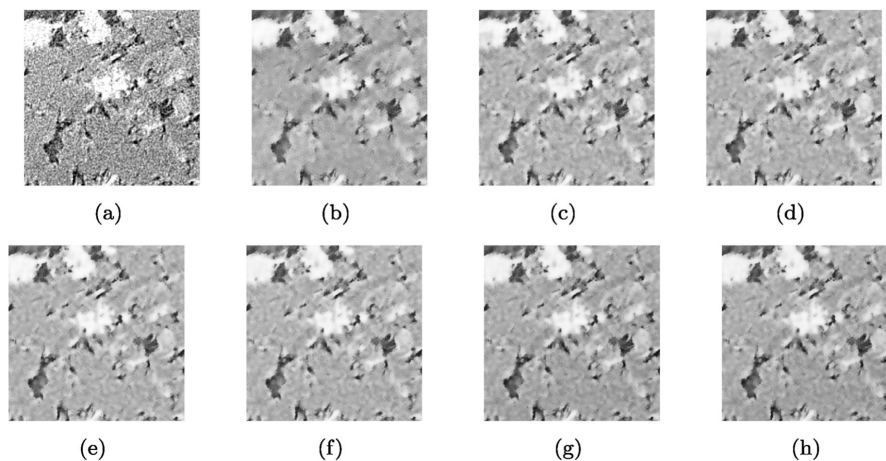


Fig. 7. Results of denoising for a slice from the test set. (a) - original image, (b) - reference image. Images enhanced with different models: (c) - L_1 loss, (d) - L_2 loss, (e) - SSIM loss, (f) - Perceptual loss (VGG1_1), (g) - Perceptual loss (VGG3_1), (h) - Perceptual loss (VGG3_4).

Table 3
No-reference metrics for trained models (mean and standard deviation are calculated for samples from the test set).

	Source	GT	L ₁	L ₂
SNR	0.108 ± 0.004	0.558 ± 0.025	0.493 ± 0.032	0.528 ± 0.034
Kong (Kong et al., 2013)	–	0.892 ± 0.012	0.898 ± 0.012	0.888 ± 0.013
	SSIM	VGG1_1	VGG3_1	VGG3_4
SNR	0.582 ± 0.040	0.590 ± 0.042	0.546 ± 0.039	0.576 ± 0.039
Kong (Kong et al., 2013)	0.893 ± 0.013	0.889 ± 0.013	0.891 ± 0.014	0.889 ± 0.014

SSIM, as the corresponding losses impose structure preservation. In our research we found that all VGG-based losses show a nearly equally CNN performance, but all of them outperform L1 and L2-based losses. The reason for that — such losses penalize differences between image high-level features (multipixel structures) rather than between low-level features (pixels) and thus they take into account some content information.

As another measure of model quality, we used the number of modes in the image histogram (Fig. 8). Histogram of the source image has only one explicit mode, and thus it may be challenging to set a threshold that separates all pixels in pores and matrix. The same is true for the ground truth image, but in this case, the distribution is narrower. It should be noticed that the histograms of the results from models, which incorporate some structure preservation, have two explicit modes - for matrix and for minerals, but there is still no peak, corresponding to the pores.

NR metrics from Table 3 show that images obtained from some of the trained CNNs have a better quality compared to the reference image (GT). In terms of SNR metric, the best models are those trained with loss functions that penalize for changes in the structure of an image (i.e., SSIM, VGG1_1, VGG3_1 and VGG3_4 losses).

Taking into account all metrics (FR and NR) and histogram shapes, we can state that the best models for supervised image denoising are CNNs with SSIM and VGG1_1 losses. It means that the loss functions which incorporate the preservation of the structure in an image make the CNN find a better local optimum while training.

The result of denoising with the DIP algorithm is presented in Fig. 9. Qualitatively, the obtained result is much better than the corresponding ground truth image used in supervised image denoising. The result was evaluated using NR metrics (Table 4), and it can be seen that the DIP algorithm yields the best result in terms of metrics. The histogram of the DIP result Fig. 9c has three explicit modes and shows the superiority of this algorithm, among others.

As a micro-CT data is a 3D composition of different azimuthal x-ray acquisition and sometimes rocks have anisotropic stratification, it was important to look at different slices of the volume (Fig. 10). Everyone can see that denoising quality remain very high.

Time comparison of the classical method (bilateral filter), DIP algorithm and CNN-based methods has been made for the image with size 256 × 256 voxels. As mentioned in section 3.3 the training time for RED-Net models was approximately 12 h and then trained model denoised the image less than 1 s. DIP algorithm performance to treat an image is 3–4 min. The bilateral filter works near 1 s but to apply it user need to spend time to find proper parameters. Thus, the DIP algorithm shows the best results in a quality of denoising but the worst results in terms of time consumption. Otherwise, the bilateral filter is much faster than DIP and even CNN, but very human dependent and in general proceed the image, not in the best way.

The main benefit of 3D CNNs is that it takes into account all three spatial dimensions (as the source data is 3D) and it seems that such a network will outperform the 2D counterpart. However, according to the recent work on segmentation ((Varfolomeev et al., 2019)), their 3D network only slightly outperforms 2D counterpart, while the training of 3D network requires more computational resource and time.

5. Conclusions

New image filters (AI-filters) have been developed based on the Residual Encoder-Decoder network (RED-Net) architecture and Deep Image Prior (DIP) algorithm. A specific feature of RED-Net architecture is that the filter preserves fine image details while processing noise and low-level corruption. To train AI-filters in a supervised setting, we used images processed by a combination of bilateral and bandpass filters. For spatial domain filtering, the bilateral filter is one of the most effective non-linear instruments to increase the signal-to-noise ratio and preserve the edges. We also applied the bandpass frequency filter to remove

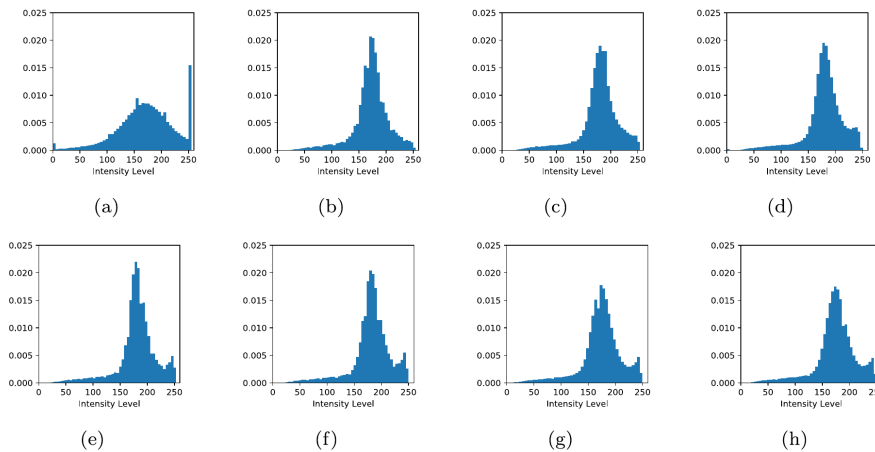


Fig. 8. Histograms of original and enhanced images from the test set. (a) - original image, (b) - reference image. Images enhanced with trained models: (c) - L₁ loss, (d) - L₂ loss, (e) - SSIM loss, (f) - Perceptual loss (VGG1_1), (g) - Perceptual loss (VGG3_1), (h) - Perceptual loss (VGG3_4).

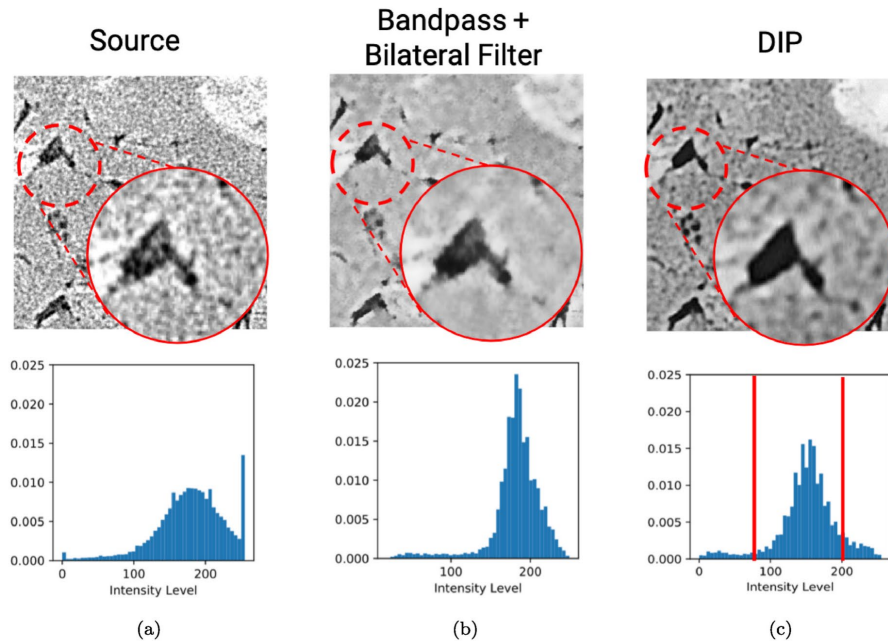


Fig. 9. Results of denoising (images and intensity distribution histograms) for a slice from the test set. (a) - original image, (b) - reference image, (c) - image denoised with the Deep Image Prior algorithm.

Table 4
No-reference metrics for Deep Image Prior algorithm (mean and standard deviation are calculated for samples from the test set).

	Source	GT	DIP
SNR	0.108 ± 0.004	0.558 ± 0.025	0.751 ± 0.057
Kong (Kong et al., 2013)	-	0.892 ± 0.012	0.936 ± 0.022

background variation (large-scale image artifacts).

The main practical advantage of AI-filter is the automatization of image processing. Applying CNN-based filters, the operator doesn't need to tune parameters or deciding on which type of filter or a combination of filters should be used for particular image processing. To build the best automated filter, different CNNs of the same architecture trained with different loss functions were tested. For CNNs comparison, we've used not only the full-reference (FR) metrics, which makes CNN

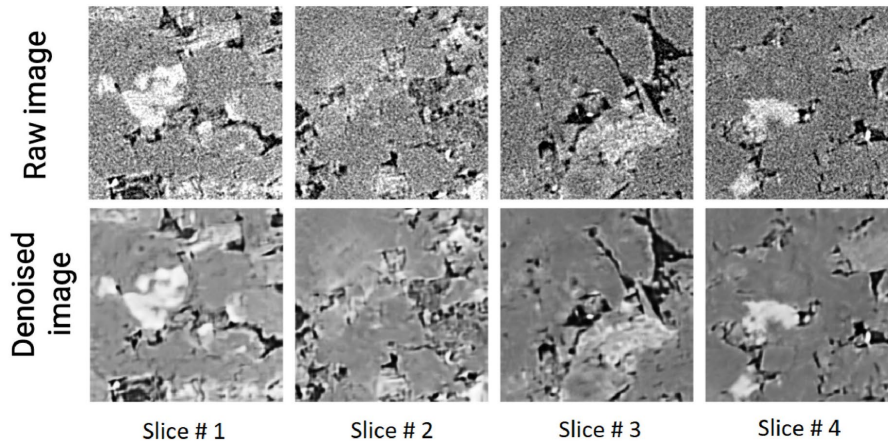


Fig. 10. Different slices of the 3D volume (original and after DIP images).

performing similar to the “ground truth” filtering procedure but also no-reference (NR) metrics, which are the standalone criteria of image quality. The AI-filters demonstrate better quality than the combination of bandpass and bilateral filters:

- full-reference (FR) metrics confirm that AI-filters significantly decrease the noise level and preserve the similarity to the original image. It does not remove the important elements of rock structure due to smoothing;
- no-reference (NR) metrics also confirm that some implementations of AI-filters work even better than “ground truth” – the benchmark images for training
- CNN with SSIM and Perceptual losses dramatically change the histogram of images: intensity distribution became bimodal with the second peak refers to high-density intrusions (Fig. 8).

A very notable visual representation of CNNs performance is presented in Fig. 11. In Fig. 11 we can see the difference between the reference image and the images enhanced with a trained model. The regions colored in red assign where the pixel values in the reference image are greater than the pixel values of the denoised one and the blue color shows the regions where the pixel values in the reference image are less than the pixel values of the denoised one. One can see that CNNs corrected intensity gradient effect and artifacts around dense intrusions.

FR and NR metrics together show that the best AI-filters are CNNs with SSIM and Perceptual VGG1_1 losses. These networks provide the highest values of SNR and SSIM metrics, very high values of PSNR metric, and significant histogram enhancement (transition from single modal to bimodal intensity distribution), as can be seen in Fig. 8. Polymodal type of histogram points that image becomes more contrast – different structural elements (pores, matrix, high-density inclusions) could be detected more precise. Unfortunately, the histogram enhancement level for CNNs is not enough to extract at least the third peak refers to pores. We also have shown that in enhancement problems, like denoising, when it is challenging to obtain the paired dataset, self-supervised methods (DIP) work better than fully supervised ones. NR metrics (SNR and Kong (Kong et al., 2013)) show that DIP has better performance even then CNNs with SSIM and Perceptual VGG1_1 losses (Tables 3 and 4). One can also mention that there are three peaks on histogram (Fig. 8). The main disadvantage of these methods is that they

are optimization-based rather than feed-forward, i.e. it is necessary to adjust a new DIP algorithm for each noisy image, that may take days to treat only one 3D model on modern GPUs. But this class of methods can be used for dataset preparation for the supervised methods for full-cycle image processing, including segmentation.

The main goal of the research to test DL algorithms as a high-quality, fast and easy in use image denoising instrument. It is especially crucial for tight rocks where segmentation strongly depends on image quality. The next step will be to develop effective workflow of how to apply this instrument for rock samples with different structure, for images obtained by another X-ray CT systems, for different ground truth dataset size. The universal workflow could be the following:

- Divide single core sample images on training and executive subsets (in relation 1 to 10);
- Apply DIP algorithm or any other high quality (and usually heavy) algorithm to training subset
- Train CNN on proceeded train images from the previous step;
- Apply CNN to the executive part of the images.

DIP approach is heavily built upon the self-supervised image denoising method. To apply DIP to all dataset is very time-consuming. To avoid the limitations, we propose to train surrogate CNN models on the generated data (training subset) and apply it to the unseen data. This approach could make it possible to obtain clean images in a few minutes on a GPU.

Another workflow could base on developing CNN trained on different data, including different rock type and image quality. In this case, we can increase the generalization of CNN and expect good denoising of new images without any additional training. Both implementations could help to develop an AI-based instrument to build high-quality 3D segmented models of rocks for DRP applications.

Computer code availability

The prepared computer code for the training and evaluation of RED-Net models is available at www.github.com/smikhail/deep-image-denoising. Also, the training of Deep Image Prior has been done based on a publicly available code at www.github.com/DmitryUlyanov/deep-image-prior.

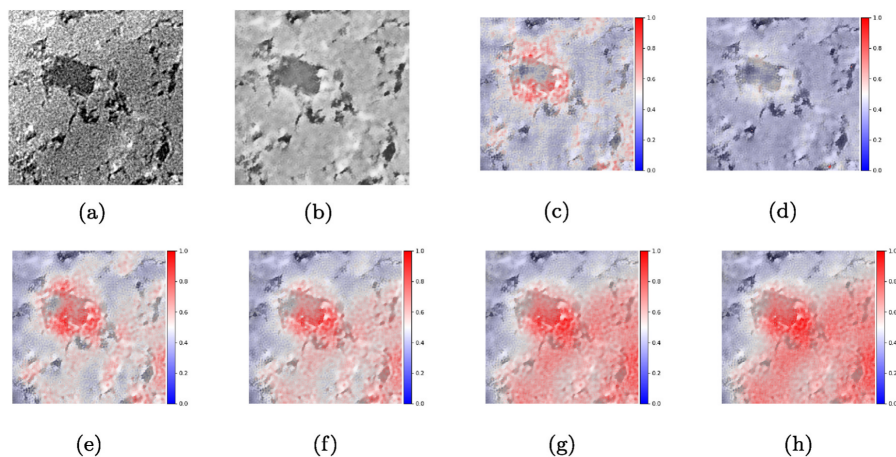


Fig. 11. Visualization of difference between the reference image and the images enhanced with a trained model. (a) - original image, (b) - reference image. Images enhanced with different models: (c) - L_1 loss, (d) - L_2 loss, (e) - SSIM loss, (f) - Perceptual loss (VGG1_1), (g) - Perceptual loss (VGG3_1), (h) - Perceptual loss (VGG3_4).

Data availability

We open-sourced the dataset used in our experiments. It can be found at <https://doi.org/10.17632/tz5zwwgs85v.1>, an open-source online data repository hosted at Mendeley Data (Ebadi, 2020).

Declaration of competing interest

The authors declare that they have no known competing financial interests or personal relationships that could have appeared to influence the work reported in this paper.

Appendix A. Supplementary data

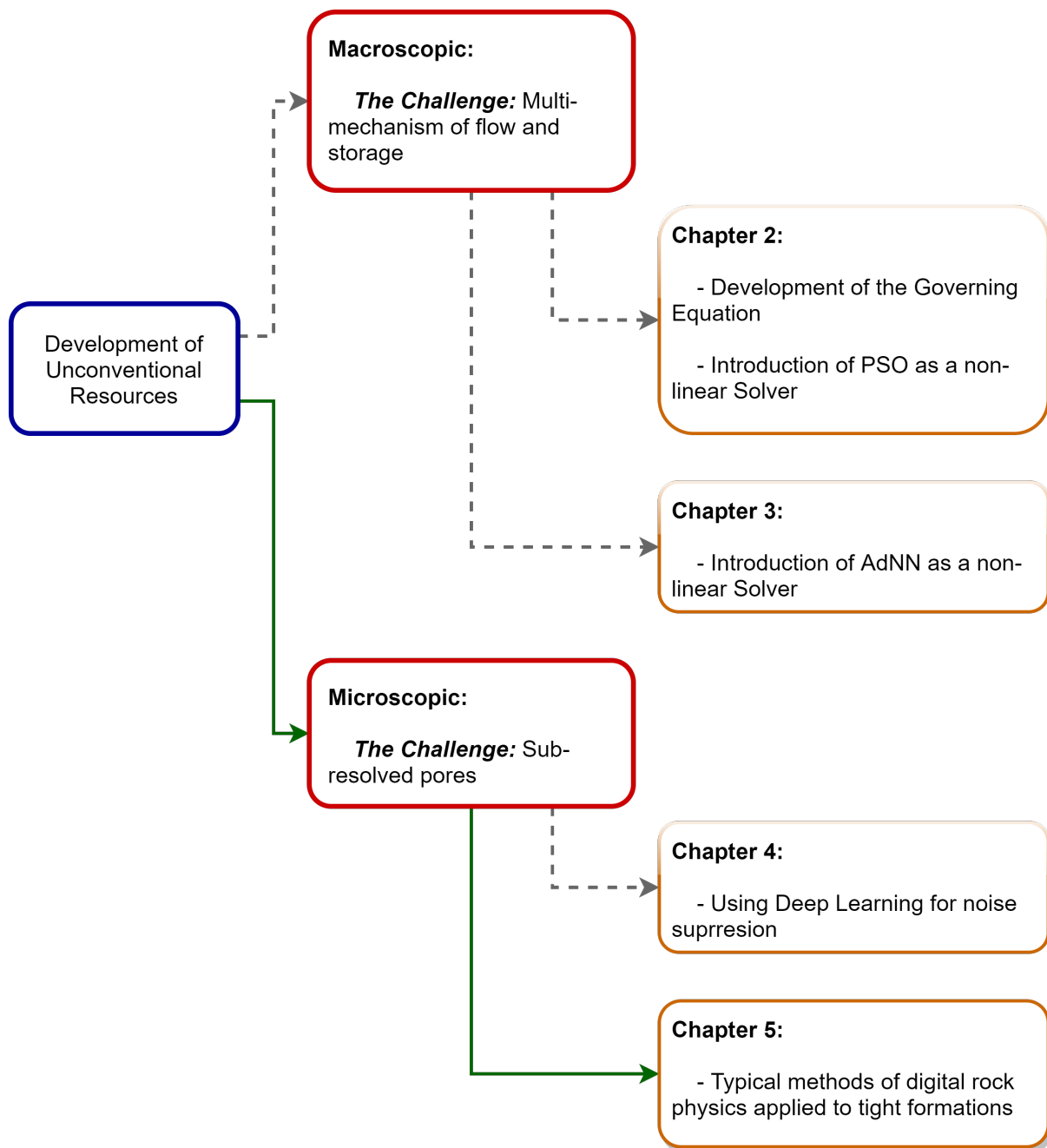
Supplementary data to this article can be found online at <https://doi.org/10.1016/j.cageo.2021.104716>.

References

- Andrá, H., Combaret, N., Dvorkin, J., Glatt, E., Han, J., Kabel, M., Keehm, Y., Krzikalla, F., Lee, M., Madonna, C., et al., 2013. Digital rock physics benchmarks—part I: Imaging and segmentation. *Comput. Geosci.* 50, 25–32.
- Bishop, C.M., 2007. *Pattern Recognition and Machine Learning* (Information Science and Statistics).
- Buades, A., Coll, B., Morel, J.-M., 2005. A review of image denoising algorithms, with a new one. *Multiscale Model. Simul.* 4 (2), 490–530.
- Buades, A., Coll, B., Morel, J.-M., 2011. Non-local means denoising. *Image Process. Line* 1, 208–212.
- Chen, H., He, X., Teng, Q., Sheriff, R.E., Feng, J., Xiong, S., 2020. Super-resolution of real-world rock microcomputed tomography images using cycle-consistent generative adversarial networks. *Phys. Rev.* 101 (2), 023305.
- Da Wang, Y., Armstrong, R.T., Mostaghimi, P., 2019. Enhancing resolution of digital rock images with super resolution convolutional neural networks. *J. Petrol. Sci. Eng.* 182, 106261.
- Dabov, K., Foi, A., Katkovnik, V., Egiazarian, K., 2007. Image denoising by sparse 3-d transform-domain collaborative filtering. *IEEE Trans. Image Process.* 16 (8), 2080–2095.
- Ebadi, M., 2020. *Micro x-ray ct images of two cores (original and filtered)*. <https://data.mendeley.com/datasets/tz5zwwgs85v/1>.
- García-García, A., Orts-Escobedo, S., Oprea, S., Villena-Martínez, V., García-Rodríguez, J., 2017. A Review on Deep Learning Techniques Applied to Semantic Segmentation. *arXiv preprint arXiv:1704.06857*.
- Goodfellow, I., Bengio, Y., Courville, A., 2016. *Deep Learning*. MIT press.
- Ioffe, S., Szegedy, C., 2015. Batch Normalization: Accelerating Deep Network Training by Reducing Internal Covariate Shift. *arXiv preprint arXiv:1502.03167*.
- Karimpouli, S., Tahmasebi, P., 2019. Segmentation of digital rock images using deep convolutional autoencoder networks. *Comput. Geosci.* 126, 142–150.
- Kingma, D.P., Ba, J., Adam, 2014. A Method for Stochastic Optimization. *arXiv preprint arXiv:1412.6980*.
- Kong, X., Li, K., Yang, Q., Wenyin, L., Yang, M., 2013. A new image quality metric for image auto-denoising. In: 2013 IEEE International Conference on Computer Vision, pp. 2888–2895.
- Krizhevsky, A., Sutskever, I., Hinton, G.E., 2012. Imagenet classification with deep convolutional neural networks. In: *Advances in Neural Information Processing Systems*, pp. 1097–1105.
- Laine, S., Karras, T., Lehtinen, J., Aila, T., 2019. High-quality self-supervised deep image denoising. In: *Advances in Neural Information Processing Systems*, pp. 6968–6978.
- Landis, E.N., Keane, D.T., 2010. X-ray microtomography. *Mater. Char.* 61 (12), 1305–1316.
- Lehtinen, J., Munkberg, J., Hasselgren, J., Laine, S., Karras, T., Aittala, M., Aila, T., 2018. Noise2noise: Learning Image Restoration without Clean Data. *arXiv preprint arXiv:1803.04189*.
- Long, J., Shelhamer, E., Darrell, T., 2015. Fully convolutional networks for semantic segmentation. In: *Proceedings of the IEEE Conference on Computer Vision and Pattern Recognition*, pp. 3431–3440.
- Mao, X., Shen, C., Yang, Y.-B., 2016. Image restoration using very deep convolutional encoder-decoder networks with symmetric skip connections. In: *Advances in Neural Information Processing Systems*, pp. 2802–2810.
- Otsu, N., 1979. A threshold selection method from gray-level histograms. *IEEE Trans. Syst. Man Cybernet.* 9 (1), 62–66.
- Paszke, A., Gross, S., Chintala, S., Chanan, G., Yang, E., DeVito, Z., Lin, Z., Desmaison, A., Antiga, L., Lerer, A., 2017. Automatic differentiation in PyTorch. In: *NIPS AutoDiff Workshop*.
- Ronneberger, O., Fischer, P., Brox, T., U-net, 2015. Convolutional networks for biomedical image segmentation. In: *International Conference on Medical Image Computing and Computer-Assisted Intervention*. Springer, pp. 234–241.
- Tikhonov, A.N., Arsenin, V.I., 1977. *Solutions of Ill-Posed Problems*, vol. 14. Winston, Washington, DC.
- Tomasi, C., Manduchi, R., 1998. Bilateral Filtering for Gray and Color Images.
- Ulyanov, D., Vedaldi, A., Lempitsky, V., 2018. Deep image prior. In: *Proceedings of the IEEE Conference on Computer Vision and Pattern Recognition*, pp. 9446–9454.
- Varfolomeev, I., Yakimchuk, I., Safonov, I., 2019. An application of deep neural networks for segmentation of microtomographic images of rock samples. *Computers* 8 (4), 72.
- Wang, Z., Simoncelli, E.P., Bovik, A.C., 2003. Multiscale structural similarity for image quality assessment. In: *The Thirty-Seventh Asilomar Conference on Signals, Systems & Computers*, vol. 2. Ieee, pp. 1398–1402, 2003.
- Wang, Z., Bovik, A.C., Sheikh, H.R., Simoncelli, E.P., et al., 2004. Image quality assessment: from error visibility to structural similarity. *IEEE Trans. Image Process.* 13 (4), 600–612.
- Wang, Y., Teng, Q., He, X., Feng, J., Zhang, T., 2019. Ct-image of rock samples super resolution using 3d convolutional neural network. *Comput. Geosci.* 133, 104314.
- Yang, G.-Z., Burger, P., Firmin, D.N., Underwood, S., 1996. Structure adaptive anisotropic image filtering. *Image Vis Comput.* 14 (2), 135–145.
- Yang, Q., Yan, P., Kalra, M.K., Wang, G., 2017a. Ct Image Denoising with Perceptive Deep Neural Networks. *arXiv preprint arXiv:1702.07019*.
- Yang, X., Jia, W., Wu, D., Poon, T.-C., 2017b. On the difference between single- and double-sided bandpass filtering of spatial frequencies. *Optic Commun.* 384, 71–77.
- Zhang, K., Zuo, W., Chen, Y., Meng, D., Zhang, L., 2017. Beyond a Gaussian denoiser: residual learning of deep cnn for image denoising. *IEEE Trans. Image Process.* 26 (7), 3142–3155.
- Zhang, Y., Tian, Y., Kong, Y., Zhong, B., Fu, Y., 2018. Residual Dense Network for Image Restoration. *arXiv preprint arXiv:1812.10477*.
- Zhao, H., Gallo, O., Frosio, L., Kautz, J., 2015. Loss Functions for Neural Networks for Image Processing. *arXiv preprint arXiv:1511.08861*.
- Zhu, X., Milanfar, P., 2010. Automatic parameter selection for denoising algorithms using a no-reference measure of image content. *IEEE Trans. Image Process.* 19 (12), 3116–3132.

5. Different methods of permeability calculation in digital twins of tight sandstones

The application of digital rock physics to tight samples can be challenging. It is due to the fact that the pores existing in the tight samples cannot be detected in the μ XCT images of the supposed sample. Hence, a particular question raises here is how much the classic methods of digital rock physics are applicable to unconventional resources like tight sandstones. The question can be considered based on two aspects of digital image processing and pore-scale simulations. The other side of the topic is how the overall procedure of digital rock physics is influenced by the type of hardware used. The presented paper has put forth tremendous efforts to understand how various combinations of image processing, pore-scale simulations and the employed hardware affect the quality of generated results of digital rock physics. The main impact of the published paper on the general trend of the research has been shown in **Figure 20**.



955

956

Figure 20: Chapter 5 in a glance

957

CRedit author statement:

958

1. **Denis Orlov:** Conceptualization, Methodology Software Validation Formal

959

analysis Investigation Resources Data Curation Writing - Original Draft

960

Writing - Review & Editing Visualization

- 961 2. **Mohammad Ebadi:** Methodology, Software, Investigation, Data curation
962 Writing - Original Draft, Writing - Review & Editing Visualization
963 3. **Ekaterina Muravleva:** Conceptualization, Formal analysis
964 4. **Denis Volkhonskiy:** Software, Investigation
965 5. **Andrei Erofeev:** Software, Investigation
966 6. **Evgeny Savenkov:** Software, Investigation
967 7. **Vladislav Balashov:** Software, Investigation
968 8. **Boris Belozеров:** Conceptualization, Resources, Supervision, Project
969 administration
970 9. **Vladislav Krutko:** Conceptualization, Resources, Supervision, Project
971 administration
972 10. **Ivan Yakimchuk:** Software, Investigation, Writing – review & editing
973 11. **Nikolay Evseev:** Software, Investigation
974 12. **Dmitry Koroteev:** Conceptualization, Writing – review & editing,
975 Supervision



Contents lists available at ScienceDirect

Journal of Natural Gas Science and Engineering

journal homepage: <http://www.elsevier.com/locate/jngse>

Different methods of permeability calculation in digital twins of tight sandstones

Denis Orlov^a, Mohammad Ebadi^{a,*}, Ekaterina Muravleva^a, Denis Volkhonskiy^a,
Andrei Erofeev^a, Evgeny Savenkov^b, Vladislav Balashov^b, Boris Belozеров^c, Vladislav Krutko^c,
Ivan Yakimchuk^d, Nikolay Evseev^d, Dmitry Koroteev^a

^a Skolkovo Institute of Science and Technology, Moscow, Russia

^b Keldysh Institute of Applied Mathematics, Russian Academy of Sciences, Moscow, Russia

^c Gazpromneft SRC, St Petersburg, Russia

^d Schlumberger Moscow Research Center, Moscow, Russia

ARTICLE INFO

Keywords:

Digital rock physics
Tight sandstones
Digital image processing
Direct simulations
Lattice-Boltzmann method
Pore network modeling

ABSTRACT

The development of tight hydrocarbon resources has a significant impact on the future of the energy market. Digital Rock Physics (DRP) is technically recognized as an effective method for characterizing reservoir rock properties. However, there is uncertainty about what result the user-defined chain of Digital Image Processing (DIP) and Pore-Scale Simulation (PSS) will produce when applying DRP. The uncertainty surrounding this technology faces even a greater deal in tight formations where a considerable portion of pores are sub-resolved and cannot explicitly be seen in the reconstructed micro-scale x-ray Computed Tomography (μ xCT) images.

Regarding the μ xCT images of Achimovskiy formation, which is classified as a tight sandstone resource, the addressed uncertainty has been evaluated based on various scenarios of well-known DIP and PSS approaches. The results show that image processing and segmentation impact on the absolute permeability values stronger than calculation methods. Furthermore, the cross-plot analysis shows that simple image processing and segmentation indicate the same trend as precise image processing and segmentation. The generated results for the studied formation show that if the experimental open porosity of a core sample is higher than 5%, μ xCT images could feasibly resolve the system of connected pores.

Credit author statement

Denis Orlov - Conceptualization, Methodology Software Validation Formal analysis Investigation Resources Data Curation Writing - Original Draft Writing - Review & Editing Visualization. Mohammad Ebadi - Methodology, Software, Investigation, Data curation Writing - Original Draft Writing - Review & Editing Visualization. Ekaterina Muravleva - Conceptualization, Formal analysis, Denis Volkhonskiy - Software, Investigation, Andrei Erofeev - Software, Investigation. Dmitry Koroteev - Conceptualization, Writing - review & editing, Supervision, Evgeny Savenkov - Software, Investigation, Vladislav Balashov - Software, Investigation, Boris Belozеров - Conceptualization, Resources, Supervision, Project administration, Vladislav Krutko - Conceptualization, Resources, Supervision, Project administration, Ivan Yakimchuk - Software, Investigation, Writing - review & editing, Nikolay Evseev -

Software, Investigation

1. Introduction

Recent advances in technologies of hydraulic fracturing and horizontal wells have made the development of tight hydrocarbon resources possible (Bezyan et al., 2019). Generally, the profitable production from unconventional reservoirs strongly depends on the accurate estimation of physical rock properties (Al-Marzouqi, 2018). The traditional experimental methods to approximate the relevant rock properties are routinely time-consuming and expensive. Although some recent experimental advances like the pressure pulse decay method have been considered eye-catching improvements in petrophysical characterization of unconventional resources, Digital Rock Physics (DRP) has drawn much attention (de Oliveira et al., 2020). It is due to the fact that DRP is

* Corresponding author.

E-mail address: Mohammad.Ebadi@skoltech.ru (M. Ebadi).

<https://doi.org/10.1016/j.jngse.2020.103750>

Received 27 April 2020; Received in revised form 6 December 2020; Accepted 8 December 2020

Available online 5 January 2021

1875-5100/© 2020 Elsevier B.V. All rights reserved.

an innovative technique of performing digital core analysis, which offers a couple of advantages compared to laboratory measurements. For instance, DRP usually causes saving time and costs (Ivanova et al., 2019). It also allows performing various numerical experiments on exactly the same sample (Grathoff et al., 2016). It also provides the researcher to conduct several analyses concurrently on one sample. Last but not least, the study of rock properties under multiple situations is remarked to be the other main advantage (Hu et al. Mostaghimi et al.).

Technically, the standard workflow of DRP can sequentially be divided into two main steps of Digital Image Processing (DIP), and Pore Scale Simulation (PSS) (Kaestner et al., 2008). The preparation of a realistic pore-scale model is the most significant target of DIP. It is typically achieved by taking a series of sequential steps starting from the projection of the rock sample with the X-ray at different angles and continues with image filtering, histogram analysis, segmentation, and 3D object reconstruction (Taud et al., 2005). Regarding the advantages of both Lagrangian and Eulerian frame of references, and their specifications of the flow fields, various scenarios of PSS are typically implemented to calculate the required rock properties (Mehmani et al., 2019, 2020).

As the ease with which a fluid can move through porous media, evaluation of permeability is undoubtedly one of the essential steps of developing unconventional hydrocarbon resources (Saxena et al., 2017). Making the classic DRP methods customized for tight resources has drawn many researchers' attentions (Ning et al., 2019). For example, advantages of micro-scale x-ray Computerized Tomography (μ CT) imaging and visualization at the pore scale have been taken to design a particular workflow based on the Pore Network Modelling (PNM) to observe the effects of pore-lining clay minerals on pore preservation and sufficient transport capability (Ma, 2016). The Parallel Lattice Boltzmann Method (PLBM) has been used to study the nanoscale effects on a 3D tube. The results of applying the same technique of PSS have been used to estimate the apparent permeability of natural nanoscale porous media of shale resources (Sun et al., 2017a). A specific workflow of DRP, which is less dependent on the users' experiences, has been developed for tight sandstones. Regarding the non-negligible effects of sub-resolved porosities in providing connectivity among the flow paths, the global thresholding has been combined with the image-based meshing strategy to form a computational domain on the 3D stack of images. Then, the Direct Simulations (DS) has been applied to calculate the absolute permeability (Verri et al., 2017). However, it has been stated that the effects of sub-resolved pores are not crucial because they are typically filled with water (Ramstad et al., 2019). To map the porosity distribution from micro to macro scale, employing a multi-scale imaging workflow has been followed. Then, the results of a 3D registered porosity map has been implemented to construct a multi-scale pore network in which regions having macro-porosity are modeled based on classic pore network manners and the elements with micro-porosity are regarded as continuous porous mediums (Ruspini et al., 2016). The capability of Scanning Electron Microscopes (SEM) to reveal the Pore Size Distribution (PSD) and pore structures has been taken to introduce a multi-scale digital rock scheme to understand the nature of fluid flow in tight sandstones (Liu et al., 2017). Due to the existence of micro and nanopores, fluid flow in tight formations deviates significantly from the outputs of conventional models. By taking the effects of boundary layers and the media deformation into accounts, a stochastic network, including the anisotropic topology, has primarily been constructed for tight formations. It has been understood that the abovementioned effects cause the reduction of pore-scale flow velocity. In other words, excluding the effects of boundary and the deformation from the computational domain could lead to the overestimation of permeability (Chen et al., 2019).

Therefore, it could typically be figured out that the permeability of various systems has generally been calculated based on three numerical methods. As a lattice of wide pores joined by throats through which transport and displacement could semi-analytically be computed, the

PNM has broadly been used under different scenarios and assumptions (Xiong et al., 2016). The Lattice Boltzmann Method (LBM) is the other approach in which its coding is noticeably straightforward, and it can conveniently be paralleled. Principally, the LBM takes the fluid as a set of particles that can move on a prescribed regular lattice (Manwart et al., 2002). The most accurate approach is direct modeling, which is based on the applying of Navier-Stokes equations on a slow steady-state incompressible flow (Mostaghimi et al., 2013; Zhang et al., 2015).

There are several papers comparing the performance of referred methods based on some synthetic or conventional samples (Ramstad et al., 2019). The results show that the PNM is the fastest method, but there are some ambiguities with the network extraction algorithms. The results can be also achieved by applying the LBM method if there would be possible to apply different scenarios of boundary conditions with less degree of complications. Naturally that the DS is capable of generating the most accurate results, although it is computationally demanding. Nevertheless, there is still no comprehensive research showing how much satisfying the discussed methods can perform in case of studying unconventional resources like clastic tight sandstones where the permeability is usually less than 1 millidarcy (mD), but porosities are typically more than 10% (Grechneva et al., 2012; Grafet al., 2014).

The current research has examined the results of applying all the referred methods on the clastic tight sandstone samples gathered from the Achimovskiy formation located in the Western Siberia, Russia (Krutko et al., 2019). Accordingly, the general workflow of DIP and different theories behind PNM, LBM, and DS methods have been discussed in the methodology. Next, the generated results have been analyzed not only as the function of applied methods but also as the consequences of implementing various scenarios of DIP. Eventually, all the results have shortly been inferred and then summarized in the conclusion.

2. Methodology

Based on the general concept of DRP, the methodology of 3D digital rock reconstruction and the applied algorithm of PSS can both be the area of uncertainty over the calculation of absolute permeability. Nowadays, there is no unified procedure for constructing a proper 3D model of the rock sample. The well-known commercial or open-source software, such as PerGeos, GeoDict, and ImageJ, provides the researchers with many instruments to perform image processing and segmentation. The only differences between this software in terms of DIP are user interface and software price. In this research, we were more focused on testing permeability calculation methods implemented in different software. However, the feasibility, accuracy, and consistency of using the referred packages have always been a severe challenge to the DRP community. Referring to the variety of DIP methods, how much the quality of the reconstructed 3D digital model can influence on the calculation of porosity and permeability remains open to questions. The validity of the final model becomes a matter of even more attentions when DRP is applied to low permeable rocks where the experimental values for macro-scale cores are not accurate enough to tune the initial parameters of the model, which is based on the micro resolution CT images of small size sample. The current section firstly discusses how technically the X-ray projections are turned into CT images. Then, it shows how the general DIP can proceed on the basis of the reconstructed CT images to form a 3D digital rock model. Finally, the various algorithms of permeability calculations are theoretically presented.

2.1. Image reconstruction

The general concept behind the reconstruction of the μ CT images has been shown in Fig. 1. After cleaning the 8 mm-diameter mini-sample with a mixture of alcohol and benzene, the dried sample is rotationally projected in the CT system. A planar X-ray detector collects magnified projection images. At the most basic level, tomographic reconstruction

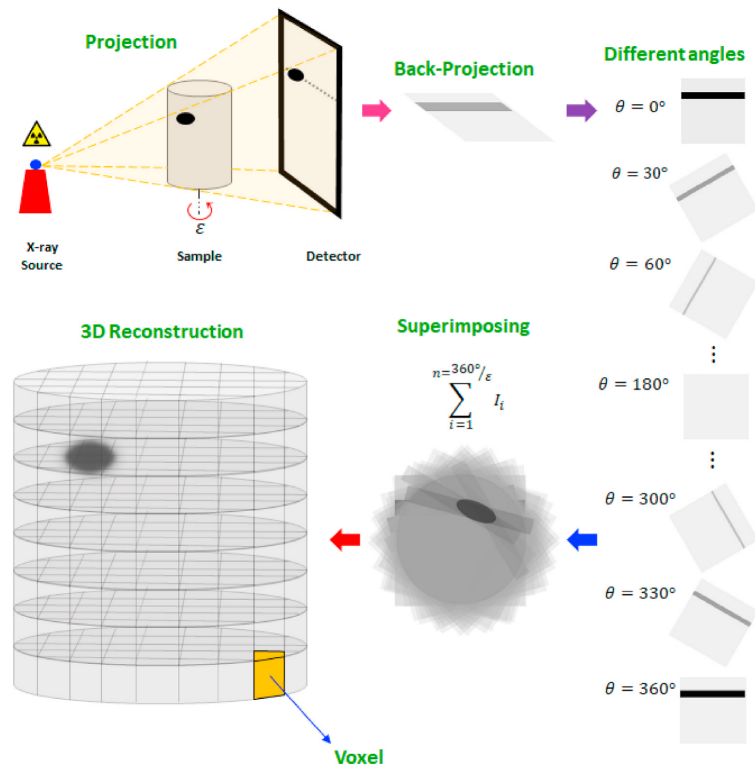


Fig. 1. Schematic reconstruction of 3D digital model based on CT images (Bultreys et al., 2016).

of projection images leads to a 3D distribution of X-ray linear attenuation coefficients with certain assumptions. Because features and phases of different materials often have various X-ray absorption properties, the supposed constructing elements can accordingly be identified from the images. Obtained back-projected images with different angles in which brightness depends on the degree of X-ray absorption are then superimposed to reconstruct the 3D digital model. Multiple scanning is the most common practice to obtain the optimized parameters of the CT system in terms of projecting low-permeable samples.

The X-ray projection can be considered as a high-quality procedure if it satisfies two essential conditions. Firstly, the X-ray should not completely be attenuated. In other words, the detector should be able to register a certain level of X-ray beam intensity after passing through the object. Increasing the energy of the emission source is known as a proper solution. The second condition is that dynamic range of resolved beam intensities should be high enough to obtain high contrast projections, i.e. detector should be capable to register signal from points with highest and lowest beam intensity without out-of-range distortion. This requirement makes it possible to distinguish more details in the 3D digital models. A case in point, the projection with high contrast causes a successful segmentation of minerals with densities close to each other like quartz and argillite. In contrast, implementing a low-contrast projection leads to the creation of voxels with similar gray-scale values, which do not apply to many segmentation algorithms. Because the best method to increase the dynamic diapason is keeping the beam intensity of the X-ray on a low level, it is required to make a trade-off for the satisfaction of referred criteria (Wang et al., 2017).

To maximize the quality of CT images, finalizing the optimum power of radiation should be followed by adjusting other significant parameters, including the number of projections, timing, and averaging. A higher number of projections makes more information available to reconstruct more representative CT images. However, more projections require more time. A high level of timing allows to increase the dynamic range, and also increase scanning time of the sample. Averaging could increase the Signal to Noise Ratio (SNR) and compensate for the adverse effects of extensive timing. Regarding the aforementioned parameters can significantly increase the duration of the CT scanning procedure. The long time of scanning subsequently leads to instabilities in X-ray generation, which means changes in the beam intensity and energy spectrum characteristics of radiation. It generally occurs due to the thermal effect shifts and blur of a focus spot. Typically, the best configuration of all the parameters is governed by the experimental conditions and obtained by the trial-and-error.

2.2. Digital image processing

The reconstruction of a 3D object from a series of 2D projections at different angles is the essential element of modern imaging methods (Ramandi et al., 2016; Diwakar and Kumar, 2018). The supposed 3D object can be created as the result of stacking the sequence of tomographically reconstructed 2D images (Kaestner et al., 2008). The existence of artifacts, roundoff errors, and different types of mathematical noises in the reconstructed CT images are the main reasons to build incorrect 3D digital models of the porous structure. Furthermore, the

visual noises are identified as the other group of phenomena which have destructive effects on the quality of CT images (Kornilov et al., 2019). In principle, visual noises are recognized as the undesired information that mainly damages the visual effects of an image showing the low contrast objects. Among various factors adversely affecting the quality of CT images, there is no doubt that artifacts are the most important one (Diwakar and Kumar, 2018). Typically, the artifacts do refer to any systematic disagreement between the gray intensity of the voxels in the reconstructed image and the actual attenuation coefficient in a corresponding point of the object (Boas and Fleischmann, 2012). Thus, applying edge-preserving filters to suppress the noise from CT images is highly essential. The main challenging task is to reduce the level of noise without losing significant features such as sharp structures, corners, and edges (Schladitz, 2011).

The methods of image denoising can be categorized based on two primary sections of spatial or transform domain filtering. In spatial domain filtering, the target is to reduce noises by applying the filtering process directly on the original noisy images. Several methods like linear and non-linear filters, anisotropic diffusion, dictionary learning techniques, non-local means filters, and deep learning algorithms are known as the principal members of spatial domain filtering. There is no doubt that bilateral filters are one of the most prominent subsets of spatial domain filtering (Eklund et al., 2013). By applying bilateral filter, the intensity values of voxels in each image are replaced by a weighted average of intensity values from surrounding voxels (Tomasi and Manduchi, 1998). The advantages of bilateral filters like non-linearity, edge-preservation, and smoothness make them great candidates to be applied to the gray-scale CT images (Landis and Keane, 2010).

The different methods like block-matching and 3D filtering, methods based on scale dependencies, shrinkage rules, wavelet transform, and threshold estimation are known as various subsets of transform domain filtering (Diwakar and Kumar, 2018). Typically, images are Fourier transformed, multiplied with the filter function, and then re-transformed into the spatial domain. Universally, attenuating high frequencies results in a smoother image in the spatial domain, and attenuating low frequencies enhances the edges. As one of the most commonly used method, the bandpass filter removes noise and background variation. It attenuates very low and very high frequencies but retains a middle-range band of frequencies (Yang et al., 2017). It means that bandpass filtering can be used to enhance edges (suppressing low frequencies) while reducing the noise at the same time (attenuating high frequencies) (Cerqueira et al., 2018).

Besides, the main idea of DRP is based on the fact that each porous media could be considered as the union of solid and empty parts. Accordingly, the segmentation techniques should be applied to the denoised gray-scale CT images to turn them into black and white versions resembling pores and solid phase, respectively. In other words, segmentation is the portioning of gray-scale CT images into disjoint regions that comparatively have a uniform density. (Sudakov et al., 2019).

The segmentation algorithms have primarily been classified into two categories: (i) global thresholding segmentation schemes and (ii) segmentation based on the local adaptive schemes. The main idea behind global thresholding schemes is the histogram representation of the intensity and discrepancy of all the gray pixels in a scene. Inherently, global segmentation methods not only do not consider the spatial distribution of intensity values but also the global voxel-based thresholding algorithms cannot generate the proper segmented images when there are intensity heterogeneities in the target regions. On the other hand, the local adaptive segmentation schemes are based on the fact that segmentation decision is made for each voxel. Commonly, taking advantage of the local information causes the generation of segmentations with better quality, but it still demands higher memory and computations (Saxena et al., 2019).

To develop a robust segmentation algorithm capable of overcoming the mentioned difficulties, taking advantage of statistical particle-based

methods has drawn many researchers' attention. The applications of Random Walker (RW) theory has innovatively provided the communities of image processing with highly efficient and practical segmentation algorithms. Receiving binary images in which even weak boundaries are respected is the eye-catching output of applying RW theory as the segmentation algorithm where occurrences of crossing the sharp intensity gradients have been avoided by consideration of imposing biases to the main body of the procedure (Grady, 2006). Running the RW theory for the segmentation of gray-scale images needs the introduction of two thresholds. All the voxels with the intensity values higher than the larger threshold are grains, and those with intensity values lower than the smaller one are labelled as pores. The proposed algorithm does make a decision on which class the middle voxels should accordingly be labelled. Since the peak of pores is comparatively very small or submerged within the peak of grains, an automatic algorithm of finding histogram knee should be applied to find the first threshold (Rosin, 2001). The second threshold with the larger value is routinely chosen at the peak of the histogram.

Due to the thresholding nature of the binarization technique, some voxels attributable to grains can instead be classified as the pore space and vice versa. In order to improve the quality of binarized outputs and address the mentioned above commonly occurring visual artifacts, it is highly recommended to take advantage of morphological transformations, which are some shift-invariant operators strongly related to Minkowski additions. In more details, Dilation and Erosion are the fundamental operators that are the basis for other similar operators as well. In the Erosion, the supposed voxel locating in the center of the kernel is the minimum of the remaining elements of the kernel. On the other hand, the value of the voxel in the Dilation is the maximum of other elements of the kernel. Also, the procedure in which the Dilation follows the Erosion is called the Opening, and its reverse mode is named Closing. Technically, the basic idea behind these operators is to probe a binary image with a pre-defined and straightforward shape to check how it misses or fits the shapes in the images (Iassonov et al., Tuller).

The procedure of image processing mentioned above has schematically been illustrated in Fig. 2. Before doing the segmentation based on the RW theory, histogram analysis of all images could be a great help to automatically find the required thresholds. The peak of histogram shown with the blue arrow is the threshold that voxels with higher intensities than are going to be labelled as grain or white parts.

The same as how green dashes show, fitting two lines, which one of them has a zero-slope to the first numerical derivation of the histogram and the other one tries to cover as many as points in the uprising region, produces an intersection that could be taken as the threshold which its value is the most substantial intensity that the relevant voxel is certainly a pore or black. The remaining middle part highlighted in gray is the zone in which further decision of segmentation is made with the RW theory.

Eventually, it is highly required to determine the Representative Elementary Volume (REV), which is the least volume beyond that the properties of the domain do not change. For the estimation of REV, a characteristic parameter such as porosity, permeability, or others is calculated for the initial 3D digital model. Then, a certain number of subsamples are randomly cropped from the initial 3D digital model. After calculating the characteristic parameter for each of subsamples, generated values are compared over the value of the initial 3D model. Next, the size of the subsamples is sequentially reduced, and the characteristic parameter is recalculated. The mean value and variation of the calculated parameter are plotted versus the corresponding subsample size. The size where the mean value and variation of the characteristic parameter become stable is known as the REV (Islam et al., 2018).

2.3. Simulation and modeling

The μ CT images provide the researchers with an evident view of pore structures. It has been taken as the main incentive to come up with

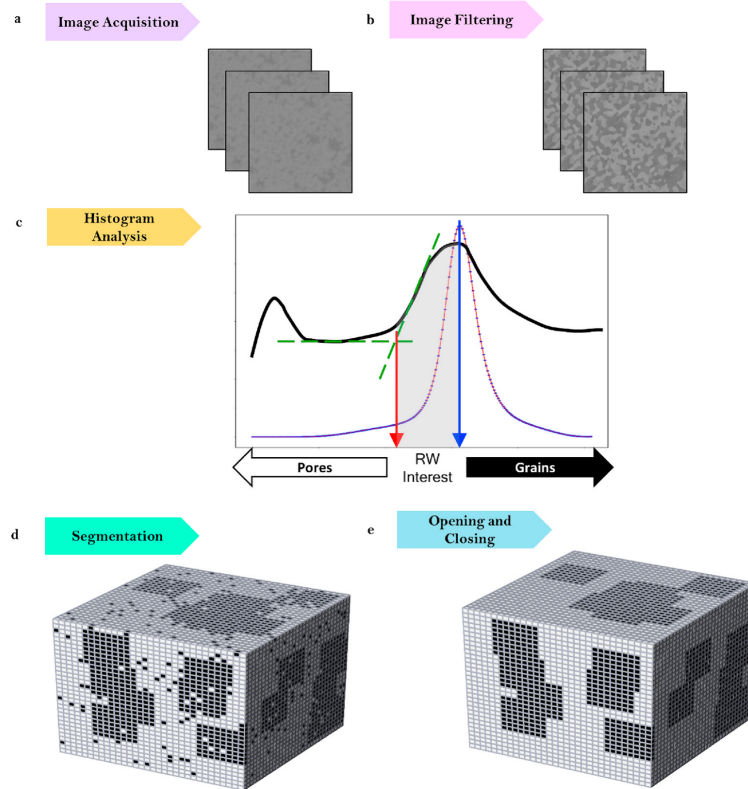


Fig. 2. DIP workflow.

a variety of numerical approaches for the calculation of rock permeability. As a result, direct solver by taking the advantages of Navier-Stokes equations, Lattice-Boltzmann method based on the Lattice Gas Automata (LGA) and the Pore Network Modeling (PNM) which concerns making the approximation of pore-throat geometry are the primary matter of importance (Sun et al., 2017b). The main idea behind all the referred methods is to extract a corresponding couple of velocity and pressure profiles to be inserted in Darcy’s law for the calculation of the permeability as below (Zhang et al., 2019; Yakimchuk et al., 2019):

$$k = -\frac{\mu \bar{U}}{\frac{\Delta P}{L}} \tag{1}$$

where μ stands for viscosity, \bar{U} is the average flow velocity in the entire flow domain and $\frac{\Delta P}{L}$ is the applied pressure difference over the length of L .

2.3.1. Direct Simulations

Regarding the incompressible, Newtonian fluid within a steady-state laminar flow, the Navier-Stokes equations are simplified as:

$$\begin{aligned} \nabla P - \mu \nabla^2 U &= 0 \\ \nabla \cdot U &= 0 \end{aligned} \tag{2}$$

with the nonslip condition at the solid-fluid interface.

The main numerical challenge in solving Equation 2 is the weak

coupling of the pressure and velocity fields. Normally, Pressure -Based Method (PBM) like the Semi Implicit Method for Pressure Linked Equations (SIMPLE) is applied to solve the resultant linear system of equations (Mostaghimi et al., 2013). Then, the averages of generated profiles are inserted into Equation 1 for the further calculations of permeability.

2.3.2. Lattice-boltzman method

Regarding the low-Mach number and the LBM method, the pressure gradient can be replaced with a uniform body force (b_f), which can produce the same flow rate as the pressure driven-flow. Basically, the LBM illustrates the evolution of a discretized particle distribution function, which represents the probability of finding an imaginary particle in a specific location of domain x with a certain velocity ξ at a particular time t . A discretization of the Boltzmann equation in time and space with the conversion of ξ into a finite set of velocities c_i generates the lattice Boltzmann equation as:

$$f_i(x + c_i \Delta t, t + \Delta t) - f_i(x, t) = -\frac{1}{\tau} [f_i(x, t) - f_i^{eq}(x, t)] \tag{3}$$

in which the distribution function of particles moving with the speed of c_i is represented with f_i . The right-hand side of the equation shows the Single Relaxation Time (SRT) Bhatnagar, Gross, and Krook (BGK) collision term, including the τ as the dimensionless relaxation time and Δt , is the time step. The f_i^{eq} known as equilibrium distribution function

is:

$$f_i^{eq} = \omega_i \rho \left[1 + \frac{c_i \cdot u}{c_s^2} + \frac{(c_i \cdot u)^2}{2c_s^4} - \frac{|u|^2}{2c_s^2} \right] \quad (4)$$

where c_i is the model-dependent sound speed, ω_i is the weight associated with the c_i , and u represents the macroscopic velocity vector. Following the D3Q19 model of velocity and the non-dimensional form of sound speed, the macroscopic quantities of density and velocity can be defined by the probability distribution function as (Eshghinejadfard et al., 2016; Wang):

$$\rho = \sum_i f_i \quad (5)$$

$$\rho u = \sum_i f_i c_i \quad (6)$$

2.3.3. Pore-network modelling

Pore-network modeling is widely used as a simplified technique developed especially for flow modeling in porous media. It consists of two main steps, including extracting the network of pores and further calculations based on hydraulic principles (Song et al. Lei). Basically, a network model is simply a coarse representation of the flow domain. Technically, the void space of the rock is represented as pores that are connected through narrower restrictions called throats (Mahanta et al., 2020). The pores and throats are usually reproduced by idealized spheres and cylinders. Based on a pore network model, the flow rate of Q for a single-phase flow between two connected pores of i and j is given by:

$$Q_{ij} = g_{p,ij} (p_i - p_j + p_c) \quad (7)$$

where p_i and p_j are the pressure in pores i and j , respectively. The p_c stands for capillary pressure, and $g_{p,ij}$ as the conductance of two adjacent pores i and j is:

$$\frac{L_{ij}}{g_{p,ij}} = \frac{L_{p,i}}{g_{p,i}} + \frac{L_t}{g_{p,t}} + \frac{L_{p,j}}{g_{p,j}} \quad (8)$$

L_{ij} is the distance from the pore-throat interface of pore i to j , and L_t is the total length of the pore throat. $L_{p,i}$ and $L_{p,j}$ are the radii of pore body i and j , respectively. Moreover, the g_p which depends on the shape of the channel can be derived from the Hagen-Poiseuille formula as:

$$g_p = k \frac{A^2 G}{\mu_p} \quad (9)$$

the dynamic viscosity of the fluid is shown by μ_p , G and A are the shape factor and cross-sectional area of the pore-network model, respectively. According to the shape of circular, equilateral and square tube, k can have one of the values of 0.6, 0.6 or 0.5623 (Zhu et al. Zhu). By adapting Equation 1, the absolute permeability of the pore network model can be calculated as:

$$K_a = \frac{\mu Q L}{A \Delta P} \quad (10)$$

where L is the length and ΔP is the pressure drop.

3. Results and discussions

The permeability of Achimovskiy formation, which is a tight hydrocarbon resource, has been calculated as a function of various algorithms and different DIP operations. Firstly, the details of the X-ray projection with the relevant parameters have been introduced. After determining the REV, the results of calculating the permeability according to 6 different approaches have been shown and discussed. Eventually, the dependency of permeability calculation on the type of

DIP has been represented as well. The important point is that 3D models discussed in the work are not representative ones in relation to core samples. The maximum achieved spatial resolution of μ XCT images was $1.2 \mu\text{m}/\text{vox}$ and the portion of pores having the diameter $> 1 \mu\text{m}$ varied in the range of 3–43 %. That is why we do not have an aim to compare results of simulations with experimental results. The main aim of the current research is to test different flow calculation methods on real rock samples with bad connectivity, small sizes of pores comparable with voxel size, and a wide range of PSD.

3.1. Imaging and REV determination

A modern General Electric v|tome|x L240 CT system which allows performing precise investigations of porous media structures on small samples has been used to project 5 samples of Achimovskiy formation. The system is equipped with 2 X-ray sources (240 kV microfocus tube and 180 kV high-power nanofocus tube) and handles large samples up to $500 \times 800 \text{ mm}$ and 50 kg. The optimized configurations of the CT system has been listed in Table 1.

Implementation of the already described DIP on the gray-scale images resulted in the generation of binary images. After stacking the finalized black & white cross-sections, they were employed to determine the REV. For this purpose, the averaged gray-scale intensity of 3D models (Krutko et al., 2019), porosity, and permeability have been observed for the corresponding sizes, Fig. 3. The results show that all the characteristic parameters have been stabilized in the range of 0.3–0.6 mm. The same procedure has been repeated for the other 4 samples. It has comparatively been concluded that the REV of Achimovskiy formation is as large as 0.6 mm or 500^3 voxels.

3.2. Calculation of porosity and permeability

Based on the previously constructed 3D models and to make sure that there is no uncertainty about the determined REV, the favorite parameters have been calculated for the size of 600^3 . The Cross-Laboratory Control DIP was performed on the 3D models in Schlumberger company. Down to the details of the Cross-Laboratory Control DIP, the implemented algorithm utilizes the spatial covariance of the image in conjunction with indicator kriging to determine object edges. The use of indicator kriging makes the thresholding local and guarantees smoothness in the threshold surface. Implementation of the method requires a priori population identification of some percentage of the image (Oh and Lindquist, 1999).

Table 2 represents the porosity of all 5 samples treated with Cross-Laboratory Control DIP. In addition, the method of Pore Size Distribution by Porosimetry has been employed to calculate the mean pore diameter (Baklanov et al., 2000).

By the consideration of REV for each sample, the absolute permeability has been calculated based on the variety of techniques mentioned in former parts. Following the Navier-Stokes equations and the general concept of DS, the permeabilities have been calculated by the means of:

- *GeoDict* as a commercial simulator with an academic licence,
- *DiMP* which is an academic simulator (Balashov et al., 2019),

Table 1

Technical Configuration of the scanning system.

Item	Value	Unit
High Voltage	60	kV
Tube Current	90	μA
Beam exit window, material	Beryllium	–
Averaging (Number of projections)	8	–
Timing (Exposure)	2000	ms
Total number of projections	2400	–
Spatial Resolution	1.2	μm
Duration of scanning	14.5	Hours

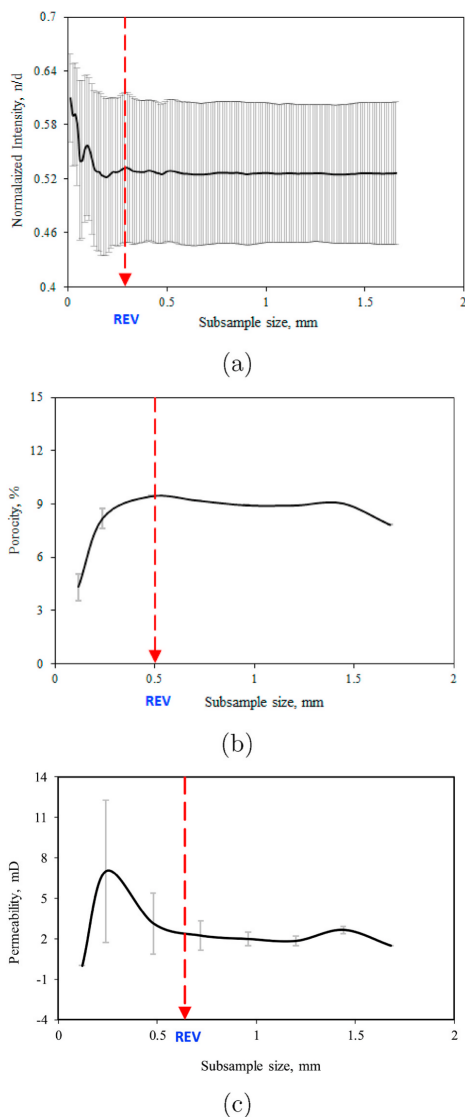


Fig. 3. REV determination of Sample E based on (a) grayscale image intensity (b) porosity (c) permeability calculated with PNM.

Table 2

Porosity and pore size of Achimovskiy samples.

Sample	Total Porosity, %	Effective Porosity, %	Mean Pore Diameter, μm
A	6.5	5.8	6.3
B	5.3	4.4	10.1
C	5.8	5.3	7.5
D	9.9	9.7	10.6
E	7	6.4	9.3

- Density functional hydrodynamics as a Schlumberger Coreflow service based on Direct HydroDynamic (Koroteev et al., 2014).

Furthermore, *PerGeos* has been used to calculate the permeability of samples based on the LBM (Golab et al., 2015). Moreover, the feasibility of applying PNM to calculate the absolute permeabilities of supposed samples has also been examined by means of *PerGeos* and implementing the open-source libraries of *pnextract* to extract the pore network and *OpenPNM* for further simulations (Raeini et al., 2017; Boujelben et al., 2018). The calculated permeabilities have been reported in Table 3 and comparatively illustrated in Fig. 4.

The data on Fig. 4 was normalized by permeability values calculated with DHD. The results show a noticeable deviation in calculated values. It can be seen that permeability depends not only on the methods (Direct Simulations, LBM or PNM) but also on the applied approach. The best matching was observed between DHD and *GeoDict* simulations. *DiMP*, in two cases, has given two times overestimation in comparison with the DHD, which had been chosen as a reference. The LBM tends to overestimate the permeability, and the PNM-based approaches generally generate the lower values. Principally, Direct Simulations demonstrate a higher level of consistency for investigated tight samples.

3.3. How DIP affects permeability

The next section of the research is concerned with the influence of various DIP procedures on the calculations of favorite parameters. The effects of taking a local or global threshold for segmentation, the cubic size of the digital rock model, and implemented types of filters to increase the quality of images have been taken into account to investigate how far they bring about changes of permeability. Generally, the 3D models constructed with the help of Manual DIP on the personal computers are computationally less expensive and much faster. In opposite, Automated DIP allows forming more precise 3D models although it is time-consuming, and its implementation requires having access to the architecture of a High-Performance Computing (HPC) unit.

To analyze the influence of various DIP procedures on the calculations, it was essential to perform calculations based on the same method and the same calculation implementation. For this purpose, we chose *DiMP* academic simulator which has been developed with help of co-authors of this paper. The permeabilities of all 5 samples have firstly been calculated based on the Manual DIP where, due to the technical limitations of the employed PCs, the binarized cubes by the implementation of the Otsu algorithm cannot have the sizes of larger than 400^3 . Following the Cross-Laboratory Control DIP, the same calculations have been performed on samples that have a size of 600^3 and have been segmented into two main phases of grains and pores, according to the Kriging-Indicator algorithm in Schlumberger company. Finally, the permeabilities of the supposed samples have also been calculated according to the outputs of applying the DIP procedure shown in Fig. 2, or known as the Automated DIP method. Using the HPC unit has made it possible to generate the segmented cubes with a size of 1400^3 through the implementation of the RW algorithm. The results have been reported in Table 4.

Table 3

Performance of different methods in terms of calculating the absolute permeability in z -direction, mD .

Sample	Methods					
	Direct Simulations			LBM	PNM	
	<i>DiMP</i>	<i>GeoDict</i>	<i>DHD</i>	<i>PerGeos</i>	<i>OpenPNM</i>	<i>PerGeos</i>
A	0.84	0.71	0.67	1.18	0.39	0.5
B	0.87	0.88	1	1.21	1.57	0.35
C	0.66	0.39	0.32	0.83	0.32	0.18
D	9.38	11.8	10.2	12.5	7.4	7.68
E	1.28	0.83	0.68	1.73	0.36	0.39

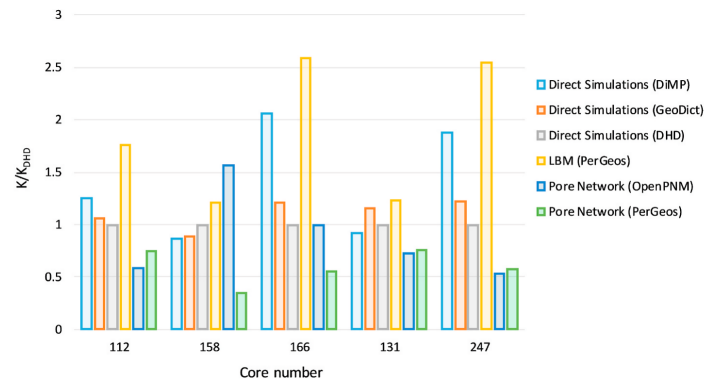


Fig. 4. Calculated permeabilities of each sample based on various methods.

Table 4
Effects of different image processing methods on the results of DiMP, mD.

Sample	Manual DIP				Cross-Laboratory Control DIP				Automated DIP			
	Effective Porosity	k_x	k_y	k_z	Effective Porosity	k_x	k_y	k_z	Effective Porosity	k_x	k_y	k_z
A	0.111	5.22	6.1	5.78	0.058	0.87	1.05	0.84	0.081	2.83	2.31	3.05
B	0.056	0	1.21	0.24	0.044	2.33	1.85	0.87	0.065	1.6	1.71	1.09
C	0.052	0.045	0	0	0.053	0.8	0.54	0.66	0.032	0	0	0
D	0.1	10.85	5.4	9.41	0.097	10.27	9.85	9.38	0.102	15.17	12.98	12.53
E	0.071	0.76	0.24	0.23	0.064	1.16	1.13	1.28	0.09	3.31	2.93	4.02

It can be interpreted that there is not a steady trend among the generated data. For example, the highest and lowest permeability values of *sample A* (for all axes) were calculated based on the results of the Manual DIP and Cross-Laboratory Control DIP, respectively. Also, the highest Z-axes permeability value of *sample B, D* and *E* was obtained for Automated DIP, but the highest value of *sample C* was calculated based on Cross-Laboratory Control DIP.

Furthermore, the anisotropic analysis of the generated results as the function of implemented various image processing methods have visually been represented in Fig. 5. *Sample A* shows isotropic behavior based on all the implemented image processing techniques. In *sample D*, it can be seen that isotropy is virtually independent of the applied DIP method, although implementation of the Manual DIP leads to the generation of a k_y relatively smaller than other values. However, applying the Manual DIP on *sample B* caused Y-axis having permeability significantly larger than the values of the X- and Z-axes. While Manual DIP and Automated DIP generated almost zero permeability for all three axes, the Cross-Laboratory Control DIP showed a low level of anisotropy for *sample C*. The Manual DIP and Cross-Laboratory Control DIP techniques produce isotropic results for *sample E*, while the Automated DIP shows a higher value for k_z .

Regarding the calculated absolute values of permeability, both the Cross-Laboratory Control DIP and Automated DIP produce relatively comparable results. It has been achieved due to using advanced instruments and techniques of image processing to generate the favorite 3D models. Another reason why Cross-Laboratory Control DIP and Automated DIP lead to similar results is that both consider the volumes, 600³ and 1400³ voxels or 0.7 and 1.7 mm respectively, which are larger than the REV (500³ voxels or 0.6 mm).

Typically, various approaches of 3D models building including image processing and the subsequently applied binarization techniques can dramatically influence porosity and permeability calculations. The main effective factors can shortly be known as the quality of image

processing (type, parameters, and consequence of applied filters), binarization type (local or global and 2D or 3D algorithms), size of the 3D models (400³, 600³, 1400³ voxels), and positions of subvolumes in the original CT cubes (for models with sizes smaller than the REV). Besides considering reported results from Table 4, outputs of applying Erosion and Dilatation as the other types of image processing have been added as well. Erosion has continuously been applied several times to *sample A* and relevant porosity and permeability have been calculated with the help of DiMP. For Dilatation the same procedure has also been applied several times, Table 5. It represents that the results of applying Erosion and Dilatation increase the range of petrophysical correlation in comparison with other sorts of results. By applying the sequential operations of Erosion and Dilatation to the initial 3D model, we can estimate the threshold for pores connectivity. In the case of core *sample A*, the threshold level for total porosity is almost 5%. The observed value is in a strong agreement with the behavior of all other data where 3D models with porosity less than 4–6% usually do not have the pore space connectivity (Table 4).

The next step was to compare various techniques of image processing and different methods of permeability calculations (DiMP, GeoDict and DHD) in a cross-plot form. The generated permeabilities of all connected 3D models in the Z direction, which coincides with the flowing direction in standard core samples, have been presented versus their corresponding porosities in Fig. 6. It is observable that all data follow the same trend. It points out that various image processing and binarization procedures result in the same geostatistical outputs. It means that all the porosity and the permeability obtained based on different processing of μ CT images satisfy a single petrophysical model. 3D core models from different DIP covers a wide range of porosity (from 4% to 14%) and permeability (from 0.01 mD to 30 mD).

The spread of permeability in Fig. 6 is the same for Manual DIP, Automated DIP, and Cross-Laboratory Control DIP. In other words, the implementation of all the discussed methods of DIP results in the same

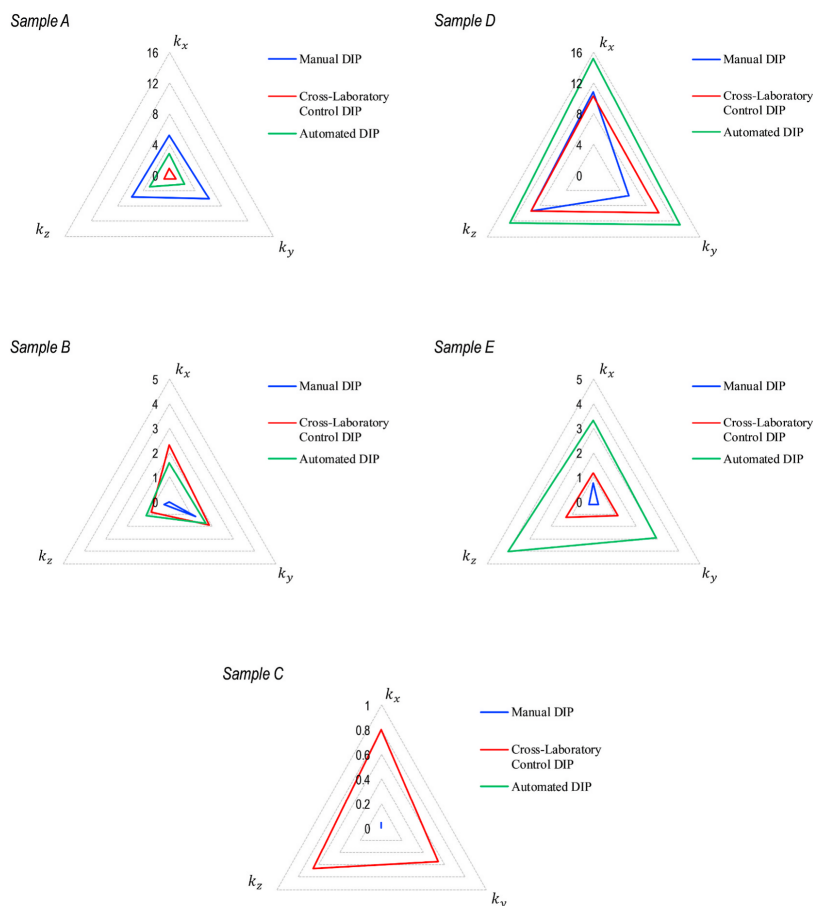


Fig. 5. Effects of image processing on the permeability anisotropy analysis.

Table 5
Results of erosion and dilation, *Sample A*.

Operation	Erosion (4 times)	Erosion (3 times)	Erosion (twice)	Erosion (once)	Original Cube	Dilation (once)	Dilation (twice)	Dilation (3 times)	Dilation (4 times)
Porosity, %	1.8	2.7	4.1	5.9	8.1	10.7	13.4	16.3	19.5
Permeability, mD	0	0	0	1.08	4.5	23.9	45.5	117	288

petrophysical model. Therefore, if we want to investigate a tight reservoir to find correlations between its petrophysical characteristics, it is not necessary to conduct complex and computationally heavy image processing and segmentation. Manual DIP for sample size less than REV could also generate a satisfactory petrophysical correlation.

4. Conclusions

The study has investigated how the employed methods of digital image processing and pore-scale simulation creates uncertainties on the final DRP results of a tight sandstone reservoir. The research has brought

both effects of the various methodologies to create the 3D digital rock models and methods to calculate the permeability on the final results into sharp focus. The absolute permeability has been calculated based on Pore Network Modeling (open-source package), Lattice Boltzmann Method, and Navier-Stokes equations. The generated results showed a significant deviation in calculated permeability values. However, the consistency among different methods of Direct Simulation is in a stronger agreement over the other methods. It should be regarded that although more accurate techniques like *nano*-CT gives rise to less uncertainty over the applied methods and more consistency among generated results, the results of *nano*-CT scanning for rocks with a high

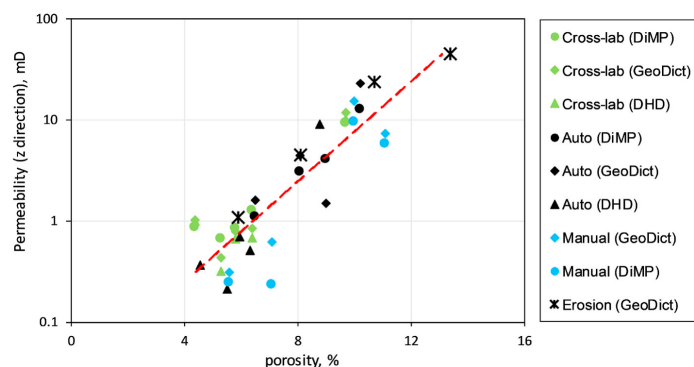


Fig. 6. Porosity - Permeability cross-plot for the various techniques of image processing. **Cross-lab**: Cross-Laboratory Control DIP. **Auto**: Automated DIP. **Manual**: Manual DIP. **Erosion**: Erosion and Dilation morphological transformations for *Sample A*.

degree of heterogeneity are not representative.

The main reason for deviation in calculated permeability values is a complex pore structure of tight sandstones. Some calculation methods are more robust to the geometry of the flow area (Direct Simulation), and some of them generate more errors in permeability calculations (Pore Network Modeling). Thus this trend in permeability deviation due to different calculation methods could be applied to any 3D model of complex structure (with a significant number of thin pore channels and high tortuosity).

The Manual DIP, Cross-Laboratory Control DIP, and Automated DIP as three different methodologies have been applied to create 3D digital rock models. The number of voxels in the final model, consistency, and consequence of image processing and binarization techniques are the main differences. The permeability deviation analyses of gathered clastic tight sandstone samples have shown that image processing and segmentation have stronger impacts on the absolute permeability values than calculation methods. The averaged standard deviations of permeability are:

- $\sigma = 0.71mD$ for the same DIP but different calculation methods, Table 3;
- $\sigma = 1.41mD$ for the same calculation method (DiMP) but different DIP, Table 4.

In other words, if you need to estimate permeability of a specific core sample, it is more important to perform reliable and accurate image processing and segmentation than using advanced calculation techniques.

However, the cross-plot analysis of clastic tight sandstone samples from Achimovskiy formation shows that studying a group of supposed cores through applying the simple DIP (Manual methods) generates the results following the same trend of those results generated by applying the precise DIP (Auto DIP). It means that to find the petrophysical correlation governing the tight samples applying simple DIP can produce a fast and reliable answer.

The open porosity threshold for pores connectivity has been estimated by using the cross-plot analysis of all available data. This threshold level for Achimovskiy formation is equal to 5%. If open porosity of core sample is higher than 5%, μ xCT could resolve the system of connected pores. Otherwise, building a reliable 3D model required implementing a more advanced technique as nano-scale X-ray Computed Tomography μ xCT, FIB-SEM, or synchrotron X-ray CT. The results have shown that by using morphological transformations (Erosion and Dilation) or other instruments of 3D model treatment, it is possible to obtain statistical representative data for Achimovskiy

formation with the help of only one X-Ray CT of one sample.

Data availability

All the grayscale μ xCT and the processed binary images have been shared at <https://data.mendeley.com/datasets/s7dn6jvrpw/1>.

Declaration of competing interest

The authors declare that they have no known competing financial interests or personal relationships that could have appeared to influence the work reported in this paper.

Acknowledgement

We would like to thank Mr. Gwenolé Tallec from Thermo Fisher Scientific to provide us with an trial license for PerGeos software. It also our great pleasure to appreciate Mr. Alexander Avdonin from Gazpromneft Science & Technology Center that his comments improved the manuscript significantly.

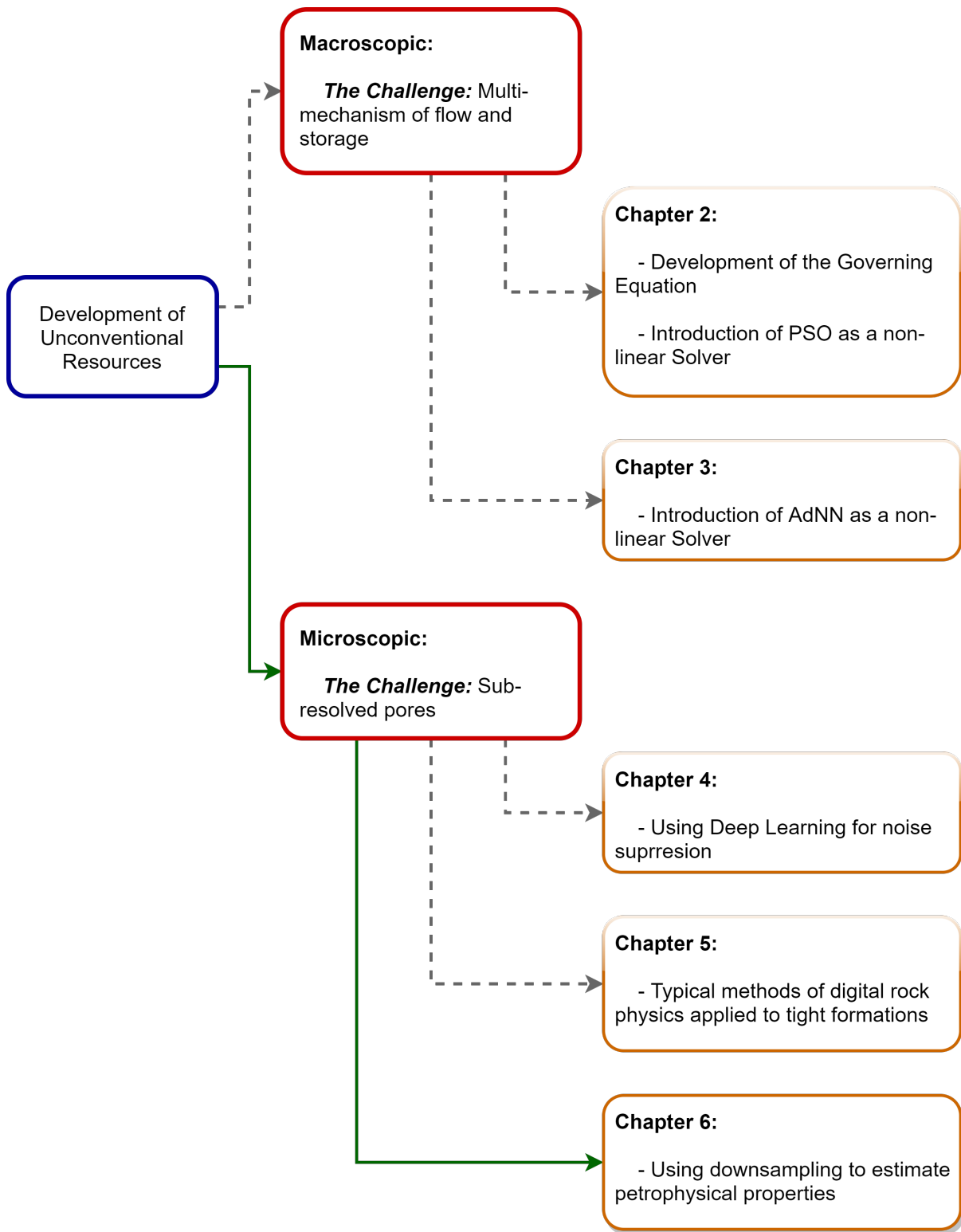
References

- Al-Marzouqi, H., 2018. Digital rock physics: using ct scans to compute rock properties. *IEEE Signal Process. Mag.* 35 (2), 121–131.
- Baklanov, M., Mogilnikov, K., Polovinkin, V., Dultsev, F., 2000. Determination of pore size distribution in thin films by ellipsometric porosimetry. *J. Vac. Sci. Technol. B: Microelectronics and Nanometer Structures Processing, Measurement, and Phenomena* 18 (3), 1385–1391.
- Balashov, V.A., Savenkov, E.B., Chetverushkin, B.N., 2019. Dimp-hydro solver for direct numerical simulation of fluid microflows within pore space of core samples. *Matematicheskoe modelirovanie* 31 (7), 21–44.
- Bezyan, Y., Ebadi, M., Gerami, S., Rafati, R., Sharifi, M., Koroteev, D., 2019. A novel approach for solving nonlinear flow equations: the next step towards an accurate assessment of shale gas resources. *Fuel* 236, 622–635.
- Boas, F.E., Fleischmann, D., 2012. Ct artifacts: causes and reduction techniques. *Imag. Med.* 4 (2), 229–240.
- Boujelben, A., McDougall, S., Watson, M., Bondino, I., Agenet, N., 2018. Pore network modelling of low salinity water injection under unsteady-state flow conditions. *J. Petrol. Sci. Eng.* 165, 462–476.
- Bultreys, T., De Boever, W., Cnudde, V., 2016. Imaging and image-based fluid transport modeling at the pore scale in geological materials: a practical introduction to the current state-of-the-art. *Earth Sci. Rev.* 155, 93–128.
- Cerqueira, R., Paladino, E., Ynumaru, B., Maliska, C., 2018. Image processing techniques for the measurement of two-phase bubbly pipe flows using particle image and tracking velocimetry (piv/ptv). *Chem. Eng. Sci.* 189, 1–23.
- Chen, M., Cheng, L., Wang, X., Lyu, C., Cao, R., 2019. Pore network modelling of fluid flow in tight formations considering boundary layer effect and media deformation. *J. Petrol. Sci. Eng.* 180, 643–659. <https://doi.org/10.1016/j.petrol.2019.05.072>.
- de Oliveira, G.L.P., Ceia, M.A., Missagia, R.M., Neto, I.L., Santos, V.H., Paranhos, R., 2020. Core plug and 2d/3d-image integrated analysis for improving permeability

- estimation based on the differences between micro-and macroporosity in middle east carbonate rocks. *J. Petrol. Sci. Eng.* 107–335.
- Diwakar, M., Kumar, M., 2018. A review on ct image noise and its denoising. *Biomed. Signal Process. Contr.* 42, 73–88.
- Eklund, A., Dufort, P., Forsberg, D., LaConte, S.M., 2013. Medical image processing on the gpu—past, present and future. *Med. Image Anal.* 17 (8), 1073–1094.
- Eshghinejadfar, A., Daróczy, L., Janiga, G., Thévenin, D., 2016. Calculation of the permeability in porous media using the lattice Boltzmann method. *Int. J. Heat Fluid Flow* 62, 93–103.
- Golab, A., Deakin, L., Ravlo, V., Mattisson, C., Carnerup, A., Young, B., Idowu, N., Al-Jeri, S., Al-Rushaid, M., et al., 2015. Digital core analysis of lower ahmadi to upper wara formations. In: *SPE Kuwait Oil and Gas Show and Conference*. Society of Petroleum Engineers.
- Grady, L., 2006. Random walks for image segmentation. *IEEE Trans. Pattern Anal. Mach. Intell.* 11, 1768–1783.
- Graf, T., et al., 2014. Vertical and horizontal integration to overcome extreme operational challenges for the achimov tight, gas-condensate formation. In: *SPE Russian Oil and Gas Exploration & Production Technical Conference and Exhibition*. Society of Petroleum Engineers.
- Grathoff, G.H., Peltz, M., Enzmann, F., Kaufhold, S., 2016. Porosity and permeability determination of organic-rich positionia shales based on 3-d analyses by fib-sem microscopy. *Solid Earth* 7 (4), 1145–1156.
- Grechneva, O.M., Malygina, O., Ignatyev, A., Zakrevskiy, K., et al., 2012. Experience in geology study and 3d modeling of achimovka formations of the urengoy field based on 3d seismic survey data. In: *SPE Russian Oil and Gas Exploration and Production Technical Conference and Exhibition*. Society of Petroleum Engineers.
- Y. Hu, R. T. Armstrong, I. Shikhov, T. T. Hung, B. Lee, P. Mostaghimi, et al., **Unsteady-state coreflooding monitored by positron emission tomography and x-ray computed tomography**, *SPE J.*
- P. Iassonov, T. Gebrenegus, M. Tuller, **Segmentation of x-ray computed tomography images of porous materials: a crucial step for characterization and quantitative analysis of pore structures**, *Water Resour. Res.* 45 (9).
- Islam, A., Chevalier, S., Sassi, M., 2018. Structural characterization and numerical simulations of flow properties of standard and reservoir carbonate rocks using micro-tomography. *Comput. Geosci.* 113, 14–22.
- Ivanova, A., Orlov, D., Mitiurev, N., Cheremisin, A., Khayrullin, M., Zhiron, A., Afanasiev, I., Sansiev, G., et al., 2019. Microstructural imaging and characterization of organic matter presented in carbonate oil reservoirs. In: *SPE Europe Featured at 81st EAGE Conference and Exhibition*. Society of Petroleum Engineers.
- Kaestner, A., Lehmann, E., Stamparoni, M., 2008. Imaging and image processing in porous media research. *Adv. Water Resour.* 31 (9), 1174–1187.
- Kornilov, A., Safonov, I., Yakimchuk, I., 2019. Blind quality assessment for slice of microtomographic image. In: 2019 24th Conference of Open Innovations Association (FRUCT). *IEEE*, pp. 170–178.
- Koroteev, D., Dinariev, O., Evseev, N., Klemin, D., Nadeev, A., Safonov, S., Gурpinar, O., Berg, S., Van Kruijsdijk, C., Armstrong, R., et al., 2014. Direct hydrodynamic simulation of multiphase flow in porous rock. *Petrophysics* 55 (4), 294–303, 0.
- Krutko, V., Belozero, B., Budenny, S., Sadikhov, E., Kuzmina, O., Orlov, D., Muravleva, E., Koroteev, D., et al., 2019. A new approach to elastic rocks pore-scale topology reconstruction based on automatic thin-section images and ct scans analysis. In: *SPE Annual Technical Conference and Exhibition*. Society of Petroleum Engineers.
- Landis, E.N., Keane, D.T., 2010. X-ray microtomography. *Mater. Char.* 61 (12), 1305–1316.
- Liu, X., Wang, J., Ge, L., Hu, F., Li, C., Li, X., Yu, J., Xu, H., Lu, S., Xue, Q., 2017. Pore-scale characterization of tight sandstone in yanchang formation ordos basin China using micro-ct and sem imaging from nm-to cm-scale. *Fuel* 209, 254–264.
- Ma, J., 2016. Pore-scale characterization of gas flow properties in shale by digital core analysis. In: *Unconventional Oil and Gas Resources Handbook*. Elsevier, pp. 127–150.
- Mahanta, B., Vishal, V., Ranjith, P., Singh, T., 2020. An insight into pore-network models of high-temperature heat-treated sandstones using computed tomography. *J. Nat. Gas Sci. Eng.* 103227.
- Manwart, C., Aaltosalmi, U., Koponen, A., Hilfer, R., Timonen, J., 2002. Lattice-Boltzmann and finite-difference simulations for the permeability for three-dimensional porous media. *Phys. Rev.* 66 (1), 016702.
- Mehmani, A., Verma, R., Prodanović, M., 2019. Pore-scale modeling of carbonates. *Mar. Petrol. Geol.* 104–141.
- Mehmani, A., Kelly, S., Torres-Verdin, C., 2020. Leveraging digital rock physics workflows in unconventional petrophysics: a review of opportunities, challenges, and benchmarking. *J. Petrol. Sci. Eng.* 107083.
- Mostaghimi, P., Blunt, M.J., Bijeljic, B., 2013. Computations of absolute permeability on micro-ct images. *Math. Geosci.* 45 (1), 103–125.
- Ning, Y., Zhang, K., He, S., Chen, T., Wang, H., Qin, G., 2019. Numerical modeling of gas transport in shales to estimate rock and fluid properties based on multiscale digital rocks. *Energy Procedia* 158, 6093–6098.
- Oh, W., Lindquist, B., 1999. Image thresholding by indicator kriging. *IEEE Trans. Pattern Anal. Mach. Intell.* 21 (7), 590–602.
- Raeni, A.Q., Bijeljic, B., Blunt, M.J., 2017. Generalized network modeling: network extraction as a coarse-scale discretization of the void space of porous media. *Phys. Rev.* 96 (1), 013312.
- Ramandi, H.L., Mostaghimi, P., Armstrong, R.T., Saadatfar, M., Pinczewski, W.V., 2016. Porosity and permeability characterization of coal: a micro-computed tomography study. *Int. J. Coal Geol.* 154, 57–68.
- Ramstad, T., Berg, C.F., Thompson, K., 2019. Pore-Scale Simulations of Single-And Two-phase Flow in Porous Media: Approaches and Applications. *Transport in Porous Media*, pp. 1–28.
- Rosin, P.L., 2001. Unimodal thresholding. *Pattern Recogn.* 34 (11), 2083–2096.
- Ruspini, L., Lindkvist, G., Bakke, S., Alberts, L., Carnerup, A., Ören, P., et al., 2016. A multi-scale imaging and modeling workflow for tight rocks. In: *SPE Low Perm Symposium*. Society of Petroleum Engineers.
- Saxena, N., Hofmann, R., Alpak, F.O., Berg, S., Dietderich, J., Agarwal, U., Tandon, K., Hunter, S., Freeman, J., Wilson, O.B., 2017. References and benchmarks for pore-scale flow simulated using micro-ct images of porous media and digital rocks. *Adv. Water Resour.* 109, 211–235.
- Saxena, N., Hows, A., Hofmann, R., Alpak, F.O., Dietderich, J., Appel, M., Freeman, J., De Jong, H., 2019. Rock properties from micro-ct images: digital rock transforms for resolution, pore volume, and field of view. *Adv. Water Resour.* 103419.
- Schluditz, K., 2011. Quantitative micro-ct. *J. Microsc.* 243 (2), 111–117.
- R. Song, Y. Wang, J. Liu, M. Cui, Y. Lei, **Comparative Analysis on Pore-Scale Permeability Prediction on Micro-ct Images of Rock Using Numerical and Empirical Approaches**, *Energy Science & Engineering*.
- Sudakov, O., Burnaev, E., Koroteev, D., 2019. Driving digital rock towards machine learning: predicting permeability with gradient boosting and deep neural networks. *Comput. Geosci.* 127, 91–98.
- Sun, H., Tao, G., Vega, S., Al-Suwaidi, A., 2017a. Simulation of gas flow in organic-rich mudrocks using digital rock physics. *J. Nat. Gas Sci. Eng.* 41, 17–29.
- Sun, H., Vega, S., Tao, G., 2017b. Analysis of heterogeneity and permeability anisotropy in carbonate rock samples using digital rock physics. *J. Petrol. Sci. Eng.* 156, 419–429.
- Taud, H., Martinez-Angeles, R., Parrot, J., Hernandez-Escobedo, L., 2005. Porosity estimation method by x-ray computed tomography. *J. Petrol. Sci. Eng.* 47 (3–4), 209–217.
- Tomasi, C., Manduchi, R., 1998. Bilateral filtering for gray and color images. In: *Sixth International Conference on Computer Vision*. (IEEE Cat. No. 98CH36271), *IEEE*, pp. 839–846.
- Verri, I., Della Torre, A., Montenegro, G., Onorati, A., Duca, S., Mora, C., Radaelli, F., Trombin, G., 2017. Development of a digital rock physics workflow for the analysis of sandstones and tight rocks. *J. Petrol. Sci. Eng.* 156, 790–800.
- P. Wang, **Lattice Boltzmann Simulation of Permeability and Tortuosity for Flow through Dense Porous Media**, *Mathematical Problems in Engineering*.
- Wang, L., Wang, S., Zhang, R., Wang, C., Xiong, Y., Zheng, X., Li, S., Jin, K., Rui, Z., 2017. Review of multi-scale and multi-physical simulation technologies for shale and tight gas reservoirs. *J. Nat. Gas Sci. Eng.* 37, 560–578.
- Xiong, Q., Baychev, T.G., Jivkov, A.P., 2016. Review of pore network modelling of porous media: experimental characterisations, network constructions and applications to reactive transport. *J. Contam. Hydrol.* 192, 101–117.
- Yakimchuk, I., Evseev, N., Korobkov, D., Varfolomeev, I., Dinariev, O., Khan, V., Koroteev, D., Orlov, D., Muravleva, E., Belozero, B., et al., 2019. Permeability and porosity study of achimov formation using digital core analysis. In: *SPE Russian Petroleum Technology Conference*. Society of Petroleum Engineers.
- Yang, X., Jia, W., Wu, D., Poon, T.-C., 2017. On the difference between single- and double-sided bandpass filtering of spatial frequencies. *Optic Commun.* 384, 71–77.
- Zhang, T., Salama, A., Sun, S., Zhong, H., 2015. A compact numerical implementation for solving Stokes equations using matrix-vector operations. *Procedia Computer Science* 51, 1208–1218.
- Zhang, L., Jing, W., Yang, Y., Yang, H., Guo, Y., Sun, H., Zhao, J., Yao, J., 2019. The investigation of permeability calculation using digital core simulation technology. *Energies* 12 (17), 3273.
- L. Zhu, C. Zhang, C. Zhang, X. Zhou, Z. Zhang, X. Nie, W. Liu, B. Zhu, **Challenges and Prospects of Digital Core-Reconstruction Research**, *Geofluids*.

6. Strengthening the digital rock physics, using downsampling for sub-resolved pores in tight sandstones

A couple of research has made great efforts to develop techniques to calculate the petrophysical properties of tight samples based on digital rock physics. The main obstacle is taking the effects of those pores that cannot be detected in the images when running various pore-scale simulations. One of the premier ideas is multi-scale imaging, in which some ideas like upscaling is applied to map between the generated results at different spatial resolutions. The same concept can synthetically be conducted with the help of a downsampling algorithm. The technique is based on artificially reducing the resolution step-by-step. Then, the established correlation between the computed porosities and the synthetic resolutions will be extrapolated to an extremely high resolution (close to zero) to find the value of the favourite parameter independence of pore size distribution. Also, the impact of the prepared paper to the roadmap of the research has been shown in **Figure 21**.



1001

1002

1003

Figure 21: Chapter 6 in a glance

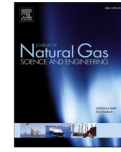
1004 **CRedit author statement:**

- 1005 1. **Mohammad Ebadi:** Conceptualization, Methodology, Software,
1006 Investigation, Writing – Original Draft, Visualization
- 1007 2. **Denis Orlov:** Conceptualization, Methodology, Validation, Formal
1008 Analysis, Data Curation, Writing – Review & Editing
- 1009 3. **Ivan Makhotin:** Software
- 1010 4. **Vladislav Krutko:** Resources, Project Administration
- 1011 5. **Boris Belozerov:** Resources, Project Administration
- 1012 6. **Dmitry Koroteev:** Writing – Review & Editing, Supervision, Project
1013 Administration



Contents lists available at ScienceDirect

Journal of Natural Gas Science and Engineering

journal homepage: <http://www.elsevier.com/locate/jngse>

Strengthening the digital rock physics, using downsampling for sub-resolved pores in tight sandstones

Mohammad Ebadi^{a,*}, Denis Orlov^a, Ivan Makhotin^a, Vladislav Krutko^b, Boris Belozerov^b, Dmitry Koroteev^a

^a Skolkovo Institute of Science and Technology, Moscow, Russia

^b Gazpromneft SRC, St Petersburg, Russia

ARTICLE INFO

Keywords:

Digital rock physics
Tight sandstones
Digital image processing
Downsampling
Sub-resolved pores
Achimovskiy formation

ABSTRACT

Employing digital rock physics (DRP) to study the petrophysical characteristics of tight sandstones is a challenging and problematic issue. The non-resolved individual pores (sub-resolved pores), which cannot be determined in micro x-ray Computed Tomography (μ CT) images, is the main reason for incorrect calculations of the petrophysical properties with DRP. We present a workflow to resolve the matter. We compute the porosity and permeability for the μ CT images of samples from tight sandstone. After that, we apply downsampling. For each downsampled model, the porosity has been calculated. Then, by approximation of the trendline into the porosity data, the porosity for an effective resolution of 0 μ m per voxel (μ m/vox), is estimated. Next, we calculate the bias to correct the computed permeability. The match between calculated parameters and lab measurements proves that the proposed workflow is a reliable approach for practical DRP applications. Further analysis shows that taking advantage of image processing for studies of tight porous media leads to more accurate results than using the conventional petrophysical models of tight resources to map the porosity to permeability.

1. Introduction

Based on the recent advances in various fields of drilling technologies, well completions and reservoir stimulations, developments of tight and ultra-tight hydrocarbon resources have turned into the backbone of booming economies in the world (Solarin and Bello, 2020; Ebadi et al., 2020b). Because of that, the leading oil companies of the global energy perspective have put forth great efforts to have commercial and stable production from the abovementioned hydrocarbon resources (Holditch, 2013; Charlez, 2016). For instance, several joint-ventures and sub-sections of Gazprom have planned to develop one of the most prominent unconventional resources of Russia.

As a set of low-permeable hydrocarbon-bearing layers located in the Western Siberia, Achimovskiy formation has theoretically been categorized as a tight sandstone resource (Nenasheva et al., 2018; Yakimchuk et al., 2019), Fig. 1. It has been formed by moving landslides of sandy and silty flows from shallow water to deep-sea conditions (Grechneva et al., 2012). The presence of tectonic and lithological screens are the main reasons why Achimovskiy formation is vertically and laterally heterogeneous (Yudin et al., 2014).

Despite all the eye-catching technological achievements, the development of unconventional resources might yet be a risky investment if it is not supported well with detailed and accurate reservoir studies (Liu et al., 2017; Almetwally and Jabbari, 2020). To fit the risk attitude of the decision-makers, applying modern methods of core analysis like Digital Rock Physics (DRP) has mainly been focused over the last decade (Bultreys et al., 2016; Wang et al., 2017). Besides the fact that DRP is an efficient method of cost control and risk management, it provides the research projects with the opportunities of performing multiple numerical experiments on exactly the same sample and implementing various analyses on one sample at the same time (Oliveira et al., 2020).

In principle, the standard workflow of DRP is divided into two main steps of Digital Image Processing (DIP), and Pore Scale Simulation (PSS) (Andr a et al., 2013a, b). The most significant target of DIP is to prepare a realistic pore-scale model for the further steps of simulation by taking a series of sequential steps starting from projecting a rock sample with x-ray from different angles and continues with Computed Tomography (CT) to generate micro x-ray CT (μ CT) images, image filtering, histogram analysis, binary segmentation, and three-dimensional (3D) object reconstruction (Karimpouli and Tahmasebi, 2019; Saxena et al., 2018).

* Corresponding author.

E-mail address: Mohammad.Ebadi@skoltech.ru (M. Ebadi).

<https://doi.org/10.1016/j.jngse.2021.103869>

Received 26 October 2020; Received in revised form 11 January 2021; Accepted 14 February 2021

Available online 24 February 2021

1875-5100/  2021 Elsevier B.V. All rights reserved.



Fig. 1. The achimovskiy formation, Russia.

However, applying the DRP method is not always easy and straightforward (Lin et al., 2016). One of the most challenging problems is the sub-resolved pores. The voxels containing sub-resolved pores are not as dark as voxels showing pores and also are not as light as those voxels which are labeled as grains (Smal et al., 2018; Lanetc et al., 2020). It is due to the fact that although x-ray energy can emit through those sub-resolved pores and have subsequent effects on the detector, their smaller sizes than the subsequent spatial resolution of the

projection cannot be recorded as an absolute dark voxel (Baveye et al., 2017; Wang and Aryana, 2020). The sub-resolved pores can be detected by going down to several nanometers using Scanning Electron Microscopy (SEM), but it is a destructive method (Xiao et al., 2020). Thanks to the recent advances in imaging equipment, it is technically possible to generate nano x-ray CT (nxCT) images and overcome the discussed limitation (Mehmani et al., 2020). But, it is physically impracticable because the projecting object should have a diameter of less than 1 mm, but the core samples have diameters of 5–30 mm (Zhu et al., 2019). For instance, the CT images of the gathered samples from Achimovskiy formation have 1.2 μm per voxel ($\mu\text{m}/\text{vox}$) as the Spatial Resolution (SR), which is still larger than a significant portion of detected pores in the mercury injection test (Yakimchuk et al., 2019). To put it more simply, overlapping the obtained SR of the reconstructed CT images with the relevant Pore Size Distribution (PSD) turned it out that a large number of pores cannot be seen in the grayscale CT images (Saxena et al., 2018; Guan et al., 2018), Fig. 2.

Therefore, the PSD of the supposed samples can explicitly be divided into two main zones of resolved pores, which can be seen in the CT images and sub-resolved ones that their recognitions need images with the higher SR (Peng et al., 2014). Accordingly, taking the effects of sub-resolved pores into account is one of the most challenging aspects of DRP. By coupling the advantages of μxCT and QEMSCAN (Quantitative Evaluation of Minerals by SCANning electron microscopy) images, representative 3D mineralogy and porosity maps were reconstructed by Ruspini et al. (2016). Then, the reconstructed maps were employed to obtain a Multi-Scale Pore Network (MSPN) representing both micro- and macro-porosity regions. Eventually, a Process-Based Method (PBM) was applied to the extracted MSPN to characterize the favorite petrophysical properties (Ruspini et al., 2016). Soulaine et al. (2016) studied the impacts of sub-resolution pores of the Berea sandstone samples on their macroscopic flow properties. Through taking advantage of the finite-volume toolbox OpenFOAM A®, flow in the fully resolved pores was described by the application of the Stokes equation, and a Darcy model was also used for the sub-resolution part. Comparing the

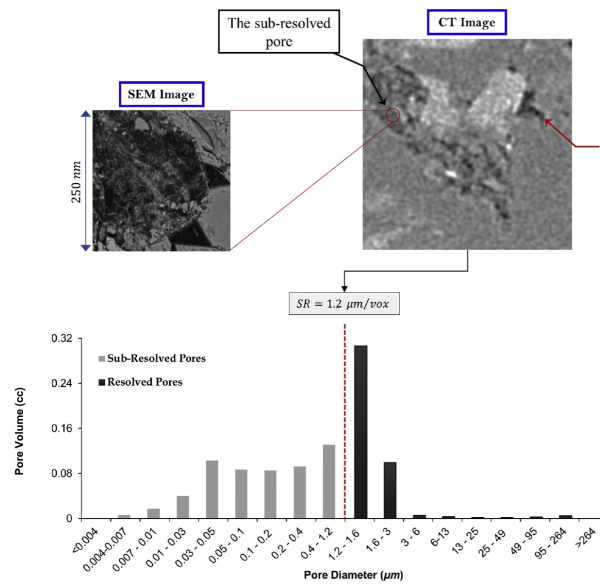


Fig. 2. Sub-resolved pores in CT and SEM images of Achimovskiy Formation.

generated results and experimental ones show that making a clear and proper interpretation of the supposed media is highly required (Soulaire et al., 2016). Regarding the limestone samples, Lin et al. (2016) developed an experimental procedure based on high-salinity contrast brine and differential imaging techniques of computed tomography to obtain 3D spatially resolved information on porosity and the connectivity. Following the various phases of solid grains, sub-resolution micro-pores within the grains, and the macro-pores, conducting an accurate three-phase segmentation causes the generation of results that are in good agreement with the results of helium porosimeter experiments (Lin et al., 2016). As a matter of concern, sub-resolved pores have been tried to be localized and quantified by applying a new algorithm proposed by Smal et al. (2018). Regarding a typical bimodal histogram of a good quality μ xCT image, 6 threshold parameters making zones for two phases of pores and grains are assigned. The mathematical iterative procedure keeps going till finding a stabilized and small difference between neighbors. The generated results show that the proposed algorithm is capable to arguably derive correct porosity estimation in comparison with measured laboratory values. Although the algorithm operates in a fully automatic manner, its performance in case of applying to the histogram of 3D models and tight sources where a more significant portion of pores is known as sub-resolved still needs more discussions (Smal et al., 2018). Shah et al. (2016) studied the petrophysical properties for different rock types varying from sandstone to carbonate samples. The samples were firstly scanned at four different resolutions, and then the generated images were fed to the two modeling techniques of Lattice Boltzmann Method (LBM) and Pore Network Modeling (PNM) for further calculation of permeability. Next, a numerical coarsening method was applied, which artificially reduces the resolution of images. The synthetically reduced-resolution images have been reintroduced to the supposed algorithm. The generated results showed the same accuracy for the favorite parameters. Therefore, it has been deduced that numerical coarsening can be considered as an essential asset in improving the computational efficiency of transport property calculations (Shah et al., 2016). Regarding the grid coarsening technique more, Chung et al. (2020) applied the agglomeration method to merge the neighboring voxels to form macro-elements. The generation of non-uniform gridding for large-scale problems is the main advantage of the agglomeration, which makes the system becomes more computationally affordable to solve. Technically, the binary images are probed with a kernel of $2 \times 2 \times 2$ voxels. If all the examined voxels are pores, the set of supposed voxels are turned into one agglomerated voxel. In case of possibility, the procedure can move further to generate the next level of agglomerated grids (Chung et al., 2020).

The current research employs a more general type of numerical coarsening algorithm known as downsampling to take the effects of sub-resolved pores more practically, effectively, and quickly. The mathematical logic behind the downsampling has firstly been discussed in the next part. Then, it will technically be discussed how the represented approach can either directly or sequentially be applied to the original high-resolution μ xCT images. After that, the main idea will be launched how the series of products by downsampling can mathematically be treated to extract the actual values of the main petrophysical parameters. Next, the set of samples from Achimovskiy formation will go through the pictured process, and the outputs will comprehensively be discussed in results and discussions. Finally, the conclusion will shortly highlight the importance of tight formation again, and it will underline the most important aspects of the implemented approach and the subsequent results.

2. Methodology

2.1. DIP

Regarding the primary concept of DIP as the digitally 3D reconstruction of a concerned sample, the roadmap begins with the x-ray

projection (Blunt et al., 2013; Hakimov et al., 2019). Within the computerized x-ray imaging, narrow beams of x-rays are aimed at a rotating object (Reshetova et al., 2019). During a Computed Tomography (CT) scan, the x-ray tube shoots narrow beams of x-rays through the object, and a special digital x-ray detector which is located directly opposite the source picks up the x-rays after leaving the object (Al-Marzouqi, 2018; Yu et al., 2020). After finishing each rotation, the recorded raw data (sinograms) are transmitted to a computer to reconstruct 2D cross-sectional grayscale images of the object based on sophisticated mathematical techniques (Chauhan et al., 2016). The slices can digitally be stacked to form a 3D representation of the object (Kaeßner et al., 2008).

Due to the number of technical reasons such as artifacts, statistical or random noises, and roundoff errors, the reconstructed μ xCT images could have insufficient quality adversely affecting the features of the final output (Diwakar and Kumar, 2018). Accordingly, it could be highly demanding to take advantage of various filters that subtract the noise component from a noisy image to find the original one with the minimum loss of features (Anas et al., 2011). Although noise suppression from μ xCT images is still considered as a challenging topic, the preservation of image boundaries and global contrast, and no generation of new artifacts are the main common criteria among all the relevant research (Schofield et al., 2020).

Denoising methods can be categorized based on two primary sections of spatial and transform domain filtering. In spatial domain filtering, the target is to reduce noises by applying the filtering process directly on the original noisy images. Several methods like linear and non-linear filters, anisotropic diffusion, dictionary learning techniques, non-local means filters, and deep learning algorithms are known as the principal members of spatial domain filtering. Undoubtedly, bilateral filters are one of the most prominent subsets of spatial domain filtering (Eklund et al., 2013). Following a bilateral filter, the intensity values of voxels in each image are replaced by a weighted average of intensity values from surrounding voxels (Tomasi and Manduchi, 1998). The advantages of bilateral filters like non-linearity, edge-preservation, and smoothness make them excellent choices to be applied to the grey-scale CT images (Landis and Keane, 2010).

Transform domain filtering is mostly known by block-matching and 3D filtering, methods based on scale dependencies, shrinkage rules, wavelet transform, and threshold estimation (Diwakar and Kumar, 2018). Generally, images are Fourier transformed, multiplied with the filter function, and then re-transformed into the spatial domain. Universally, attenuating high frequencies results in a smoother image in the spatial domain, and attenuating low frequencies enhances the edges. As one of the most commonly used methods, the bandpass filter removes noise and background variation. It attenuates very low and very high frequencies but retains a middle-range band of frequencies (Yang et al., 2017; Mafi et al., 2019). It means that bandpass filtering can be used to enhance edges (suppressing low frequencies) while reducing the noise at the same time (attenuating high frequencies) (Cerqueira et al., 2018; Chow and Paramesran, 2016).

Besides, the main idea of DRP is based on the fact that each porous media could be considered as the union set of solid and empty parts. As a consequence, the segmentation techniques should be applied to the denoised grey-scale CT images to turn them into black and white versions resembling pores and solid phase, respectively. In other words, segmentation is the portioning of grey-scale CT images into disjoint regions that comparatively have a uniform density (Taud et al., 2005).

The segmentation algorithms have primarily been classified into two categories: (i) global thresholding segmentation schemes and (ii) segmentation based on the local adaptive schemes. The main idea behind global thresholding schemes is the histogram representation of the intensity and discrepancy of all the grey pixels in a scene. Inherently, global segmentation methods not only do not consider the spatial distribution of intensity values but also they cannot generate the proper segmented images when there are intensity heterogeneities in the target

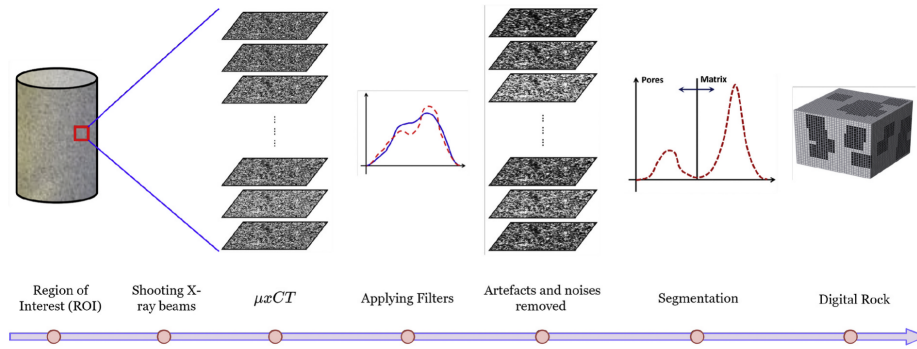


Fig. 3. The DIP workflow to construct a digital rock.

regions. On the quite contrary, the local adaptive segmentation schemes are based on the fact that segmentation decision is made for each voxel. Regularly, taking advantage of the local information causes the generation of segmentations with better quality, but it still demands higher memory and computations (Verri et al., 2017).

To develop a robust segmentation algorithm capable of overcoming the difficulties mentioned above, taking advantage of statistical particle-based methods has drawn many researchers' attention. The applications of Random Walker (RW) theory in other fields of DIP has given fresh impetus to the communities of DRP to represent a highly efficient and practical segmentation algorithm (Grady, 2006). Receiving binary images in which even weak boundaries are respected is the eye-catching output of applying RW theory as the segmentation algorithm where occurrences of crossing the sharp intensity gradients have been avoided by consideration of imposing biases to the main body of the procedure (Haque and Neubert, 2020). Running the RW theory for the segmentation of grey-scale images needs the introduction of two thresholds. All the voxels with the intensity values higher than the larger threshold are grains, and those with intensity values lower than the smaller one are

labeled as pores. The proposed algorithm does make a decision on which class the middle voxels should accordingly be labeled. Since the peak of pores is comparatively very small or submerged within the peak of grains, an automatic algorithm of finding histogram knee should be applied to find the first threshold (Grady, 2006). The second threshold is routinely chosen at the peak of the histogram.

Because of the thresholding nature of the binarization method, the resultant binary images could contain some numerous imperfection. In fact, some voxels attributable to pores could alternately be classified as the matrix part and vice versa (Halisch et al., 2016). Morphological transformations are a collection of nonlinear and shift-invariant operators strongly related to Minkowski additions (Jin et al., 2018). Morphological transformations probe an image with a small template known as the structuring kernel. The structuring kernel is positioned at all possible locations in the image, and it is compared with the corresponding region of voxels (Mostaghimi et al., 2016). Erosion and Dilation are the primary operators that are the foundations for other similar transformations as well. The voxel in the center of the structuring kernel is turned into the minimum or maximum of other elements located in the

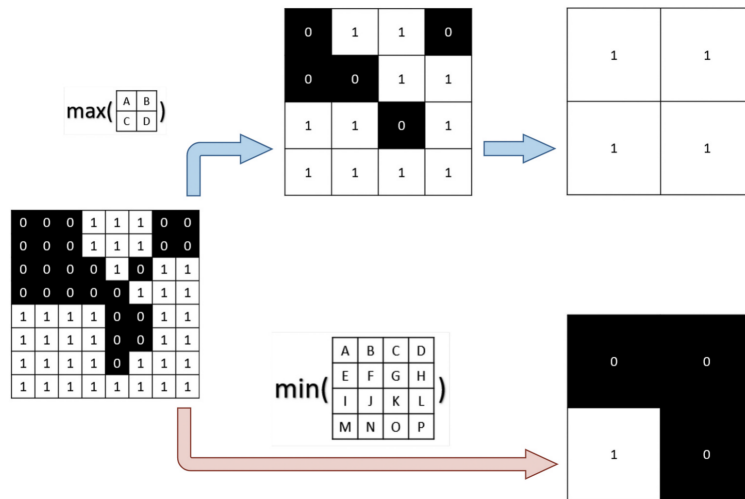


Fig. 4. The schematic procedure of the downsampling algorithm. The blue arrow represents the sequential downsampling with the maximum operator and the kernel size of 2×2 . The red arrow shows the direct downsampling with the minimum operator and the kernel size of 4×4 .

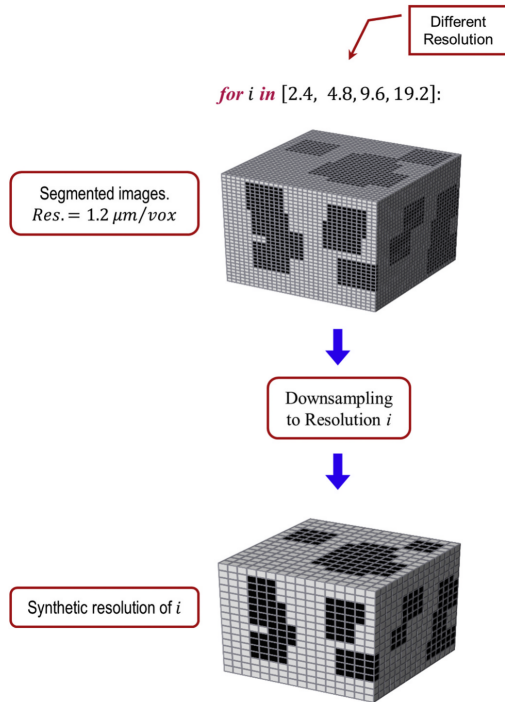


Fig. 5. Application of sequential downsampling on a digital porous media with the maximum operator.

structuring kernel of Erosion or Dilation, respectively (Mostaghimi et al., 2016). The pictured procedure has been depicted in Fig. 3.

2.2. Direct numerical simulation (DNS)

The permeability of the determined REV can be calculated by using Darcy’s law as:

$$k = 10^3 \mu \frac{\langle v \rangle}{\langle \nabla(p) \rangle} \tag{1}$$

where k is the permeability (md), μ stands for fluid viscosity (cp), $\langle v \rangle$ and $\langle \nabla(p) \rangle$ are the superficial averages of velocity (cm/sec) and pressure gradient (atm/cm) over the supposed computational domain provided with the binary images, respectively (Bezvan et al., 2019). In terms of universal conservation laws and following a slow, steady-state, and incompressible flow having negligible inertial forces, the Navier-Stokes equations with the following form can be employed to calculate v and p of all voxels labeled as pores.

$$\begin{aligned} \nabla \cdot v &= 0 \\ \nabla p - \mu \nabla^2 v &= 0 \end{aligned} \tag{2}$$

which is usually completed with no-slip boundary conditions between black and white voxels (Aziz et al., 2020).

Although fluid properties and geometry are the only inputs for further simulations, it should highly be considered that there are not any analytical solutions for Equation 2 in the case of complex morphologies. Thanks to the recent tremendous advances of high-resolution imaging techniques such as μ xCT, it is now possible to accurately describe the

geometry of the complex pore space (Mostaghimi et al., 2012). Among a few numbers of numerical methods that can handle the weak coupling of the velocity and pressure fields, the Semi-Implicit Method for Pressure Linked Equations (SIMPLE) algorithm is the most well-known iterative solver which is widely applied to solve Equation 2 for the concerned digital porous media (Saxena et al., 2017b).

2.3. Downsampling

The numerical coarsening or generally known as downsampling is one of the primary Digital Image Processing (DIP) methods in which the spatial resolution is going to be reduced while keeping the same i-dimensional representation [53]. Regarding a signal as $x = (x_n)$, downsampling x by n can be commonly viewed as pre-filtering x with a linear filter $g = (g_k)$, generating a signal $u = (u_n)$, and then decimating u by i , receiving a signal $v = (v_n)$ where $v_n = u_{in}$ for all n (Starnoni et al., 2017). Practically, the direct or sequential forms of applying the downsampling algorithm, the taken operator (f) of downsampling, and the kernel-size of n as hyperparameters are principally known as the primary sources of uncertainties. Fig. 4 shows two various possible scenarios of downsampling implemented to a schematic segmented μ xCT image.

Following the key concept of downsampling, the finalized binary cube of a sample with an initial high resolution could be applied with the coarsening algorithm (Chung et al., 2020). For instance, a direct procedure of the coarsening algorithm relying on the concept of turning $2 \times 2 \times 2$ neighboring voxels into a single cube based on the maximum operator is graphically illustrated in Fig. 5. The result is a downsampled cube that has the same physical length but with a two times lower resolution. After calculating the favorite parameters of the formed downsampled cube, the algorithm proceeds to the next step where the initial cube undergoes the next iteration of resolution reduction in which $4 \times 4 \times 4$ neighboring voxels are turned into a single voxel having four times lower resolution (Eklund et al., 2013).

2.4. Transform for biases

A systematic offset has been reported when comparing the DRP results of porosity and permeability with those measured in the lab (Ebadi et al., 2020a). More in-depth information shows that DRP analysis results in an underestimation of porosity by a factor of close to 0.5, and overestimation of permeability up to the one magnitude of order (Saxena et al., 2017a). It is due to the fact that the quality of DRP results strongly depends on a variety of determinants like the quality and cleanness of reconstructed μ xCT images (Shah et al., 2016). In more details, the porosity calculated by DRP can adversely be impacted by every element of DIP workflow shown in Fig. 3, including the biases imposed by various methods of segmentation. In principle, the research laboratory is usually implemented on 40 mm cylindrical core plugs while DRP computations are conducted on 4 mm size cubes taken out from the larger core plugs used for laboratory measurements. In other words, the DRP computations are typically made on $\frac{1}{1000}$ th of the sample used for laboratory measurements (Saxena et al., 2018). The referred substantial difference in the physical size of the investigated samples leads to the creation of bias in the computed results even for the ideally homogeneous samples with no geological layering within the plugs. The addressed biases should properly be corrected before making the comparison between DRP results and laboratory measurements. In view of that, the correlation has been recommended by (Saxena et al., 2019) as:

$$\frac{k_f}{k_A} = \beta \tag{3}$$

where k_f stands for the permeability which is calculated based on the Images, and k_A shows the Actual permeability by regarding the effects of sub-resolved pores. k_A can be inferred if the effects of bias (β) is taken

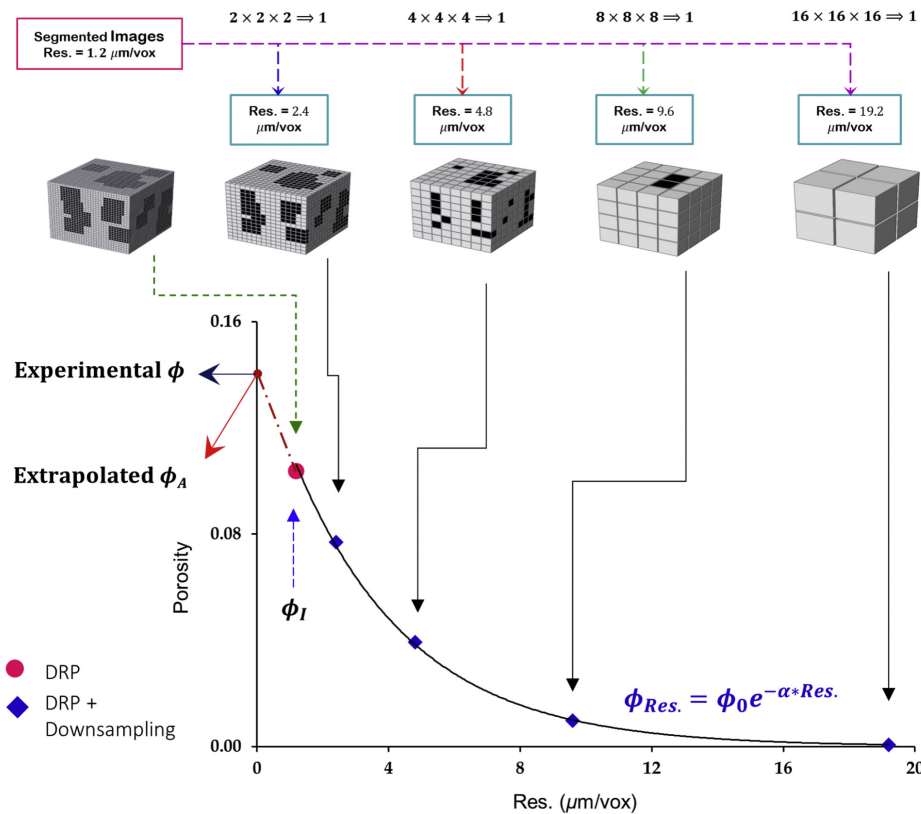


Fig. 6. Implementation of downsampling to take effects of sub-resolved pores into account.

into account. Statistically, the β has been represented as the function of corrections made to porosity, and (Saxena et al., 2017b) has addressed it as:

$$\beta = \left(\frac{\phi_A}{\phi_I}\right)^3 \left(\frac{1 - \phi_I}{1 - \phi_A}\right)^2 \quad (4)$$

similarly, ϕ_I and ϕ_A show the Image and Actual porosities, respectively. It should be highlighted that ϕ_A takes the resolved and sub-resolved pores together.

2.5. The proposed approach

As described above, the determination of the ϕ_A is the main idea behind removing the effects of biases causing overestimation of k_A . To calculate the ϕ_A from the images with sub-resolved pores, taking advantages of downsampling, described in part 2.3, can be considered a significant plus from the point of view of precision and robustness (Shah et al., 2016). Following the finalized binary cube and the consequent downsampled representations shown in Fig. 5, the porosity for each resolution can be calculated through the ratio of black voxels over the total number of voxels (Chung et al., 2020). Then, an exponential trendline is fitted to the scatter plot of porosity versus resolution for each sample. The intersection of the trendline with the y-axis, where the resolution has its highest theoretical value of 0 μm/vox

(Eklund et al., 2013), could show the porosity very close to the experimental values for tight sandstones. The estimated value can adequately be taken as ϕ_A . The supposed procedure has been illustrated in Fig. 6.

The previous studies show that the reduction of resolution leads to less detection of pores, and subsequently, a lower estimation of porosity (Saxena et al., 2019; Bazaikin et al., 2017). For the simulation of the same observations, the downsampling with the maximum operator, which causes the synthetic reduction of porosity, has been selected.

3. Results and discussions

The introduced dataset by (Orlov et al., 2020), including the μ CT images and their corresponding binary ones based on Automated DIP, have been used to conduct the current study. The dataset has been formed based on imaging five samples and then applied with a comprehensive DIP which has shortly been described in part 2.1. More details about the generation of the referenced images and the implemented DIP have thoroughly been discussed in (Orlov et al., 2021). All the grayscale and binary images of the dataset have the sizes of 1400 × 1400 voxels. For each one of the five samples, Fig. 7 shows one grayscale slice and its corresponding binary.

Besides, GeoDict software has been used to calculate k_I based on Equation 2. It should be remarked that all the addressed μ CT and binary images have a spatial resolution of 1.2 μm/vox. Both the lab

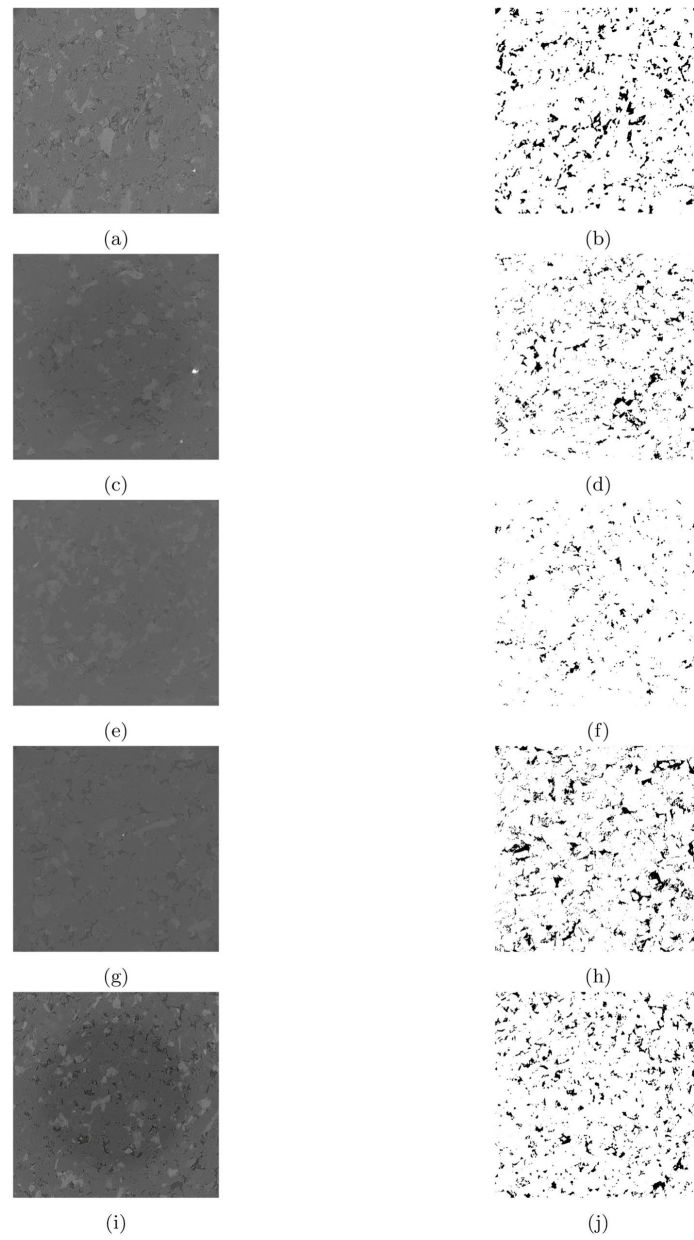


Fig. 7. (a)–(b): Sample a, (c)–(d): Sample B, (e)–(f): Sample C, (g)–(h): Sample D, (i)–(j): Sample E

measurements and image-based calculated values have been reported in Table 1.

To accurately estimate ϕ_A , the represented approach in part 2.5 has been implemented. As depicted in Fig. 6, the digital rock model of each

sample with the spatial resolution of $1.2 \mu\text{m}/\text{vox}$ has been downsampled to lower resolutions based on the direct mode and the maximum operator. After fitting an exponential trendline into the scattered data, the ϕ_A has been estimated by introducing the theoretical resolution of $0 \mu\text{m}/$

Table 1
Porosity and permeability (mD) of selected samples.

Sample	ϕ_{lab}	k_{lab}	ϕ_I	k_I
A	0.133	0.33	0.081	4.46
B	0.112	0.15	0.065	1.58
C	0.905	0.06	0.031	0.12
D	0.146	1.06	0.103	22.9
E	0.131	0.16	0.078	1.5

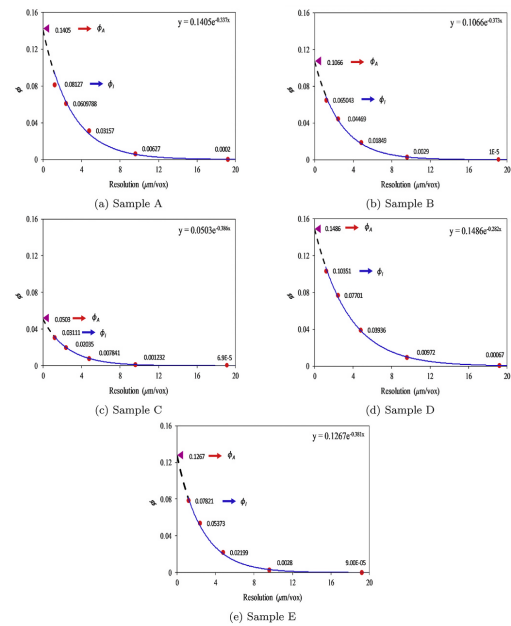


Fig. 8. The estimation of ϕ_A based on the proposed approach for all samples.

Table 2
 ϕ_A and β after downsampling corrections.

Sample	ϕ_A	β
A	0.140	5.90
B	0.106	4.82
C	0.050	4.40
D	0.149	3.28
E	0.127	4.74

vox into the corresponding correlation. The results are in Fig. 8.

The estimated ϕ_A and the corresponding β , stated by Equation 4, for each sample has been reported in Table 2.

The significance of applying the downsampling method and validation of the estimated ϕ_A have been shown in Fig. 9.

It can be deduced that that results of ϕ_A are much closer to the measured ϕ_{lab} . In more details, the mean of $\frac{\phi_A}{\phi_{lab}}$ is almost equals to the unity ($\overline{\phi_{Ra}} = 0.9099$) while the mean of results for $\frac{\phi_I}{\phi_{lab}}$ is almost 37.53% less ($\overline{\phi_{Ra}} = 0.624$). It can be reasoned based on sub-resolved pores, which cannot be detected in the images.

Next, the estimated ϕ_A should be taken to calculate the k_A . Apart from what has been discussed for Equation 3, a couple of studies have introduced other models to map the ϕ_A to k_A in tight systems. In keeping

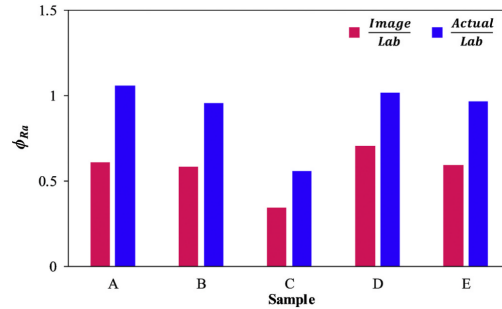


Fig. 9. The porosity Ratio (ϕ_{Ra}) of generated results, $\frac{\phi_I}{\phi_{lab}}$ vs. $\frac{\phi_A}{\phi_{lab}}$.

Table 3
The k_A (mD) based on different models.

Sample	Equation 3	Equation 5	Equation 6
A	0.52	13.92	2.02
B	0.23	1.59	0.52
C	0.03	0.04	0.05
D	3.82	23.38	2.78
E	0.32	5.75	1.16

with the advantages of an exponential trendline, Abbasi et al. (2016) have shown that:

$$k_A = 0.00173e^{64.01\phi_A} \quad (5)$$

In the same way (Du, 2019), has stated the following model by investigation of 35 tight sandstone samples.

$$k_A = 0.0076 \times 1.4879^{100\phi_A} \quad (6)$$

The estimation of k_A as the function of all the refereed models have been made and reported in Table 3. Furthermore, the comparison of the produced k_A versus their lab measurements in terms of permeability Ratio ($k_{Ra} = \frac{k_I}{k_{lab}}$ and $\frac{k_A}{k_{lab}}$) have been depicted in Fig. 10.

As it has already been referred, the generated k_I are larger than the k_{lab} almost for a magnitude of order ($\overline{k_{Ra}} = 11.40$). Not only applying Equations 5 could not result in the generation of satisfying k_A but also in cases of A and E it has caused more deviations. $\overline{k_{Ra}}$ for the results of applying Equations 5 is 22.31. While using Equation 6 can make the resultant k_A close to lab measurements ($\overline{k_{Ra}} = 4.10$), the calculated k_A by Equation 3 are eye-catchingly similar to k_{lab} ($\overline{k_{Ra}} = 1.82$). It should noticeably be considered that applying Equation 3 to estimate k_A results in more deviations in comparison with using other methods. In fact, the implementation of Equation 3 leads to the generation of satisfying results only if the supposed case study has ϕ_I greater than a specific threshold. In more detail (Orlov et al., 2021), have shown that if the ϕ_I is greater than 5%, then it is possible to conduct the correction method.

Additionally, the quality of linear regression among the generated k_A and k_{lab} is the other point of comparison between the result of using Equation 3 and Equation 6, Fig. 11. The results of $R^2 = 0.9942$ shows that the model fits the data very well. Above and beyond, the calculations based on Equation 3 shown in part (b) not just caused the generation of results close to lab measurements ($\overline{k_{Ra}} = 1.82$); they can still fit the data perfectly by the R^2 of 0.9812. As depicted in part (c), results generated by Equation 6 does not fit data well ($R^2 = 0.7695$) although the generated k_A are closer to k_{lab} than k_I .

Finally, the cross-plot analysis of all computed data has been carried out and performed in Fig. 12. It can be observed that petrophysical

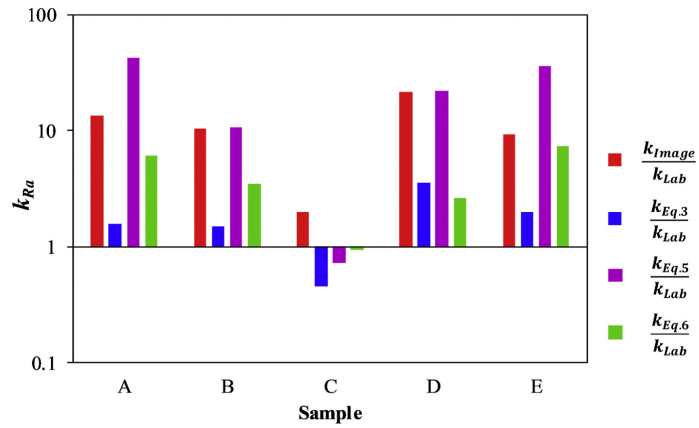


Fig. 10. The comparison of k_I and k_A over the k_{lab} in terms of permeability Ratio (k_{Ra}) based on various models.

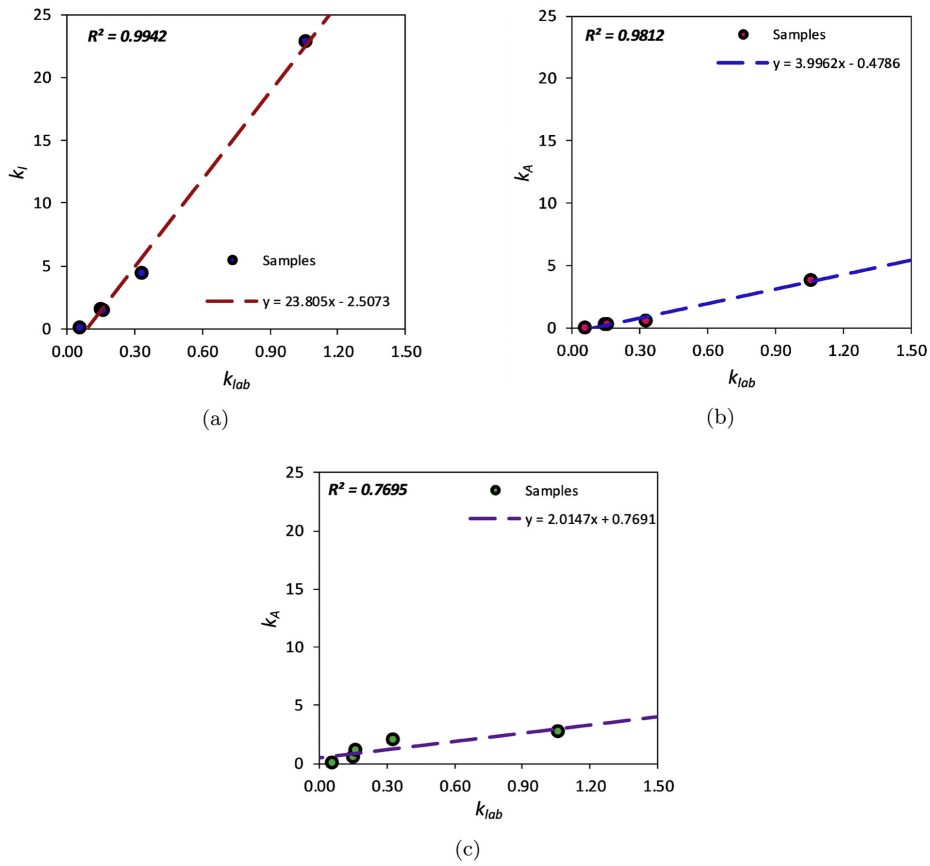


Fig. 11. Regression analysis of calculated k_A . (a) k_I vs. k_{lab} based on the images (b) k_A vs. k_{lab} based on Equation 3 (c) k_A vs. k_{lab} based on Equation 6.

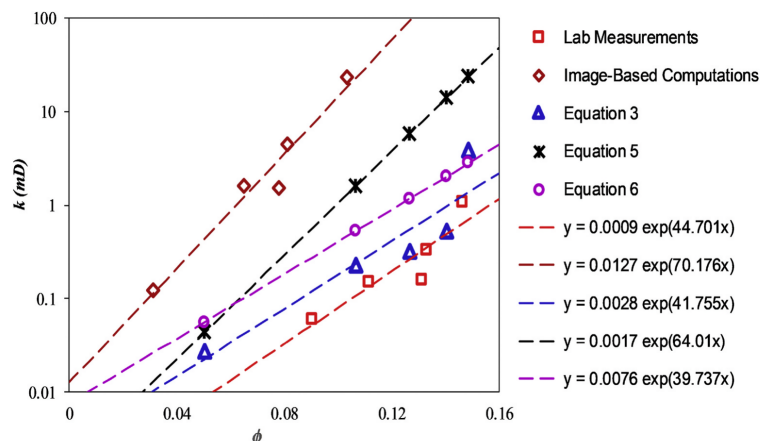


Fig. 12. The cross-plot of permeability vs. porosities.

parameters computed directly based on the available μ xCT images are required to be shifted both horizontally and vertically to be as close as possible to the experimental values. It can be interpreted that the estimation of φ_A by means of downsampling has been successful enough. However, it could be inferred that applying methods based on removing biases is more useful than using correlation to map φ_A to the appropriate k_A . It is due to the fact the proposed method makes attempt to remove the referred biases from the early stages of DIP, and correct the model before running the permeability computations. Comparing the slope and intercept of the exponential trendline fitted to the data generated by using Equation 3 are closer to the same values of the trendline generated by lab measurements than other methods.

4. Conclusion

The energy supply in the future can be guaranteed by the adequate development of tight hydrocarbon resources. The DRP is one of the most effective methods to determine petrophysical parameters. However, the classical DRP cannot generate results close enough to lab measurements in tight porous media because the μ xCT images cannot show the sub-micron pores properly.

Therefore, it is required to employ auxiliary methods to take the effects of sub-resolved pores into account and estimate the core-scale permeability and porosity based on μ xCT images. Downsampling has been remarked as a DIP technique that synthetically can reduce the spatial resolution of supposed images without their physical dimensions. Measuring the model's porosity after each step of downsampling with different kernel sizes and fitting an exponential trendline into the scatter data provides the opportunity to estimate the porosity at $0 \mu\text{m}/\text{vox}$ which is the highest theoretical resolution including the pores with all possible sizes. It must be underlined that using the proposed workflow useful if φ_f is greater than 5%. The resultant φ_f and φ_A can be taken to calculate the inherent bias of DIP. Then, it is possible to calculate the actual permeability for samples whose k_f have already been calculated. The analysis shows that the proposed workflow to determine the porosity and permeability with the consideration of sub-resolved pores can generate results that strongly agree with the lab measurements. On the topic of sub-resolved pores, multi-scale modeling is globally recognized as a standard workflow to characterize petrophysical parameters (Zhao et al., 2018; Wu et al., 2019). Table 4 provides a comparison between this happening often method in the literature and the proposed approach, which takes advantage of downsampling.

Table 4

The advantages of the proposed approach versus multi-scale modeling.

Requirement	Proposed Approach	Multi-scale Modeling
Scans with different resolutions	-	+
Registration	-	+
3D model	Binary, only connected pores do matter	Segmented, high uncertainties due to upscaling
Computations	Only 1 time permeability computation on a 1400^3 voxel model	Computations on different scales for large models ($> 2000^3$ voxels)

Credit author statement

Mohammad Ebadi: Software, Resources, Supervision, Project administration. Denis Orlov: Data curation, Writing – original draft, Visualization, Project administration. Ivan Makhotin: Conceptualization, Methodology, Validation, Formal analysis, Investigation, Resources, Writing – original draft, Writing – review & editing, Supervision, Project administration. Vladislav Krutko: Conceptualization, Methodology, Software, Validation, Formal analysis, Investigation, Data curation, Writing – original draft, Writing – review & editing, Visualization. Boris Belozero: Conceptualization, Methodology, Software, Validation, Formal analysis, Investigation, Data curation, Writing – original draft, Writing – review & editing, Visualization. Dmitry Korteov: Conceptualization, Methodology, Software, Validation, Formal analysis, Investigation, Resources, Data curation, Writing – original draft, Writing – review & editing, Visualization.

Declaration of competing interest

The authors declare that they have no known competing financial interests or personal relationships that could have appeared to influence the work reported in this paper.

References

Abbasi, S., Singh, T., Pritchard, T., 2016. Error and impact of porosity-permeability transform in tight reservoir. J. Nat. Gas Sci. Eng. 35, 354–361.

- Al-Marzouqi, H., 2018. Digital rock physics: using CT scans to compute rock properties. *IEEE Signal Process. Mag.* 35 (2), 121–131.
- Almetwally, A., Jabbari, H., Apr, 2020. Experimental investigation of 3d printed rock samples replicas. *J. Nat. Gas Sci. Eng.* 76, 103192.
- Anas, E.M.A., Kim, J.G., Lee, S.Y., Hasan, M.K., 2011. Comparison of ring artifact removal methods using flat panel detector based CT images. *Biomed. Eng. Online* 10 (1), 72.
- Andrá, H., Combaret, N., Dvorkin, J., Glatt, E., Han, J., Kabel, M., Keehm, Y., Krzikalla, F., Lee, M., Madonna, C., Marsh, M., Mukerji, T., Saenger, E.H., Sain, R., Saxena, N., Ricker, S., Wiegmann, A., Zhan, X., 2013a. Digital rock physics benchmarks—part I: imaging and segmentation. *Comput. Geosci.* 50, 25–32.
- Andrá, H., Combaret, N., Dvorkin, J., Glatt, E., Han, J., Kabel, M., Keehm, Y., Krzikalla, F., Lee, M., Madonna, C., Marsh, M., Mukerji, T., Saenger, E.H., Sain, R., Saxena, N., Ricker, S., Wiegmann, A., Zhan, X., 2013b. Digital rock physics benchmarks—part II: computing effective properties. *Comput. Geosci.* 50, 33–43.
- Aziz, R., Niasar, V., Erfani, H., Martínez-Ferrer, P.J., 2020. Impact of pore morphology on two-phase flow dynamics under wettability alteration. *Fuel* 268, 117315.
- Baveye, P.C., Pot, V., Garnier, P., 2017. Accounting for sub-resolution pores in models of water and solute transport in soils based on computed tomography images: are we there yet? *J. Hydrol.* 555, 253–256.
- Bazaikin, Y., Gurevich, B., Iglauer, S., Khachkova, T., Kolyukhin, D., Lebedev, M., Lisitsa, V., Reshetova, G., 2017. Effect of CT image size and resolution on the accuracy of rock property estimates. *J. Geophys. Res.: Solid Earth* 122 (5), 3635–3647.
- Bezyan, Y., Ebadi, M., Gerami, S., Rafati, R., Sharifi, M., Koroteev, D., 2019. A novel approach for solving nonlinear flow equations: the next step towards an accurate assessment of shale gas resources. *Fuel* 236, 622–635.
- Blunt, M.J., Bijeljic, B., Dong, H., Garbri, O., Iglauer, S., Mostaghimi, P., Paluszny, A., Pentland, C., 2013. Pore-scale imaging and modelling. *Adv. Water Resour.* 51, 197–216.
- Bultreys, T., Boever, W.D., Cnudde, V., 2016. Imaging and image-based fluid transport modeling at the pore scale in geological materials: a practical introduction to the current state-of-the-art. *Earth Sci. Rev.* 155, 93–128.
- Cerqueira, R., Paladino, E., Ynumaru, B., Maliska, C., 2018. Image processing techniques for the measurement of two-phase bubbly pipe flows using particle image and tracking velocimetry (PIV/PTV). *Chem. Eng. Sci.* 189, 1–23.
- Charlez, P.A., 2016. Geopolitics of unconventional resources outside north America. In: *SPE Annual Technical Conference and Exhibition*. Society of Petroleum Engineers.
- Chauhan, S., Rühaak, W., Khan, F., Enzmann, F., Mielke, P., Kersten, M., Sass, I., 2016. Processing of rock core microtomography images: using seven different machine learning algorithms. *Comput. Geosci.* 86, 120–128.
- Chow, L.S., Paramesran, R., 2016. Review of medical image quality assessment. *Biomed. Signal Process. Contr.* 27, 145–154.
- Chung, T., Wang, Y.D., Armstrong, R.T., Mostaghimi, P., 2020. Voxel agglomeration for accelerated estimation of permeability from micro-CT images. *J. Petrol. Sci. Eng.* 184, 106577.
- Diwakar, M., Kumar, M., 2018. A review on CT image noise and its denoising. *Biomed. Signal Process. Contr.* 42, 73–88.
- Du, S., 2019. Prediction of permeability and its anisotropy of tight oil reservoir via precise pore-throat tortuosity characterization and “umbrella deconstruction” method. *J. Petrol. Sci. Eng.* 178, 1018–1028.
- Ebadi, M., Makhotin, I., Orlov, D., Koroteev, D., 2020a. Digital rock physics in low-permeable sandstone, downsampling for unresolved sub-micron porosity estimation. In: *SPE Europe Featured at 82nd EAGE Conference and Exhibition*. Society of Petroleum Engineers.
- Ebadi, M., Zabihifar, S.H., Bezyan, Y., Koroteev, D., 2020b. A nonlinear solver based on an adaptive neural network, introduction and application to porous media flow. *J. Nat. Gas Sci. Eng.* 103749.
- Eklund, A., Dufort, P., Forsberg, D., LaConte, S.M., 2013. Medical image processing on the GPU – past, present and future. *Med. Image Anal.* 17 (8), 1073–1094.
- Grady, L., Nov, 2006. Random walks for image segmentation. *IEEE Trans. Pattern Anal. Mach. Intell.* 28 (11), 1768–1783.
- Grechneva, O.M., Malygina, O., Ignatyev, A., Zakrevskiy, K., 2012. Experience in geology study and 3d modeling of achimovka formations of the urengoy field based on 3d seismic survey data. In: *SPE Russian Oil and Gas Exploration and Production Technical Conference and Exhibition*. Society of Petroleum Engineers.
- Guan, K.M., Nazarova, M., Guo, B., Tchelepi, H., Kovscek, A.R., Creux, P., 2018. Effects of image resolution on sandstone porosity and permeability as obtained from x-ray microscopy. *Transport Porous Media* 127 (1), 233–245.
- Hakimov, N., Zolfaghari, A., Kalantari-Dahaghi, A., Negahban, S., Gunter, G., 2019. Pore-scale network modeling of microporosity in low-resistivity pay zones of carbonate reservoir. *J. Nat. Gas Sci. Eng.* 71, 103005.
- Halisch, M., Steeb, H., Henkel, S., Krawczyk, C.M., 2016. Pore-scale tomography and imaging: applications, techniques and recommended practice. *Solid Earth* 7 (4), 1141–1143.
- Haque, L.R.I., Neubert, J., 2020. Deep learning approaches to biomedical image segmentation. *Informatics in Medicine Unlocked* 18, 100297.
- Holditch, S.A., 2013. Unconventional oil and gas resource development – let’s do it right. *Journal of Unconventional Oil and Gas Resources* 1–2, 2–8.
- Jin, X., Yu, C., Wang, X., Liu, X., Li, J., Jiao, H., Su, L., 2018. Multi-scale digital rock quantitative evaluation technology on complex reservoirs. In: *SPE Asia Pacific Oil and Gas Conference and Exhibition*. Society of Petroleum Engineers.
- Kaestner, A., Lehmann, E., Stampanoni, M., 2008. Imaging and image processing in porous media research. *Adv. Water Resour.* 31 (9), 1174–1187.
- Karimpouli, S., Tahmasebi, P., 2019. Segmentation of digital rock images using deep convolutional autoencoder networks. *Comput. Geosci.* 126, 142–150.
- Landis, E.N., Keane, D.T., 2010. X-ray microtomography. *Mater. Char.* 61 (12), 1305–1316.
- Lanetz, Z., Zhuravljov, A., Jing, Y., Armstrong, R.T., Mostaghimi, P., 2020. Coupling of transient matrix diffusion and pore network models for gas flow in coal. *J. Nat. Gas Sci. Eng.* 103741.
- Lin, Q., Al-Khulaifi, Y., Blunt, M.J., Bijeljic, B., 2016. Quantification of sub-resolution porosity in carbonate rocks by applying high-salinity contrast brine using x-ray microtomography differential imaging. *Adv. Water Resour.* 96, 306–322.
- Liu, X., Wang, J., Ge, L., Hu, F., Li, C., Li, X., Yu, J., Xu, H., Lu, S., Xue, Q., 2017. Pore-scale characterization of tight sandstone in yanchang formation ordos basin China using micro-CT and SEM imaging from nm- to cm-scale. *Fuel* 209, 254–264.
- Mafi, M., Martín, H., Cabrerizo, M., Andrian, J., Barreto, A., Adjouadi, M., 2019. A comprehensive survey on impulse and Gaussian denoising filters for digital images. *Signal Process.* 157, 236–260.
- Mehmani, A., Kelly, S., Torres-Verdin, C., 2020. Leveraging digital rock physics workflows in unconventional petrophysics: a review of opportunities, challenges, and benchmarking. *J. Petrol. Sci. Eng.* 190, 107083.
- Mostaghimi, P., Armstrong, R.T., Gerami, A., Hu, Y., Jing, Y., Kamali, F., Liu, M., Liu, Z., Lu, X., Ramandi, H.L., Zamani, A., Zhang, Y., 2016. Pore scale characterisation of coal: an unconventional challenge. In: *Abu Dhabi International Petroleum Exhibition & Conference*. Society of Petroleum Engineers.
- Mostaghimi, P., Blunt, M.J., Bijeljic, B., Dec, 2012. Computations of absolute permeability on micro-CT images. *Math. Geosci.* 45 (1), 103–125.
- Nenasheva, M., Okunev, M., Sleta, N., Timirgalin, A., Zhukov, V., Garensikh, D., Volkov, G., Priklonsky, O., 2018. The best practices and approaches for replication of achimov formation development technologies (Russian). In: *SPE Russian Petroleum Technology Conference*. Society of Petroleum Engineers.
- Oliveira, G.L.P., Ceia, M.A., Missagia, R.M., Neto, L.L., Santos, V.H., Paranhos, R., 2020. Core plug and 2d/3d-image integrated analysis for improving permeability estimation based on the differences between micro- and macroporosity in middle east carbonate rocks. *J. Petrol. Sci. Eng.* 193, 107335.
- Orlov, D., Ebadi, M., Koroteev, D., Makhotin, I., Belozorov, B., Krutko, V., Yakimchuk, I., Evseev, N., 2020. Dataset for Different Methods of Permeability Calculation in Thin-Pore Tight Sandstones, V1. *Mendeley Data*. <https://doi.org/10.17632/s7dn6jvrpw.1>.
- Orlov, D., Ebadi, M., Muravleva, E., Volkhonskiy, D., Erofeev, A., Savenkov, E., Balashov, V., Belozorov, B., Krutko, V., Yakimchuk, I., Evseev, N., Koroteev, D., 2021. Different methods of permeability calculation in digital twins of tight sandstones. *J. Nat. Gas Sci. Eng.*
- Peng, S., Marone, F., Dultz, S., 2014. Resolution effect in x-ray microcomputed tomography imaging and small pore’s contribution to permeability for a berea sandstone. *J. Hydrol.* 510, 403–411.
- Reshetova, G., Cheverda, V., Lisitsa, V., Khachkova, T., 2019. Multiscale digital rock modelling for reservoir simulation. In: *SPE/IATMI Asia Pacific Oil & Gas Conference and Exhibition*. Society of Petroleum Engineers.
- Ruspini, L.C., Lindkvist, G., Bakke, S., Alberts, L., Carnerup, A.M., Ören, P.E., 2016. A multi-scale imaging and modeling workflow for tight rocks. In: *SPE Low Perm Symposium*. Society of Petroleum Engineers.
- Saxena, N., Hofmann, R., Alpak, F.O., Berg, S., Dieterich, J., Agarwal, U., Tandon, K., Hunter, S., Freeman, J., Wilson, O.B., 2017a. References and benchmarks for pore-scale flow simulated using micro-CT images of porous media and digital rocks. *Adv. Water Resour.* 109, 211–235.
- Saxena, N., Hofmann, R., Alpak, F.O., Dieterich, J., Hunter, S., Day-Stirrat, R.J., 2017b. Effect of image segmentation & voxel size on micro-CT computed effective transport & elastic properties. *Mar. Petrol. Geol.* 86, 972–990.
- Saxena, N., Hows, A., Hofmann, R., Alpak, F.O., Dieterich, J., Appel, M., Freeman, J., Jong, H.D., 2019. Rock properties from micro-CT images: digital rock transforms for resolution, pore volume, and field of view. *Adv. Water Resour.* 134, 103419.
- Saxena, N., Hows, A., Hofmann, R., Alpak, F.O., Freeman, J., Hunter, S., Appel, M., 2018. Imaging and computational considerations for image computed permeability: operating envelope of digital rock physics. *Adv. Water Resour.* 116, 127–144.
- Schofield, R., King, L., Tayal, U., Castellano, I., Stirrup, J., Pontana, F., Earls, J., Nicol, E., 2020. Image reconstruction: Part 1 – understanding filtered back projection, noise and image acquisition. *Journal of Cardiovascular Computed Tomography* 14 (3), 219–225.
- Shah, S., Gray, F., Crawshaw, J., Boek, E., 2016. Micro-computed tomography pore-scale study of flow in porous media: effect of voxel resolution. *Adv. Water Resour.* 95, 276–287.
- Smal, P., Gouze, P., Rodriguez, O., 2018. An automatic segmentation algorithm for retrieving sub-resolution porosity from x-ray tomography images. *J. Petrol. Sci. Eng.* 166, 198–207.
- Solarin, S.A., Bello, M.O., 2020. The impact of shale gas development on the u.s. economy: evidence from a quantile autoregressive distributed lag model. *Energy* 205, 118004.
- Soulaine, C., Gjetvaj, F., Garing, C., Roman, S., Russian, A., Gouze, P., Tchelepi, H.A., 2016. The impact of sub-resolution porosity of x-ray microtomography images on the permeability. *Transport Porous Media* 113 (1), 227–243.
- Starnoni, M., Pokrajac, D., Neilson, J., Sep, 2017. Computation of fluid flow and pore-space properties estimation on micro-CT images of rock samples. *Comput. Geosci.* 106, 118–129.
- Taud, H., Martínez-Angeles, R., Parrot, J., Hernández-Escobedo, L., 2005. Porosity estimation method by x-ray computed tomography. *J. Petrol. Sci. Eng.* 47 (3–4), 209–217.
- Tomasi, C., Manduchi, R., 1998. Bilateral filtering for gray and color images. In: *Sixth International Conference on Computer Vision (IEEE Cat. No.98CH36271)*. Narosa Publishing House.

- Verri, I., Torre, A.D., Montenegro, G., Onorati, A., Duca, S., Mora, C., Radaelli, F., Trombin, G., 2017. Development of a digital rock physics workflow for the analysis of sandstones and tight rocks. *J. Petrol. Sci. Eng.* 156, 790–800.
- Wang, L., Wang, S., Zhang, R., Wang, C., Xiong, Y., Zheng, X., Li, S., Jin, K., Rui, Z., 2017. Review of multi-scale and multi-physical simulation technologies for shale and tight gas reservoirs. *J. Nat. Gas Sci. Eng.* 37, 560–578.
- Wang, Y., Aryana, S.A., Sep. 2020. Pore-scale simulation of gas flow in microscopic permeable media with complex geometries. *J. Nat. Gas Sci. Eng.* 81, 103441.
- Wu, Y., Tahmasebi, P., Lin, C., Ren, L., Dong, C., 2019. Multiscale modeling of shale samples based on low- and high-resolution images. *Mar. Petrol. Geol.* 109, 9–21.
- Xiao, Q., Yang, Z., Wang, Z., Qi, Z., Wang, X., Xiong, S., 2020. A full-scale characterization method and application for pore-throat radius distribution in tight oil reservoirs. *J. Petrol. Sci. Eng.* 187, 106857.
- Yakimchuk, I., Evseev, N., Korobkov, D., Varfolomeev, I., Dinariev, O., Khan, V., Koroteev, D., Orlov, D., Muravleva, E., Belozerov, B., Krutko, V., Kondratev, A., 2019. Permeability and porosity study of achimov formation using digital core analysis. In: *SPE Russian Petroleum Technology Conference*. Society of Petroleum Engineers.
- Yang, X., Jia, W., Wu, D., Poon, T.-C., 2017. On the difference between single- and double-sided bandpass filtering of spatial frequencies. *Optic Commun.* 384, 71–77.
- Yu, H., Fan, J., Xia, J., Liu, H., Wu, H., 2020. Multiscale gas transport behavior in heterogeneous shale matrix consisting of organic and inorganic nanopores. *J. Nat. Gas Sci. Eng.* 75, 103139.
- Yudin, A., Tarakanov, I., Klyubin, A., Ablaev, A., Zharikov, M., Vashkevich, A., Yaskin, I., Sabirov, L., 2014. Channel fracturing improves stimulation efficiency by 30% in the achimov gas condensate formation. In: *nSPE Russian Oil and Gas Exploration & Production Technical Conference and Exhibitio*. Society of Petroleum Engineers.
- Zhao, T., Zhao, H., Ning, Z., Li, X., Wang, Q., 2018. Permeability prediction of numerical reconstructed multiscale tight porous media using the representative elementary volume scale lattice Boltzmann method. *Int. J. Heat Mass Tran.* 118, 368–377.
- Zhu, L., Zhang, C., Zhang, C., Zhou, X., Zhang, Z., Nie, X., Liu, W., Zhu, B., 2019. Challenges and prospects of digital core-reconstruction research. *Geofluids* 1–29.

1026

7. Conclusions and Future Research

1027

In general, the current thesis has tried to investigate how it is possible to maximize

1028

production from unconventional resources with the help of artificial intelligence. It is believed

1029

that taking the effects of multi-scale phenomena of flow and storage and their noticeable degree

1030

of nonlinearity in unconventional resources into account in terms of modelling and simulation

1031

is the most critical macroscopic challenge. The prepared research has tried to determine

1032

whether using various artificial intelligence methods can overcome the supposed difficulty.

1033

Published papers in **Chapters 2** and **3** have shown that using metaheuristic algorithms and

1034

neural networks can perform efficiently for 1D systems although their performances for more

1035

complex systems are still questionable. To put it more simply, it is still not clear that the same

1036

performance will be obtained if the introduced ideas are applied to 2D and 3D cases.

1037

Moreover, the other challenge that should be considered is the applicability of the

1038

proposed methods to the compositional models. In compositional models, it is required to use

1039

the equation of states, adding another level of nonlinearity to the governing equations. For

1040

instance, the fluid flow of condensate or rich gases in the ultra-tight porous media of shale gas

1041

resources can be considered as an in-depth topic of research where not only the complexity of

1042

the geometry is a challenge but also which equation of states should be applied is another aspect

1043

of uncertainty. In fact, the interaction among the various forms of storage in terms of a single

1044

equation of state describing the fluid properties in shale gas resources is a topic that can be

1045

regarded as an important topic of research for future studies.

1046

Following the microscopic analyses of tight formations, the critical point is that a large

1047

portion of pores in the tight formations has a size less than the spatial resolution of μ xCT images

1048

that causes them not to be detected in the μ xCT images. They are technically addressed as "sub-

1049 resolved" pores. The current state of digital rock physics cannot analyze the tight formations,
1050 and it is highly required to take advantage of modern technologies and methods like machine
1051 learning and advanced image processing.

1052 First, the μ xCT images are typically suffering from noises and artefacts. They can lead
1053 to the wrong segmentation results. Hence, it is highly required to remove the noise elements
1054 from the images. Using a suitable set of filters for noise suppression can be time-consuming.
1055 Also, each type of filter has a specific set of parameters that are supposed to be determined by
1056 the user. Although a couple of unsupervised methods can independently improve the quality
1057 of images, using them is still time-consuming. Therefore, it has been tried to use a deep learning
1058 approach that is trained based on unsupervised approaches but implemented on GPUs, **Chapter**
1059 **4**. The next step of research that should be regarded is replacing some accurate but time-
1060 consuming segmentation algorithms with deep learning approaches.

1061 The next step is to understand how much results of using classic pore-scale simulations
1062 are reliable in applying them to the models built based on μ xCT images from tight formations
1063 where many details are missed in the images. **Chapter 5** has shown that it is much-needed to
1064 use modern imaging techniques and simulation methods to improve the quality of digital rock
1065 physics and make them comparable with lab results. As a result, it has been tried in **Chapter 6**
1066 to develop and use a hybrid method of image processing, downsampling and empirical
1067 approaches to estimate the key petrophysical properties of porosity and permeability of the
1068 sample based on the extrapolation of the interpreted correlations. Even though the generated
1069 results are in good agreement with the experimental reports, there are still some challenges.
1070 The estimated properties are bulk values, and it is unclear how the local effects of sub-resolved
1071 pores and their distributions are. A clearer picture of sub-resolved pores can be obtained with
1072 the help of some more advanced technologies like Scanning Electron Microscopic (SEM).

1073 However, mapping extremely high-resolution SEM images to the μ xCT images could be a
1074 critical question for the next level of research. Even if a suitable model of sub-resolved pores
1075 distribution can be obtained, the next question is which technique of pore-scale simulation
1076 should be followed. Taking the sub-resolved pores as a porous material, it is recommended to
1077 use Stokes-Brinkman equations. The topic that can be regarded as the next step of research is
1078 how to make sure that the results of the simulation are valid. Of course, checking the computed
1079 capillary pressure and relative permeability curves of the model with the experimental results
1080 is always a promising method, but the puzzle of how the sub-resolved pores are distributed is
1081 still unanswered. Some modern techniques like Positron Emission Tomography (PET) can
1082 show the advancement of the injecting fluid in the pore-scale. Those observations at the pore-
1083 scale can be taken as an analytical solution to validate the developed models based on μ xCT
1084 images. Arranging the described idea and turning it into action can be an exciting research topic
1085 for interested readers.

1086 Last but not least, mapping between macroscopic and microscopic scales is one of the
1087 most critical steps in the proposed workflow. To the last knowledge of the author, upscaling in
1088 unconventional resources is still open to endless questions. An outstanding research topic is
1089 investigating a multi-scale AI-based approach that can reflect a proper value of petrophysical
1090 properties to a grid block in a continuum-scale simulator based on microscopic properties
1091 already obtained and interpreted.

1092

References

1093

1094 [1] Mohaghegh SD. Reservoir modeling of shale formations. *Journal of Natural Gas*
1095 *Science and Engineering* 2013;12:22–33. doi:10.1016/j.jngse.2013.01.003.

1096 [2] Esmaili S, Mohaghegh SD. Full field reservoir modeling of shale assets using advanced
1097 data-driven analytics. *Geoscience Frontiers* 2016;7:11–20.
1098 doi:10.1016/j.gsf.2014.12.006.

1099 [3] Bryndzia LT, Heath JE, Suarez-Rivera R, Cole DR, Kharaka YK, Ilgen AG, et al. Shales
1100 at all scales: Exploring coupled processes in mudrocks. *Earth-Science Reviews*
1101 2017;166:132–52. doi:10.1016/j.earscirev.2016.12.013.

1102 [4] Solarin SA, Bello MO. The impact of shale gas development on the U.S economy:
1103 Evidence from a quantile autoregressive distributed lag model. *Energy*
1104 2020;205:118004. doi:10.1016/j.energy.2020.118004.

1105 [5] WANG H, MA F, TONG X, LIU Z, ZHANG X, WU Z, et al. Assessment of global
1106 unconventional oil and gas resources. *Petroleum Exploration and Development*
1107 2016;43:925–40. doi:10.1016/S1876-3804(16)30111-2.

1108 [6] Holditch SA. Unconventional oil and gas resource development – Let’s do it right.
1109 *Journal of Unconventional Oil and Gas Resources* 2013;1–2:2–8.
1110 doi:10.1016/J.JUOGR.2013.05.001.

1111 [7] Cuss RJ, Krooss BM, Gensterblum Y, Amann-Hildenbrand A, Zoback MD, Ghanizadeh
1112 A, et al. Gas transport and storage capacity in shale gas reservoirs – A review. Part A:
1113 Transport processes. *Journal of Unconventional Oil and Gas Resources* 2015;12:87–

- 1114 122. doi:10.1016/j.juogr.2015.08.001.
- 1115 [8] Charlez PA. Geopolitics of Unconventional Resources Outside North America. SPE
1116 Annual Technical Conference and Exhibition, Society of Petroleum Engineers; 2016.
1117 doi:10.2118/181405-MS.
- 1118 [9] JPT staff _. Techbits: Defining Unconventional Resources. Journal of Petroleum
1119 Technology 2013;65:36–9. doi:10.2118/0113-0036-JPT.
- 1120 [10] Ashayeri C, Ershaghi I. OPEC and Unconventional Resources. SPE Annual Technical
1121 Conference and Exhibition, Society of Petroleum Engineers; 2015. doi:10.2118/174961-
1122 MS.
- 1123 [11] Holditch SA. Unconventional oil and gas resource development – Let’s do it right.
1124 Journal of Unconventional Oil and Gas Resources 2013;1–2:2–8.
1125 doi:10.1016/j.juogr.2013.05.001.
- 1126 [12] Aguilera RF, Ripple RD, Aguilera R. Link between endowments, economics and
1127 environment in conventional and unconventional gas reservoirs. Fuel 2014;126:224–38.
1128 doi:10.1016/j.fuel.2014.02.063.
- 1129 [13] Wang T, Lin B. Impacts of unconventional gas development on China’s natural gas
1130 production and import. Renewable and Sustainable Energy Reviews 2014;39:546–54.
1131 doi:10.1016/j.rser.2014.07.103.
- 1132 [14] Aguilera RF. Effects of technological progress and external costs on upstream petroleum
1133 supply. Journal of Petroleum Science and Engineering 2021;202:108522.
1134 doi:10.1016/j.petrol.2021.108522.

- 1135 [15] Jacquet JB, Pathak R, Haggerty JH, Theodori GL, Kroepsch AC. Research fatigue in
1136 unconventional oil and gas boomtowns: Perceptions, strategies and obstacles among
1137 social scientists collecting human subjects data. *Energy Research & Social Science*
1138 2021;73:101918. doi:10.1016/j.erss.2021.101918.
- 1139 [16] Hill CB, Yadav OP, Khan E. Systemic risk analyses for potential impacts of onshore
1140 unconventional oil and gas development on public health and the environment: A critical
1141 review. *Science of The Total Environment* 2021;786:147512.
1142 doi:10.1016/j.scitotenv.2021.147512.
- 1143 [17] McClung MR, Moran MD. Understanding and mitigating impacts of unconventional oil
1144 and gas development on land-use and ecosystem services in the U.S. *Current Opinion in*
1145 *Environmental Science & Health* 2018;3:19–26. doi:10.1016/j.coesh.2018.03.002.
- 1146 [18] Solarin SA, Gil-Alana LA, Lafuente C. An investigation of long range reliance on shale
1147 oil and shale gas production in the U.S. market. *Energy* 2020;195:116933.
1148 doi:10.1016/j.energy.2020.116933.
- 1149 [19] Yang H, Han X, Wang L. Is there a bubble in the shale gas market? *Energy*
1150 2021;215:119101. doi:10.1016/j.energy.2020.119101.
- 1151 [20] Wang W, Fan D, Sheng G, Chen Z, Su Y. A review of analytical and semi-analytical
1152 fluid flow models for ultra-tight hydrocarbon reservoirs. *Fuel* 2019;256:115737.
1153 doi:10.1016/j.fuel.2019.115737.
- 1154 [21] Liu H-H, Zhang J. An efficient laboratory method to measure the combined effects of
1155 Knudsen diffusion and mechanical deformation on shale permeability. *Journal of*

- 1156 Contaminant Hydrology 2020;232:103652. doi:10.1016/j.jconhyd.2020.103652.
- 1157 [22] Zhong Y, She J, Zhang H, Kuru E, Yang B, Kuang J. Experimental and numerical
1158 analyses of apparent gas diffusion coefficient in gas shales. Fuel 2019;258:116123.
1159 doi:10.1016/j.fuel.2019.116123.
- 1160 [23] Li D, Xu C, Wang JY, Lu D. Effect of Knudsen diffusion and Langmuir adsorption on
1161 pressure transient response in tight- and shale-gas reservoirs. Journal of Petroleum
1162 Science and Engineering 2014;124:146–54. doi:10.1016/j.petrol.2014.10.012.
- 1163 [24] Gao Q, Han S, Cheng Y, Li Y, Yan C, Han Z. Apparent permeability model for gas
1164 transport through micropores and microfractures in shale reservoirs. Fuel
1165 2021;285:119086. doi:10.1016/j.fuel.2020.119086.
- 1166 [25] Ahmed T. Fractured Reservoirs. Reservoir Engineering Handbook, Elsevier; 2019, p.
1167 1311–88. doi:10.1016/B978-0-12-813649-2.00017-7.
- 1168 [26] Sun H, Yao J, Fan D, Wang C, Sun Z. Gas transport mode criteria in ultra-tight porous
1169 media. International Journal of Heat and Mass Transfer 2015;83:192–9.
1170 doi:10.1016/j.ijheatmasstransfer.2014.11.075.
- 1171 [27] Sun H, Tao G, Vega S, Al-Suwaidi A. Simulation of gas flow in organic-rich mudrocks
1172 using digital rock physics. Journal of Natural Gas Science and Engineering 2017;41:17–
1173 29. doi:10.1016/j.jngse.2017.02.018.
- 1174 [28] Danso DK, Negash BM, Ahmed TY, Yekeen N, Omar Ganat TA. Recent advances in
1175 multifunctional proppant technology and increased well output with micro and nano
1176 proppants. Journal of Petroleum Science and Engineering 2021;196:108026.

- 1177 doi:10.1016/j.petrol.2020.108026.
- 1178 [29] Al Hinai A, Rezaee R, Esteban L, Labani M. Comparisons of pore size distribution: A
1179 case from the Western Australian gas shale formations. *Journal of Unconventional Oil
1180 and Gas Resources* 2014;8:1–13. doi:10.1016/j.juogr.2014.06.002.
- 1181 [30] Yu H, Chen J, Zhu Y, Wang F, Wu H. Multiscale transport mechanism of shale gas in
1182 micro/nano-pores. *International Journal of Heat and Mass Transfer* 2017;111:1172–80.
1183 doi:10.1016/J.IJHEATMASSTRANSFER.2017.04.050.
- 1184 [31] Guo C, Xu J, Wu K, Wei M, Liu S. Study on gas flow through nano pores of shale gas
1185 reservoirs. *Fuel* 2015;143:107–17. doi:10.1016/j.fuel.2014.11.032.
- 1186 [32] Chen G, Lu S, Zhang J, Pervukhina M, Liu K, Wang M, et al. A method for determining
1187 oil-bearing pore size distribution in shales: A case study from the Damintun Sag, China.
1188 *Journal of Petroleum Science and Engineering* 2018;166:673–8.
1189 doi:10.1016/j.petrol.2018.03.082.
- 1190 [33] Zhang Y, Li D, Sun X, Li P. New theoretical model to calculate the apparent
1191 permeability of shale gas in the real state. *Journal of Natural Gas Science and
1192 Engineering* 2019;72:103012. doi:10.1016/j.jngse.2019.103012.
- 1193 [34] Yang D, Wang W, Chen W, Tan X, Wang L. Revisiting the methods for gas permeability
1194 measurement in tight porous medium. *Journal of Rock Mechanics and Geotechnical
1195 Engineering* 2019;11:263–76. doi:10.1016/j.jrmge.2018.08.012.
- 1196 [35] Xia Y, Jin Y, Chen KP, Chen M, Chen D. Simulation on gas transport in shale: The
1197 coupling of free and adsorbed gas. *Journal of Natural Gas Science and Engineering*

- 1198 2017;41:112–24. doi:10.1016/j.jngse.2017.02.024.
- 1199 [36] Fink R, Amann-Hildenbrand A, Bertier P, Littke R. Pore structure, gas storage and
1200 matrix transport characteristics of lacustrine Newark shale. *Marine and Petroleum*
1201 *Geology* 2018;97:525–39. doi:10.1016/j.marpetgeo.2018.06.035.
- 1202 [37] Chen Y, Jiang S, Zhang D, Liu C. An adsorbed gas estimation model for shale gas
1203 reservoirs via statistical learning. *Applied Energy* 2017;197:327–41.
1204 doi:10.1016/j.apenergy.2017.04.029.
- 1205 [38] Shang F, Zhu Y, Hu Q, Zhu Y, Wang Y, Du M, et al. Characterization of methane
1206 adsorption on shale of a complex tectonic area in Northeast Guizhou, China:
1207 Experimental results and geological significance. *Journal of Natural Gas Science and*
1208 *Engineering* 2020;84:103676. doi:10.1016/j.jngse.2020.103676.
- 1209 [39] Pan Z, Connell LD. Reservoir simulation of free and adsorbed gas production from
1210 shale. *Journal of Natural Gas Science and Engineering* 2015;22:359–70.
1211 doi:10.1016/j.jngse.2014.12.013.
- 1212 [40] Belyadi H, Fathi E, Belyadi F. Shale initial gas-in-place calculation. *Hydraulic*
1213 *Fracturing in Unconventional Reservoirs*, Elsevier; 2019, p. 27–34. doi:10.1016/B978-
1214 0-12-817665-8.00003-5.
- 1215 [41] Belyadi H, Fathi E, Belyadi F. Multiscale fluid flow and transport in organic-rich shale.
1216 *Hydraulic Fracturing in Unconventional Reservoirs*, Elsevier; 2019, p. 35–45.
1217 doi:10.1016/B978-0-12-817665-8.00004-7.
- 1218 [42] Takkiri-Borujeni A, Fathi E, Kazemi M, Belyadi F. An integrated multiscale model for

- 1219 gas storage and transport in shale reservoirs. *Fuel* 2019;237:1228–43.
1220 doi:10.1016/j.fuel.2018.10.037.
- 1221 [43] Pang Y, Tian Y, Soliman MY, Shen Y. Experimental measurement and analytical
1222 estimation of methane absorption in shale kerogen. *Fuel* 2019;240:192–205.
1223 doi:10.1016/j.fuel.2018.11.144.
- 1224 [44] Ahmed T. Fundamentals of Reservoir Fluid Flow. *Reservoir Engineering Handbook*,
1225 Elsevier; 2019, p. 331–456. doi:10.1016/B978-0-12-813649-2.00006-2.
- 1226 [45] Cui G, Liu J, Wei M, Shi R, Elsworth D. Why shale permeability changes under variable
1227 effective stresses: New insights. *Fuel* 2018;213:55–71. doi:10.1016/j.fuel.2017.10.068.
- 1228 [46] Canale RP, Chapra SC. Numerical methods for engineers. *Mathematics and Computers*
1229 *in Simulation* 1991;33:260. doi:10.1016/0378-4754(91)90127-O.
- 1230 [47] Behl R, Cordero A, Torregrosa J, Alshomrani A. New Iterative Methods for Solving
1231 Nonlinear Problems with One and Several Unknowns. *Mathematics* 2018;6:296.
1232 doi:10.3390/math6120296.
- 1233 [48] Saheya B, Chen G, Sui Y, Wu C. A new Newton-like method for solving nonlinear
1234 equations. *SpringerPlus* 2016;5:1269. doi:10.1186/s40064-016-2909-7.
- 1235 [49] Tsiptsis IN, Liimatainen L, Kotnik T, Niiranen J. Structural optimization employing
1236 isogeometric tools in Particle Swarm Optimizer. *Journal of Building Engineering*
1237 2019;24:100761. doi:10.1016/j.jobbe.2019.100761.
- 1238 [50] Sibalija T V. Particle swarm optimisation in designing parameters of manufacturing

- 1239 processes: A review (2008–2018). *Applied Soft Computing* 2019;84:105743.
1240 doi:10.1016/j.asoc.2019.105743.
- 1241 [51] Oliva D, Elaziz MA, Elsheikh AH, Ewees AA. A review on meta-heuristics methods for
1242 estimating parameters of solar cells. *Journal of Power Sources* 2019;435:126683.
1243 doi:10.1016/j.jpowsour.2019.05.089.
- 1244 [52] Wang T, Sui S, Tong S. Data-based adaptive neural network optimal output feedback
1245 control for nonlinear systems with actuator saturation. *Neurocomputing* 2017;247:192–
1246 201. doi:10.1016/j.neucom.2017.03.053.
- 1247 [53] Gao S, Liu J. Adaptive neural network vibration control of a flexible aircraft wing
1248 system with input signal quantization. *Aerospace Science and Technology*
1249 2020;96:105593. doi:10.1016/j.ast.2019.105593.
- 1250 [54] Wang L, Wang S, Zhang R, Wang C, Xiong Y, Zheng X, et al. Review of multi-scale
1251 and multi-physical simulation technologies for shale and tight gas reservoirs. *Journal of*
1252 *Natural Gas Science and Engineering* 2017;37:560–78.
1253 doi:10.1016/J.JNGSE.2016.11.051.
- 1254 [55] Ma J. Pore-Scale Characterization of Gas Flow Properties in Shale by Digital Core
1255 Analysis. Elsevier Inc.; 2015. doi:10.1016/B978-0-12-802238-2.00004-3.
- 1256 [56] Du S. Prediction of permeability and its anisotropy of tight oil reservoir via precise pore-
1257 throat tortuosity characterization and “umbrella deconstruction” method. *Journal of*
1258 *Petroleum Science and Engineering* 2019;178:1018–28.
1259 doi:10.1016/J.PETROL.2019.03.009.

- 1260 [57] Zhu L, Zhang C, Zhang C, Zhou X, Zhang Z, Nie X, et al. Challenges and Prospects of
1261 Digital Core-Reconstruction Research. *Geofluids* 2019;2019:1–29.
1262 doi:10.1155/2019/7814180.
- 1263 [58] Andrä H, Combaret N, Dvorkin J, Glatt E, Han J, Kabel M, et al. Digital rock physics
1264 benchmarks-Part I: Imaging and segmentation. *Computers and Geosciences*
1265 2013;50:25–32. doi:10.1016/j.cageo.2012.09.005.
- 1266 [59] Marsh M, Zhang S. Introduction to Digital Rock Physics and Predictive Rock Properties
1267 What is Digital Rock Physics ? n.d.
- 1268 [60] Saxena N, Hows A, Hofmann R, Alpak FO, Dietderich J, Appel M, et al. Rock properties
1269 from micro-CT images: Digital rock transforms for resolution, pore volume, and field
1270 of view. *Advances in Water Resources* 2019;134:103419.
1271 doi:10.1016/J.ADVWATRES.2019.103419.
- 1272 [61] Diwakar M, Kumar M. A review on CT image noise and its denoising. *Biomedical*
1273 *Signal Processing and Control* 2018;42:73–88. doi:10.1016/j.bspc.2018.01.010.
- 1274 [62] Chow LS, Paramesran R. Review of medical image quality assessment. *Biomedical*
1275 *Signal Processing and Control* 2016;27:145–54. doi:10.1016/j.bspc.2016.02.006.
- 1276 [63] Blunt MJ, Bijeljic B, Dong H, Gharbi O, Iglauer S, Mostaghimi P, et al. Pore-scale
1277 imaging and modelling. *Advances in Water Resources* 2013;51:197–216.
1278 doi:10.1016/J.ADVWATRES.2012.03.003.
- 1279 [64] Xiong Q, Baychev TG, Jivkov AP. Review of pore network modelling of porous media:
1280 Experimental characterisations, network constructions and applications to reactive

- 1281 transport. *Journal of Contaminant Hydrology* 2016;192:101–17.
1282 doi:10.1016/J.JCONHYD.2016.07.002.
- 1283 [65] Chung T, Wang YD, Armstrong RT, Mostaghimi P. Approximating permeability of
1284 microcomputed-tomography images using elliptic flow equations. *SPE Journal*
1285 2019;24:1154–63. doi:10.2118/191379-PA.
- 1286 [66] Chung T, Wang Y Da, Armstrong RT, Mostaghimi P. Voxel agglomeration for
1287 accelerated estimation of permeability from micro-CT images. *Journal of Petroleum*
1288 *Science and Engineering* 2019:106577. doi:10.1016/J.PETROL.2019.106577.
- 1289 [67] Ma J, Basics HFC, Data O, Problems C. Chapter 4 - Pore-Scale Characterization of Gas
1290 Flow Properties in Shale by Digital Core Analysis. In: Wierenga B, editor. vol. 121,
1291 Boston: Gulf Professional Publishing; 2016, p. 127–50.
1292 doi:https://doi.org/10.1016/B978-0-12-802238-2.00004-3.
- 1293 [68] Wildenschild D, Sheppard AP. X-ray imaging and analysis techniques for quantifying
1294 pore-scale structure and processes in subsurface porous medium systems. *Advances in*
1295 *Water Resources* 2013;51:217–46. doi:10.1016/j.advwatres.2012.07.018.
- 1296 [69] Wang Y, Teng Q, He X, Feng J, Zhang T. CT-image of rock samples super resolution
1297 using 3D convolutional neural network. *Computers & Geosciences* 2019;133:104314.
1298 doi:10.1016/J.CAGEO.2019.104314.
- 1299 [70] Shaik AR, Al-Ratrout AA, AlSumaiti AM, Jilani AK. Rock Classification Based on
1300 Micro-CT Images using Machine Learning Techniques. Day 2 Tue, November 12, 2019,
1301 SPE; 2019. doi:10.2118/197651-MS.

- 1302 [71] Soulaine C, Tchelepi HA. Micro-continuum Approach for Pore-Scale Simulation of
1303 Subsurface Processes. *Transport in Porous Media* 2016;113:431–56.
1304 doi:10.1007/s11242-016-0701-3.
- 1305 [72] Smal P, Gouze P, Rodriguez O. An automatic segmentation algorithm for retrieving sub-
1306 resolution porosity from X-ray tomography images. *Journal of Petroleum Science and*
1307 *Engineering* 2018;166:198–207. doi:10.1016/J.PETROL.2018.02.062.
- 1308 [73] Chauhan S, Rühaak W, Khan F, Enzmann F, Mielke P, Kersten M, et al. Processing of
1309 rock core microtomography images: Using seven different machine learning algorithms.
1310 *Computers & Geosciences* 2016;86:120–8. doi:10.1016/j.cageo.2015.10.013.
- 1311 [74] Oulhaj H, Amine A, Rziza M, Aboutajdine D. Noise Reduction in Medical Images -
1312 comparison of noise removal algorithms -. *2012 International Conference on*
1313 *Multimedia Computing and Systems, IEEE;* 2012, p. 344–9.
1314 doi:10.1109/ICMCS.2012.6320218.
- 1315 [75] Arsalan M, Kim DS, Lee MB, Owais M, Park KR. FRED-Net: Fully residual encoder–
1316 decoder network for accurate iris segmentation. *Expert Systems with Applications*
1317 *2019;122:217–41.* doi:10.1016/j.eswa.2019.01.010.
- 1318 [76] Mostaghimi P, Blunt MJ, Bijeljic B. Computations of Absolute Permeability on Micro-
1319 CT Images. *Mathematical Geosciences* 2013;45:103–25. doi:10.1007/s11004-012-
1320 9431-4.
- 1321 [77] Saxena N, Hofmann R, Alpak FO, Dietderich J, Hunter S, Day-Stirrat RJ. Effect of
1322 image segmentation & voxel size on micro-CT computed effective transport &

1323 elastic properties. *Marine and Petroleum Geology* 2017;86:972–90.

1324 doi:10.1016/j.marpetgeo.2017.07.004.

1325